Performance and Thermal Impact Analysis of Single Cell Solid Oxide Fuel Cell by Utilizing Different Fuels and its Upgradation to Stack Level

Tariq Nawaz Chaudhary

Submitted for the degree of Doctor of Philosophy

Heriot-Watt University
School of Engineering and Physical Sciences/IMPEE
February, 2018

ABSTRACT

A numerical model of a single planar and stack of solid oxide fuel cell (SOFC) is developed by coupling dynamics of electrochemical reacting flows, heat transfer, and thermal impacts (thermal strains and stresses) of solid electrolyte and porous electrodes for analysing the cell performance. The model is tested and the simulation results of hydrogen fuel SOFC performance are verified with the bench mark data of International Energy Agency (IEA) for co-flow case. Modelling results from test cases show that the coupling is necessary as the electrochemical and thermal properties of the cell strongly depends on temperature. The thermal strains and stresses generated in the cell are then predicted by implementing the temperature profile obtained from the decoupling (the thermal properties of materials are independent of temperature) and coupling simulations. The distributions of thermal strains and stresses, from which the locations with higher values are identified, provide data for optimizing design of SOFC.

The thermal impacts of the cell are investigated by employing alternative fuels such as methane. The methane steam reforming (MSR) and water gas shift (WGS) reactions are strongly temperature dependents and play the key role on both the cell performance and thermal impacts. It has been found that temperature decreases along the main flow direction because of MSR reactions dominancy. The thermal strains and stresses generated in methane based SOFC are less than those by hydrogen fed SOFC if both operate to produce identical power.

The parametric study is performed to investigate the effect of operating conditions such as inlet temperature, flow rates, flow configurations (co-flow and counter flow), geometrical parameters (porosity, change in cell thickness), and operating voltage on the cell performance and thermal impact. It has been identified that the inlet temperature has significant effect on the cell performance and thermal impact. The co-flow configuration offers better thermo-mechanical stability. The higher operating voltage results in lower thermal strain and stress generation.

The methane fuel model is upgraded to the stack level and the performance of the 8 cells connected in parallel flow configuration has been investigated. The effect of Lanthanum Chromite interconnect between two cells on the cell performance has been analysed by investigations of the distributions of chemical species, reaction rates, temperature, and thermal strain and stress for each cell. It has been recognized that the difference in the performance of the bottom and top cells as compared to the cells in between them is high because of the presence of the interconnect. The temperature distribution along the stack

height is non-uniform which leads to non-uniform thermal strain and stress generation. The non-uniform thermal strain and stress generation increases the possibilities of the cell failure which must be taken into account for cell design and operation monitoring.

Dedication

This thesis is dedicated to my parents Muhammad Nawaz and Naeem Akhter, my wife Gulsaria, my son Muhammad Sayyam and my daughter Amaya.

Acknowledgements

I would like to start it by thanking all the ones who really helped me through this thesis. I mainly have thanked those people by myself (maybe for several times), but I still feel that those thanks are not sufficient enough. Even within this acknowledgement, I really do not think that I could express everything or could thank them in the best possible manner. Thereby during writing this acknowledgement, I prayed to God and requested him to help them in their lives as they help me through my life. God bless them all. Among these people firstly, I would like to thank my family. They are the ones who really helped me with whatever they could and supported me up with whatever they have. Thereby I would like to thank my father, my mother, my wife, my son, my daughter, my brothers, and my sister.

Greatest thanks to Dr. Baixin Chen to accept me as his student (this is what I am mostly proud of). I learned several things from him during the span of my PhD research. With several duties in hold, he guided me in the best possible manner and helped me through several severe difficulties. Through his suggestions, supports, guidelines, and helps this thesis could be made. Therefore I would like to thank him with the best I can for all of these helps.

I am grateful to Dr. Jin Xuan for sharing his knowledge about the fuel cell and giving his valuable suggestions regarding my research. I appreciate the help from Dr. Meng Ni of Poly Technique University Hong Kong to provide useful information at different stage of my research.

I would like to acknowledge the financial support from University of Engineering and Technology, Lahore, Pakistan in terms of providing the scholarship under Faculty Development Program to pursue my PhD studies at Heriot Watt University.

A special thanks to our research group members especially Dr. Marius Dewar, Dr. Sorush Khajepor, Mr. Mubbashar Mehmood and Mr. Umer Saleem, for their technical support and advice throughout the project.

Finally, I would like to thank Mr. Aftab Aziz for his continuous support. During my research period he helps me a lot in setting up the computers and the software which I required for my research and thesis write up.

ACADEMIC REGISTRY

Research Thesis Submission

Name*:*	Tariq Nawaz Chaudhary		
School:	EPS		
Version: *(i.e. First, Resubmission, Final)*	Final	Degree Sought:	PhD

Declaration

In accordance with the appropriate regulations I hereby submit my thesis and I declare that:

1) the thesis embodies the results of my own work and has been composed by myself
2) where appropriate, I have made acknowledgement of the work of others and have made reference to work carried out in collaboration with other persons
3) the thesis is the correct version of the thesis for submission and is the same version as any electronic versions submitted*.
4) my thesis for the award referred to, deposited in the Heriot-Watt University Library, should be made available for loan or photocopying and be available via the Institutional Repository, subject to such conditions as the Librarian may require
5) I understand that as a student of the University I am required to abide by the Regulations of the University and to conform to its discipline.
6) I confirm that the thesis has been verified against plagiarism via an approved plagiarism detection application e.g. Turnitin.

* *Please note that it is the responsibility of the candidate to ensure that the correct version of the thesis is submitted.*

Signature of Candidate*:*		Date:	

Submission

Submitted By *(name in capitals):*	TARIQ NAWAZ CHAUDHARY
Signature of Individual Submitting:	
Date Submitted:	

For Completion in the Student Service Centre (SSC)

Received in the SSC by *(name in capitals):*			
Method of Submission *(Handed in to SSC; posted through internal/external mail):*			
E-thesis Submitted (mandatory for final theses)			
Signature:		Date:	

Table of Contents

ABSTRACT ii
Dedication iv
Acknowledgements v
ACADEMIC REGISTRY vi
Table of Contents vii
Lists of Figures xi
Lists of Tables xvi
Glossary xvii
List of Publications by the Candidate xviii
Chapter 1 – Introduction 1
1.1 Background 1
1.2 Research Objectives 3
1.3 Thesis Outline 4
Chapter 2 – Fuel Cell 5
2.1 Introduction 5
2.2 History 6
2.3 Working Principle 7
2.4 Types of Fuel Cells 9
2.5 Solid Oxide Fuel Cell 11
2.5.1 Development History 11
2.5.2 General Operating Principle 11
2.5.3 Materials for SOFC Components 12
2.5.4 SOFC Configurations 14
2.5.5 Fuel for SOFC 17
2.6 Summary 18
Chapter 3 – Literature Review 19
3.1 Experimental Work 19
3.1.1 Electrochemical Performance 19
3.1.2 Thermal Performance 21
3.2 Numerical Studies 23
3.2.1 Structural Properties of PEN 23
3.2.2 Flow Configurations 24
3.2.3 Heat and Mass Transport 24
3.2.4 Multi-component Modeling 25
3.2.5 Thermal and Mechanical Stress Models 25

3.2.6 MSR and WGS Model 27
3.3 Summary 28
Chapter 4 – Mathematical Modelling 30
4.1 Model Descriptions 30
4.2 Model Assumptions 31
4.3 Coupling Mechanism 31
4.4 Governing Equations 33
4.4.1 Mass Conservation 33
4.4.2 Momentum Conservation 34
4.4.3 Energy Conservation 34
4.5 Electrochemical Model 35
4.6 Chemical Reaction Model of Methane with Water 37
4.7 Thermal Strain and Strain Gradients 38
4.8 Thermal and Mechanical Stresses 39
4.9 Active Surface Area 40
4.10 Boundary Conditions 41
4.11 Summary 42
Chapter 5 – Reacting Flow Coupling with Thermal Impacts in a single Solid Oxide Fuel Cell with Hydrogen Fuel 43
5.1 Introduction 43
5.2 Mesh Quality 43
5.3 Model Verification 44
5.4 Results and Discussion 50
5.4.1 The Effects of the Material Porosity on the Cell Performance and Thermal Impacts 51
5.4.2 Current Density and Temperature Distribution 52
5.4.3 Species Distribution 53
5.4.4 Effect of Inlet Temperature on Cell Performance 54
5.4.5 Effect of Material Properties (Ionic Conductivity) on Cell Performance 56
5.4.6 Thermal Strain 60
5.4.7 Thermal Strain Gradient 65
5.4.8 Thermal and Mechanical Stresses 68
5.4.9 Effect of Operating Voltage on Thermal Strain Generation 71
5.4.10 Effect of Boundary Restriction on the Stress Generation 73
5.5 Summary 74
Chapter 6 – Thermal Impact and Performance analysis of Methane Fueled SOFC 76

6.1 Introduction 76
6.2 Methane Model Description 77
6.3 Methane Model Verification 77
6.4 Results and Discussion 78
6.4.1 Electrochemical Performance 78
6.4.2 Species Distribution 80
6.4.3 Temperature Distribution 84
6.4.4 Reaction Rates Distribution 86
6.4.5 Heat source/sink related with MSR and WGS 88
6.4.6 Heat Source and reaction rate for electrochemical reaction 89
6.4.7 Thermal Strain and Stress Distribution 90
6.5 Summary 93
Chapter 7 - Parametric Study to Investigate the Effect of Operating Conditions on the Cell Performance and Thermal Impact 94
7.1 Introduction 94
7.2 Results and Discussion 94
7.2.1 Effects of the Inlet Temperature on the Cell Performance and Thermal Impact ..94
7.2.2 Effect of the Porosity on the Cell Performance and Thermal Impact 99
7.2.3 Effect of the Flow Configurations on the Cell Performance and Thermal Impact 104
7.2.4 Effects of the Air Fuel Ratio on the Cell Performance and Thermal Impact 108
7.2.5 Effect of the Cell Thickness on the Cell Performance and Thermal Impact 113
7.2.6 Effects of the Operating Voltage on the Cell Performance 119
7.3 Summary 123
Chapter 8 – SOFC Stack Modeling 125
8.1 Introduction 125
8.2 Results and Discussion 126
8.2.1 Electrochemical Performance 126
8.2.2 Species Distribution 127
8.2.3 Reaction Rate 128
8.2.4 Temperature distribution 129
8.2.5 Thermal strain and stress distribution 131
8.3 Summary 134
Chapter 9 – Conclusions and Future Work Suggestions 135
9.1 Conclusions 135
9.2 Future Work Suggestions 137

Appendix A – Fuller Diffusion Volume Coefficients [231].....139
Appendix B – Thermal and Mechanical Properties [165].....139
Appendix C – Nomenclatures and Abbreviations 140
References.....148

Lists of Figures

Figure 1.1 Energy consumption by region, 1990 – 2035 (quadrillion Btu) [2] 1

Figure 1.2 Comparison of fuel cells and combustion based system efficiencies [40] 3

Figure 2.1 Comparison of energy paths from fuel into electricity for fuel cell and conventional power plant [57] 6

Figure 2.2 Elementary structure of the fuel cell [70] 8

Figure 2.3 Basic working principle of an SOFC [82] 12

Figure 2.4 Tubular SOFC configuration [21] 15

Figure 2.5 Planar SOFC configuration [21] 16

Figure 2.6 Integrated planar SOFC configuration [107] 16

Figure 2.7 (a) Electrolyte-supported (b) Anode-supported (c) Cathode-supported [107] ... 17

Figure 3.1 Voltage and power density vs. current density at different operating temperatures from 600 to 800 °C [127, 129]. 20

Figure 3.2 VI characteristic curves for 1.4 and 3 bar pressure at operating temperature from 750 to 800 °C [130]. 20

Figure 3.3 Voltage versus current for numerical and experimental studies [133]. 21

Figure 3.4 Fuel cell temperature versus furnace temperature [138]. 22

Figure 4.1 The geometrical outline of a single planar SOFC on cross section (a) and 3D sketch (b). 30

Figure 4.2 Thermal conductivity of the fluids and ionic conductivity of the electrolyte material at different temperatures. 32

Figure 4.3 Dynamic Viscosity of the fluid, species consumption rate at different temperatures 32

Figure 5.1 Voltage and power density against current density for reference and improved exchange current density cases (decoupled models). The Bench mark current density range is 2430 – 2661 A/m^2 and power density range is 1754 – 1868 W/m^2 [50]. 48

Figure 5.2 Current Density distribution from without porosity based conductivity relation case at section F (refer to section 5.4). 49

Figure 5.3 Temperature distribution from without porosity based conductivity relation case at section F. 49

Figure 5.4 V-I characteristics with and without porosity based conductivity relation cases. . 52

Figure 5.5 Current density distribution from porosity based conductivity relation case at section F. 53

Figure 5.6 Temperature distribution from porosity based conductivity relation case at section F. 53

Figure 5.7 Species mass fraction distribution at sections A and C. 54

Figure 5.8 Current density and electrolyte ionic conductivity vs inlet temperature. 55

Figure 5.9 Temperature difference distribution at section B. 56

Figure 5.10 Electrolyte ionic conductivity and temperature distributions at section B for c-d models. 57

Figure 5.11 Temperature distributions at section Es for c-d models 58

Figure 5.12 Voltage and power versus current density for d-model (constant ionic conductivity) and c-model (variable ionic conductivity). 59

Figure 5.13 Relative change in current density generation between c-d models. 60

Figure 5.14 Thermal strain distribution from decoupled (top) and coupled (bottom) models at sections A, B and C. 61

Figure 5.15 Relative change in thermal strain generation between c-d models at sections A, B and C. 62

Figure 5.16 Relative change in thermal strain generation between c-d models at sections F and G. 63

Figure 5.17 Thermal strain distribution from c-d models at section Es. 64

Figure 5.18 Relative change in thermal strain generation between c-d models at section Es. 64

Figure 5.19 Thermal strain gradients [m^{-1}] (x, y, and z components) distribution from c-d models at sections A, B and C. 66

Figure 5.20 Relative change in thermal strain gradients (x, y and z components) between c-d models at sections A, B and C, respectively. 67

Figure 5.21 Thermal stress distribution from c-d models at sections A, B and C. 69

Figure 5.22 Thermal stress distribution from c-d models at Es. 70

Figure 5.23 Von Mises Stresses distribution from c-d models at sections A, B and C. 71

Figure 5.24 Thermal strain distribution from c-d models at sections A, B and C. 72

Figure 5.25 Relative change in thermal strain generations between 0.7 V and 0.5 V at sections A, B and C. 72

Figure 5.26 Von Mises Stress distribution at section B for different boundary restrictions. One side fixed (left side), both sides fixed (right and left), front and back, and top and bottom. 74

Figure 6.1 Cross section view of a single planar SOFC running on methane. 77

Figure 6.2 Voltage and power density against current density. 78

Figure 6.3 Voltage versus current density for c-d models. 79

Figure 6.4 Relative change in current density generations at different cell voltage between c-d models. 80

Figure 6.5 Species mole fraction distributions at section D. 81

Figure 6.6 CH_4 and CO mole fraction distributions at sections Es and F. 82

Figure 6.7 H_2 and H_2O mole fraction distributions at sections Es and F. 83

Figure 6.8 Temperature distribution from c-d models at section B. 84

Figure 6.9 Temperature distribution at sections Es and F 85

Figure 6.10 Temperature distribution at sections F and G. 85

Figure 6.11 MSR and WGS reaction rates distribution at section D. 86

Figure 6.12 MSR and WGS reaction rates distributions at sections Es and F. 87

Figure 6.13 MSR and WGS heat sink/source distributions at section D. 88

Figure 6.14 MSR and WGS heat sink/source distributions at sections Es and F. 89

Figure 6.15 Electrochemical reaction rate and heat source distributions at sections F. 90

Figure 6.16 Thermal strain distribution at sections A (a), B (b) and C (c). 91

Figure 6.17 Thermal stress distribution from coupled models at sections A, B and C 92

Figure 6.18 Electrolyte thermal stress distribution from coupled models at section Es. 92

Figure 7.1 V-I characteristics at different operating temperatures. 95

Figure 7.2 Temperature distribution from different operating temperatures at section B. 96

Figure 7.3 Thermal strain distribution at sections A (a), B (b) and C (c). Rows from top 1^{st}, 2^{nd}, 3^{rd}, 4^{th} and 5^{th} at 800 °C, 850 °C, 900 °C, 950 °C and 1000 °C, respectively. 97

Figure 7.4 Relative change in thermal strain generations between different operating temperatures at sections A, B and C. 98

Figure 7.5 Thermal stress distribution from different operating temperatures at section B. ..99

Figure 7.6 Active surface area versus porosity. 100

Figure 7.7 V-I Characteristics at different porosities.....101

Figure 7.8 Relative change in average current density generations at different cell voltage between different porosity cases. 101

Figure 7.9 H_2 mole fraction distribution from different porosity cases at sections D and F. 102

Figure 7.10 Temperature distribution from different porosity cases at section B. 103

Figure 7.11 Relative change in temperature distribution between different porosity cases at section B.....103

Figure 7.12 Thermal stress distribution from different porosity cases at section B. 104

Figure 7.13 V-I Characteristics for co and counter flow configurations. 105

Figure 7.14 Current density distribution for co and counter flow configurations at section F. 106

Figure 7.15 Temperature distribution for co and counter flow configurations at section B. 107

Figure 7.16 Thermal strain distribution from co-flow (top) and counter flow (bottom) configurations at sections A (a), B (b) and C (c). 107

Figure 7.17 Thermal stress distribution from co and counter flow configurations at section B. 108

Figure 7.18 V-I Characteristics at different A/F ratios. 109

Figure 7.19 Relative change in average current density generations at different voltages between various air/fuel ratio cases. 109

Figure 7.20 Temperature distribution for different A/F ratios at section B. 110

Figure 7.21 Relative change in temperature distribution between different air/fuel ratio cases at section B.....111

Figure 7.22 Thermal strain distribution at different AFRs at sections A (a) 15.769 (d) 31.537 (g) 63.074, B (b) 15.769 (e) 31.537 (h) 63.074 and C (c) 15.769 (f) 31.537 (i) 63.074.....112

Figure 7.23 Thermal stress distribution from different A/F ratio cases at section B. 113

Figure 7.24 V-I Characteristics for different electrolyte thickness cases. 114

Figure 7.25 Relative change in current density generations at different voltages between different cell thickness cases.....115

Figure 7.26 Temperature distribution from different electrolyte thickness cases at section B. 116

Figure 7.27 Relative change in temperature distribution between different cell thickness cases at section B. 116

Figure 7.28 Thermal strain distribution at different electrolyte thickness cases (from top first, second and third row at 100E-6m, 150E-6 m and 200E-6 m, respectively) at sections A (a), B (b) and C (c). 118

Figure 7.29 Thermal stress distribution from different electrolyte thickness cases at section B. 118

Figure 7.30 V-I Characteristics at different operating voltages. 119

Figure 7.31 Methane mole fraction distribution from different operating voltages at section D. 120

Figure 7.32 Temperature distribution from different operating voltages at section B. 121

Figure 7.33 Thermal strain distribution for 0.7 V (top) and at 0.4 V (bottom) at sections A (a), B (b) and C (c). 122

Figure 7.34 Relative change in thermal strain generations between 0.7 V and 0.4 V cases at sections A, B and C. 122

Figure 7.35 Thermal stress distribution from different operating voltages at section B. 123

Figure 8.1 Stack of Planar SOFC consists of 8 cells. The cell length, width and height is in m. 126

Figure 8.2 V-I Characteristics of different cells. 127

Figure 8.3 Methane and hydrogen mole fraction distributions for different cells at section D. 128

Figure 8.4 MSR reaction rate distribution for different cells at section D. 129

Figure 8.5 Temperature distribution for different cells at section B. 130

Figure 8.6 Temperature distribution in the centre of the 8 cells at section Es. 131

Figure 8.7 Thermal strain distribution at section A. 132

Figure 8.8 Thermal strain distribution at section Es. 133

Figure 8.9 Thermal stress distribution for various cells at section B. 134

Lists of Tables

Table 2.1 Characteristics of different types of fuel cells [51, 56, 63, 69, 70, 75-79].....10

Table 4.1 Parameters used to Calculate Active Surface Area.....41

Table 5.1 Mesh Quality.....44

Table 5.2 Geometrical, Operational, Mechanical and Electrochemical Parameters available in IEA report [50].....46

Table 5.3 Geometrical, operational, Mechanical and Electrochemical Parameters taken from the literature. 47

Table 5.4 Comparisons of present results with IEA.....50

Table 8.1 Properties of Lanthanum Chromite.....126

Glossary

The nomenclatures and abbreviations are listed in Appendix – C.

List of Publications by the Candidate

Journal Papers

1. T.N. Chaudhary and B.Chen, Reacting Flow Coupling with Thermal Impacts in a single Solid Oxide Fuel Cell **(To be Submitted)**
2. T.N. Chaudhary and B.Chen, Investigation of methane steam reforming and water gas shift reactions effect on Solid Oxide fuel cell performance and thermal impact (**To be Submitted**)

Seminar and Conference Presentations

1. Poster presentation in EPS, PGR annual poster event 2013 (Winner of the event and received first prize).
2. Poster presentation in IMPEE first conference held in 2014 at Heriot Watt University.
3. Oral presentation in 12th Meeting of Electrochemical Society (ECS) held in October 2015 in USA. (Awarded travel grant to attend the meeting)

Other Publications

1. T.N. Chaudhary, F.H. Shah, M. Farooq, A. Qamar, A.R. Sajid "Enhancement in overall thermal efficiency of a Gas Turbine power plant using combined cycle system", Journal of Faculty of Engineering & Technology, vol 23, issue 2, (2016), pp. 49-57
2. A.O. Mohammed, T.N. Chaudhary, M. Akram "Economic benefits of Gas Turbine compressor washing at different intervals", Journal of Faculty of Engineering & Technology, vol 24, issue 2, (2017), (accepted).

Chapter 1 – Introduction

1.1 Background

Energy plays an important role in the sustainable development of the country [1]. There are several definitions of the sustainable development and in the most common form it is define as, development that meets the need of the present without compromising the ability of future generations to meet their own needs [1]. Overall energy consumption is closely linked to the population and economic growth. The latest projections imply that the total world energy consumption will increase at an average annual rate of 1.6 % from 2008 to 2035 [2] as shown in Figure 1.1. In total the world energy consumption will increase from 591 to 770 quadrillion Btu in next 18 years [2] .

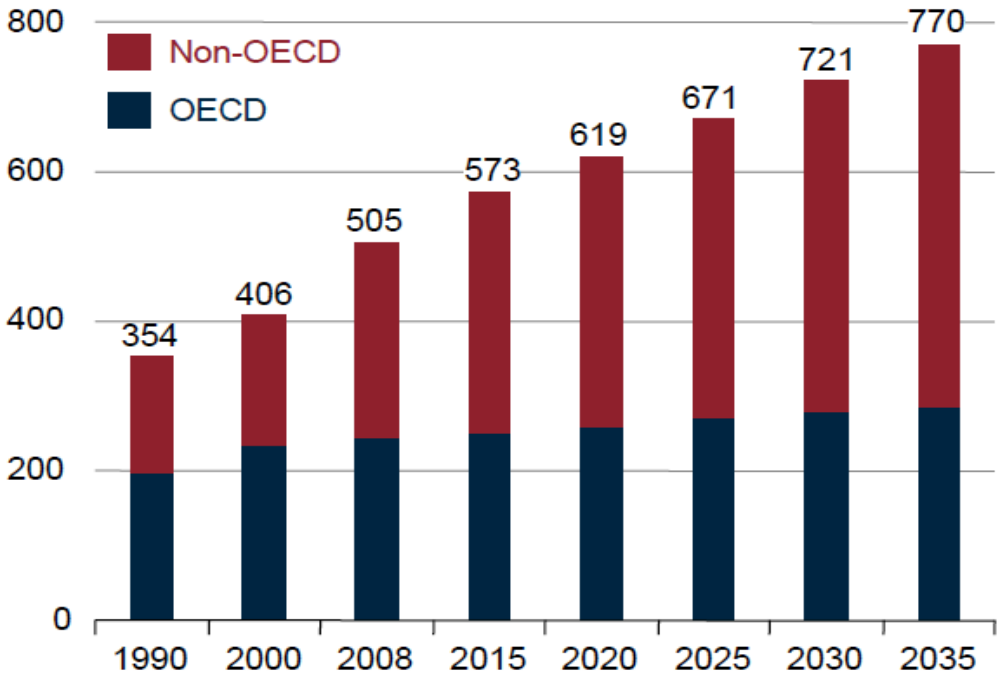

Figure 1.1 Energy consumption by region, 1990 – 2035 (quadrillion Btu) [2]

Conventional power generation systems based on principle of 'heat engine' by burning fossil fuels (oil, natural gas, and coal) have been used for 25 decades [3-7]. The efforts have been made continually to improve the energy conversion efficiencies [8, 9], meanwhile to reduce the emission pollutions such as SO_x, NO_x and CO_2 which badly affect the environment [10, 11] . The thermal efficiency of the gas turbine power plants is 30 – 35 % [8], engines running on gaseous fuel is around 30 – 44 % [12], turbo-charged diesel engine 45 – 54% [13] and the efficiency of combined cycle power plants can reach up to 60 % [8, 9].

CO_2 which is known as a greenhouse gas is the main contributor in climate change and related environmental issues [14, 15]. Increasing the concentration of carbon dioxide in the atmosphere will result in an increase in the earth surface temperature [14]. It is predicted that over the last century the earth surface temperature has increased about 0.6 ^oC [14, 16]. It has been estimated that maintaining the increase, as usual, in the consumption of the fossil fuels may result in an increase of earth surface temperature between 2 to 6 ^{o} C in next century [14, 15, 17]. According to 4^{th} assessment report of Intergovernmental Panel on Climate Change (IPCC) [18], the three options to keep the temperature increases to 2, 4 and 6 °C with keeping CO_2 concentration of 450 ppm, 750 ppm and 1200 ppm, respectively.

To meet the demands on energy, dwindling world fossil fuel resources and requests on mitigation of air pollution, there is an urgent need of more reliable, efficient and clean energy sources. Among various energy conversion technologies, such as photovoltaics and wind turbines, fuel cells are widely recognized as the next generation of power generator in both mobile and stationary uses because they can provide both heat and power, have high fuel to electricity conversion efficiency and low environmental impacts [19-28].

Fuel cell running on pure hydrogen fuel is a near to zero CO_2 emission device [27, 29]. The fuel cells utilizing hydrocarbon fuels instead of pure hydrogen has sensible CO_2 emission at the exhaust [27, 29]. The exhaust of the fuel cell consists of H_2O and CO_2 and CO_2 is separated before compression for transportation and storage [30, 31]. The energy consumes to capture CO_2 during fuel cell operation is low enough as compared to other methods of CO_2 capture from fossil fuels fuelled plants [32].

Among various types of fuel cells, solid oxide fuel cell (SOFC) is most promising because of its high electrical efficiency, internal steam reforming, cogeneration, fuel flexibility and insignificant emissions [33-35]. The electrical efficiency of SOFC is about 63 percent, as reported by Ludger Blum [36] and can be further enhanced by integrating with other power generating systems such as gas turbine [30, 36-38]. The electrical efficiency of SOFC-GT technology is close to 70% with 90% CO_2 removal [31, 39, 40], which means implicitly lowering the environmental impacts, benefiting the mitigation of global warming, compared to other power generation systems [33]. The comparison between fuel cells and combustion based system efficiencies is shown in Figure 1.2.

Solid oxide fuel cell consists of a solid electrolyte which is sandwiched between two porous electrodes known as anode and cathode structure (often referred as PEN – Positive electrode – Electrolyte – Negative electrode). The operating temperature in SOFC ranges from 400 °C to 1000 °C, which leads to fast electrochemical reactions and larger ionic conductivity. SOFCs are suitable as a power device for stationary power generations, combined cycle power plants, transportation and military applications [34, 37, 41-45]. However, the high operating temperatures pose significant challenges, such as long start-up time [46-48] , the requirement of high quality electrolyte material [45, 46, 49], and thermal impacts [45, 46, 48], which diminishes the SOFCs practicality for applications as the portable power sources, such as the auxiliary power units for automobiles.

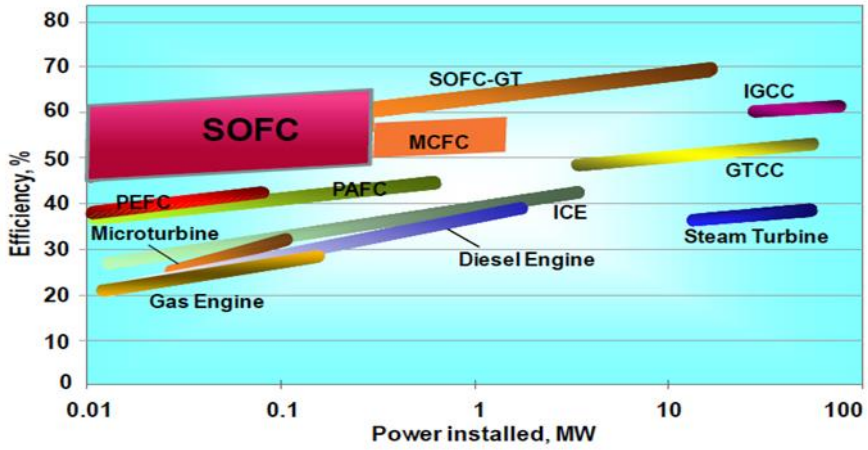

Figure 1.2 Comparison of fuel cells and combustion based system efficiencies [40]

1.2 Research Objectives

To further improve the thermal stability and broaden the adoption, the mechanisms of thermal impact generations in SOFCs are investigated in this study by numerical simulations of coupling the dynamics of electrochemical reacting flows, heat transfer, and thermal impacts. Two coupling mechanisms are investigated on modeling the SOFC performance and thermal impacts: decoupling mechanism, on which the material properties are predicted at operating temperature, and the coupling mechanism, the material properties are predicted at local temperature.

The research work can be summarized as following four main aspects of SOFCs thermal impacts numerical modeling. First is the construction of a numerical model of a single planar solid oxide fuel cell (SOFC) by coupling dynamics of electrochemical reacting flows, heat transfer, and thermal impacts (thermal strains and stresses) of solid electrolyte and porous electrodes for analyzing the cell performance. The benchmark data [50] is used as a reference to compare the simulation results of the developed model. Then is the investigations of the thermal impacts and performance of SOFC running on methane by determining the contributions of the different reacting heat sources/sinks to the temperature distribution of fluids and on PEN of the cell. The sensitivity analysis of the cell performance and design parameters on thermal impacts are conducted before final upgradation of the single cell SOFC modeling to the stack level.

1.3 Thesis Outline

The thesis is organized as follows;

Chapter 1 outlines the background and the objectives of the study in terms of globally increasing demands of the energy and environmental impacts, alternative solution and provides overviews of the research objectives. Chapter 2 is the introduction to the performance mechanism of different types of fuel cells and their applications especially focusing on SOFCs. Chapter 3 presents the comprehensive literature review on SOFC studies. Chapter 4 describes the coupling mechanism, methodology of modelling development, including the theories and the governing equations. Chapter 5 discusses the results of hydrogen based model, model validation, coupling of material properties with temperature, strains and stresses generated in the cell. The model is further developed and tested by employing fuels with complex structure, such as methane, to investigate the contributions of complex reacting flows with multiple exothermic and endothermic reactions to the generation of thermal impacts, which are explained in Chapter 6. Chapter 7 presents the effects of the different operational and geometrical parameters on the cell performance and thermal impacts. Chapter 8 demonstrates the cell up gradation to the stack level and the effect of the interconnect material on the cell performance. Finally, the conclusions and future work are presented in Chapter 9.

Chapter 2 – Fuel Cell

This chapter provides the basic knowledge about the fuel cell, history of the fuel cells, working principle and characteristics summary of different types of fuel cells. Special attention is paid to SOFC development, configurations, materials use for different components and fuels employ in SOFC.

2.1 Introduction

A fuel cell is an open thermodynamic system. Fuel cell converts the chemical energy of the fuel directly into the electrical energy through electrochemical reactions. The electrical energy can be utilized to power the electronic devices, vehicles, buildings, or be supplied to the electric grids. The by-products during electrochemical reactions are heat and water. The operation of the fuel cell is much similar to a battery. The energy is stored in the battery and with the use it is depleted. On the other hand a fuel cell continuously converts the chemical energy into the electrical energy as long as it has the supply of the fuel and oxidant [35, 51-54].

Unlike combustion engines, the fuel is not burnt in the fuel cell. The energy conversion path of the fuel cell is simpler and shorter than conventional power plant, as shown in Figure 2.1. It converts the fuel energy into electricity more efficiently than the combustion based methods. The efficiency of the fuel cell does not depend on the Carnot limitations and the efficiency of the hydrogen fuel cell operated engine vehicles is up to 65%, compared to 25% petrol driven car engines [25, 55].

The salient features of the fuel cells are low to zero emissions, variety of fuels utilization, low maintenance, quiet in operation, highly reliable and long lasting system [52, 56].

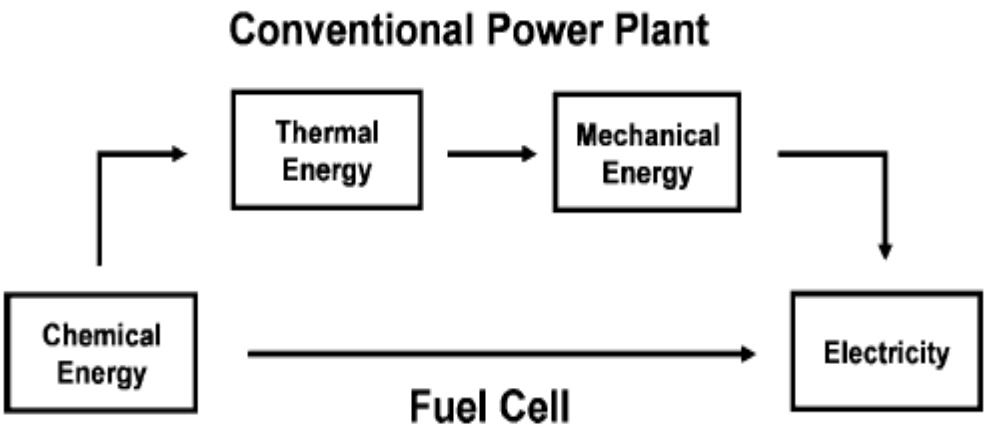

Figure 2.1 Comparison of energy paths from fuel into electricity for fuel cell and conventional power plant [57]

2.2 History

The first fuel cell was developed by the William Robert Grove in 1839 [57]. The principle of the fuel cell was discovered accidently during an experiment. The Groove connected the two electrodes together and observed that the current is flowing in the opposite direction, consuming the hydrogen and oxygen. A platinum electrode was immersed in nitric acid and zinc electrode in zinc sulphate. He named the apparatus as gas battery. In 1842, Groove connected 4 gas batteries in series to make the gas chain and current of 12 A was generated at 1.8 V. The electrodes corrosion and material instability restricted the use of Grove's fuel cell in real [57-62].

In 1893, Friedrich Wilhelm Ostwald, known as the chemistry-physics founder, experimentally analysed the interconnection of the different fuel cell components: electrodes, electrolyte, oxidizing and reducing agents, anions and cations. Further development in the field of fuel cell chemistry was based on his research. In 1896, William W. Jacques developed the first fuel cell (Direct Carbon Fuel Cell) with practical applications, and in 1900, Walther Nernst first employed zirconium as solid electrolyte [63].

In 1930, Francis Bacon, a chemical engineer at Cambridge University England, started his research on the fuel cell. Bacon in 1958 produced the first alkaline fuel cell [58, 60].

In the 1950s – 1960s, the USA National Aeronautics and Space Administrator's (NASA) used fuel cell to meet the need of electrical energy in extended missions to space. The NASA fuel cell is of alkaline type which uses hydrogen as fuel and oxygen as oxidant. In space flight, the fuel cell provides three basic functions: (i) electricity to power the spacecraft, (ii) water for drinking and cooling the equipment, (iii) heat to keep the astronauts from freezing [54, 60, 61].

A direct methanol fuel cell was developed in 1990 by NASA in coordination with the University of Southern California. The traditional batteries are replaced with direct methanol fuel cell in some applications. It is expected to gain space in the market because they have a higher lifetime as compared to the lithium ion battery and can be recharged by simply changing the cartridge of fuel. These types of fuel cells are being developed by Samsung (Korea), Toshiba, Hitachi, NEC and Sanyo (Japan) [63].

Now there are many companies manufacturing the fuel cells for different applications. The most common applications of the fuel cells are in buses, cars, trucks, motorcycles, ships, aircrafts, forklifts and train [64-66]. Fuel cells are also used in military applications, mobile phones, laptops and other portable electronic devices [64-67]. The electric power generated from the fuel cells utilizes in large scale applications such as shopping malls, warehouses, hospitals, schools and banks [65, 66]. The traffic signals, vending and vacuum cleaner machines are also operated on fuel cell. Fuel cells are involved in converting the methane gas, produced from water treatment and waste dumps, into electricity generation [68]. As we can see, in different areas fuel cells have extensive applications.

2.3 Working Principle

The elementary structure of the fuel cell is shown in Figure 2.2. A fuel cell consists, in principle, of three main components, two electrodes known as anode and cathode separated by an electrolyte. Electrodes are porous and have good electronic conductivity. An electrolyte plays an important role in the electrochemical reaction; it allows only ions to pass through. In other words an electrolyte has a good ionic conductivity [35].

The electrochemical reaction in hydrogen based fuel cell is divided into two half reactions, the oxidation half reaction and the reduction half reaction. For example when a proton conducting electrolyte is used in a fuel cell, the reaction at anode is half

oxidation reaction in which hydrogen decomposes into positively charged ions (protons) and negatively charged electrons. The protons pass thorough the electrolyte membrane while the electrons flow through an external circuit to generate electricity. After passing through the circuit the electrons move towards cathode [54, 69].The reaction at anode is;

$$H_2 \longrightarrow 2H^+ + 2e^- \tag{2.1}$$

Oxygen enters at the cathode and reacts with the electrons and the positively charged ions (protons) those pass thorough electrolytes. Sometimes depending upon the configuration of the fuel cell, oxygen picks up the electrons and pass thorough the electrolyte towards anode, there it reacts with protons. Oxygen reaction is a reduction half reaction and as a result water is produced [52, 58].The reaction at cathode is;

$$\tfrac{1}{2}\,O_2 + 2H^+ + 2e^- \longrightarrow H_2O \tag{2.2}$$

The overall chemical reaction is

$$H_2 + \tfrac{1}{2}O_2 \longrightarrow H_2O \tag{2.3}$$

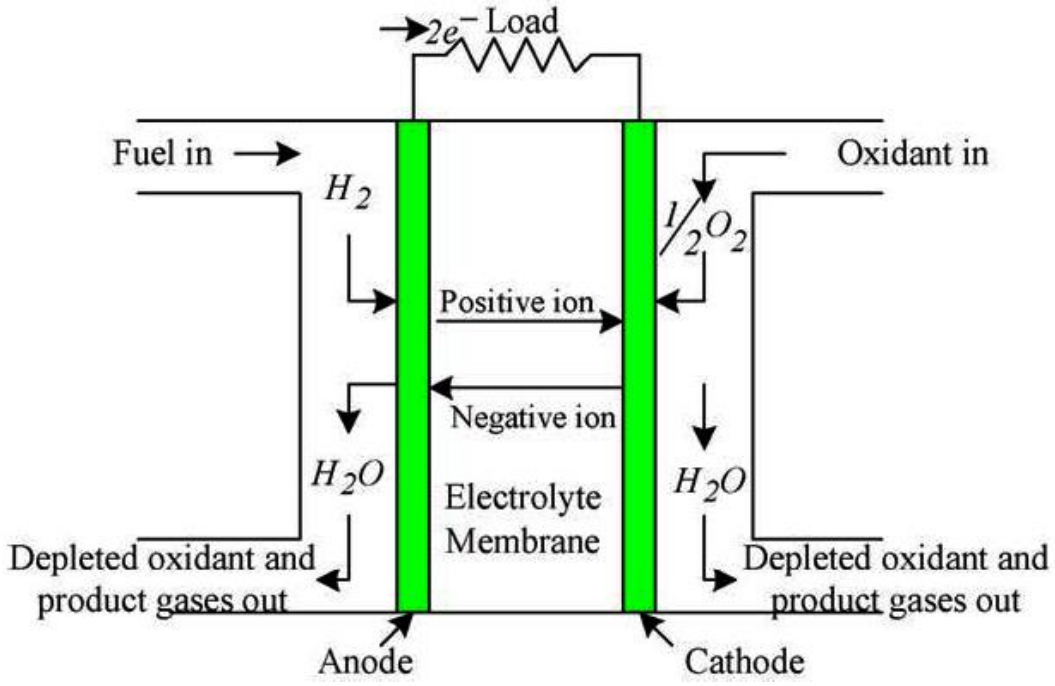

Figure 2.2 Elementary structure of the fuel cell [70]

The voltage produce by a single fuel cell is low and approximately about 0.7 volt. In order to get the desired output of the voltage, the fuel cells are connected in series. This connection of fuel cells is known as fuel cell stack [71-73].

2.4 Types of Fuel Cells

The working principle of all types of the fuel cell is the same. They differentiate from each other according to the materials use for the electrolyte membrane, operating temperature and reactant type. The six major types of the fuel cell are as following [21, 51, 74, 75];

1. Direct Methanol Fuel Cell (DMFC)
2. Polymer Electrolyte Membrane Fuel Cell (PEMFC)
3. Alkaline Fuel Cell (AFC)
4. Phosphoric Acid Fuel Cell (PAFC)
5. Molten Carbonate Fuel Cell (MCFC)
6. Solid Oxide Fuel Cell (SOFC)

Table 2.1 briefly explains the properties of different types of fuel cells.

Table 2.1 Characteristics of different types of fuel cells [51, 56, 63, 69, 70, 75-79]

Parameters	Name of the Fuel Cell					
	DMFC	PEMFC	AFC	PAFC	MCFC	SOFC
Operating Temperature (°C)	50 – 120	50 – 100	50 – 200	150 – 200	600 – 700	400 – 1000
Reaction at Anode	$CH_3OH + H_{20} \longrightarrow CO_2 + 6H^+ + 6H^-$	$H_2 \longrightarrow 2H^+ + 2e^-$	$H_2 + 2(OH^-) \longrightarrow 2H_2O + 2e^-$	$H_2 \longrightarrow 2H^+ + 2e^-$	$H_2 + CO_3^{2-} \longrightarrow H_2O + CO_2 + 2e^-$	$H_2 + O_2^- \longrightarrow H_2O + 2e^-$
Reaction at Cathode	$3O_2 + 12H^+ + 12H^- \longrightarrow 6H_2O$	$1/2O_2 + 2H^+ + 2e^- \longrightarrow H_2O$	$1/2O_2 + H_2O + 2e^- \longrightarrow 2(OH)^-$	$1/2O_2 + 2H^+ + 2e^- \longrightarrow H_2O$	$1/2O_2 + CO_2 + 2e^- \longrightarrow CO_3^{2-}$	$1/2O_2 + 2e^- \longrightarrow O_2^-$
Fuel	CH_3OH	Pure H_2	Pure H_2	Pure H_2	H_2, CO, CH_4, other hydrocarbons	H_2, CO, CH_4, other hydrocarbons
Electrical Efficiency	40%	40 – 50 %	45 – 60 %	40 – 45%	45 – 55%	40 – 65%
***CHP Efficiency**	80%	70 – 90 %	>80%	>85%	>80%	~90%
Cogeneration	No	No	No	Yes	Yes	Yes
Internal Reforming	Not applicable	No	No	No	Only with Steam	Only with Steam
Common Electrolyte	Solid Polymer Membrane	Solid Organic Polymer	Liquid solution of KOH	Phosphoric acid (H_3PO_4)	Lithium and Potassium carbonate supported by ($LiAlO_2$)	Stabilized solid oxide electrolyte ($Y2O_3$, ZrO_2)
Reactant Ion	H^+	H^+	OH^-	H^+	CO_3^{2-}	O^{2-}
Cell Voltage	0.2 – 0.4	1.1	1.0	1.1	0.7 – 1.0	0.8 – 1.0
Power density (kW/m^3)	~0.6	3.8 – 6.5	~1	0.8 – 1.9	1.5 – 2.6	0.1 – 1.5
System Output	Up to 1.5 kW	<1kW – 250 kW	10kW – 100kW	50kW – 1MW	<1kW – 1MW	1kW – 2MW
Start-up time	Sec-min	Sec-min	Sec-min	Hours	Hours	Hours
Applications	Replace batteries in mobile phones, laptops and other portable applications	Residential, Un-interruptible/backup, different types of transport applications, remote area power supplies, emergency services such as hospitals and banking	Military and Space applications, Transports	Provide heat and power to schools, office buildings, hospitals, hotels, water treatment plants	Large stationary power and CHP applications, transportations	Auxiliary power units, Military applications, remote area, CHP
Advantages	Reduced cost due to absence of fuel reformer	High power density, rapid start-up, solid electrolyte reduces corrosion	Cost effective because of less amount of catalyst use, no corrosion problems, high efficiency, rapid start-up,	Increased tolerance to CO_2, Water management is not very much difficult, Higher efficiency with CHP	Fuel flexible, High efficiency, inexpensive catalysts	High efficiency, fuel flexible, Solid electrolyte reduces electrolyte management issues,
Drawbacks	Low efficiency and power density, methanol cross-over and poisonous by-product	Sensitive to fuel impurities (CO, H_2S), Expensive platinum catalyst, Water management issues	Intolerant to CO_2, CO and S, handling problems due to liquid electrolyte	Long start-up time, corrosion and sulphur poisoning,	Electrolyte instability, intolerance to sulphur, long star -up time	Thermal management issues, Long start-up time, intolerance to sulphur ,

*CHP = Combined Heat and Power

2.5 Solid Oxide Fuel Cell

2.5.1 Development History

The development on SOFC has been started since 1899 by Walther Nernest. Nernst developed a solid component, known as Nernst mass, which consists of 85% ZrO_2 and 15 % Y_2O_3. In 1937, Emil Baur and H. Preis developed a first SOFC prototype which was operated at 1000 °C [59, 80-82]. It was found that most effective electrolyte could be produced by 30% lithium zirconate, 10% clay and 60% Nernst mass. But the cost of the required materials was too high [83]. The more focused studies on SOFC began in 1943 after the work of Carl Wagner who attributed the electrical conductivity in mixed oxides such as dopes ZrO_2 to the presence of oxygen vacancies [82]. The research on SOFC technology began to accelerate in late 1950s [80].

In 1962, Weissbart and Ruka, researcher at Westinghouse, developed a fuel cell system by using 85% ZrO_2 and 15% CaO, a variation on the Nernst mass material, as electrolyte and material used for electrodes was porous platinum. Westinghouse joined with Siemens in 1998 and found Siemens-Westinghouse which became the key developer of Tubular SOFC technology [57, 80, 83]. From the mid-1990s to date, many different types of the materials and designs of SOFC have been invented. Among various designs anode-supported planar SOFCs became more popular because of its performance and cost considerations [82]. Around the year 2000, interest in distributed generation of SOFC peaked but SOFC was not ready for commercialization. The major challenges which hinder the commercialization of SOFC are its competitive cost and reliable performance with desired operating characteristics [82, 83]. Since 2000 research and development activities of SOFC have continued to be active in both academic community and industry. Academic researchers mainly focus on the fundamental theory such as modeling, simulation, and investigation of catalysis and electrolyte property, etc., while the industry developers mainly focus on developing the prototypes [83].

2.5.2 General Operating Principle

Solid oxide fuel cell consists of a solid electrolyte which is sandwiched between two porous electrodes named as anode and cathode. The operating temperature of SOFC is high, ranges between 500 – 1000 °C, and at these temperatures the ionic conduction of oxygen ions or protons takes place. The material use for the SOFC electrolyte should be

highly chemically and mechanically stable, have good ionic conductivity and dense enough to avoid mixing of gases. At the anode electrochemical oxidation of the fuel takes place and at the cathode electrochemical reduction reaction occurs. Normally hydrogen is used as a fuel because of its highly electrochemical activity but carbon monoxide can also be used along with hydrogen. Due to high operating temperature the internal reforming of the fuel is feasible and hydrocarbons such as methane can also be employed as a fuel. Oxygen or air is used as an oxidant. The oxygen ions are used as a charge carrier in an SOFC and results in water generation at anode. The driving force between fuel and oxidant is the chemical potential gradient of ions across the electrolyte. The basic working principle of an SOFC based on O^{2-} conducting electrolyte is illustrated in Figure 2.3 [38, 59, 82, 84].

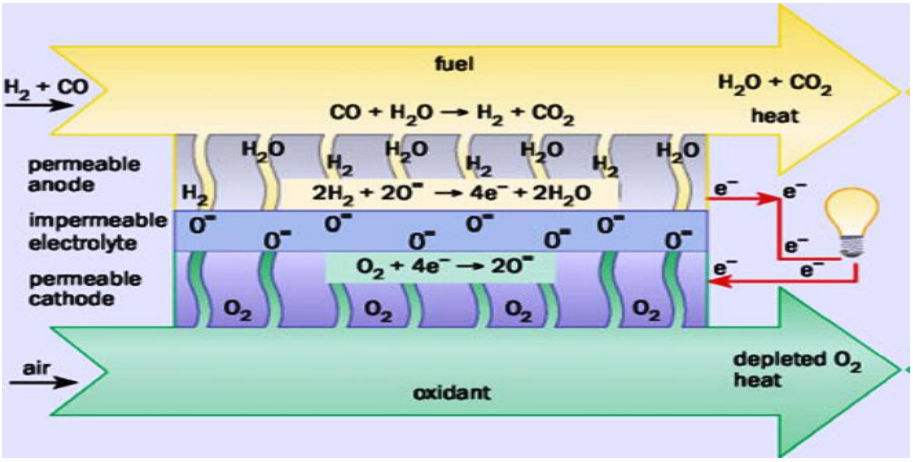

Figure 2.3 Basic working principle of an SOFC [82]

2.5.3 Materials for SOFC Components

Yttria-Stabilized Zirconia (YSZ) is the most common electrolyte material used for SOFC system because of its high ion conductivity, good mechanical properties, chemical stability and negligible electronic conductivity. The ionic conductivity limitations for YSZ are below 750 °C [82, 84-88] which refers that it is not suitable for electrolyte supported SOFCs operating blow 750 °C. The other common materials use for the electrolyte are Scandia stabilized zirconia Sc_2O_3-ZrO_2 (SSZ), Gd or Sm-doped CeO_2 (CGO or SDC), and Sr- and Mg-substituted $LaGaO_3$ (LSGM). The minimum operating temperature of these systems depends on both the ionic conductivity and a realistic assessment of a minimum film thickness that can be reliably manufactured.

SSZ has higher conductivity, good stability in oxidizing and reducing environment as compared to YSZ. The implementation problems related with SSZ are price, availability and degradation [89-92]. The conductivity of LSGM is also higher than YSZ and it is suitable to use at temperature about 600 – 700 °C. At this temperature range the YSZ based SOFCs do not have adequate power density. The LSGM has stability problem and further research into this material is required [93].

To enhance the electrochemical reactions, it is desired that the materials for the anode and cathode have high catalytic activity and electronic conductivity under the operating temperature (400 – 1000^{o}C normally). Meanwhile, from the structure point of view, it requests that the thermal deformations of materials must be associated with each other for both electrodes and electrolyte to maintain the designed sandwich structure [90, 91].

The most common material used for anode is Nickel/YSZ cermet (ceramic metal composite). This mixture of YSZ serve as an ion conduction component, and Ni metal having good electronic conduction and catalytic activity perform the functionality of anode. The major drawback of Ni is its reaction with oxygen which forms NiO (Nickel Oxide). The NiO covers more space than Ni, producing stresses in the electrode, due to which the electrode can crack and as a result the structure of the electrode even the whole cell will be affected. When hydrocarbons are used as a fuel, the sulphur contents and carbon formation create problems at anode. In addition to the electrochemical characteristics, other issues such as thermal expansion coefficients, which limits the choice of the materials [90, 91, 94]. Efforts have been made to remove the issue of thermal expansion mismatching between YSZ electrolyte and Ni/YSZ anode by developing new materials such as Ni-Al_2O_3 and Ni-TiO_2 [90]. One of the approaches to limit the carbon formation is to lower the operating temperature. Yttria-doped ceria (YDC) layer can be added to Ni/YSZ anodes in order to enhance the cell performance and resistance to carbon deposition [95]. One of the candidates for anode material is Cu/YSZ as Cu does not catalyse carbon formation and have more tolerance to sulphur contents than Ni/YSZ [96]. Chromites and Titanates are most widely studied perovskites due to their stability in reducing environment. Strontium Titanate ($SrTiO_3$) is chemically stable and shows good electronic conduction on reduction because of the presence of Ti^{3+}. Like other perovskites its electrical conductivity could be enhanced by donor doping with tri or pentavalent oxides such as La^{3+}, Y^{3+} or Nb^{5+} [90, 97-99].

The structure of the cathode is porous like anode and must allow fast mass transport of the reactant and product gases such as water (in case of proton conducting electrolyte).The most widely used and studied cathode material is perovskite based strontium-doped lanthanum manganite ($La_{0.84}Sr_{0.16}$) MnO_3, (LSM), which is a p-type conductor. LSM is a good catalyst for dissociation of oxygen molecules at higher temperatures, and its thermal expansion coefficient matches well with YSZ electrolyte but its ionic conductivity is relatively low [59, 69, 90, 95, 100]. The activation losses on cathode side are due to low ionic conductivity and any material which can efficiently catalyse the formation of oxygen ions can help to reduce these losses. For example a composite cathode, LSM/YSZ, gives better oxygen ion conductivity and greater active area, improves the overall catalytic activity even at lower temperature [43]. Another problem of LSM is its chemical compatibility with YSZ electrolyte. It reacts with YSZ electrolyte and forms $La_2Zr_2O_7$ and also $SrZrO_3$ depending upon the strontium level. $La_2Zr_2O_7$ and $SrZrO_3$ are insulating and highly resistive, which refers to the interface delamination and loss in the cell performance [101]. In order to incorporate this issue, increase the conductivity of LSM to match its thermal expansion coefficient close to YSZ, alternative cathode materials has been used. One of the most extensively studied perovskite cathode material for SOFC is Sr doped lanthanum cobaltite ($La_{1-x}Sr_x$)CoO_3 (LSC) and addition of iron on cobalt site which forms ($La_{1-x}Sr_x$)($Co_{1-y}Fe_yO_{3)}$ (LSCF) which further improves the cell performance [93, 100, 102].

2.5.4 SOFC Configurations

The most common SOFC configurations are tubular and planar. An overview of the tubular SOFC is shown in Figure 2.4. Tubular configuration consists of two tubes, an external tube known as cell tube, and an inner tube called as air injection and guidance tube which is made of alumina (Al_2O_3). The outer and inner surface of the cell tube consists of anode side and cathode side respectively, and in between anode and cathode solid electrolyte lies. The preheated air passes though the injection tube and enters into the bottom of the cell tube and flows over cathode surface through space between the injection and cell tubes. The cell tube is closed at one end. The fuel gas flows over the anode surface around the exterior of the cell tube and in a direction parallel to the air flow. Oxygen ions pass through cathode and electrolyte and reacts with fuel and generates electric current [21]. A major advantage of this type of cell is the elimination of gas tight seal between cells as one end of each cell support tube is closed [103].

However, tubular approach has disadvantages such as high manufacturing costs, low power density and higher ohmic losses because of longer current paths and large voids within the stack structure [21, 53, 59, 82].

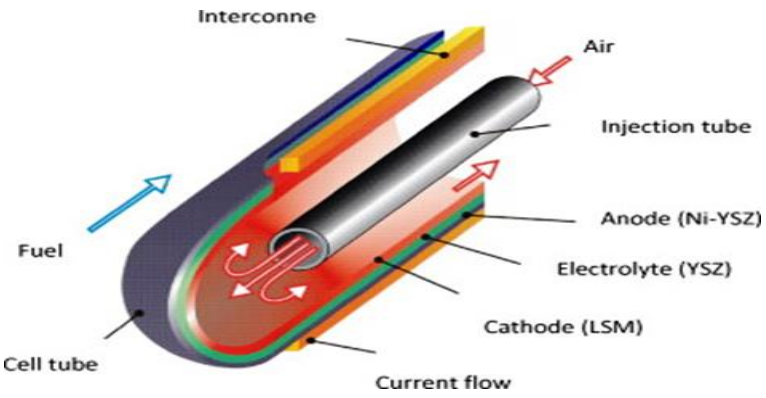

Figure 2.4 Tubular SOFC configuration [21]

Generally, planar configuration is constructed of a positive-electrolyte-negative electrode (PEN), interconnect top and bottom of the cell stack, air and fuel channels, as shown in Figure 2.5. The fuel gas channel is between the anode and the separator plate and on the other side the air channel is located between the cathode and separator plate [21]. Planar SOFC has low costs and basic manufacturing processes, simplicity in fabrication, high power density, and lower ohmic losses than tubular SOFC. According to the flow direction of the oxidant and fuel inside the cell, the planar SOFCs offer three configurations namely co-flow, counter flow and cross flow. The drawbacks of planar SOFC are the need of high temperature gas sealing between the cell components, brittleness in tension and thermal stresses at the interfaces between different cells which can cause the mechanical degradation [21, 53, 59, 82, 104].

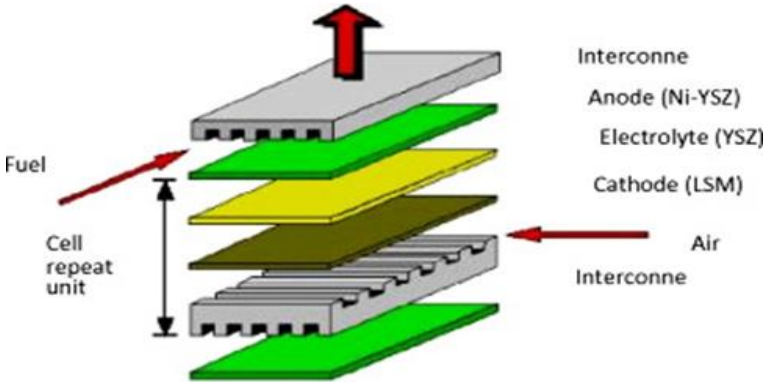

Figure 2.5 Planar SOFC configuration [21]

Integrated planar SOFC (IP-SOFC), as shown in Figure 2.6) is an innovative fuel cell concept developed by Rolls-Royce. IP-SOFC is a cross between tubular and planar configurations, seeks to borrow thermal compliance properties from tubular geometry and low cost component fabrication and shorter current paths from planar geometry [105-107].

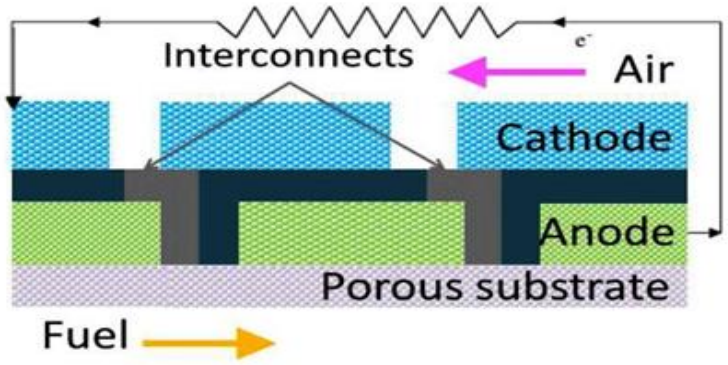

Figure 2.6 Integrated planar SOFC configuration [107]

Further depending on the thickness of electrode and electrolyte layer, the SOFCs are classified into three categories named as electrolyte supported, anode-supported and cathode supported. The configurations are displayed in Figure 2.7. The electrolyte supported cells have strong mechanical strength due to thick dense electrolyte. Since the ohmic losses are higher because of low electrolyte conductivity and to reduce these losses, the SOFC is operated at higher temperature, around 1000 °C. In anode-supported SOFC, a thin electrolyte is placed on top of the thick anode. As the electrical conductivity of anode is high and thin electrolyte is employed, the ohmic losses and operating temperature of anode-supported SOFCs is lower than electrolyte supported

SOFCs. However, a thicker anode leads to increase the concentration losses due to mass transport limitation. SOFCs with cathode supported structure are similar to anode-supported structure and can be operate at lower temperature because of thin electrolyte used. A thicker cathode may limit the supply of reactants to the reaction sites which results in higher concentration polarisation losses. The electrical conductivity of cathode is lower than anode, resulting in higher ohmic losses than those generated in anode-supported structure [21, 41, 74, 107, 108].

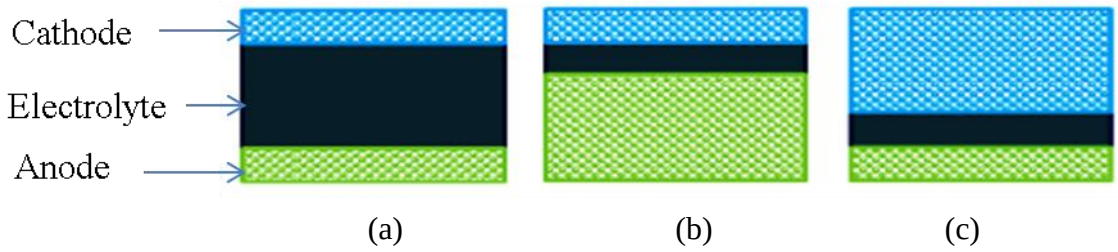

Figure 2.7 (a) Electrolyte-supported (b) Anode-supported (c) Cathode-supported [107]

2.5.5 Fuel for SOFC

One of the biggest benefits of SOFCs is its fuel flexibility and a wide range of fuels can be employed in SOFCs. It is not poisoned by CO, which is the case in low temperature fuel cells, and CO can be used as a fuel in SOFCs. The other potential fuels are hydrogen, methane, long chain hydrocarbons, ethanol, methanol, biogas, ammonia, hydrogen sulphide, etc. [98, 109-112].

When using hydrogen as a fuel in SOFC, the electrochemical reactions are as following:
At the anode

$$H_2 + O^{2-} \longrightarrow H_2O + 2e^- \tag{2.4}$$

At the cathode

$$\frac{1}{2}O_2 + 2e^- \longrightarrow O_2^- \tag{2.5}$$

The overall reaction is

$$H_2 + \frac{1}{2}O_2 \longrightarrow H_2O \quad (2.6)$$

Methane being readily available, abundant in quantity, cheap and having existing delivery infrastructure is considered as one of the most suitable fuels for SOFCs. The direct electrochemical oxidation of hydrocarbons such as methane is possible but not recommended in SOFC due to the risk of carbon formation and instead methane steam reforming reaction is used. Even, in case of methane direct electrochemical oxidation, the carbon decomposition is less than the higher hydrocarbon fuels. The methane reacts with steam and produce hydrogen and carbon monoxide. The reaction is known as methane steam reforming. The carbon monoxide further reacts with steam and produces hydrogen and this reaction is called as water gas shift reaction (WGS) [59, 93, 113-115].

Further details about the fuels use in SOFCs can be found in the literature [109, 116-126].

2.6 Summary

This Chapter dealt with the description of the fuel cell, working principle and performance mechanism of different types of fuel cells. Special attention was paid to the SOFC development history, materials for different components, configurations and utilization of different fuels. The YSZ electrolyte, YSZ/Ni anode and LSM cathode are most widely used materials. The planar SOFC is simple to fabricate, easy to make into various shapes, and has higher power density. The hydrogen is used as a fuel. Due to high operating temperature steam reforming of hydrocarbon fuels such as methane is feasible in SOFCs.

Chapter 3 – Literature Review

The present chapter gives a review of the current stage of the art of SOFC model development by focusing on the problems related with SOFC performance. The Chapter is divided into two main sections first the section 3.1 experimental work and the second section 3.2 numerical studies.

3.1 Experimental Work

The processes related to the SOFC performance are complex and to investigate these processes by experiments are lengthy and costly. However, some data and key parameters such as electrochemical performance of the cell should be determined experimentally and used to compare the simulation results, as they are necessary for a better understanding and accuracy of CFD models. The following sections present a review on the experimental studies performed to find the electrochemical and thermal performance of SOFCs. The experimental work performed to develop and investigate the effect of new materials on SOFC performance is not included in this study.

3.1.1 Electrochemical Performance

The experiments were performed to investigate the effect of operating temperature on the cell electrochemical performance [106, 127-129]. It was found that current density and power generation is higher at high operating temperature, as shown in Figure 3.1. It was Seidler et al. [130] who studied the influence of temperature and pressure on the cell performance. Their results indicated that temperature has more effect on the cell performance than pressure; however, at high pressure the increase in temperature is more beneficial, as can be seen from Figure 3.2.

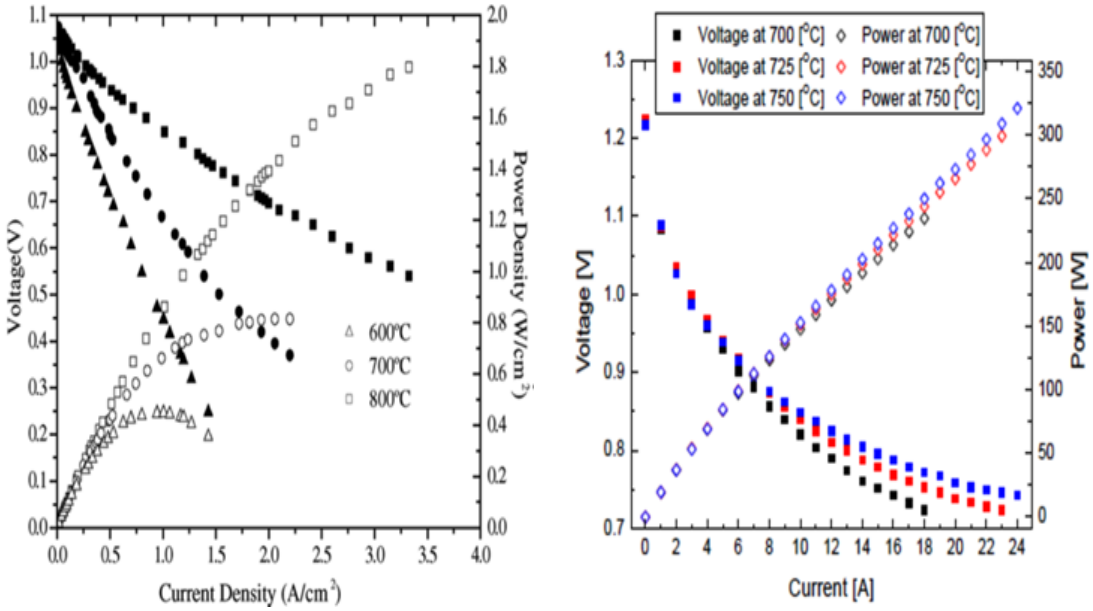

Figure 3.1 Voltage and power density vs. current density at different operating temperatures from 600 to 800 °C [127, 129].

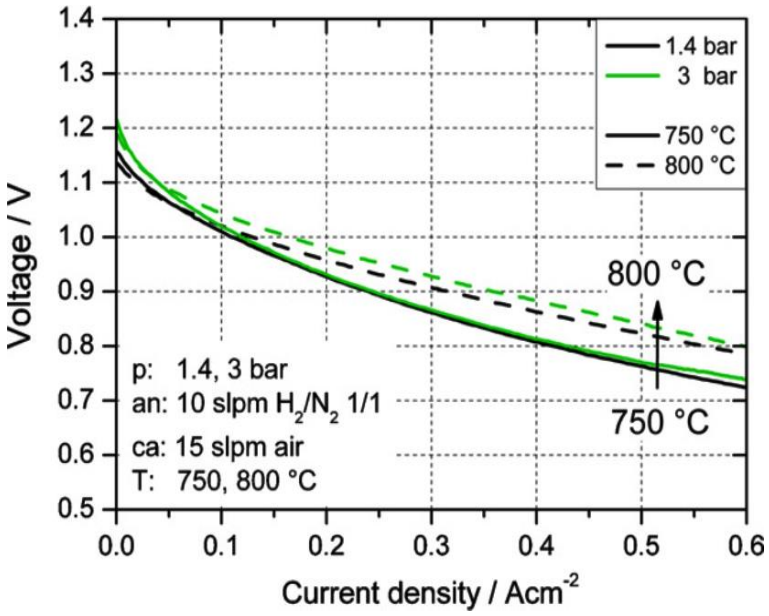

Figure 3.2 VI characteristic curves for 1.4 and 3 bar pressure at operating temperature from 750 to 800 °C [130].

The effect of the contact resistance on the cell performance were analyzed by Jung et al. [131] and Luo et al. [132]. The increase in the resistance hinders the electron flow which results in the decrease of current density of the cell. It was suggested that contact resistance can be reduced by applying appropriate compressive load. Andreassi et al.

[133] obtained V-I characteristic curve from experiment and used to compare his numerical model. It can be seen from Figure 3.3 that both curves show a good agreement.

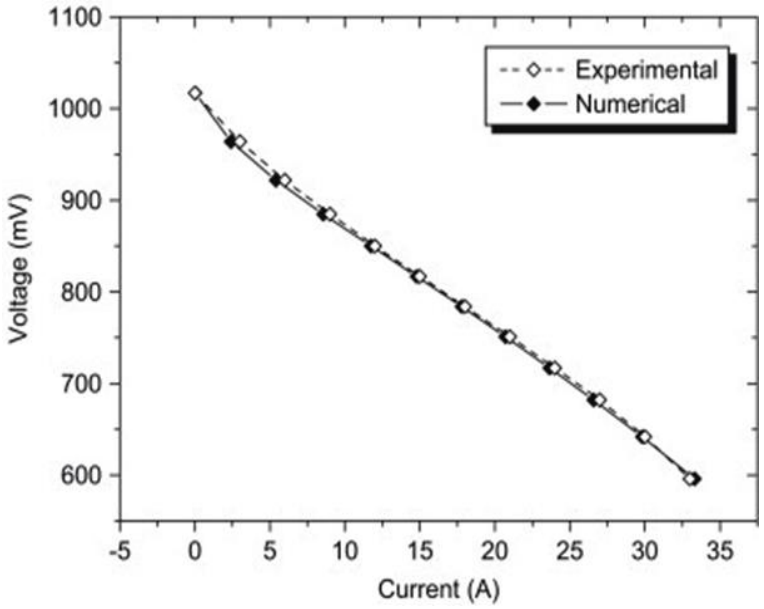

Figure 3.3 Voltage versus current for numerical and experimental studies [133].

Bedogni et al. [134] noticed that the effect of diffusion losses is more prominent at lower hydrogen concentration/ higher current density. The effect of different fuel compositions and mass flow rates were investigated and it was found that the operating conditions influence the fuel cell performance. Lawlor et al. [135] carried out experimental and numerical studies for microtubular (MT) SOFCs by considering the influence of co-flow, counter flow and cross flow configurations. The results showed that for all three configurations the flow regime has no observable impact on the electrical performance and the temperature distribution. It was not clear that why the temperature was always higher, just above the center of the MT-SOFC, further investigations need to be carried out.

3.1.2 Thermal Performance

Yakabe et al. [136] and Fischer et al. [137] estimated the residual stresses in the electrolyte of anode supported SOFCs by X-ray diffraction method. Shao et al. [124]

observed that the temperature of solid electrolyte can be as high as 850 °C in a single chamber SOFC due to the exothermic reaction occurring in the anode. Hao et al. [138] demonstrated that the cell temperature is higher than the furnace temperature because of the exothermic reaction which occurs at the anode/electrolyte interface. Figure 3.4 illustrates the relation between the fuel cell and furnace temperatures.

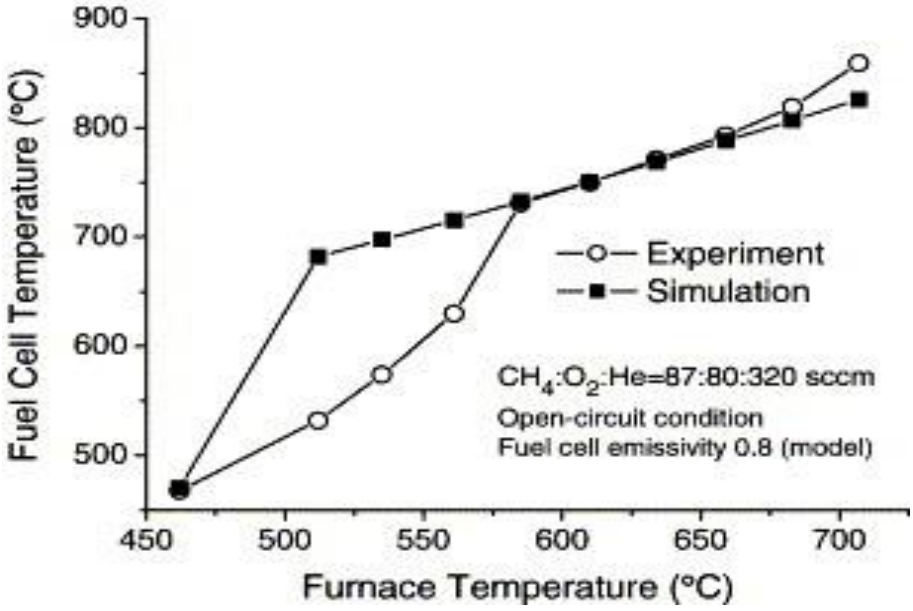

Figure 3.4 Fuel cell temperature versus furnace temperature [138].

Razbani et al. [139] explored the effect of current density on the temperature distribution and cell performance. The maximum temperature was identified at the top right corner of the cell (air inlet and fuel outlet corner). Temperature gradient became higher with increase in current density and this was due to higher polarization at higher current density. It was concluded that the fuel cell performs more efficient at higher oven temperature and referred to a more uniform temperature distribution and lower polarization. Morel et al. [140] predicted that the temperature gradient occurred in SOFC because of the temperature rise at the inlet of the anode which is related to the partial and complete oxidation of methane at the anode. Akhtar et al. [141] investigated the effect of active surface area on temperature distribution and their results prevailed that the active surface area affects the temperature distribution. Fleischhauer et al. [142] performed fracture analysis on electrolyte supported SOFC within the environment of actual operating system. The cracks are more likely to be produced at anode side because of the large thermal expansion coefficient mismatch with electrolyte. It has been observed for the stacks operating more than 4,000 hours that the leakage around

some cracks can cause structural changes in the anode which may initiate the local burning of the fuel. The burnt fuel results in an increase of temperature, concentration of water and oxygen which can oxidize the Nickel. The cracks lead to uneven mechanical pre-load and the stacks own weight. The stresses generated during even distribution of the pre-load are very small but the amount of the stresses could be increased in case of unevenly distribution over the cell area. It remains unclear that how the microstructural changes within the anode during the cell operation will affect the residual stresses.

3.2 Numerical Studies

The processes related with SOFC performance are complex, which coupled the exothermic electrochemical reactions, mass and heat transfer, and the investigations on mechanisms of these coupling processes by experiments are lengthy and costly. Numerical modeling is a suitable approach for understanding the mechanisms involved and for optimizing the SOFC design and performance. The following sections provide a review on the development of computational models for predicting SOFC performances.

3.2.1 Structural Properties of PEN

The effect of porous electrodes properties (porosity and pore size) and operating conditions (inlet mass flow rate and fuel compositions were investigated by Bove and Ubertini [143] and Shi and Xue [144]. The medium porosity should be included to find the effective mass transport through porous electrodes. With the increase of inlet mass flow rates, the cell performances are improved consistently for both homogenous and heterogeneous electrode design. The heterogeneous electrodes showed better cell performance than homogenous electrodes because of slightly more uniform distributions of hydrogen and oxygen. Hosseini et al. [145] compared the predicted V-I curve with the experimental data of similar geometry that was reported by Ceramic Fuel Cell Ltd (CFCL). They had suggested that anode diffusion layer with porosity of 0.2 and 0.4 is beneficial for SOFC operation because of less temperature drop and uniform temperature distribution. A constant permeability was used in the model and investigations of their dependence on the porosity need further research.

3.2.2 Flow Configurations

The effect of the co-flow, counter flow and cross flow configurations on the distribution of cell temperature, current density and species were investigated by Recknagle et al. [146] and Hoa et al. [147]. It was recognized that co-flow has more uniform temperature distribution than other configurations which offers better thermal structural stability, meanwhile, high power density is generated in counter flow case. The results of Larrain et al. [148] indicated that the flow pattern in central feed configuration is similar to that of co-flow configuration. The electrochemical performance of the cell is quite similar for counter flow and central feed configurations, whereas, the temperature is higher in counter flow.

3.2.3 Heat and Mass Transport

Most of mass transfer models early developed [149, 150] for modeling the transportation of gases through porous materials (anode and cathode) are those on the basis of molecular diffusions and neglected the contribution from convections. Tseronis et al. [151] developed a model to couple the mass transfer of hydrogen gas through porous electrode with that in the gas flow channel by a multidimensional model. They found that the concentration gradient of hydrogen in porous electrode is higher than that in the channel because of its lower effective diffusivity. The model is an isothermal model and did not include the effects from heat transfer. It is Camprubi and Fueyo who discussed the effects of 'Multimodal' or convection flux [152] and showed that convective flux may account for 18 percent of the global molar flux. Camprubi et al. [153] then, in continuation to their previous work, developed a model for multicomponent mass transfer using OpenFOAM (Open Field and Manipulation), an open source finite volume method based software. It was evidenced from the multicomponent mass transfer model that the mass transfer of gases through porous electrodes depends on the structural properties of materials, such as pore size. The pore size of materials of anode and cathode for SOFC is, in fact, comparable to mean free path of the gas molecules, under which conditions the convection plays the same role with those of molecular diffusion and Knudsen diffusion and should be taking into account in both of mass and heat transfer models.

3.2.4 Multi-component Modeling

Smirnov et al. [154] performed a multi-physics simulations of fuel cell based on multi-component modeling and found that heat transfer and species transport are the important factors for fuel cell modeling. The effect of co-flow and cross flow configurations on temperature distribution showed that temperature distribution is uniform in co-flow as compared to cross flow configuration. Qi et al. [155] results indicated that air inlet temperature on cathode side has more effects on temperature distribution and cell performance in comparison of other flow parameters. It was observed in Hussain et al. [156] model that ohmic Overpotential from anode side is the largest contributor to the cell potential loss. The ionic conductivity of the material is mainly responsible for the ohmic overpotential and should be enhanced to improve the cell performance. The modeling work of Severson and Assadi [157] and Navasa et al. [158] provided an evidence that increase in the operating temperature results in the decrease of ohmic and activation overpotentials which refers to larger current and power density generation. They have also recorded that the effect of fuel utilization on the cell performance is higher at cell voltage below 0.4 V. Chinda et al. [159] examined the effect of electrodes ionic and electronic conducting particles size ratio and porosity on the cell performance. The performance of the SOFC was found enhanced by equating the volume fraction of ion and electron conducting particles of solid part of electrodes. Xie and Xue [160] observed that the consumption of hydrogen and air and production of water depends on the operating temperature and larger fraction of the hydrogen in the fuel mixture enhances the fuel cell performance. From the review study of Janardhanan and Deutschmann [161] and numerical model of Yang [162] it is concluded that the processes in SOFCs are complex and interdependent and any modeling effort regarding coupling of mass and heat transport and properties of materials should account for improvement in SOFC performance and design. The Yang model included heat transfer through convection only.

3.2.5 Thermal and Mechanical Stress Models

The thermal stress generation depends on temperature distribution and it is important to use the cell temperature to calculate the thermal strain and stress generations. Fischer and Seume [163] evaluated the different mechanism of heat generation and absorption on the thermal stresses developed in the solid structure of the fuel cell. Atkinson and Seluck [164] measured the residual stresses in the ceramic membrane by curvature

measurement technique. Selimovic et al. [165] performed steady state and transient thermal stresses analysis by coupling electrochemical, thermal and structural modeling. They had calculated the stresses generated during the heat up, the startup and the shutdown process. Arata et al. [166] coupled thermo-electro-chemical model to predict the temperature distribution and then the thermal stresses in tubular SOFCs. Their results showed that thermal expansion mismatch between the cell layers have significant effect on the probability of the cell survival. In another study, Arata et al. [167] investigated the effect of electrochemical and mechanical degradation on the structural reliability of the anode-supported planar SOFC stack during long term operation and thermal cycling. It was noticed that a subtle change in the mechanical properties of the materials and interactions between the components may govern their failure. Lin et al. [168] developed a model by using a finite element analysis (FEA) to investigate the effect of sealing design on thermal stresses of planar SOFCs. Zhang et al. [169] performed an analytical study to investigate the effect of cell dimensions on the stresses distribution and estimate the failure probability of the anode by a Weibull theory. Sushrut and Jeong [170] also used the Weibull theory to predict the failure probability of the SOFC cathode. Ihringer el at [171] performed Raman spectroscopy to analysed the mechanical stress at electrode/electrolyte interfaces. Pianko et al. [172] developed a model to investigate the effect of flow channels and fuel cell arrangements on thermal stress generated in anode-supported micro-tubular solid oxide fuel cell (MT-SOFC). The effects of the temperature obtained and the maximum axial tensile stresses generated for both circular and hexagonal stack design were compared. It was difficult to identify which of the considered MT-SOFC stack design was suitable for the optimum solution. The comparison between different channel configurations indicates that external air cooling was the best solution from thermal stress point of view. Peksen et al. [173] analysed the thermomechanical behaviour of SOFC stack during heating up, start up and shut down stages. The results indicated that the stress within the initial stages of the heating-up phase is the most crucial during fuel cell stack operation. It was also identified that the thermal strain greatly influenced by the local temperature and the thermomechanical stress generation depending on the thermal strain. Recently Piyanko et al. [174] investigated the principal stresses by implementing the temperature distribution obtained from thermos-fluid model into thermo-mechanical model. Both models were solved separately. It is predicted that the larger stress generates at lower cell voltage.

3.2.6 MSR and WGS Model

Due to uncertain details and complex reaction processes of hydrocarbon fuels, most modeling approaches within literature have focused on using H_2 as fuel [157, 175-178]. The endothermic internal steam reforming reaction and exothermic electrochemical reaction are separated and consequently may lead to big temperature gradients in porous layers. The close coupling of internal steam reforming and electrochemical reactions gives a good heat transfer [179]. Yuan et al. [180] investigated the effect of geometrical parameters on the cell performance. Their results indicated that the species and temperature distribution were affected by both internal reforming reactions and electrochemical reaction. Hosseini et al. [145] showed that the change in geometrical and microstructural parameters have influences on species and the temperature distribution as well as on the cell overpotentials. Zhu and Kee [181] found that an increase in fuel utilization results in higher concentration overpotential. Hussain et al. [156] predicted that the ohmic overpotential was the main contributor to the cell potential loss. Fan et al. [182] determined the effect of anode material on reaction kinetics. The cell behaves differently at various anode materials as each material has different reaction kinetics and thermal properties. Ni [183] analyzed the SOFC performance at different operating conditions. The increase in temperature results in a higher current density as higher temperature facilitates the direct internal reforming reaction. He also mentioned that the decrease in cell potential caused by higher current density generation. Kee et al. [184] employed different syngas mixtures derived from pre-processing of hydrocarbons, coal and biomass gasification. They have concluded that power density strongly depends on composition, especially H_2 level in fuel mixture. They also emphasized that fuel must be free from impurities (sulfur and carbon contents) as they can disturb the cell structure and ultimately effect the cell performance. Pramuanjaroenkij et al. [185] tested the cell at different operating temperatures by considering different electrolyte materials. The results showed that cell with YSZ electrolyte have higher power density at higher operating temperature. The models were developed by Ho et al. [186] and Andersson et al. [187] to observe the effect of change in temperature and air inlet velocity on temperature, current density and species distributions. Fischer and Seume [163] emphasized on predicting the accurate temperature distribution as the species, current density distributions and reaction rates depend on it.

3.3 Summary

The literature review on the experimental and numerical studies on SOFC development draws following conclusions. Most of the experimental studies focused on the mechanisms of electrochemical performance of the SOFC. The species concentrations and temperature distributions, however, are rarely measured experimentally due to the technical difficulties. There is no data available for reference.

Computational models are a suitable approach in investigations of the mechanisms of reacting flows related, such as transportations of mass, heat and momentum and chemical reactions of cell performance. The cell performances of numerical models were tested by comparing the simulation results (implementing the electrochemical mechanisms) with experimental data. The models were developed to investigate the effect of the geometrical parameters and flow configurations on the cell performance. The cell geometrical and material properties influence the cell performance and optimized parameters should be chosen for cell designs. It has been observed that co-flow configuration shows a uniform temperature distribution and has advantage of thermo- mechanical structural stability over counter and cross flow configurations. Modelling simulations indicated that the operating temperature has a significant effect on the cell performance. Regarding to the transportation mechanisms, it has been concluded that the convection, in addition to molecular and Knudsen diffusion or heat conduction, of mass and heat transport must be considered in the modellings. The thermal and mechanical stress models were developed to account for the stresses generated during manufacturing and different methods (x ray diffraction method, Raman spectroscopy and Weibull theory) were used to predict the cell failure. The SOFCs are high temperature fuel cells (400 – 1000 °C) and due to temperature difference between cell temperature and ambient temperature thermal stresses are generated in the cell. The thermal stress generation is compulsory in order to locate the high stress areas which may cause the cell failure. The methane fuel SOFC models base on anode supported configurations were developed to investigate the effect of the cell geometrical parameters, different anode materials, operating temperatures and fuel compositions on the cell performance. The SOFCs operate at high temperature and favour the internal steam reforming of the hydrocarbon fuels. The MSR is an endothermic and WGS is slightly exothermic reaction. The temperature and species distribution depends on the reaction rate of the chemical and electrochemical reactions.

It is necessary to predict the heats generated and consumed during the chemical and electrochemical reactions and their contribution to thermal impacts.

From the literature review, it has been realized that the models developed so far consider the thermal properties of the fluids and materials as the constants predicted by the operating temperature. However, for SOFCs, the reacting flows in the cell generate a temperature distribution, which leads the local temperature is different to the operational temperature, which is fixed constant once cell operation conditions identified, due to exothermic electrochemical reactions. The differences are significant at a range of 200 – 300 ^{o}C [146, 165, 188]. Such a difference, obviously, must be carefully considered when calculate the thermal properties of the fluids and materials for modeling cell performance, especially, the thermal impacts. This is one of the knowledge gaps identified from literature reviews.

The second one is that no comprehensive investigations have been taken on the effects of the porosities of anode and cathode (due to the variants of materials or the different structures of materials) on their transportation characteristics and further on the cell performance and thermal impacts.

Meanwhile, it must be clarified that the knowledge gap of coupling the reacting flows with thermal impacts for SOFCs had been identified by literature reviews conducted about 4 years ago, when there was no publications founded from the literature for such a fully developed model [154-160] . Based on the first literature review, the PhD study was considered to develop a SOFC model to coupling the reacting flows with the cell thermal impacts, with focusing on the modelling of thermal impacts. The developments of reacting and thermal impacts models in this study are the independent works from those published recently [174, 189]

The details of the studies can be found and are descripted in the following chapters.

Chapter 4 – Mathematical Modelling

The model description of a single planar SOFC and assumptions made to develop a numerical model are discussed firstly in this chapter. The principles of construction of a coupling mechanism model and the governing equations for the mass transfer, fluid flow, heat and charge transport are detailed, which include the electrochemical and chemical reactions mechanisms, the predictions of the mechanical and thermal stresses and the calculations of active surface area for the porous electrodes.

4.1 Model Descriptions

As shown in Figure 4.1 a 2D and b 3D schematic diagram of a single planar solid oxide fuel cell, the planar SOFC in general is structured with the PEN attached top and bottom the air and fuel channels. In physics, it can be viewed as the multicomponent flows with heat and mass transfers in both channels and electrochemical reacting flows in sandwiched porous materials (PEN).

The cell geometrical parameters are given in Table 5.2 of Chapter 5. The mechanical, thermal and electronic properties of YSZ electrolyte, Ni/YSZ anode and LSM cathode taken from literature [50, 181, 190] can be found from Table 5.2 and Table 5.3.

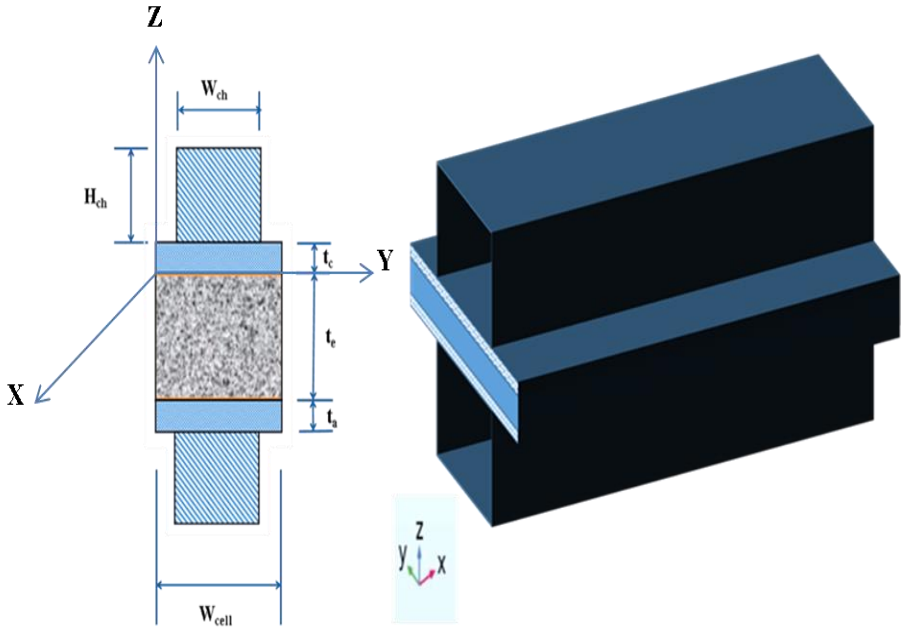

(a) (b)

Figure 4.1 The geometrical outline of a single planar SOFC on cross section (a) and 3D sketch (b).

4.2 Model Assumptions

To develop the numerical simulation model, the following assumptions are made according to the performance analysis: the reaction flow is steady flow with reactant gas mixtures follow the ideal gas law; the electrochemical reactions are considered to only take place at the electrode/electrolyte interfaces; the continuity is considered at the interface of the different components; the ohmic heating due to movement of the electrons is neglected as electrical conductivity is higher than ionic conductivity; the electrolyte is solid and impermeable; all ceramic components exhibit linear elastic behavior; the outer surfaces of anode and cathode are acted as current collectors; the temperature difference is used to calculate the thermal strain and stresses; whereas temperature gradients are employed to determine the thermal strain gradients.

4.3 Coupling Mechanism

As having been discussed in chapter 3, the numerical models developed and applied to SOFC performance and thermal strain and stress predictions are the models that all thermal properties of materials (fluids and PENs) and electrochemical and chemical reactions were estimated by the operating temperature of the cell, which means that they are all the constants once the operating temperature taken. However, those thermal properties, in fact from the principles of SOFC performance, should be predicted by the cell local temperature because the processes involved in SOFCs are interdependent and strongly thermal coupled with each other. For examples, the current density generation depends on the ionic conductivity of the material which is a strong function of the temperature, as shown in Figure 4.2.

Assumptions on thermal decoupling the processes make the model simple, while, lead to uncertainties, especially for the prediction of electrochemical performance and thermal impacts.

The thermal properties of the materials change with temperature which is the case in SOFCs and can be seen in Figure 4.2 and Figure 4.3. In this study, we construct a model by employing the cell local temperature to predict the thermal properties, which is referred as the ‘coupling model’, while, those models developed and used in the existed studies as reviewed in last chapter as ‘decoupling model’.

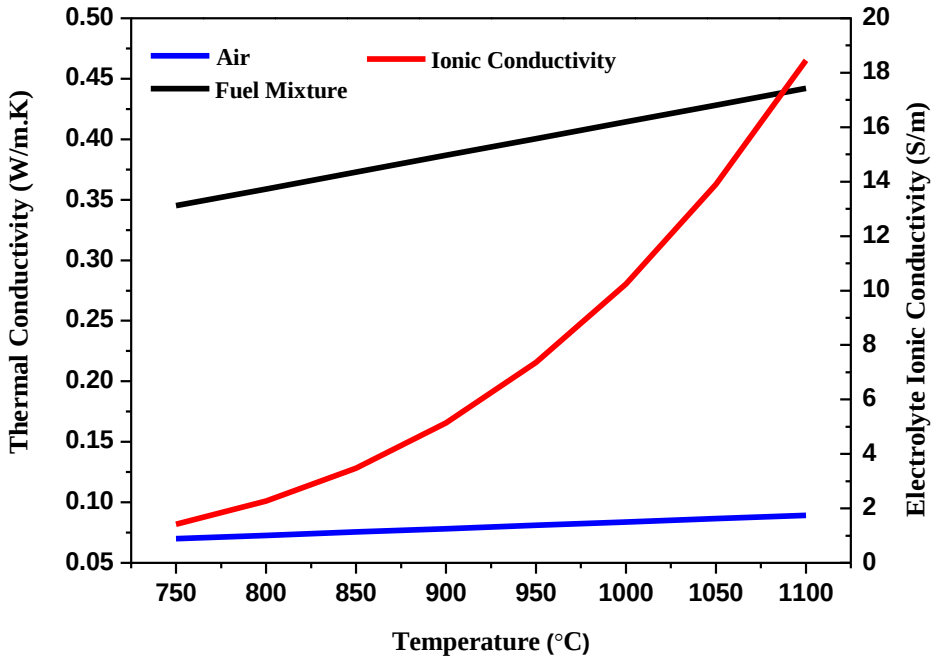

Figure 4.2 Thermal conductivity of the fluids and ionic conductivity of the electrolyte material at different temperatures.

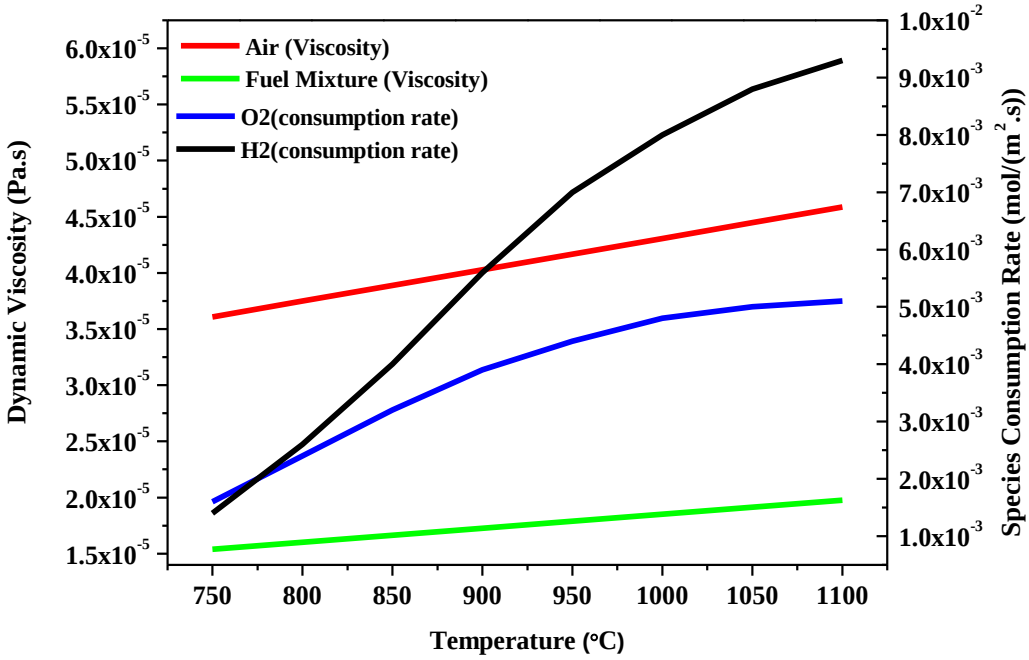

Figure 4.3 Dynamic Viscosity of the fluid, species consumption rate at different temperatures

4.4 Governing Equations

At the steady state performance of SOFCs, Navier-Stokes equations based numerical model, coupling equations of fluid flow, energy and kinetic chemical reactions within/without porous media, are applied for simulation of multicomponent fluid flows through a fuel cell by means of Finite Element Method (FEM). The flow of the gases in the air and the fuel channels is considered as the laminar flow because the Re is in the range of 0.5 – 13. The direct numerical simulations are applied and the following equations are solved for the air and the fuel channels, porous electrodes and solid electrolyte respectively.

4.4.1 Mass Conservation

The mass transfer of *i*th species is driven by convection, diffusion and chemical reactions. The Mixture Average method is used to calculate the diffusive flux in the channels. In porous electrode the diffusion is described by molecular and Knudsen diffusion, for which Dusty Gas Model is applied [191] .

$$\nabla.(\rho \boldsymbol{u} Y_i) = \nabla.\left(\rho D_i^{mk} \nabla Y_i + \rho Y_i D_i^{mk} \frac{\nabla M_n}{M_n}\right) + R_i \tag{4.1}$$

where R_i is a source/sink term for production/consumption of species due to chemical reactions. For a SOFC based on O^{2-} ions conducting electrolyte, at anode, the hydrogen is consumed and water is produced, therefore:

$$R_{H2} = -\frac{M_{H_2}}{2F} i_a \tag{4.2}$$

$$R_{H2O} = \frac{M_{H_2O}}{2F} i_a \tag{4.3}$$

The oxygen is consumed at cathode side, so that:

$$R_{O2} = -\frac{M_{O_2}}{4F} i_c \tag{4.4}$$

where F is Farady's Constant($Cmol^{-1}$). The diffusion coefficient D_i^{mk} (m^2/s) is calculated as;

$$D_i^{mk} = (\varepsilon/\tau)\left(\frac{D_i^m D_i^k}{D_i^m + D_i^k}\right) \tag{4.5}$$

The molecular diffusion (D_i^m) and Knudsen diffusion coefficients (D_i^k) are given by;

$$D_i^m = \frac{1-Y_i}{\sum_{j\neq i}^{N} \frac{X_j}{D_{ij}}} \quad , \quad D_i^k = \frac{R_p}{3}\sqrt{\frac{8RT}{\pi M_i}} \tag{4.6}$$

where D_{ij} $(m^2 s^{-1})$ is multicomponent Maxwell Stefan Diffusion coefficient, which is function of pressure and temperature. It is estimated by using FSG (Fueller, Schettler and Giddings) model [192]:

$$D_{ij} = \frac{10^{-7}T^{1.75}\left(\frac{1}{M_i}+\frac{1}{M_j}\right)^{0.5}}{P\left[V_i^{\frac{1}{3}}+V_j^{\frac{1}{3}}\right]^2} \tag{4.7}$$

M_i $(gmol^{-1})$ and V_i $(cm^3 mol^{-1})$ are the molecular weight and the molecular diffusion volume of the component i, respectively. The values of the molecular diffusion volume for different components can be found from Appendix A.

4.4.2 Momentum Conservation

The Navier-Stokes based equations are solved for gas flow channels and in porous media Brinkman resistance force is used to model the momentum transport.

$$\rho(u\cdot\nabla)u + \frac{\mu}{B}\boldsymbol{u} = -\nabla p + \mu\nabla^2 u + \frac{1}{3}\mu\nabla(\nabla\cdot u) + F_m \tag{4.8}$$

where μ is the dynamic viscosity (Pa.s), F_m is body force (N/m^3) and B is the permeability (m^2). The temperature dependent relations are used to calculate the viscosity of the each species and are taken from the literature [155]. The equations attain to Brinkman equation in the porous media, where the convection terms are small and dominate by the Darcy law.

4.4.3 Energy Conservation

The heat transfer in the cell consists of convection due to gas flows, molecular conduction of fluids and solid (including porous particles), and heat generated due to the electrochemical reactions. The electrodes are porous in thermal equilibrium with gas under the steady flow conditions. The electrolyte is dense and non-porous and only heat

conduction energy equation is applicable. The general equation for the heat transfer is as follows;

$$\nabla \cdot \left(\rho_i C_{p_i} \boldsymbol{u_i} T_i\right) = \nabla \cdot \left(\mathrm{k_i^{eff}}\, \nabla \mathrm{T}\right) + Q \tag{4.9}$$

The effective thermal conductivity k^{eff} in the porous electrodes is given by [185]:

$$\mathrm{k_i^{eff}} = \varepsilon k_{if} + (1-\varepsilon) k_s \tag{4.10}$$

where k_{if} and k_s are the thermal conductivities of the fluid and solid respectively. The heat source Q (Wm^{-2}) in equation (4.9) is calculated by:

$$Q = -\Delta H . \frac{i}{2F} \tag{4.11}$$

where $\Delta H (kJmol^{-1})$ is enthalpy of the reaction and i average current density (Am^{-2}).

4.5 Electrochemical Model

The electrochemical reactions of the energy conversion in a solid oxide fuel cell are the reactions of oxidation of hydrogen. The oxygen anions at cathode transfer through electrolyte and react with hydrogen at the anode/electrolyte interface:

The electrochemical reaction at cathode is

$$\frac{1}{2}\, O_2 + 2e^- \longrightarrow O^{2-} \tag{4.12}$$

The electrochemical reaction at anode is

$$H_2 + O^{2-} \longrightarrow H_2O + 2e^- \tag{4.13}$$

Thus the overall chemical reaction is

$$H_2 + \frac{1}{2} O_2 \longrightarrow H_2O \ (\Delta H_{1173} = -250[kJmol^{-1}]) \tag{4.14}$$

The local current distribution is expressed by using Butler- Volmer kinetic expression. The concentration dependent kinetics equation is used to set up the local current distribution.

$$i_a = i_{a,0}\left\{\frac{c_{h_2}}{c_{h_2,ref}}\exp\left(\frac{\alpha_a^a F}{RT}\,\eta_{act}\right) - \frac{c_{h_2o}}{c_{h_2o,ref}}exp\left(\frac{-\alpha_c^a F}{RT}\,\eta_{act}\right)\right\} \quad (4.15)$$

$$i_c = i_{c,0}\left\{\exp\left(\frac{\alpha_a^c F}{RT}\,\eta_{act}\right) - \frac{c_{O_2}}{c_{O_2,ref}}exp\left(\frac{-\alpha_c^c F}{RT}\,\eta_{act}\right)\right\} \quad (4.16)$$

where $i_{a,0}$ and $i_{c,0}$ are the anode and cathode exchange current densities [A/m^2], respectively. c_{h_2}, c_{h_2o} and c_{O_2} are the molar concentrations of hydrogen, water and oxygen (mol/m^3). $c_{h_2,ref}$, $c_{h_2o,ref}$ and $c_{O_2,ref}$ are the reference concentrations of hydrogen, water and oxygen, respectively. The charge transfer coefficients α_a^a, α_c^a , α_a^c and α_c^c are those of anodic and cathodic on anode side with values are 2 and 1 and those on cathode side with values of 1.4 and 0.6 respectively.

The charge conservation equations are used to describe the electric current transport through porous electrodes

$$\nabla \cdot (-\sigma_i \nabla \varphi_i) = Q_i \quad (4.17)$$

where i=1,2 for electric and ionic, Q_i the current source terms, σ_i the conductivities of the electrodes. The values of σ_i can be found from Table 5.2 and Table 5.3 of Chapter 5. The electrolyte is solid and impermeable to gases and only ionic transport allows.

The activation overpotential/losses at anode and cathode are evaluated by using the following expressions:

$$\eta_{act,i} = \phi_{s,i} - \phi_{l,i} - \Delta\phi_{eq,i} \quad (4.18)$$

Where i=1,2 for anode and cathode, ϕ_s and ϕ_l are electronic and ionic potentials of the electrodes. $\Delta\phi_{eq}$ is the equilibrium potential and in this case the value is zero for anode and 1 for cathode. The cell voltage V_{cell} is set at the outer surface of cathode and zero voltage is set at the outer surface of the anode. The V_{cell} is given by:

$$V_{cell} = \Delta\phi_{eq,c} - \Delta\phi_{eq,a} - V_{pol} \quad (4.19)$$

Where V_{pol} is the polarization. In this model V_{pol} is set in the range 0.05 to 0.3 volts.

Since FEM is used to solve the governing equations and the current is calculated at each node by embedding the ohmic losses. The mass transport model is used to solve the pressure distribution and the current is calculated at each node corresponding to the concentration. Therefore, it is not necessary to include separate expressions for ohmic and concentration overpotentials in FEM, as they are integral part of the numerical solution [193].

4.6 Chemical Reaction Model of Methane with Water

Due to high operating temperature of SOFCs the internal reforming of the methane is possible and it affects the cell thermal condition. Methane steam reforming (MSR) is an endothermic reaction and expressed as;

$$CH_4 + H_2O \longrightarrow CO + 3H_2 \ (\Delta H_{\mathrm{MSR}} = \ 226[kJmol^{-1}]) \tag{4.20}$$

Water gas shift (WGS) reaction is slightly exothermic and is described as;

$$CO + H_2O \longrightarrow CO_2 + H_2 \ (\Delta H_{WGS} = \ -35[kJmol^{-1}]) \tag{4.21}$$

The reaction rates in the literatures vary greatly due to use of different methods, different material structures and different amounts of catalyst [194-199]. The expressions for the reaction kinetics involved in methane steam reforming and water gas shift reaction determined by Haberman and Young [197] and employed in [180, 183, 200] are adopted in this study.

$$R_{MSR} = k_{rf} \left\{ p_{ch_4} \cdot p_{H_2O} - \left(\frac{p_{H_2}^3 \cdot p_{co}}{K_{eq_r}} \right) \right\} \qquad (mol \cdot m^{-3} \cdot s^{-1}) \tag{4.22}$$

$$R_{WGSR} = k_{sf} \left\{ p_{H_2O} \cdot p_{co} - \left(\frac{p_{H_2} \cdot p_{co_2}}{K_{eq_s}} \right) \right\} \ (mol \cdot m^{-3} \cdot s^{-1}) \tag{4.23}$$

where $k_{rf,}\, k_{sf}$ and $K_{eq_r}\ K_{eqs}$ are forward reaction rate constants ($mol \cdot m^{-3} \cdot Pa^{-2} \cdot s^{-1}$) and equilibrium constants (Pa^2)for reforming and shifting reactions, respectively. The forward rate constants for methane and water gas shift reactions can be estimated by [197],

$$k_{rf} = \ 2395 \cdot exp(-231266/(R \cdot T)) \tag{4.24}$$

$$k_{sf} = \ 0.0171 \cdot exp(-103191/(R \cdot T)) \tag{4.25}$$

The equilibrium constants for both reactions are defined as functions of temperature by the following empirical relations,

$$\begin{aligned} K_{eqr} = \ & 1.0267 \cdot 10^{10} \cdot \exp(-(0.2513 \cdot Z^4) + (0.3665 \cdot Z^3) \\ & + (0.5810 \cdot Z^2) - \ (27.134 \cdot Z) + \ 3.2770) \end{aligned} \tag{4.26}$$

$$K_{eqs} = \ \exp(-(0.2935 \cdot Z^3) + (0.6351 \cdot Z^2) + (4.1788 \cdot Z) + \ 0.3169) \tag{4.27}$$

where $Z = \frac{1000}{T(K)} - 1$ and T is in Kelvin

4.7 Thermal Strain and Strain Gradients

The change in temperature plus the thermal expansion mismatch between different layers produce thermal strain in the cell. The thermal strains generated in the cell can result in the separation of the layers or micro cracks in the weaker layer. The temperature difference distribution for coupled and decoupled models is used to calculate the thermal strain generation in the cell. Thermal strain is a scalar quantity and relation used to calculate the thermal strain is as follows;

$$\varepsilon_{th} = \ \alpha \Delta T \tag{4.28}$$

where α is thermal expansion coefficient (1/K) and ΔT is temperature difference (K) between the cell temperature and strain free reference temperature. The thermal expansion coefficients for anode, electrolyte and cathode are listed in Appendix – B.

Thermal strain gradients are determined by implementing the spatial (x_i) gradient of temperature by,

$$\frac{\partial \varepsilon_{th}}{\partial x_i} = \alpha \frac{\partial T}{\partial x_i} \tag{4.29}$$

4.8 Thermal and Mechanical Stresses

The thermal strains together with the mechanical properties (Young's Modulus of Elasticity) of the materials, varied for each layer of the cell, are applied to calculate the thermal stresses. The thermal stresses are calculated by:

$$\sigma_{th} = \varepsilon_{th} E \tag{4.30}$$

where E is the Young's Modulus of Elasticity (GPa). The value of the Modulus of Elasticity for anode, electrolyte and cathode is given in Appendix – B.

The mechanical stresses generated in the cell structure are investigated by the application of Von Mises stress criterion. The Von Mises stresses are related with elastic strain of the material. The elastic strain is the difference of total strain and the thermal strain while the total strain is calculated by change in displacement. There is no external load whereas the fluid pressures and temperatures are considered as the load on the cell. The Von Mises stress criterion suggests that the yielding of the material begins when the second deviatoric stresses invariant J_2 reaches at the critical value. The criterion can be written in terms of the elements of Cauchy's stresses tensor:

$$J_2 = 1/6\left((\sigma_{11}-\sigma_{22})^2 + (\sigma_{22}-\sigma_{33})^2 + (\sigma_{33}-\sigma_{11})^2\right) + (\sigma_{12})^2 + (\sigma_{23})^2 + (\sigma_{13})^2 \tag{4.31}$$

The Von Mises criterion is implemented as:

$$F = \sqrt{3\,J_2} - \sigma_{ys} \tag{4.32}$$

where σ_{ys} is yield stresses level and $\sqrt{3\,J_2}$ is Von Mises stresses denoted as σ_{mises} . The total stresses are calculated as:

$$\sigma_{total} = \sigma_{th} + \sigma_{Mises} \tag{4.33}$$

4.9 Active Surface Area

The electrochemically active surface area per unit volume of the porous electrode (m^2/m^3) developed by Costamagna et al. [201] based on the particle coordination number in binary random packing of spheres, given as [145, 156, 159]:

$$A_v = \pi \sin^2\theta \,.\, r_{el}^2 n_t n_{el} n_{io} \frac{Z_{el} Z_{io}}{Z}\, P_{el} P_{io} \tag{4.34}$$

where θ is the contact angle between ion and electron conducting particles; n_t is total number of particle per unit volume; n_{el} and n_{io} are the number fractions of the electrode and ion conducting particles respectively; Z_{el} and Z_{io} are the coordination number of the electron and ion conducting particles; Z is the total average number of contacts of each particle which is equal to 6 [201] and P_{el} and P_{io} are the probabilities for the electron and ion conducting particles to belong to connecting ends of the composite.

All the parameters required to calculate the A_v can be calculated from [201, 202]:

$$n_t = \frac{1 - \varepsilon}{\left(\frac{4}{3}\right)\pi r_{el}^3 [n_{el} + (1 - n_{el})\left(\frac{r_{io}}{rel}\right)^3]} \tag{4.35}$$

Where ε is the electrode porosity, and:

$$n_{el} = \frac{\varphi_{el}}{[\varphi_{el} + ((1 - \varphi_{el})/\left(\frac{r_{io}}{r_{el}}\right)^3)]} \tag{4.36}$$

$$n_{io} = 1 - n_{el} \tag{4.37}$$

$$Z_{el} = 3 + \frac{Z - 3}{\left[n_{el} + (1 - n_{el})\left(\frac{r_{io}}{r_{el}}\right)^2\right]} \tag{4.38}$$

$$Z_{io} = 3 + \frac{(Z - 3)\left(\frac{r_{io}}{r_{el}}\right)^2}{\left[n_{el} + (1 - n_{el})\left(\frac{r_{io}}{r_{el}}\right)^2\right]} \tag{4.39}$$

$$P_i = \left[1 - \left(2 - \frac{Z_{i-i}}{2}\right)^{2.5}\right]^{0.4} \tag{4.40}$$

where i = 1, 2 for ionic and electronic particles and Z represents the average coordination number and is calculated between the particles as [156, 159],

$$Z_{i-i} = \frac{n_i Z_i^2}{Z} \tag{4.41}$$

The values of the parameters used to calculate the above equations and finally active surface area is listed in Table 4.1.

Table 4.1 Parameters used to Calculate Active Surface Area

Parameter	Value
Volume fraction of electron conducting particles φ_{el}	0.5 [201]
Radius of electron conducting particles r_{el} (μm)	0.1[202]
Radius of ion conducting particles r_{io} (μm)	0.1 [202]
Porosity of the electrodes ε	0.4

The value of the reactive surface area per unit volume of porous electrode calculated from equation (4.34) is 386236 [m^{-1}].

4.10 Boundary Conditions

The channel inlet BCs of species, fluid flows and energy are set by given mass fractions of each species, mass flow rates, and temperature, while, the zero pressure and flux gradients for outlet BCs. The channel wall is considered as a rigid adiabatic wall with a

no slip interface with fluids. For solid mechanics zero displacement and load boundary conditions are applied for the external walls of the PEN structure.

4.11 Summary

This chapter presented the details about the coupling mechanism and geometries of the single planar SOFC. The assumptions made for modelling the cell are described. The governing equations are explained. The mechanisms involved in the electrochemical and chemical reactions are listed. The relations involved in the calculation of the mechanical and thermal stresses are explained. The method to calculate the active surface area is demonstrated. Finally, the boundary conditions are highlighted.

Chapter 5 – Reacting Flow Coupling with Thermal Impacts in a single Solid Oxide Fuel Cell with Hydrogen Fuel

The developed model described in Chapter 4 is applied to the simulations of a single planar SOFC running on Hydrogen and thermal impact on the cell performance. The numerical results are verified by comparing with the date of International Energy Agency (IEA). The effects of the different parameters on the cell electrochemical and thermal performance are analyzed and discussed.

5.1 Introduction

The material properties of PEN, as discussed in the previous chapters depend on the porosity and temperature. In literature independent porosity and operating temperature base relations are used to calculate the material properties [139, 188, 190, 193, 200, 203-206]. The model is developed in Chapter 4 by incorporating all the parameters which affect the cell performance. Simulations are carried out by Comsol multiphysics computer software. The dependency of the numerical solutions on the mesh quality is explained. The electrochemical and thermal performance results of the coupling and decoupling simulations, for a co-flow configuration, are compared with the results of bench mark data of International Energy Agency (IEA) [50] . The effect of the operating temperatures and material properties such as porosity and conductivity on the cell performance has been investigated. The thermal strain and their gradients are predicted by using the temperature difference and gradient distribution. The thermal and Von Mises stresses are calculated for both cases by implementing the temperature profile and areas for maximum stress generation are highlighted. The effect of the boundary restrictions on the stresses generated in the cell is also studied. Finally it is evident that coupling is necessary as temperature plays an important role in the electrochemical and thermal performance of SOFC.

5.2 Mesh Quality

The mesh quality plays an important role in the accuracy and stability of numerical solutions. The model is tested for 8 different numbers of elements from 7400 to 148000 to check the stability of the solution. The finer the resolutions, the much CPU time needed and more cost. User define option available in Comsol is used to set the mesh size. The current density produced during the cell operation, the heat generated and the thermal stresses in the cell are examined for all the 8 meshes. It has been found that

from 7400 to 29600 the value of the current density change significantly (from 3004 to 3413.9 A/m^2) and then the variations are only 0.017% as shown in Table 5.1. As such, the mesh with 29600 elements is adopted for rest of simulation cases. Similarly, the changes in maximum temperature of the cell for mesh sets between 7400 and 29600 are from 1175 °C to 1150 °C and then approaching to negligibly small. Thermal stresses are also change only 0.041% at 29600 mesh elements. As such, the mesh with 29600 elements is adopted for the rest of simulation cases.

Table 5.1 Mesh Quality

Total Number of Elements (in the Anode /Cathode)	Current Density (A/m^2)		Temperature (°C)		Thermal Stresses (MPa)	
	Value	% variation between two mesh elements	Value	% variation between two mesh elements	Value	% variation between two mesh elements
7400 (840/840)	3004	~	1143	~	2190.3	~
14800 (1680/1680)	3421.4	-12.199	1154	-0.953	2197	-0.304
29600 (3360/3360)	3413.9	0.219	1149	0.435	2190.9	0.278
44400 (5040/5040)	3433.5	-0.570	1148	0.087	2190	0.041
59200 (6720/6720)	3434.1	-0.017	1148	0	2189.8	0.009
74000 (8400/8400)	3434.6	-0.014	1147	0.087	2189.7	0.004
101750 (11550/11550)	3435	-0.011	1147	0	2189.6	0.004
148000 (16800/16800)	3435.9	-0.026	1147	0	2189.7	-0.004

5.3 Model Verification

The data of bench mark case of International Energy Agency (IEA) [50] is used as a reference to compare the simulation results of the model. In the verification simulations, the conductivities of porous electrodes and electrolyte are considered as independent of porosity and operating temperature. The density, specific heat capacity and thermal

conductivity of the solid electrolyte and porous electrodes are listed in Table 5.2 and Table 5.3. The geometrical and operational parameters, material properties and electrochemical parameters used in the test and verified cases can be found from Table 5.2 and Table 5.3, respectively. The electrochemical performance for the co-flow cell configuration is shown in Figure 5.1. The average current density is measured by implementing the electrochemical parameters available in the literature. The value of the average current density for test case is 3711.6 A/m^2 at 0.7 V. It is found that the exchange current densities on anode and cathode sides of 175 and 140 A/m^2 made the results good match to those of Bench Mark results of IEA [50]. The average current density for verified case is 2664 A/m^2 at 0.7 V, as shown in Figure 5.1. The value of the cell voltage, maximum current density, maximum solid temperature and air and fuel outlet temperature is compared with the Bench Mark results of International Energy Agency (IEA) and are given in Table 5.4.

The current density distribution for the verified case at anode/electrolyte interface along the cell length and width is shown in Figure 5.2. The maximum current density 3954 A/m^2 is at the cell inlet and decreases along the flow direction because of the species consumption. The temperature distribution is plotted at anode/electrolyte interface along the cell length for the verified case and results are displayed in Figure 5.3. The heat generation at anode/electrolyte interface because of the electrochemical reaction results in higher cell temperature of 1098 °C. The generated heat is transferred to incoming cool air and the maximum temperature lies at the cell outlet.

The results of the present study and those from Bench mark case are detailed in Table 5.4. The results of the present study showed a good agreement with the Bench Mark results. The 14.50 % of air and 81.50% of fuel is utilized. The overall discrepancy in both results is smaller than 2.9%. Because of the limited availability of data in the bench mark case, such as detail data of the exchange current densities, material properties for the porous electrodes and the flow rates, no further the comparisons are made.

Table 5.2 Geometrical, Operational, Mechanical and Electrochemical Parameters available in IEA report [50].

Description	Value	Description	Value
Channel Width ($W_{ch)}$ (mm)	3	Operating Voltage (V)	0.7
Rib Width ($W_{rib)}$ (mm)	2.56	Hydrogen inlet mass fraction	0.5
Single Cell Width ($W_{cell\ )}$(mm)	5.56	Oxygen inlet mass fraction	0.23
Single Cell Length (L) (mm)	100	Water inlet mass fraction	0.5
Channel height (H_{ch}) (mm)	1	Electrolyte Heat Conductivity (k_e) (W/m*K)	2
Anode thickness (t_a) (mm)	0.05	Electrolyte Heat Capacity (cp) (J/kg*K)	400
Cathode thickness (t_c) (mm)	0.05	Electrolyte Density (ρ_e) (kg/m^3)	6600
Electrolyte thickness (t_e) (mm)	0.150	Anode electronic conductivity, (δ_{a_e}) (S/m)	[((9.5 x 10^7)/T_{oper}) exp(-1150/T_{oper})]
Pressure (p) (bar)	1	Cathode electronic conductivity, (δ_{c_e}) (S/m)	[((4.2 x 10^7)/T_{oper}) exp(-1200/T_{oper})]
Temperature (T) (K)	1173	Electrolyte ionic conductivity, (δ_{e_i}) (S/m)	3.34 x 10^4 exp(-1200/T_{oper})

Table 5.3 Geometrical, operational, Mechanical and Electrochemical Parameters taken from the literature.

Description	Value	Description	Value
Anode and Cathode porosity (ε)	0.4 [160, 183]	Cathode Density (ρ_c) (kg/m3)	5300 [190]
Anode and cathode (k) permeability (m^2)	6.2E-13[181]	Anode reference exchange current density $i_{o\_}a$ (A/m^2)	1320 [156]
Tortuosity (τ)	$\varepsilon^{-0.5}$ [144]	Anode anodic charge transfer coefficient, α_a^a	2 [114, 133, 207]
Average Pore Diameter (D_p) (μm)	1 [183, 203]	Anode cathodic charge transfer coefficient, α_a^c	1 [114, 133, 207]
Fuel mass flow (kg/s)	4.255E-8 [208]	Cathode reference exchange current density $i_{o\_}c$ (A/m^2)	400 [156, 201]
Air mass flow (kg/s)	3.404E-6[208]	Cathode anodic charge transfer coefficient, α_c^a	1.4 [114, 133]
Anode Heat Conductivity (k_a) (W/m*K)	6 [190]	Cathode cathodic charge transfer coefficient, α_c^c	0.6 [114, 133]
Anode Heat Capacity (cp) (J/kg*K)	600 [190]	Anode effective electronic conductivity, (δ_{a_e}) (S/m)	(1-ε)*[((9.5 x 10^7)/T_{oper}) exp(-1150/T_{oper})] [209]
Anode Density (ρ_a) (kg/m3)	7740 [190]	Cathode effective electronic conductivity, (δ_{c_e}) (S/m)	(1-ε)* [((4.2 x 10^7)/T_{oper}) exp(-1200/T_{oper})] [209]
Cathode Heat Conductivity (kc) (W/m*K)	10 [45]	Anode effective ionic conductivity, (δ_{a_i})	(1-ε)*3.34 x 10^4 exp(-1200/T_{oper}) [209]

Cathode Heat Capacity (cp) (J/kg*K)	607 [190]	Cathode effective ionic conductivity, (δ_{a_i})	$(1-\varepsilon)*3.34 \times 10^4$ $\exp(-1200/T_{oper})$ [209]

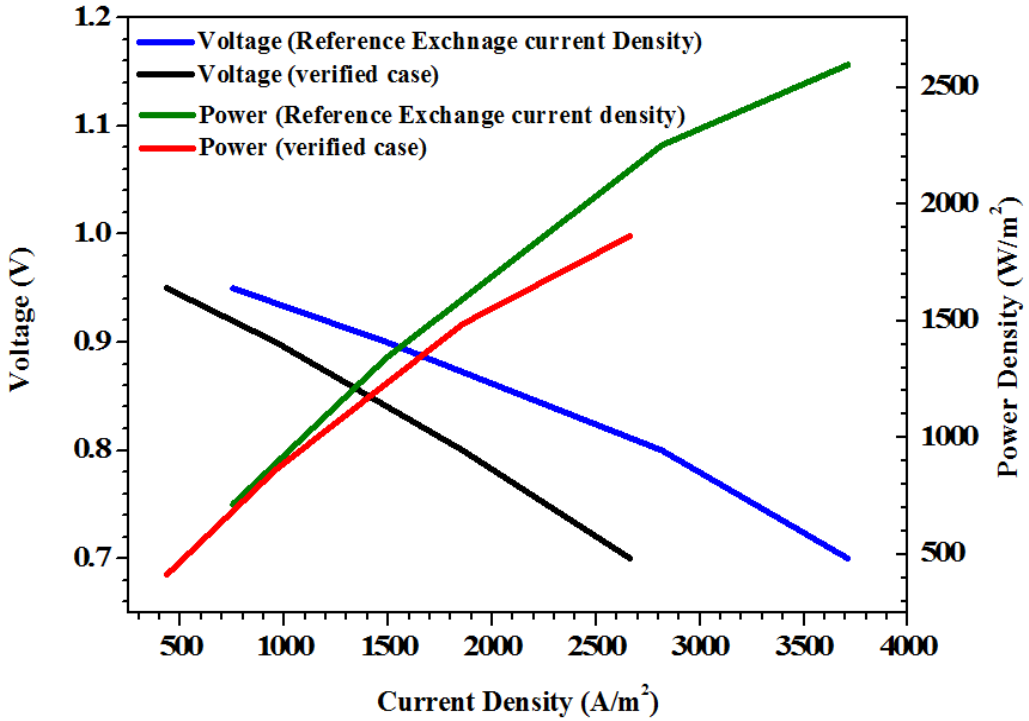

Figure 5.1 Voltage and power density against current density for reference and improved exchange current density cases (decoupled models). The Bench mark current density range is 2430 – 2661 A/m^2 and power density range is 1754 – 1868 W/m^2 [50].

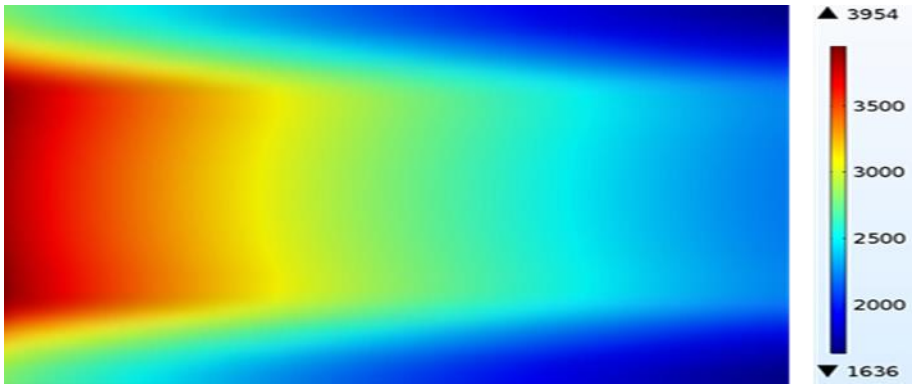

Figure 5.2 Current Density distribution from without porosity based conductivity relation case at section F (refer to section 5.4).

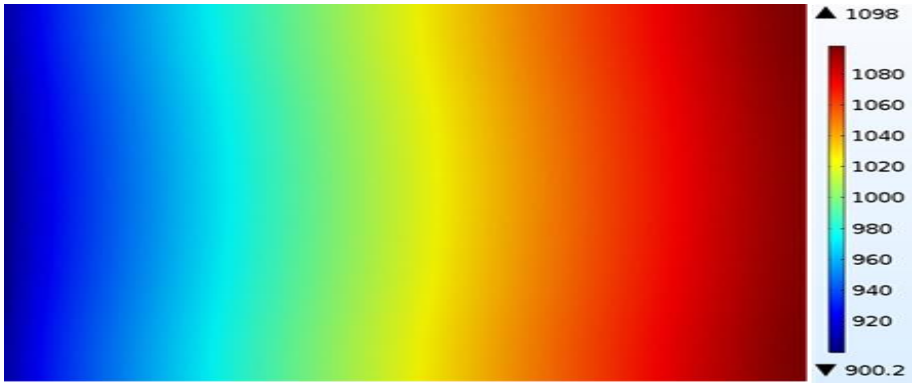

Figure 5.3 Temperature distribution from without porosity based conductivity relation case at section F.

Table 5.4 Comparisons of present results with IEA

Parameter	Present Study Results	IEA	Errors between the present study and IEA results
Cell Voltage (V)	0.7	0.702 – 0.722	0.3 %
Average Current Density A/m^2	2664	2430 – 2661	0.11 %
Average Power Density W/m^2	1864.8	1754 – 1868	0.18 %
Maximum Current Density A/m^2	3954	3,725 – 3,957	2.86 %
Maximum Solid Temperature (°C)	1098	1,048 – 1,098	0 %
Air outlet Temperature (°C)	1089.6	1,048 – 10,68	2.02 %
Fuel Outlet Temperature (°C)	1095.8	1,048 – 10,68	2.60 %

5.4 Results and Discussion

The orientation of the figure is as given in Figure 4.1 and the geometrical parameters are listed in Table 5.2. The cell is constructed by setting the electrolyte, anode and fuel channel below while cathode and air channel above the 0 of the axes.

In order to understand the mechanism inside the fuel cell, the results are plotted at different locations. The positions along cell length (X) are considered on the horizontal sections (X-Y) at y= 2.71E-6 m and the centre of anode (z = -175E-6 m), electrolyte (z = -75 E-6 m), cathode (z = 25 E-6 m), and fuel channel (z = -7.0 E-6), which are referred as section A, B, C and D, respectively.

The vertical sections (Y-Z) considered are the sections at three different locations of close to the inlet (x = 1.0 E-3 m), at the centre (x = 50 E-3m) and close to the outlet (x = 99 E-3 m), which are named as section Es.

Two horizontal sections are at the interface of anode/electrolyte (z = -150E-6m) and the interface of cathode/electrolyte (z =0), which are referred as section F and section G, respectively.

The comparison results from coupled and decoupled models are referred as "c-d models comparison" in order to avoid the repetition in the thesis.

5.4.1 The Effects of the Material Porosity on the Cell Performance and Thermal Impacts

The anode and cathode are porous electrodes and their electronic and ionic conductivities depend on porosity and temperature. The porosity dependent relations for anode and cathode conductivities are used in the case studies. The anode, cathode and electrolyte materials are different and the properties used in the cases studies are listed in Table 5.2 and Table 5.3. The current density generation depends on the conductivities and addition of porosity term in the relations results in less current density. The current densities at different cell voltages with and without porosity based conductivity relation are presented in Figure 5.4. The current density at 0.7V for without porosity based conductivity is 2664 A/m^2 and 2519.8 A/m^2 for porosity based conductivity case. The difference in current density for both cases is 5.4%.

The amount of the heat generation depends on the current density. The maximum cell temperature is 1085 °C as shown in Figure 5.6.

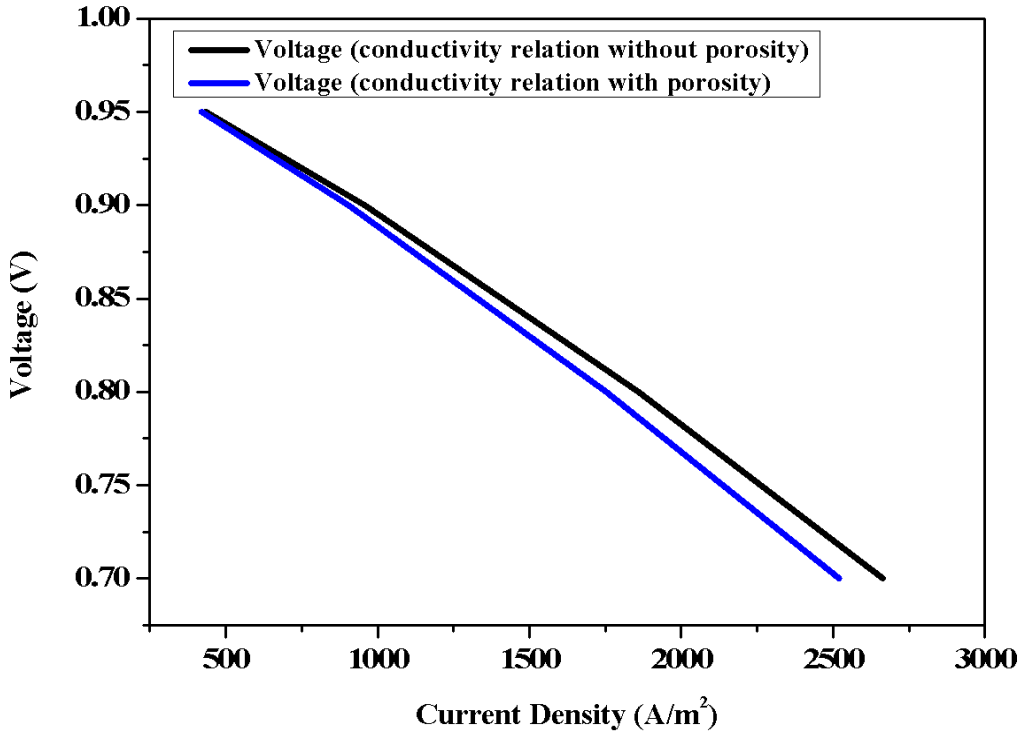

Figure 5.4 V-I characteristics with and without porosity based conductivity relation cases.

5.4.2 Current Density and Temperature Distribution

The current density distribution along the cell length is predicted and the results are shown in Figure 5.5. The maximum current density is 3697 A/m^2 and matches with Bench mark results. The current density distribution is not uniform. The maximum current density is located at inlet because of higher concentration of fuel and air. Along the cell length the species consume and concentrations drops as a result the current density decreases along the cell length. The difference in maximum current density generation for the cases with and without porosity based conductivity is 6.5 %.

The temperature distribution is essential as the transportation properties, such as electrochemical reaction, thermal strain and stress generation and the material properties (ionic and electronic conductivity), are strongly linked with temperature. Therefore temperature profile is obtained by coupling fluid flow, species transport, electrochemical reactions, heat transfer and thermal impact. The temperature distribution at anode/electrolyte interface along the cell length and width is depicted in Figure 5.6. At inlet the temperatures is 900 °C and because of the heat generated by electrochemical reactions the temperature increases and reaches to a maximum value 1085 °C which is in the range of Bench mark data. The maximum cell temperature is

1.2 % less than the verified case (porosity independent constant conductivity). The increase in the temperature is along the direction of the flow. The maximum temperature is at the air/fuel outlet.

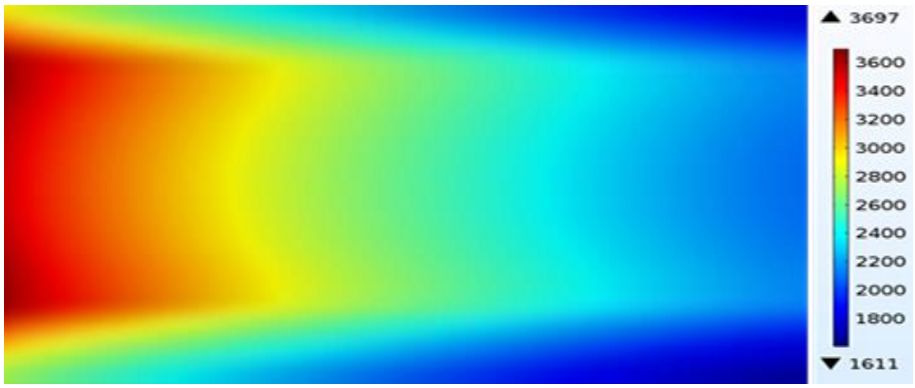

Figure 5.5 Current density distribution from porosity based conductivity relation case at section F.

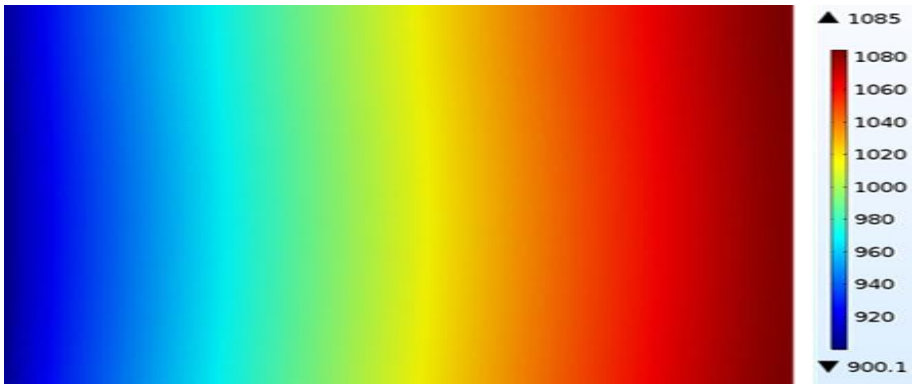

Figure 5.6 Temperature distribution from porosity based conductivity relation case at section F.

5.4.3 Species Distribution

The performance of the SOFC depends upon the species distribution. To demonstrate the details, they are investigated in terms of species mass fractions, as shown in Fig. 5.7, the oxygen mass fraction in the centre of cathode along the cell length. The Oxygen consumptions by the electrochemical reaction lead to a drop from maximum 0.233 at inlet to minimum 0.20 at outlet.

The hydrogen mass fraction decreases nonlinearly from 0.5 at inlet to 0.097 at outlet due to nonlinear chemical reactions, as shown in Figure 5.7. The distribution profile of water shows an opposite trend as it produces during the electrochemical reaction. The mass fraction of water increases from minimum 0.5 at inlet to maximum 0.903 at outlet.

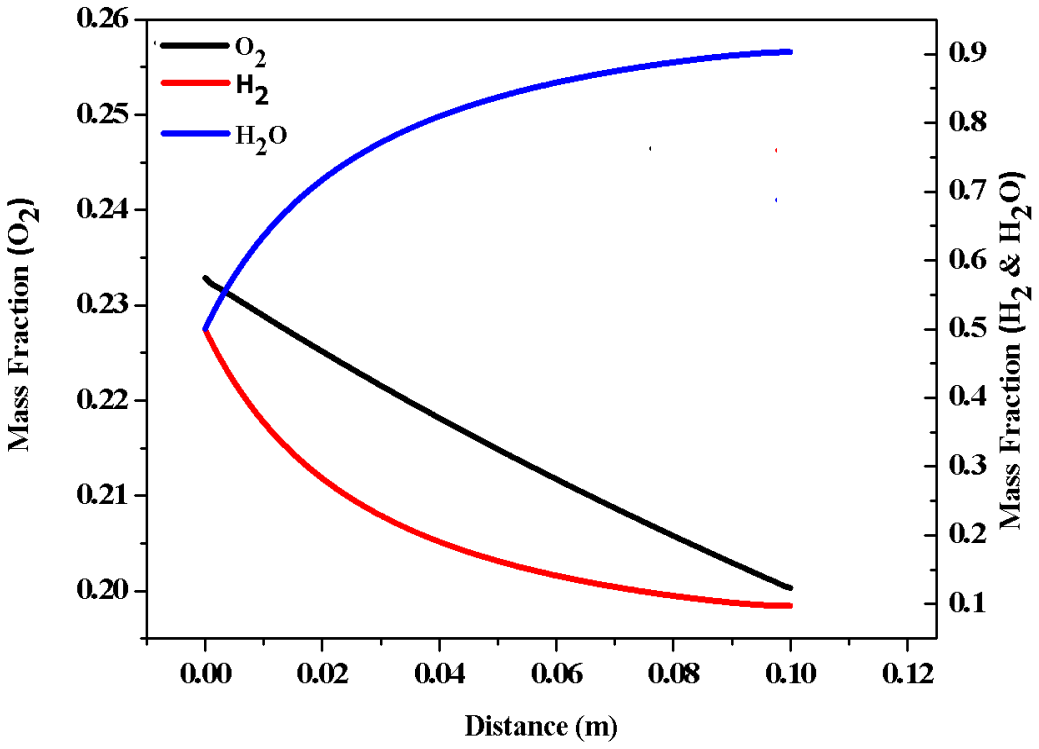

Figure 5.7 Species mass fraction distribution at sections A and C.

5.4.4 Effect of Inlet Temperature on Cell Performance

The model is tested at different inlet temperatures. The current density increases by varying the temperature between 800 °C to 1000 °C which are 1727.8 A/m^2 and 2976.4 A/m^2, respectively. The increase in current density is 72.3%. This is due to the increases in ionic conductivity as increase in temperature, and can be seen in Figure 5.8. The temperature dependent relations for the ionic conductivity of porous electrodes and the solid electrolyte are used to investigate the effect on the cell performance. The relations are listed in Table 5.2. The minimum conductivity at 800 °C is 2.67 (S/m) and reaches to value of 10.238 (S/m) at 1000°C.

The effect of different inlet temperatures on the temperature distribution in the centre of the electrolyte along the cell length is taken to demonstrate the results, which is indicated in Figure 5.9. Obviously, the increase in inlet temperature results in more heat generation and as a consequence the cell temperature increases. The maximum temperature difference at 800 °C is 908.97 °C and reaches to 1191.95 °C at 1000 °C inlet temperature. The increase in cell temperature difference is 31.13%. The increase in cell temperature difference results in higher thermal strain and stress generation.

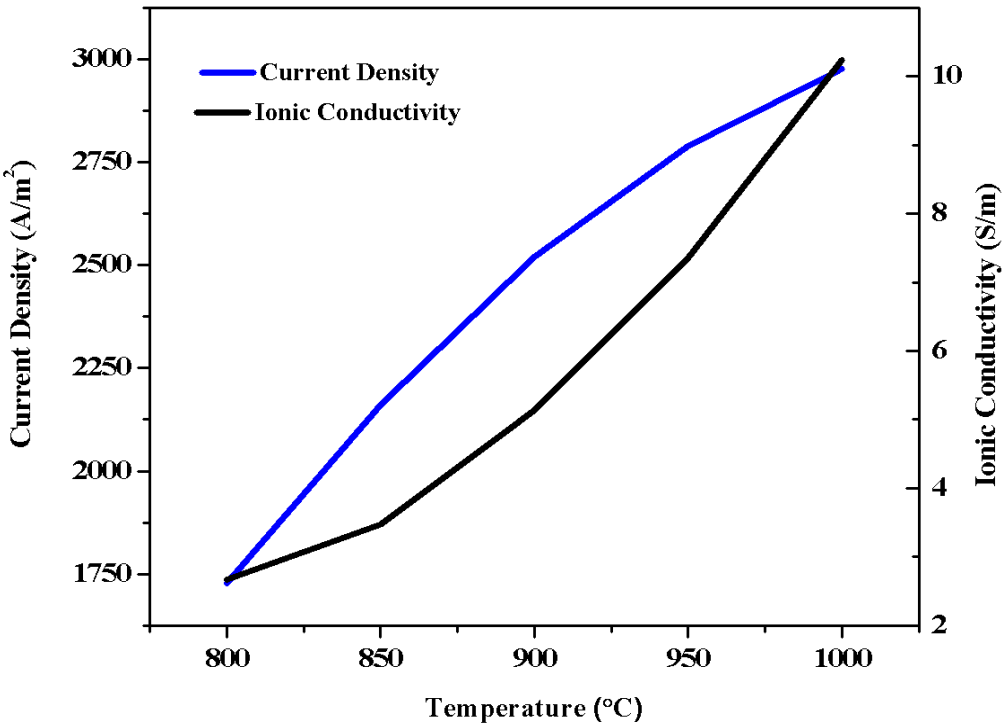

Figure 5.8 Current density and electrolyte ionic conductivity vs inlet temperature.

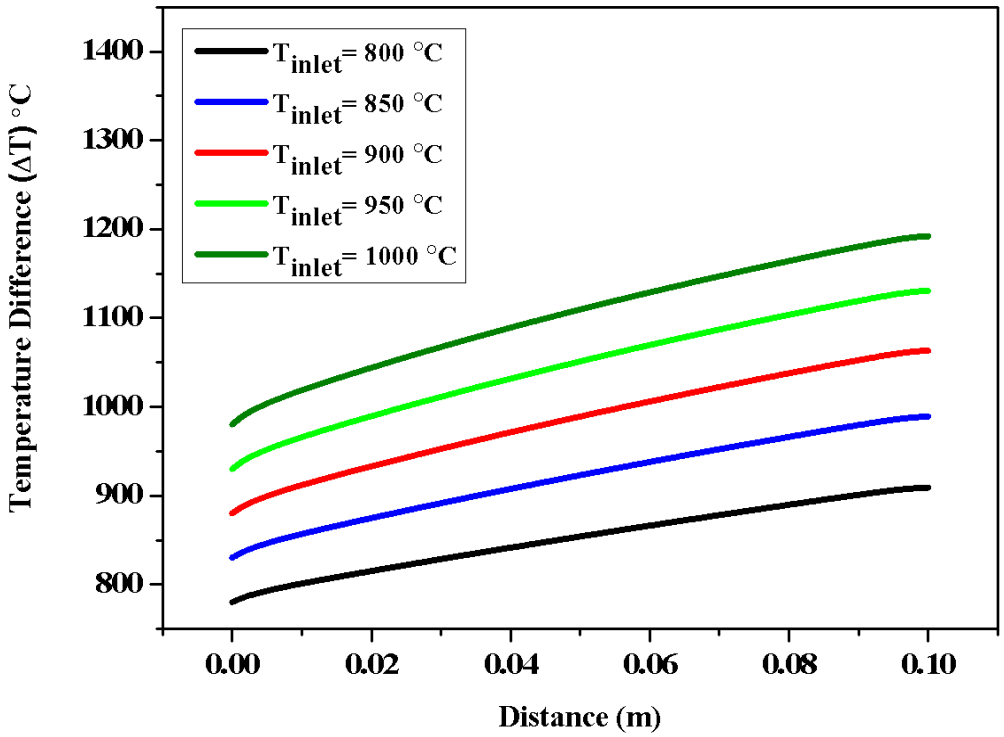

Figure 5.9 Temperature difference distribution at section B.

5.4.5 Effect of Material Properties (Ionic Conductivity) on Cell Performance

As mentioned in chapter 3, most of existed models (decoupled) are built by using operating temperature (fluid temperature at inlet) which means a constant value of the ionic conductivity is used for simulations. The cell is tested for different inlet temperatures and it has been observed that the performance of the cell significantly changed with change in temperature [106, 127-129]. Therefore, it is necessary to predict the temperature distribution more carefully by coupling the thermal related parameters of the model with cell local temperature. This effect is checked by the coupling model (refer to section 4.3) developed by this study. The effect of the cell local temperature on the ionic conductivity of the electrolyte is shown in Figure 5.10. The conductivity in decoupled model is constant 5.137 S/m but in coupled model the ionic conductivity varies from 5.137 to 21.43 S/m. The temperature distribution from c-d models is improved, as show in Figure 5.10 in the centre of electrolyte along the cell length. Both the temperature and the temperature difference are changed, the temperature increases from 1083 °C to 1128 °C by replacing the operating temperature with cell local temperature in ionic conductivity relation. The temperature difference between maximum and minimum cell temperature changes from 183 °C to 228 °C. The relative

change in maximum temperature between coupled and decoupled models is 4%; meanwhile the relative change in ionic conductivity is 76.03 %.

The predicted temperature distributions by c-d models in the centre of the electrolyte at three different positions are shown in Figure 5.11. It is obvious that the temperature is higher at anode/electrolyte interface as where the exothermic-electrochemical reactions take place. The sudden drops in the temperature crossing the anode/electrolyte and cathode/electrolyte interfaces are due to the difference in thermal conductivities of anode and electrolyte. The thermal conductivity at the interfaces is predicted as;

$$k = \frac{2k_1k_2}{k_1+k_2} \tag{5.1}$$

According to the heat flux identification crossing the anode/electrolyte and cathode/electrolyte interfaces.

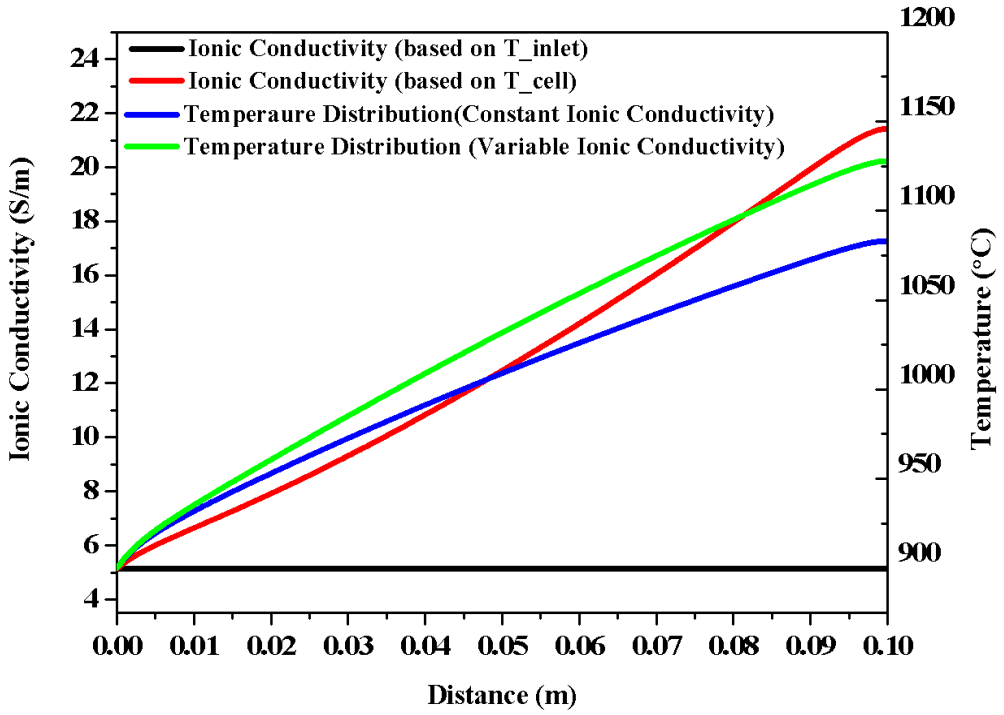

Figure 5.10 Electrolyte ionic conductivity and temperature distributions at section B for c-d models.

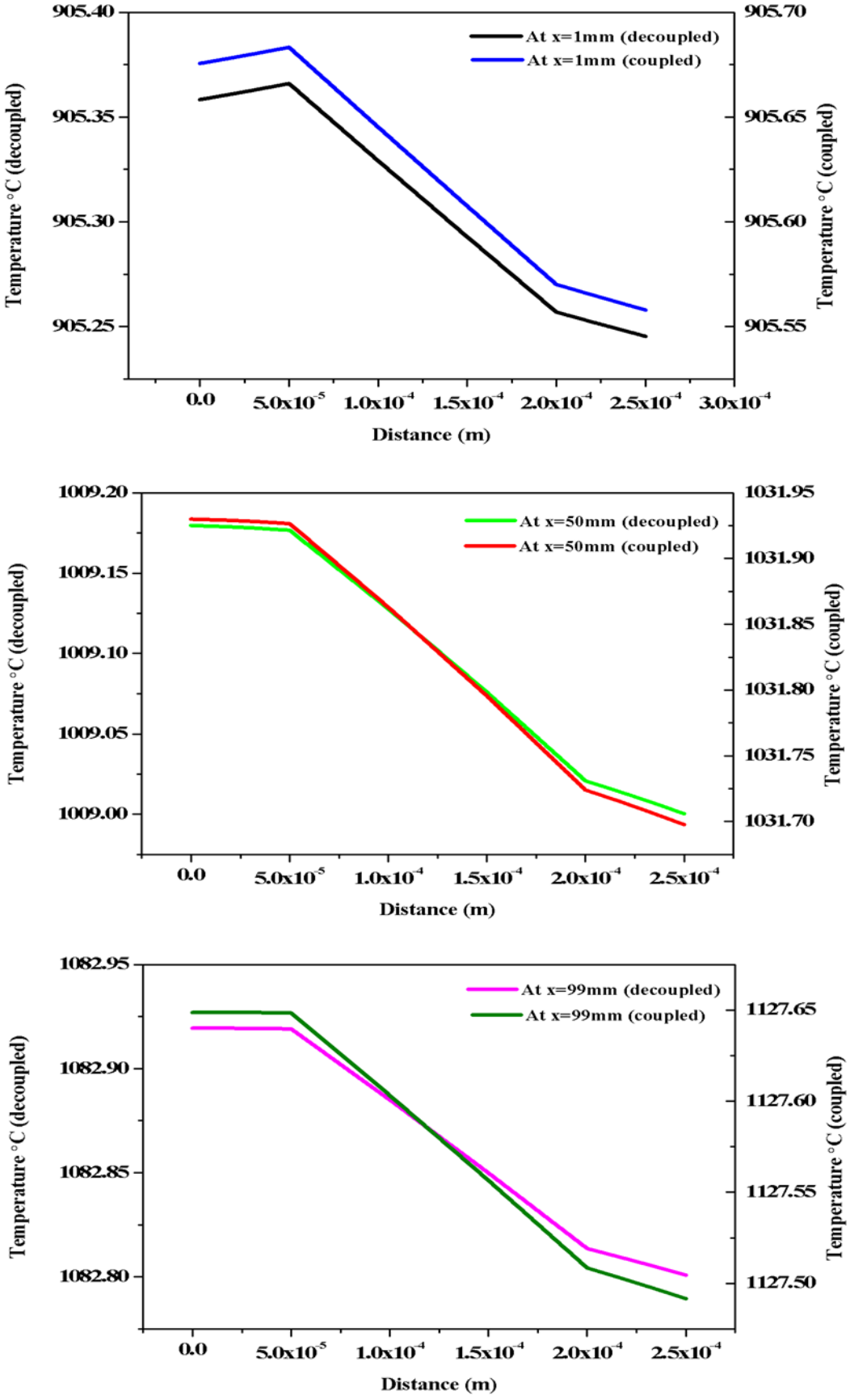

Figure 5.11 Temperature distributions at section Es for c-d models

The c-d models predict different electrochemical performance, which is checked by V-I and P-I curves as displayed in Figure 5.12. The average current densities at 0.7 V for c-d models are 3134.84 A/m^2 and 2519.75 A/m^2, respectively. The relative change (δ) in currrent density generation for both models is calculated by,

$$\text{Relative Change } (\delta) = \frac{(\delta_c - \delta_d)}{\delta_c} \times 100 \tag{5.2}$$

where the subscritp ‘c’ and ‘d’ stand for coupled and deoupled models. It is evidenced that the effects of coupling and decoupling are significant, as shown in Figure 5.13. The lower the cell operating voltage, the more sensitive to the coupling/decoupling model options, relative change at cell voltage 0.95 V is 6.46 % and increases with the decrease in cell voltage because of larger current density generation. The relative change at 0.7 V reaches to 19.6 % which refers to greater current density generation by coupled model.

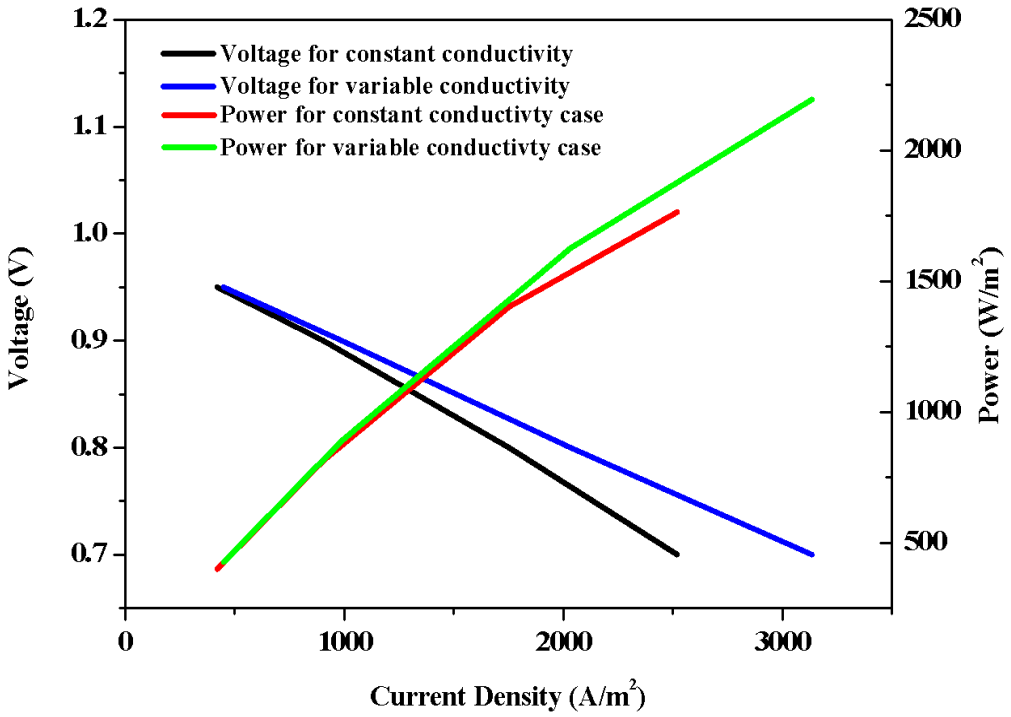

Figure 5.12 Voltage and power versus current density for d-model (constant ionic conductivity) and c-model (variable ionic conductivity).

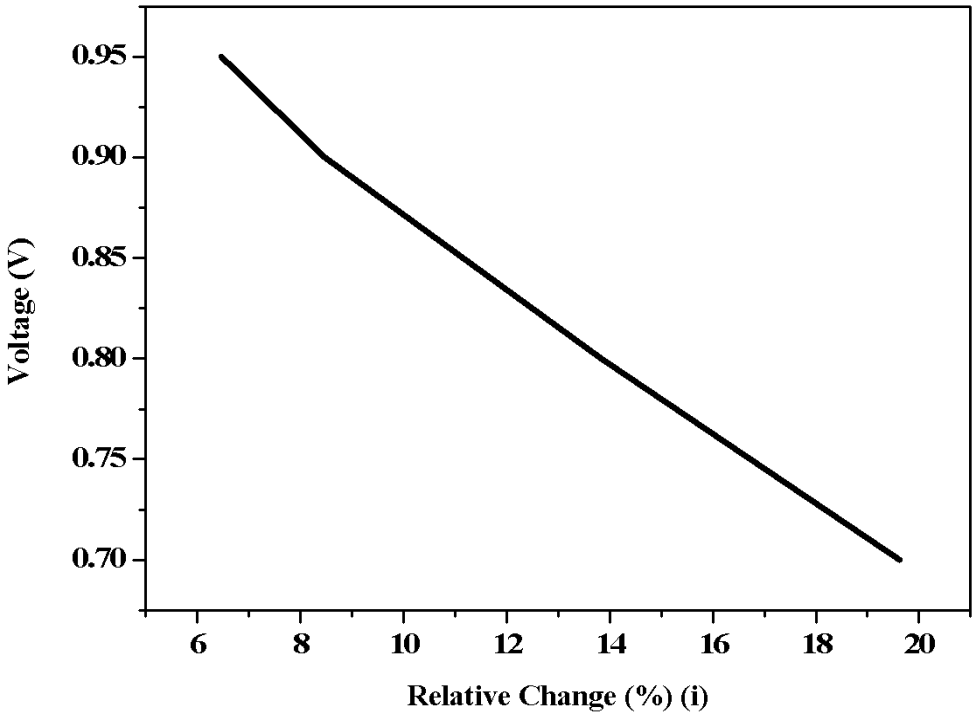

Figure 5.13 Relative change in current density generation between c-d models.

5.4.6 Thermal Strain

The thermal expansion mismatch among anode, electrolyte and cathode can cause the insufficient operations of the cell and even break down. The thermal strain (defined by Eq 4.32) is predicted by predictions of temperature differences from temperature distribution and thermal expansion coefficients of electrolyte and porous electrodes. The thermal strain distribution from c-d models in the centre of anode, electrolyte and cathode are given in Figure 5.14. The higher cell temperature results in larger temperature difference and towards greater thermal strain generation in the cell. It should be noticed from the results that the thermal deformations of anode, cathode, and electrolyte in this sandwiched PEN are different, mismatched with each other, which are predicted from both the coupling and decoupling models. The thermal strains in all three components are higher from coupled model than those from decoupled model. The thermal strain generation for both models is largest in the anode because of the higher thermal expansion coefficient. The thermal strain in anode increases from 0.0138 (decoupled model) to 0.0144 (coupled model). The maximum thermal strain in electrolyte for decoupled and coupled models is 0.0106 and 0.0111, respectively. The

thermal strain in cathode is larger than electrolyte. The maximum thermal strain in cathode for decoupled and coupled models is 0.0117 and 0.0122, respectively.

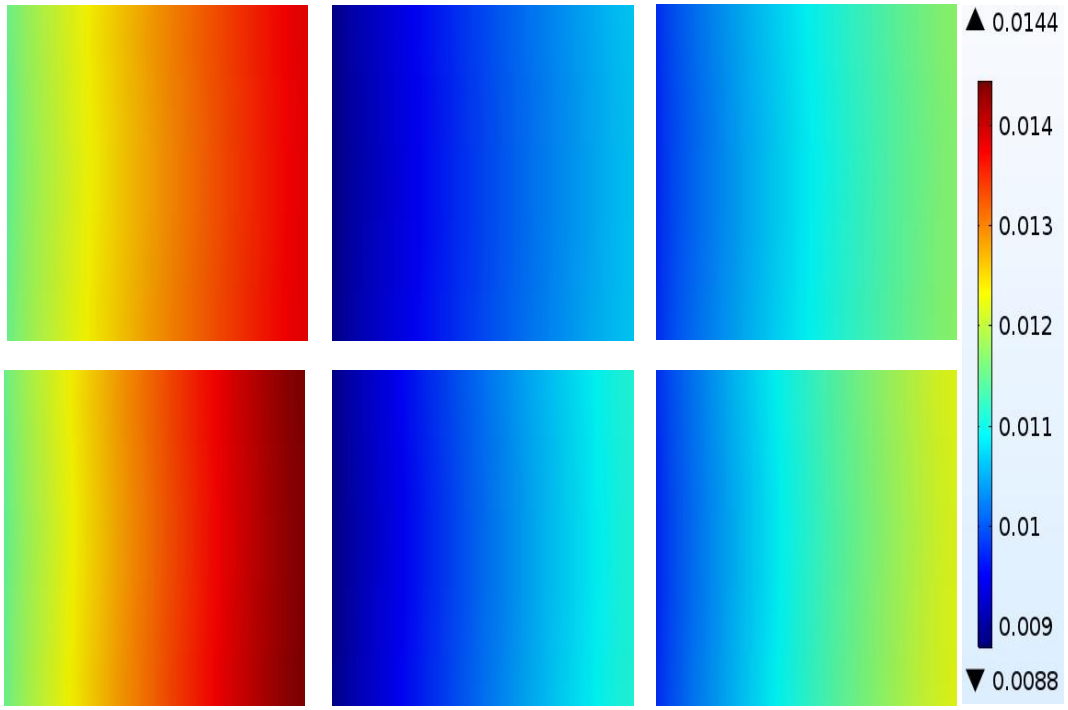

Figure 5.14 Thermal strain distribution from decoupled (top) and coupled (bottom) models at sections A, B and C.

To identify the difference in thermal impacts predicted by c-d models, the relative change in thermal strains generation along the cell length in the centre of anode, electrolyte and cathode is calculated. The δ in equation 5.2 represents the relative change in thermal strain generation. The results are shown in Figure 5.15 . The maximum relative change for anode, electrolyte and cathode is 4% and located near the cell outlet.

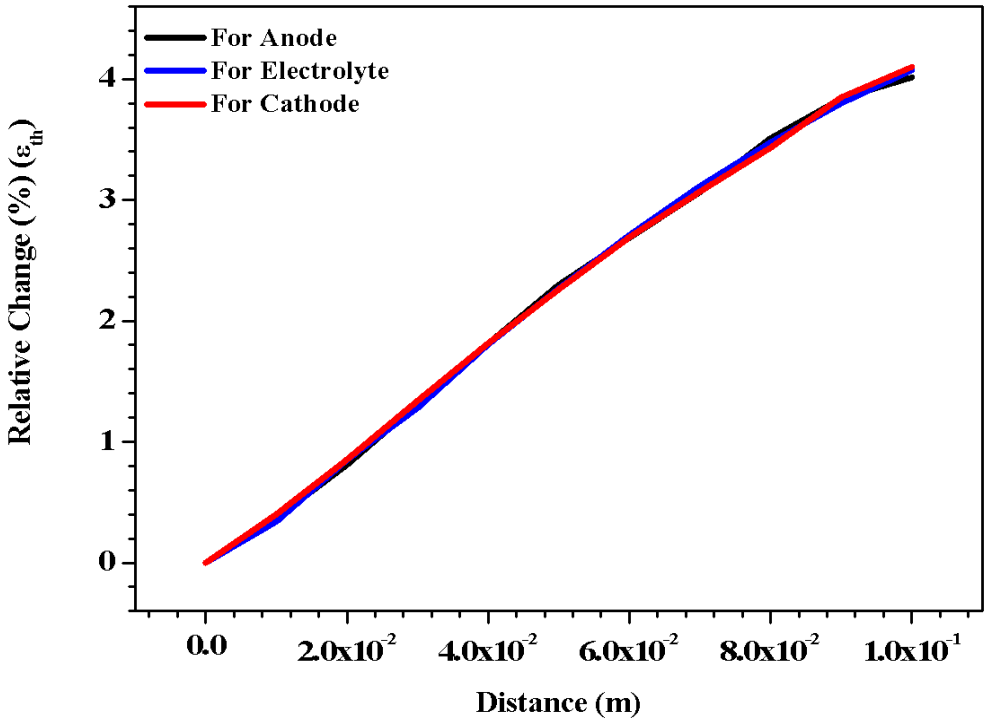

Figure 5.15 Relative change in thermal strain generation between c-d models at sections A, B and C.

The thermal expansion coefficients mismatch between various cell components creates the difference in thermal strain generation. The difference in thermal expansion coefficient between anode/electrolyte is higher than cathode/electrolyte. The larger differences in thermal expansion coefficient between anode/electrolyte result in greater thermal strain generation. The relative change in thermal strain generation between c-d models at anode/electrolyte and cathode/electrolyte interfaces along the cell length is displayed in Figure 5.16. The maximum relative change, near the cell outlet, at cathode/electrolyte interface 4.5 % is higher than maximum relative change at anode/electrolyte interface 3.9 %.

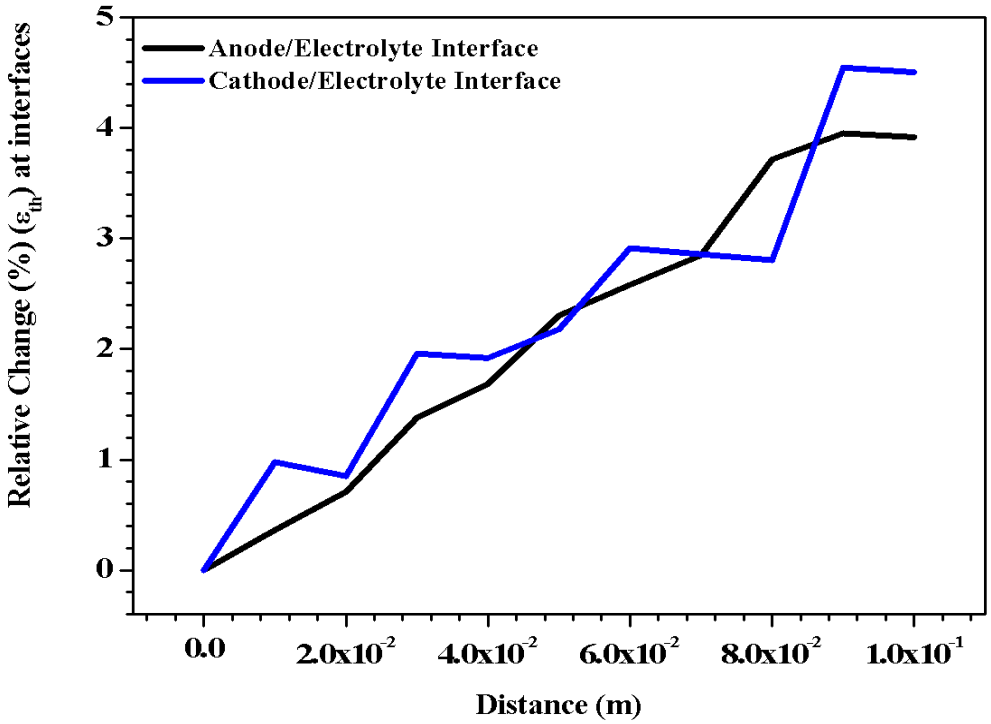

Figure 5.16 Relative change in thermal strain generation between c-d models at sections F and G.

The thermal strain distribution predicted by c-d models in the centre of anode, electrolyte and cathode along the cell thickness is predicted at three different locations (close to the inlet, in the centre and close to the outlet of the cell). It is evident from the Figure 5.17 that the thermal strain generation in anode for both models and at all positions is larger than those of electrolyte and cathode. The maximum thermal strain for all the components located near the cell outlet due to larger temperature difference at this location. The maximum thermal strain generated, for coupled model, in anode, electrolyte and cathode is 0.01398, 0.01075 and 0.01183, respectively. The results for relative change between coupled and decoupled models thermal strain generation along the cell thickness at different locations are displayed in Figure 5.18. The relative change near the cell inlet is 0.1 % and reaches to 1.14 % near the cell outlet. The relative change along the cell thickness is lower as compared to the relative change along the cell length which refers larger temperature variation along the main flow direction.

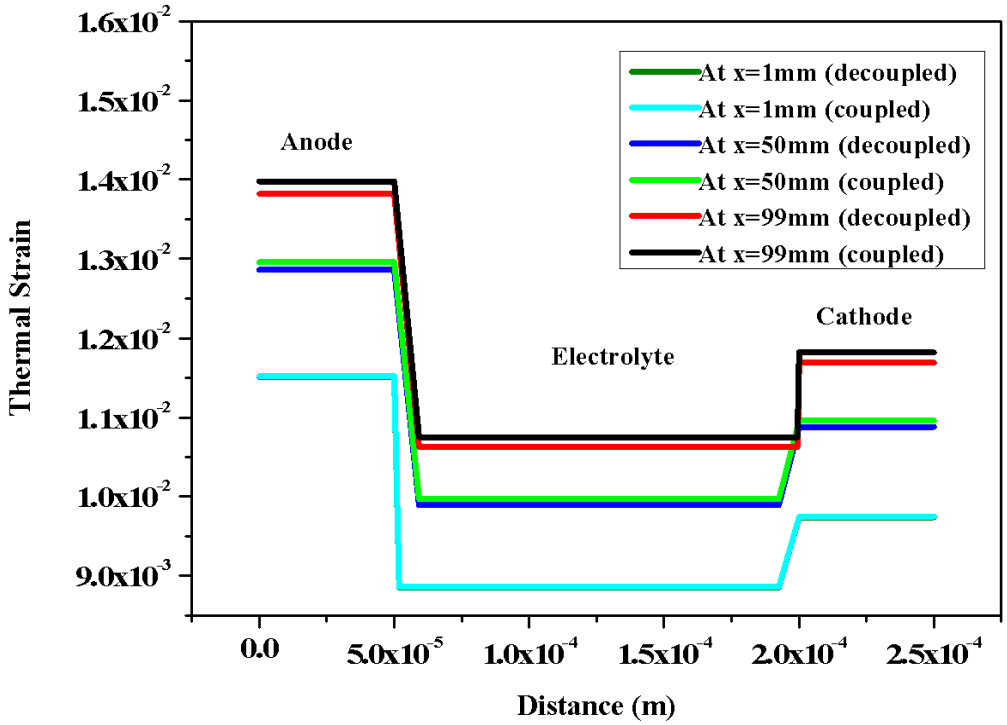

Figure 5.17 Thermal strain distribution from c-d models at section Es.

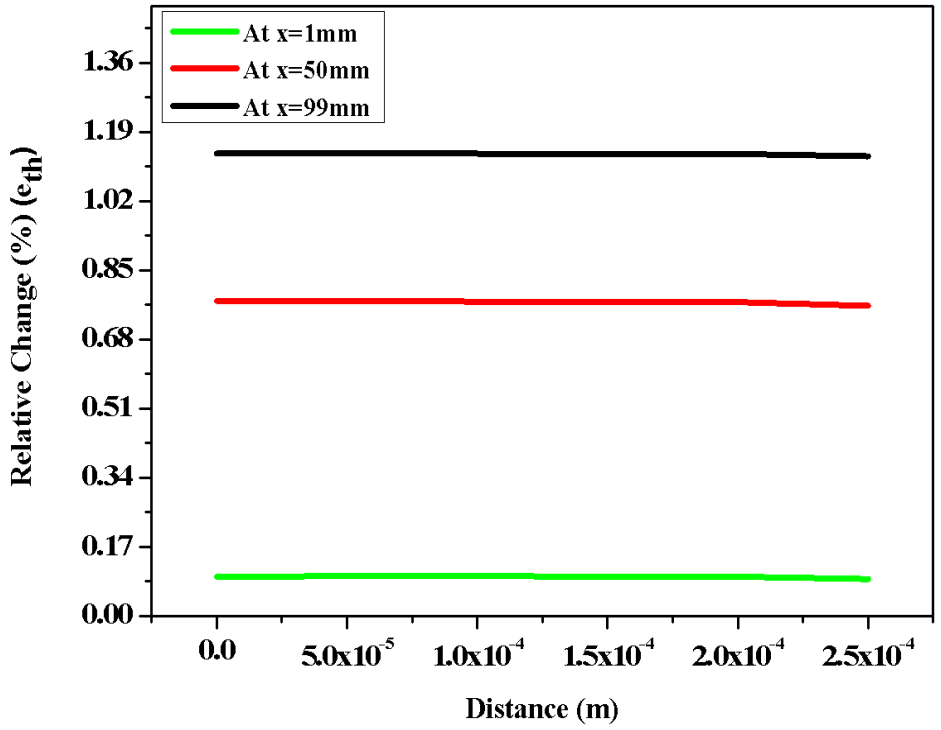

Figure 5.18 Relative change in thermal strain generation between c-d models at section Es.

5.4.7 Thermal Strain Gradient

The thermal strain gradients [m^{-1}] are calculated from temperature gradients and thermal expansion coefficient of anode, electrolyte and cathode. The gradients in x, y and z directions predicted by c-d models in the centre of anode, electrolyte and cathode are shown in Figure 5.19. The positive and negative signs indicate the increase (or tension) and decrease (or release) in thermal strain, in the cell. From decoupled and coupled models, the maximum thermal strain gradients in x direction are 0.0885 [m^{-1}] and 0.0938 [m^{-1}] in anode; 0.0747 [m^{-1}] and 0.0792 [m^{-1}] in cathode, respectively and 0.0655 [m^{-1}] and 0.0695 [m^{-1}] in electrolyte, which is lower than those in anode and cathode. The results indicate that all three components are under tension in x direction. The thermal strain gradients in y direction are higher predicted by coupled model as compared to those by decouple models for all three components of PEN. It can be observed from Figure 5.19 that all the components undergo tension and release associatively in y direction, however, the magnitudes of thermal strain gradient are different from each other. Unlike what happed in x and y directions, the anode is tensed, while, electrolyte and cathode are both released with the order of magnetite of -0.015 [m^{-1}] and -0.042 [m^{-1}] respectively.

The impact of the c-d models on thermal strain gradients is estimated by calculating the relative change in x, y and z directions. The results in the centre of anode, electrolyte and cathode are shown in Figure 5.20. The maximum relative changes, for all three components, along x and y direction are 23 % and 21%, respectively. And those along z direction, for electrolyte and cathode, are almost identical, which are 24.5 % and 24 %. The maximum relative change 15 % in anode is lower than those of cathode and electrolyte, which indicates that the effect of coupling along z direction is higher in electrolyte and cathode. The reasons are the lower temperature gradient on anode side as electrochemical reactions take place at anode/electrolyte interface whereas it is higher on cathode side as the heat is taken away by the incoming cool air.

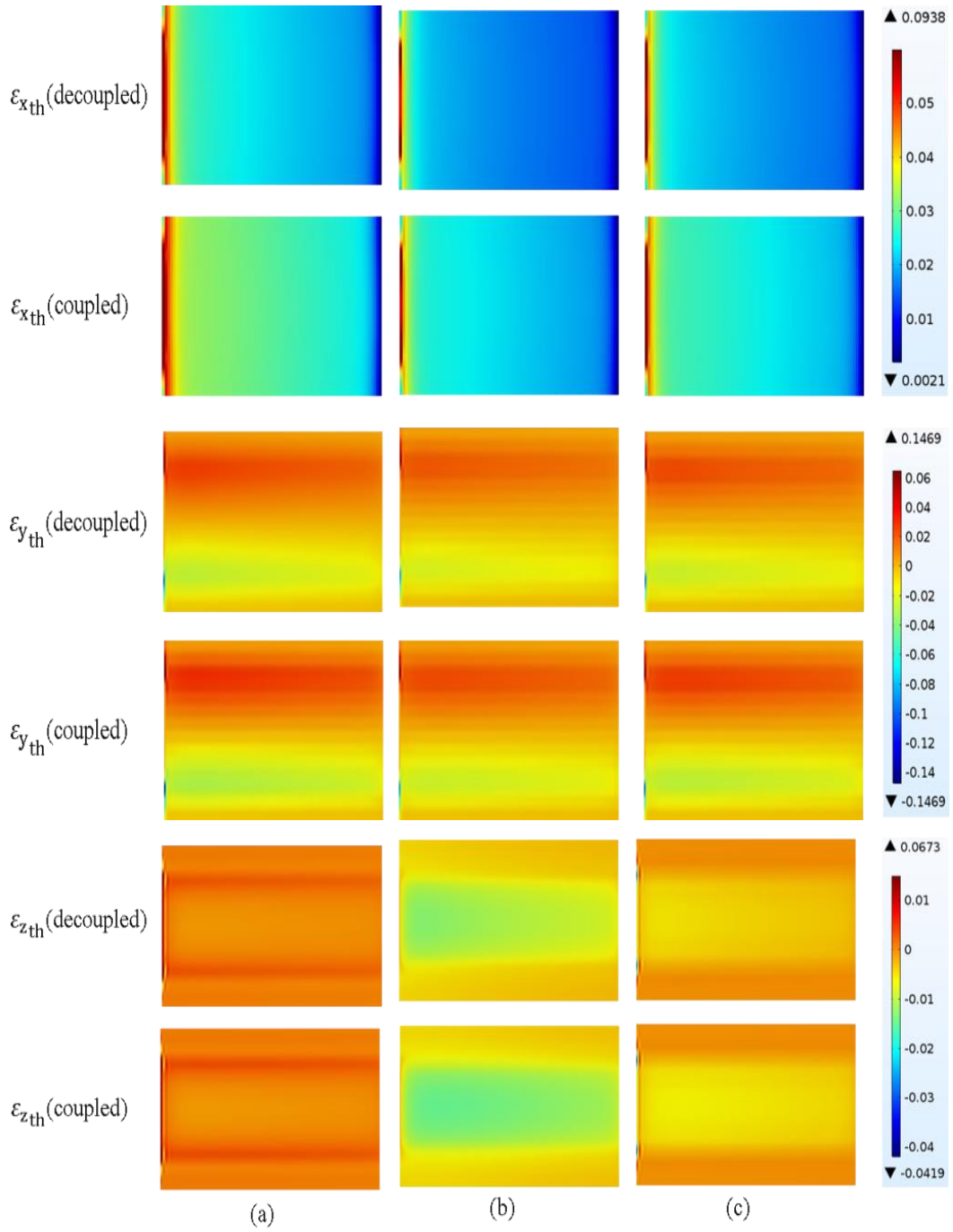

Figure 5.19 Thermal strain gradients [m^{-1}] (x, y, and z components) distribution from c-d models at sections A, B and C.

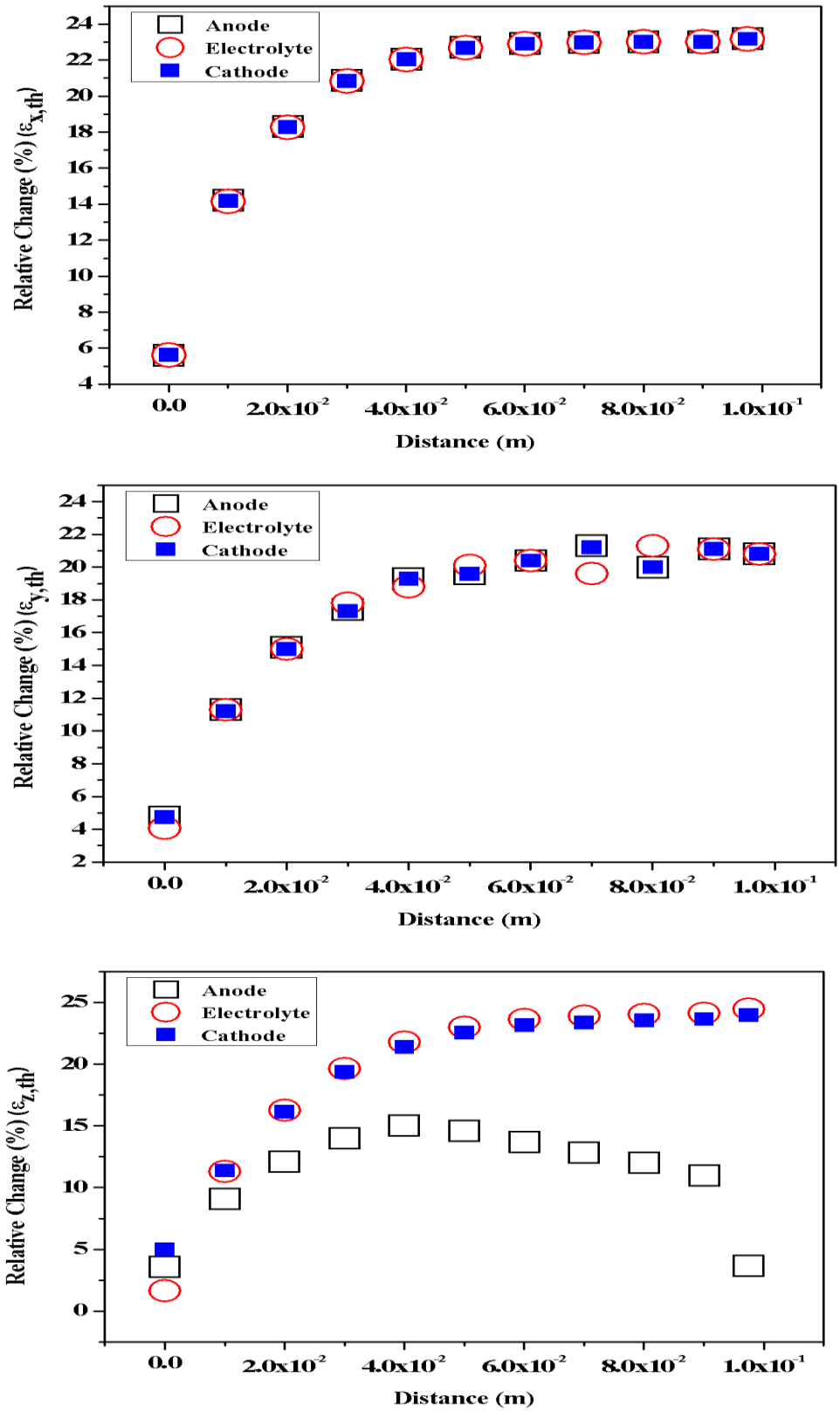

Figure 5.20 Relative change in thermal strain gradients (x, y and z components) between c-d models at sections A, B and C, respectively.

5.4.8 Thermal and Mechanical Stresses

The thermal stresses should have the same behaviours, in general, with those of thermal strain of each component of PEN, as the Young's modules of each component are constant, which can be found from the Appendix – B, according to Eq 4.30. However, due to the difference in order of magnitude of Young's modules, the values of thermal stresses of one component are different with others even experienced the same strains. Taking the same spatial positions as those in section 5.4.6, in the centre of anode, electrolyte and cathode along the cell length, the predicted thermal stress and mechanical stresses are discussed as follows. The results from c-d models for thermal stress distribution in studied special locations can be found from Figure 5.21. The maximum thermal stresses generated in centre of anode from c-d models are 792.33 MPa and 760.2 MPa, while, those generated in the centre of electrolyte are 2382.1 MPa and 2285.79 MPa. The cathode has less thermal stress generation, which are 426.53 MPa and 409.29 MPa, respectively. The high thermal stress generated in the electrolyte is because of the properties of the material (YSZ) used for SOFC electrolyte, of which the Young's Module is 215 GPa, much larger than that of anode and cathode.

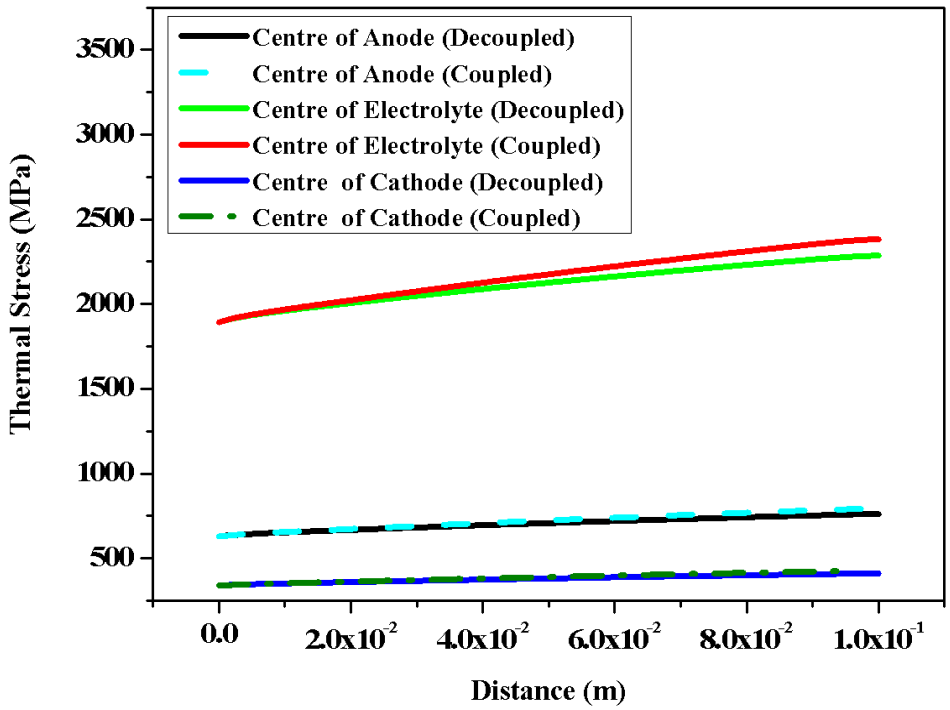

Figure 5.21 Thermal stress distribution from c-d models at sections A, B and C.

As demonstrated in Figure 5.22, the electrolyte thermal stress profiles are as same as those of thermal strain shown in Figure 5.17. The maximum thermal stress of 3095.88 MPa from coupled and 2970.86 MPa from decoupled model are at the interface with anode and close to the cell outlet because of the higher temperature at this position. Because the difference in Young's modules and thermal expansion coefficient among materials, the thermal stress close to the cell outlet at anode/electrolyte interface is 3095.88 MPa and drops to 2619.26 MPa at cathode/electrolyte interface, the thermal stresses predicted by decoupled model are relative lower, which are 2970.86 MPa to 2513.55 MPa respectively.

The relative changes in thermal stress generation by c-d models are similar with those of thermal strain, shown in Figure 5.18, at the same locations along the cell thickness, which are 0.036 %, 2.25 % and 4.01 % at close to inlet, the centre, and close to the outlet, respectively.

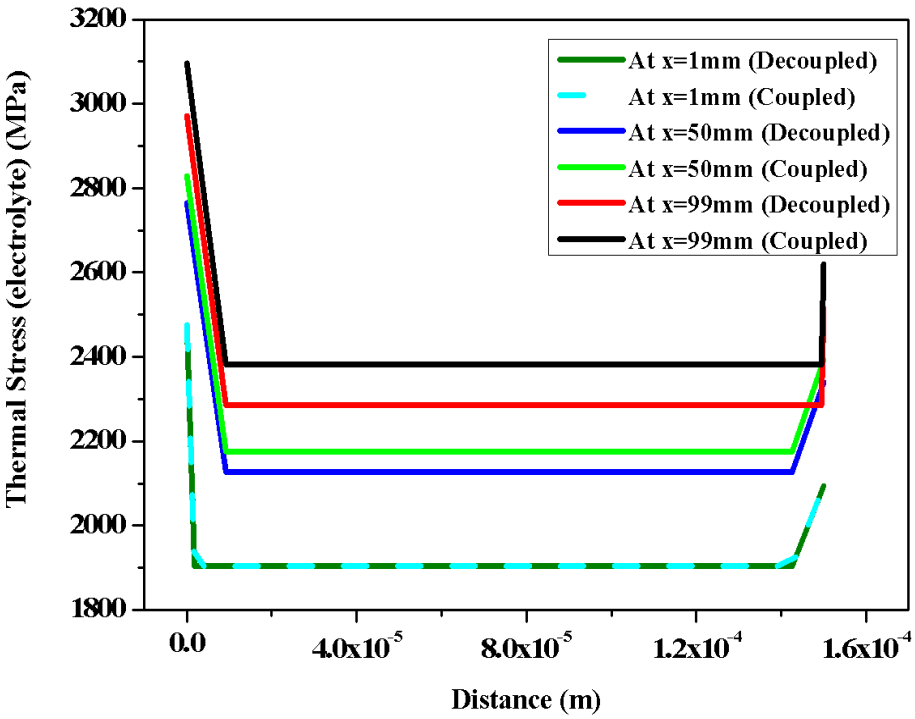

Figure 5.22 Thermal stress distribution from c-d models at Es.

The Von Mises stress distribution at the same location, along the cell length from c-d models are checked, as displayed in Figure 5.23. The Von Mises stresses depend on the elastic strain of the material. The Von Mises stress is calculated by fixing the both ends (right and left) of the cell. The Von Mises stress is higher for coupled scenario. Unlike thermal stress the maximum Von Mises stress generated in the electrolyte. The maximum Von Mises stress generated in the centre of electrolyte for coupled and decoupled models is 2327.94 MPa and 2383.52 MPa, respectively. The maximum Von Mises stress generated in the centre of anode for decoupled and coupled models is 736.32 MPa and 756.1 MPa respectively. The maximum Von Mises stress generated in the centre of cathode for both scenarios is 409.53 MPa and 419.73 MPa. The maximum Von Mises for all three components is located close to the air/fuel outlet. The variations near inlet and outlet boundaries are larger because of the fixed position at these locations. The distribution along the cell length is uniform and variation in stress values is not significant.

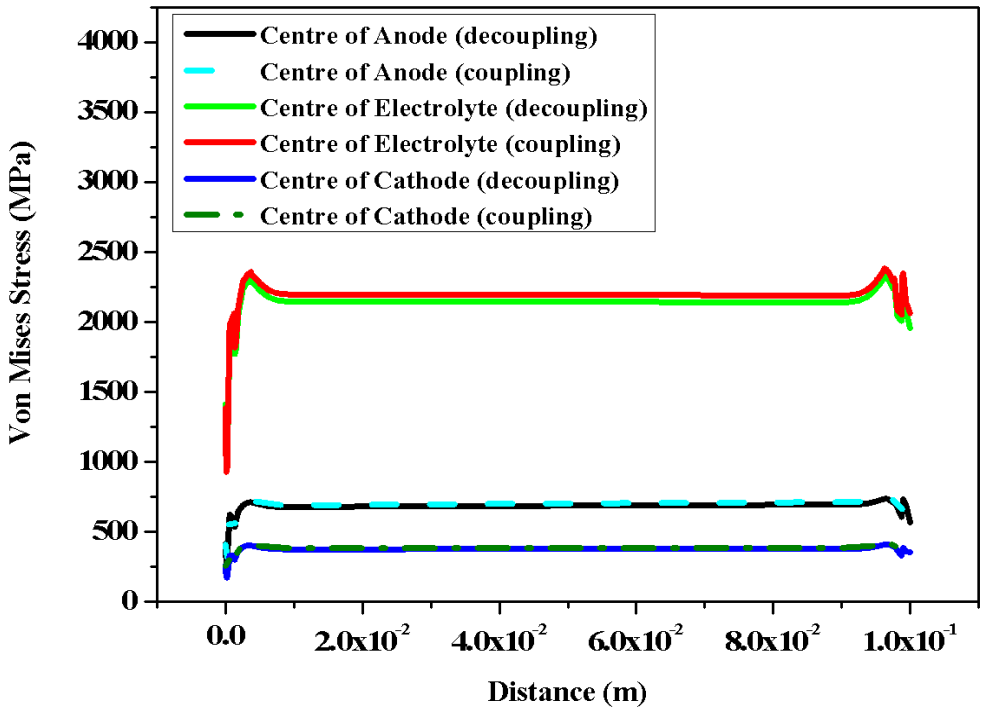

Figure 5.23 Von Mises Stresses distribution from c-d models at sections A, B and C.

5.4.9 Effect of Operating Voltage on Thermal Strain Generation

The effect of the operating voltage on the cell electrochemical performance and thermal impact is investigated by varying the voltage from 0.7 V to 0.5 V. The lower cell voltage results in larger current density and more heat which leads to higher cell local temperature. The differences in average current density and maximum cell temperature between 0.7 V and 0.5 V are 1700.9 A/m^2 and 221 °C. The higher cell local temperature results in larger temperature difference which refers to greater thermal strain generation. The thermal strain distribution in anode, electrolyte and cathode at 0.5 V along the cell length is shown in Figure 5.24. The anode has larger thermal strain generation 0.0173. The maximum thermal strain generated in electrolyte and cathode is 0.0133 and 0.0146, respectively.

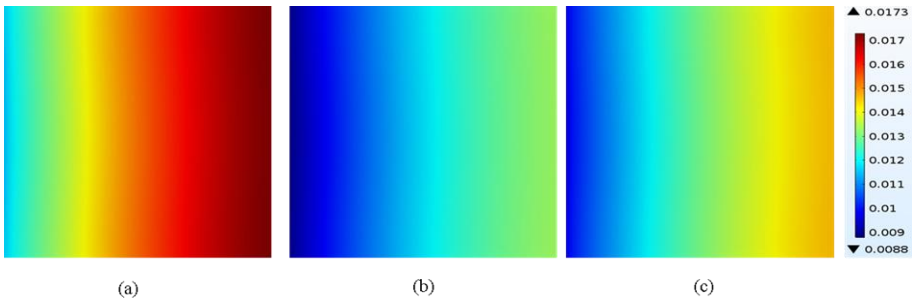

Figure 5.24 Thermal strain distribution from c-d models at sections A, B and C.

The effect of the operating voltage on the cell thermal impact is predicted by calculating the relative change in thermal strain generation by using the following relation,

$$\text{Relative Change } (\varepsilon\_\text{th}) = \frac{(\varepsilon_{th,0.5\,V} - \varepsilon_{th,0.7\,V})}{\varepsilon_{th,0.7\,V}} \times 100 \qquad (5.3)$$

The results are shown in Figure 5.25. The maximum relative change 20% observe for anode, electrolyte and cathode which shows that the thermal strain generations at 0.7 V is lower as compared to 0.5 V.

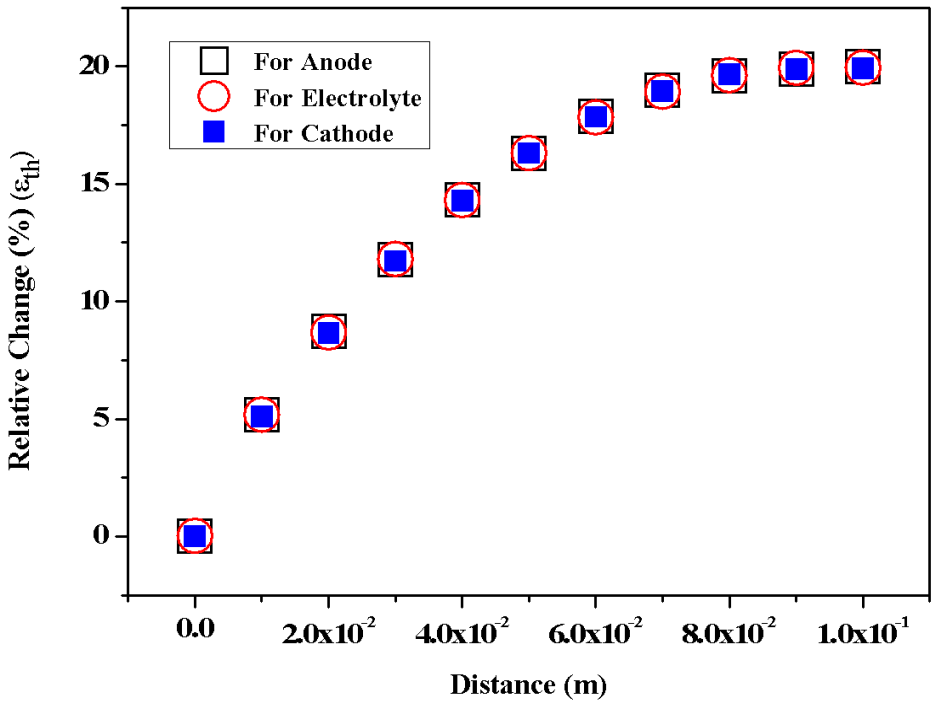

Figure 5.25 Relative change in thermal strain generations between 0.7 V and 0.5 V at sections A, B and C.

5.4.10 Effect of Boundary Restriction on the Stress Generation

The coupled model is tested for stress generation by restricting the different boundaries. The thermal boundary conditions are same and there is no change in thermal stresses. The boundary restrictions have effects on elastic strain which results in change of Von Mises stresses. The Von Mises stress distribution in the centre of the electrolyte along the cell length for various boundary restrictions is illustrated in Figure 5.26. The maximum Von Mises stress in both sides fix (left and right) condition is 2191.7 MPa which is located at air/fuel inlet. The one side (left) fix case is like a cantilever beam and has maximum Von Mises stress 1870.7 MPa at fix end and reduce to 188.52 MPa at free end. The maximum Von Mises stress in front and back sides restricted condition is 4096 MPa and located at the same position. The maximum Von Mises stress for top and bottom sides fix is 3738.1 MPa and close to fuel/air outlet. The highest stress is generated in front and back side restricted condition because of larger elastic strain generation. The maximum Von Mises stress for one side restricted condition is less as compared to other cases. The average Von Mises stress in one side restricted condition is 311.80 MPa. Therefore, the boundary restrictions effect the stress generation and can be reduced by properly fix the cell sides.

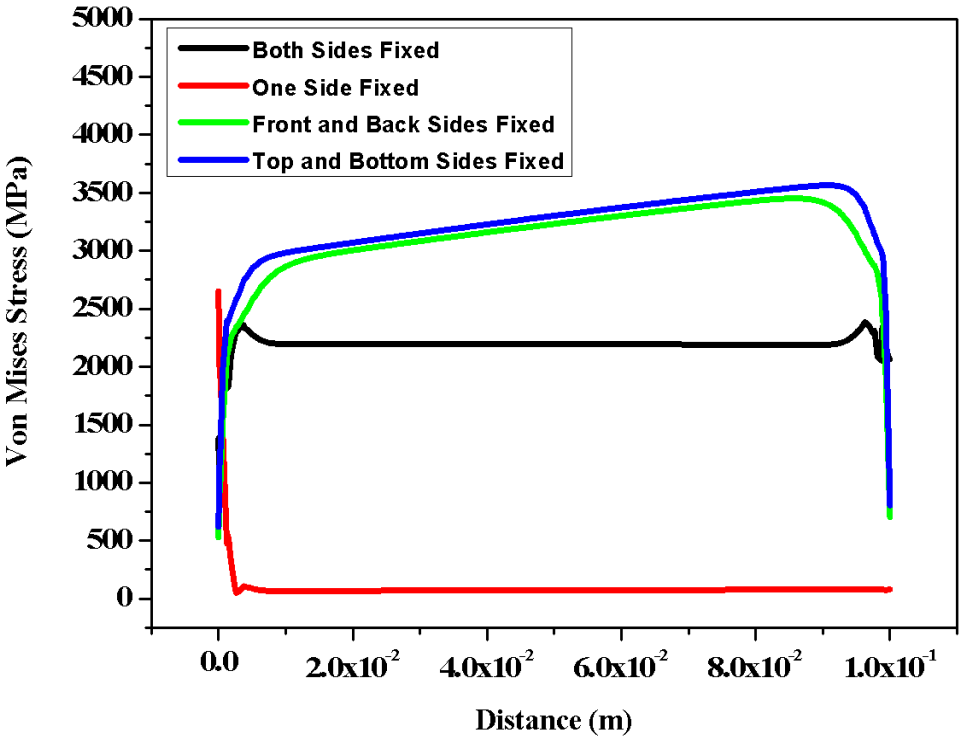

Figure 5.26 Von Mises Stress distribution at section B for different boundary restrictions. One side fixed (left side), both sides fixed (right and left), front and back, and top and bottom.

5.5 Summary

Numerical model of a single planar SOFC has been developed by coupling fluid flow, mass transport, reacting flows and heat transfer equations. The model is validated with IEA bench mark data. The current density, temperature and species distribution along the cell length are shown. The effect of different temperatures on the cell performance has been investigated. The electrochemical performance of the cell depends on the material properties such as ionic conductivity which is a function of temperature. It is necessary to determine the temperature distribution as electrochemical and thermal performance of the cell depends on temperature. The effect of different temperatures, material properties, operating voltage and boundary restrictions on the cell performance has been investigated. The increase in temperature has more effect on electrochemical performance than thermal performance. The thermal strain and thermal strain gradients are calculated for decoupled and coupled models. The maximum thermal strain generated in the anode because of the larger thermal expansion coefficient than electrolyte and cathode. The larger thermal strain results in thermal expansion which

can disturb the cell structure and sometimes leads to the cell fracture. The thermal strain gradient results indicated that anode and cathode are under tension and electrolyte is under compression. The PEN structure material is brittle and it is important to investigate the stresses in these sections. The maximum thermal and Von Mises stresses are generated in the electrolyte at air/fuel outlet along the cell length. The maximum thermal stress along the cell height is located at anode/electrolyte interface. The efforts should be made to reduce these stresses as they can cause separation of layers or micro-cracks in the weaker layers. Hence thermal strains and stresses play an important role in the performance of the SOFC and should be reduced.

Chapter 6 – Thermal Impact and Performance analysis of Methane Fueled SOFC

This chapter reports the numerical results of single planar methane SOFC. The temperature and species distributions are predicted at different cell locations. The mechanisms of heat generation and consumption during electrochemical and chemical reactions are studied in depth.

6.1 Introduction

As explained in Chapter 2, Solid oxide fuel cell is most promising because of its high electrical efficiency, environmental friendliness, fuel flexibility and internal steam reforming [33-35]. Fuel flexibility is mainly due to high operating temperature of SOFC (500 – 1000 °C) [35, 185, 210]. The CO which poisons the low temperature fuel cells can be used as a fuel in SOFC.

In case of pure Hydrogen being used as a fuel, the hydrogen is consumed and water is produced due to electrochemical reaction. The byproduct during electrochemical reaction is heat which is utilized to meet the heat requirement of internal steam reforming reaction. Natural gas is available in abundance and considered as the most suitable fuel for SOFC stationary applications [123]. The internal methane steam reforming reaction enables the conversion of methane into CO and H_2. The water gas shift reaction follows the methane steam reforming which further converts the CO into CO_2 and H_2. The models studied so far considered methane steam reforming reaction in anode-supported SOFC. The decrease in electrolyte thickness helps to lower the required operating temperature range for SOFC operation. The decrease in temperature results in high electrolyte resistance which consequently reduces the thermal stability and overall performance of the cell. The purpose of this chapter is to analyze the performance and thermal impact of electrolyte supported methane fueled SOFC. Also most of the models described in Chapter 3 deal with electrochemical performance, species and temperature distributions and rare models have considered the thermal strains and stresses generated in the cell. First time a comprehensive model is developed to unravel the relation between distributions of chemical and electrochemical reactions, species, temperature, thermal strains and stresses.

6.2 Methane Model Description

A schematic diagram of a single planar solid oxide fuel cell running on methane is shown in Figure 6.1. A fuel composition of 17.10%CH_4, 26.26%H_2, 49.34%H_2O, 2.94%CO and 4.36% CO_2 by mole is used on the anode side. Air (21% Oxygen and 79% Nitrogen) is used as an oxidant on cathode side. The H_2 from fuel channel reacts, at anode/electrolyte interface, with O_2 ions from air channel and generates water and electricity. The remaining gas mixture leaves the cell from fuel and air channel outlets.

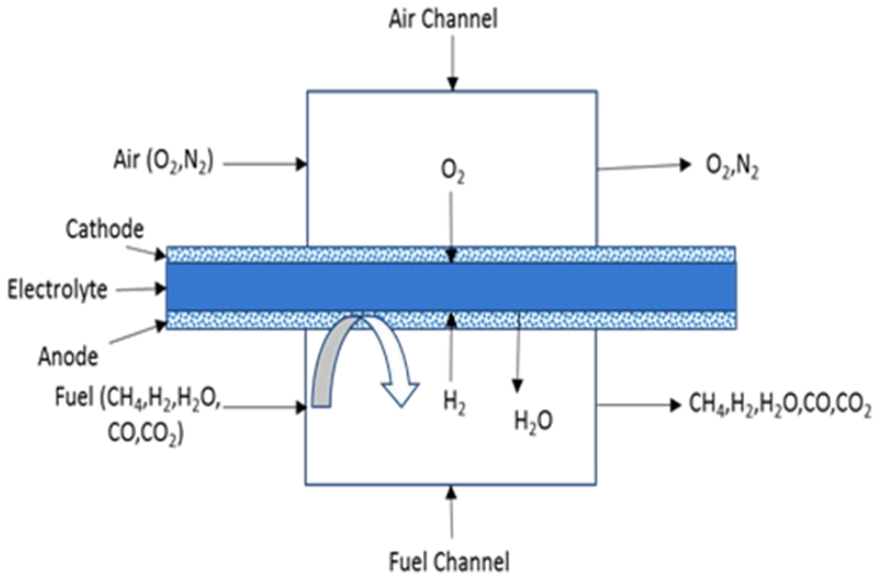

Figure 6.1 Cross section view of a single planar SOFC running on methane.

6.3 Methane Model Verification

Numerical results of a SOFC model are only approximations of real conditions and verification is a necessary step to make the model reliable and accurate. To verify the model a voltage of 0.7 V is employed and the mass flow of the fuel and air is set as 1.64E-6 kg/s and 8.788E-6 kg/s respectively, with an operating temperature of 900 °C and pressure of 1 bar. The values of anode and cathode exchange current densities are same as those of hydrogen model. The electrochemical performance curve which is obtained from the present study is presented in Figure 6.2. The average current density predicted by the model at 0.7 V is 3152.18 A/m^2 and well matches with the results of IEA report [50]. The average current density in the IEA report is in the range of 2535 –

3058.5 A/m^2 [50]. The power density is calculated by multiplying the cell voltage with current density. The average power density at 0.7 V is 2206.53 A/m^2.

The difference between both results is within 3%. The reasons for discrepancy are same as those explained in Chapter 5. The verified model is then used for further simulation studies.

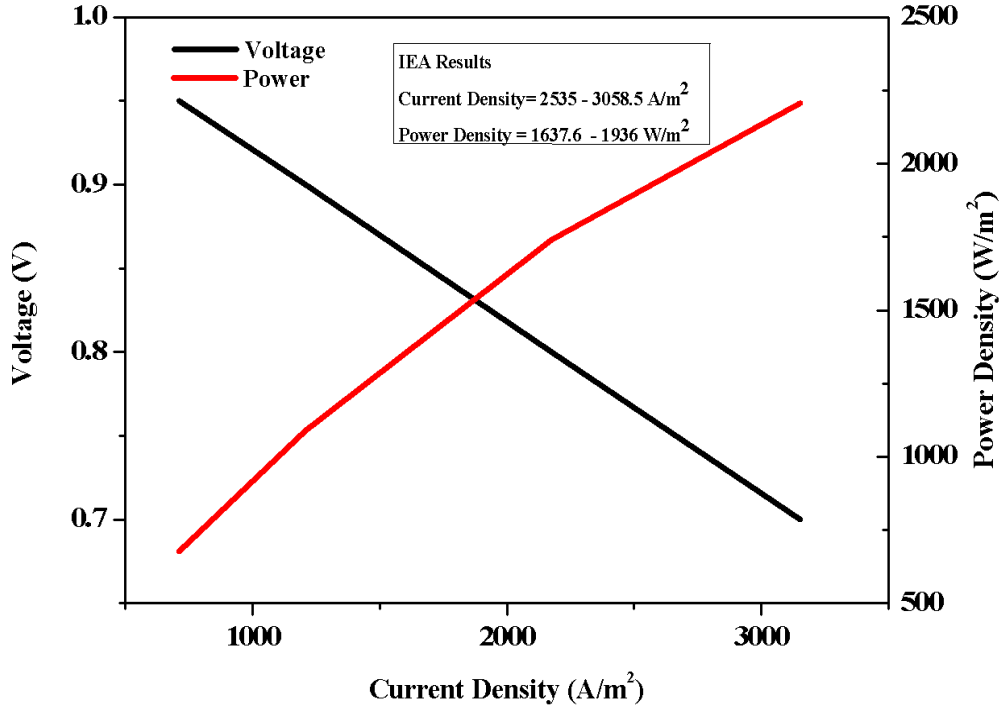

Figure 6.2 Voltage and power density against current density.

6.4 Results and Discussion

6.4.1 Electrochemical Performance

The verified model is based on coupling mechanism. The electrochemical performance which is predicted by c-d models at different cell voltage is shown in Figure 6.3. The average current densities at 0.7 V from c-d models are 3152.18 A/m^2 and 3757.81 A/m^2, respectively. The current density generation in decoupled model is higher because of greater cell operating temperature which results in constant and larger value of ionic conductivity. The ionic conductivity in coupled model decreases because of the cell local temperature drops.

The impact of the coupling on the electrochemical performance of the cell is identified by determining the relative change for current density generation between c-d models. It is found that the effects of c-d are significant, as shown in Figure 6.4. The negative sign represents the overestimation of the current density generation in decoupled model. The results are opposite to those of hydrogen model such as at high operating voltage 0.95 V the relative change is -28.3 % and decreases with decrease in the cell voltage. The relative change at 0.7 V reaches to -19.21% which refers to lower current density generation by coupled model.

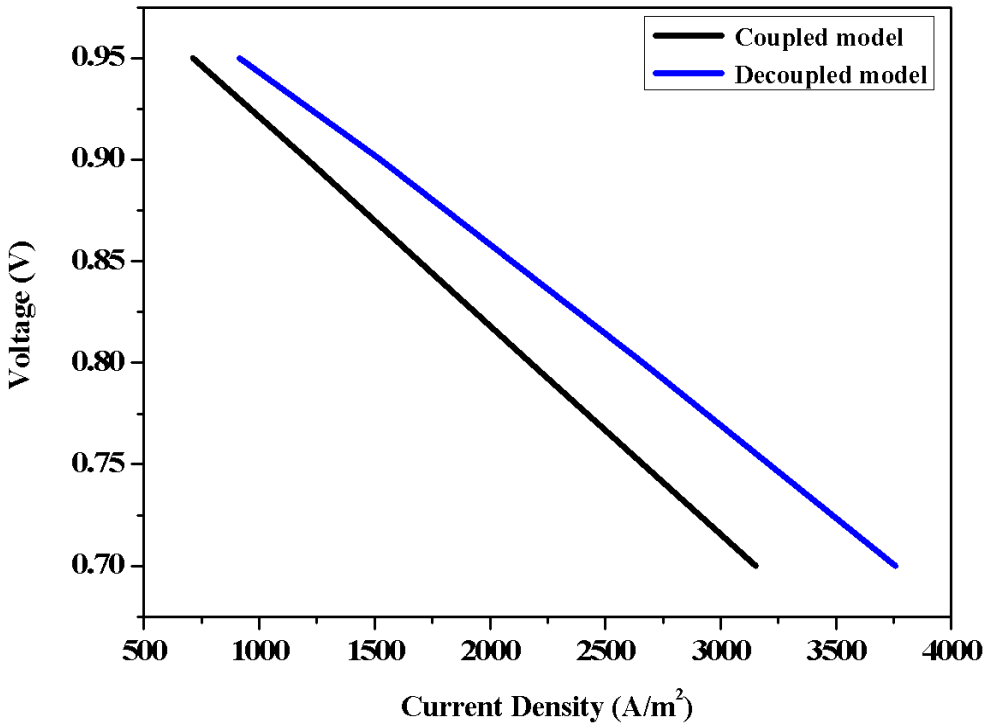

Figure 6.3 Voltage versus current density for c-d models.

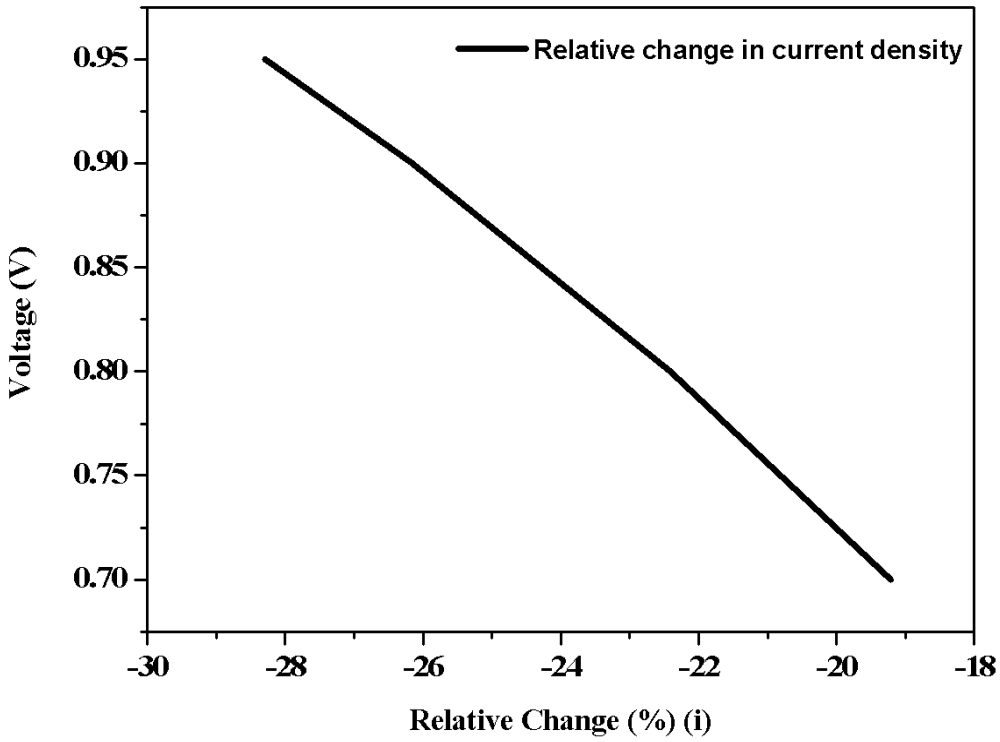

Figure 6.4 Relative change in current density generations at different cell voltage between c-d models.

6.4.2 Species Distribution

The species molar fraction distributions are investigated in the centre of the fuel channel along the cell length and the results are displayed in Figure 6.5. The CH_4 consumption by MSR reaction leads to drop from maximum 0.171 at inlet to minimum 0.04 at outlet. Same for H_2O, as shown in Figure 6.5, decreases nonlinearly from 0.4934 at inlet to 0.366 at outlet. The distribution profile of H_2 shows opposite trend as it generates during both chemical reactions. The mole fraction of H_2 increases from minimum 0.2626 at inlet to maximum 0.435 at outlet. The CO generates by MSR reaction and consumes to produce CO_2 during WGS reaction. The reaction rate of WGS reaction is lower than MSR and that is why the effect of WGS reaction rate on CO consumption is not visible. The mole fraction of CO is higher at outlet 0.11 than 0.0294 at inlet. The variation in CO_2 mole fraction is small and it varies between 0.0436 at inlet to 0.0445 at outlet.

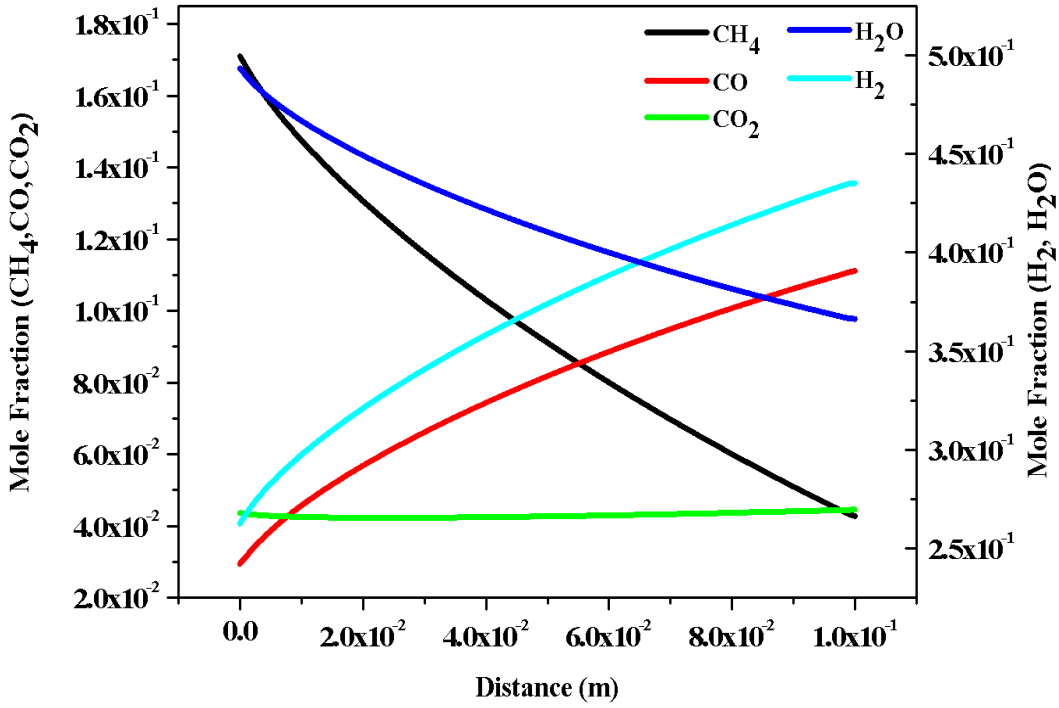

Figure 6.5 Species mole fraction distributions at section D.

To further analyze the distribution of the species inside the cell the mole fractions of CH_4 and CO are plotted along the cell thickness at three different positions, as shown in Figure 6.6. The CH_4 distribution profile is same at all three positions. The CH_4 mole fraction is highest in the fuel channel and decreases towards anode/electrolyte interface because of the higher reaction rate which results in larger consumption. The distribution profile of CO is opposite to CH_4. The negative sign of WGS reaction rate supports the fact that WGS reaction is reversed and results in higher CO mole fraction. The change in mole fraction of CO from fuel channel towards anode/electrolyte interface is not significant. The mole fraction of CO near the inlet slightly increases in anode and decreases close to outlet.

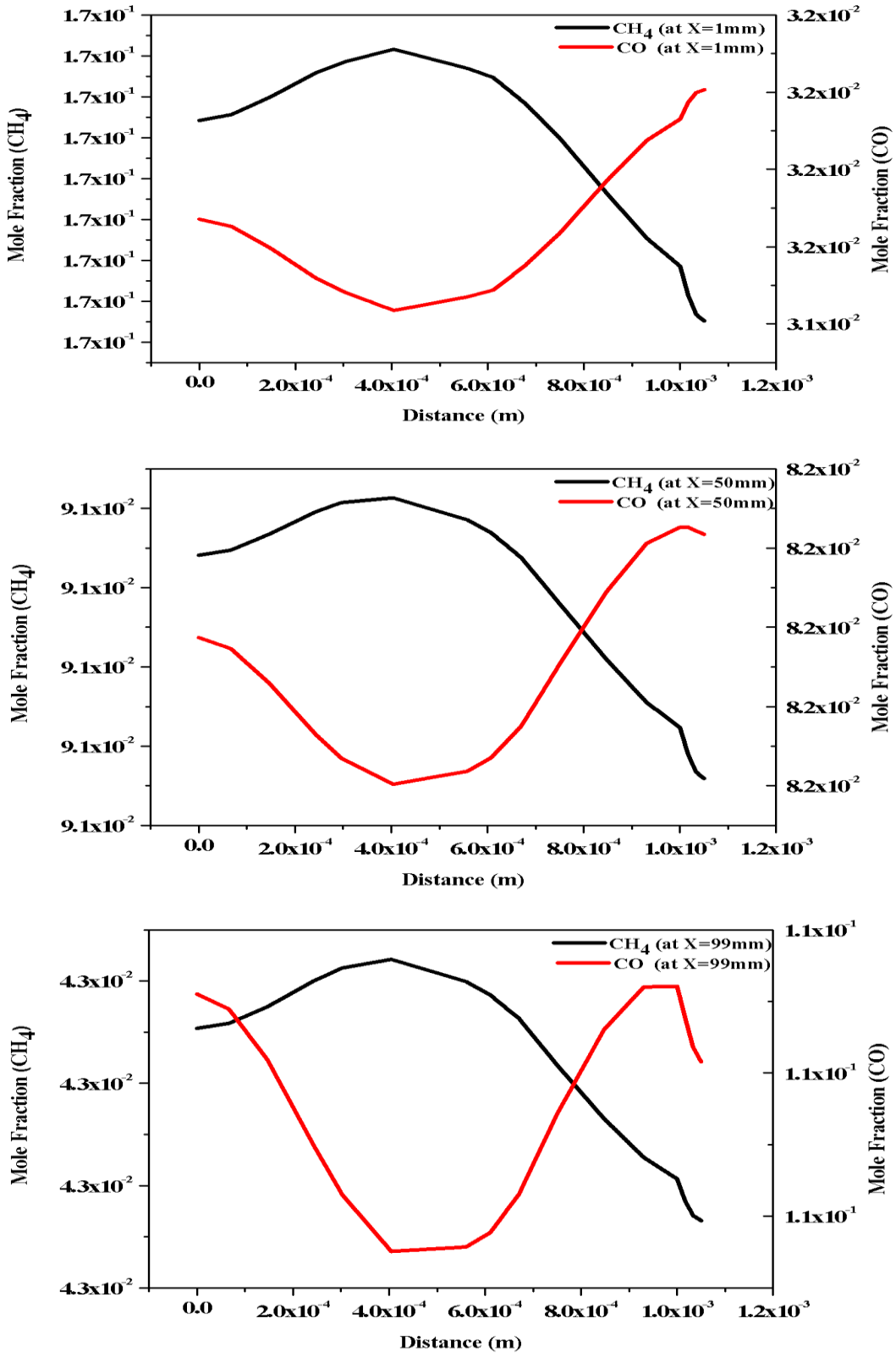

Figure 6.6 CH_4 and CO mole fraction distributions at sections Es and F.

The mole fraction distributions of H_2 and H_2O at the same positions are illustrated in Figure 6.7. The H_2 mole fraction is higher in the fuel channel and decreases towards

anode/electrolyte interface because of its consumption during the electrochemical reaction. The trend of H_2O mole fraction is opposite as it produces during electrochemical reaction and consumes during MSR and WGS reactions.

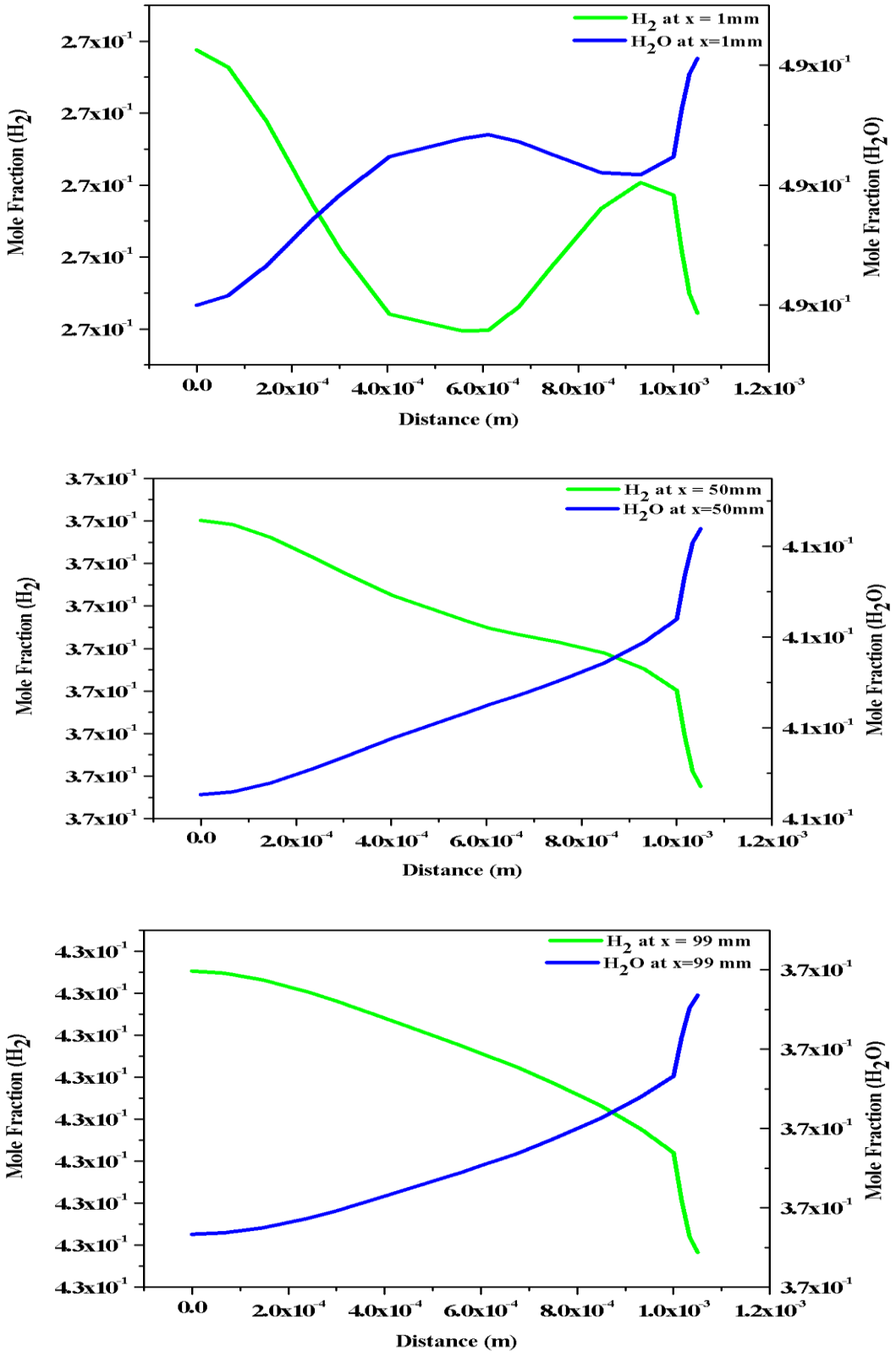

Figure 6.7 H_2 and H_2O mole fraction distributions at sections Es and F.

6.4.3 Temperature Distribution

The heat is generated during WGS and electrochemical reactions while consumed by MSR reaction which results in the drop of cell local temperature, as can be seen in Figure 6.8. The differences in maximum and minimum cell local temperature predicted by c-d models are 51.61 °C and 48.88 °C, respectively. The relative change in maximum and minimum temperature between c-d models is 5.3% and is calculated by the relation as follows,

$$\text{relative change } (\Delta T) = \frac{(T_{max}-T_{min})_c - (T_{max}-T_{min})_d}{(T_{max}-T_{min})_c} \times 100 \qquad (6.1)$$

The predicted temperature distributions from c-d models along the cell thickness at the same locations as those of species distributions are shown in Figure 6.9. The temperature at anode/electrolyte interface is 8 °C higher than those of in the channel because of the heat generation during electrochemical reaction at this location. The temperature distribution from fuel channel towards cathode/electrolyte interface has similar trend, as can be seen from Figure 6.10. However the difference in temperature is higher which is due to the heat taken away by the incoming air.

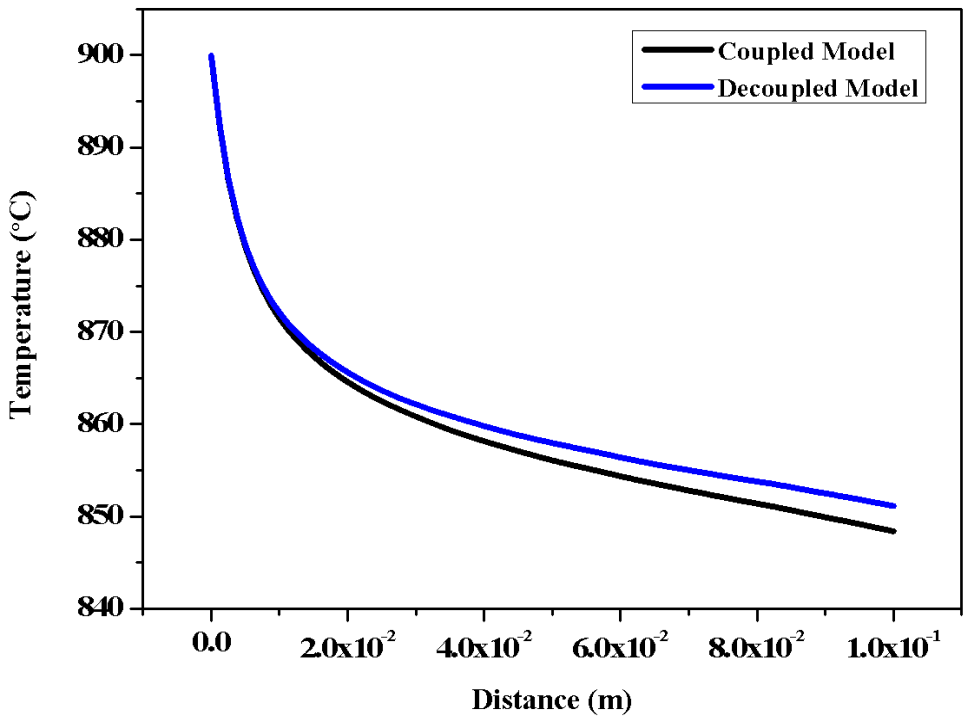

Figure 6.8 Temperature distribution from c-d models at section B.

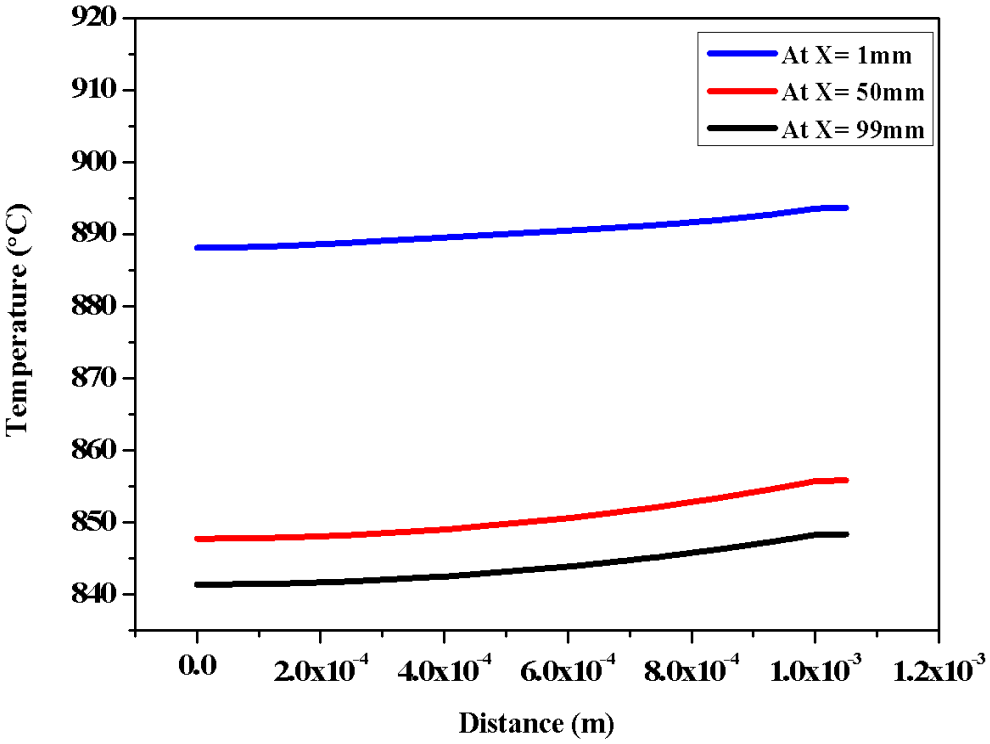

Figure 6.9 Temperature distribution at sections Es and F.

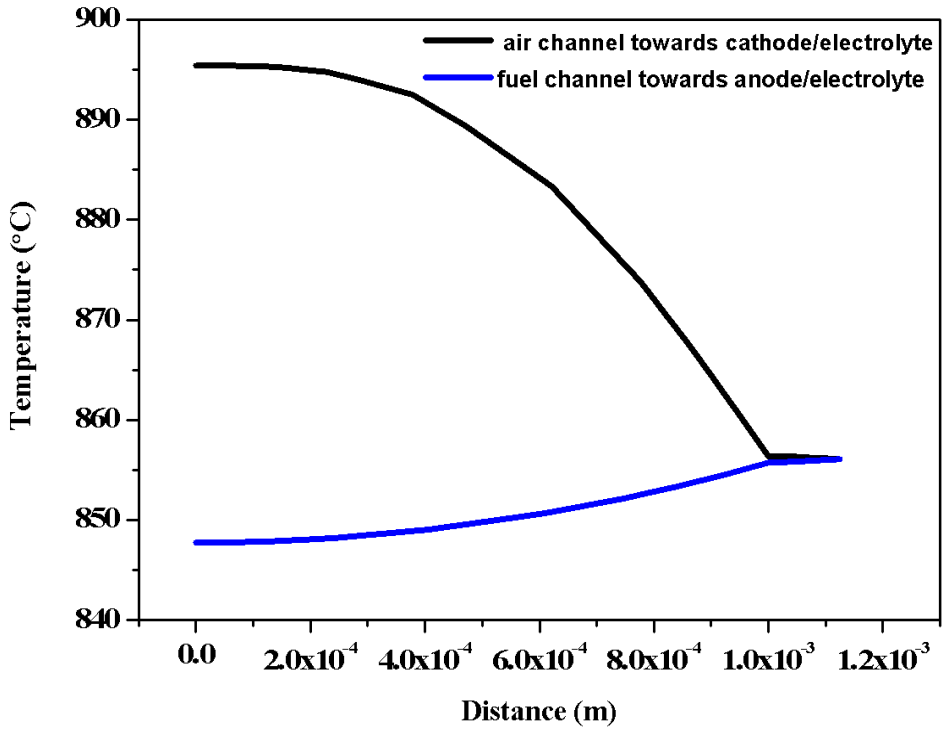

Figure 6.10 Temperature distribution at sections F and G.

6.4.4 Reaction Rates Distribution

The MSR and WGS reaction rates depend on temperature and their distributions in the centre of the fuel channel along the cell length are shown in Figure 6.11. The MSR reaction rate decreases nonlinearly from 105 mol/m^{3}s at inlet to 31.2 mol/m^{3}s at outlet. The distribution profile of WGS reaction rates shows an opposite trend as it is in equilibrium. The WGS reaction rate increases from minimum -3.2 mol/m^{3}s at inlet to maximum 4.5 mol/m^{3}s at outlet. The negative sign means the reaction is reverse which refers to the fact that generation of CO and H_2 occurred instead of consumption. However because of MSR reaction dominancy this is not visible in Figure 6.5.

The MSR reaction rate increases from fuel channel towards anode/electrolyte interface because of high temperature at interface, as shown in Figure 6.12. The WGS reaction rate distribution trend is opposite as it decreases along the same position.

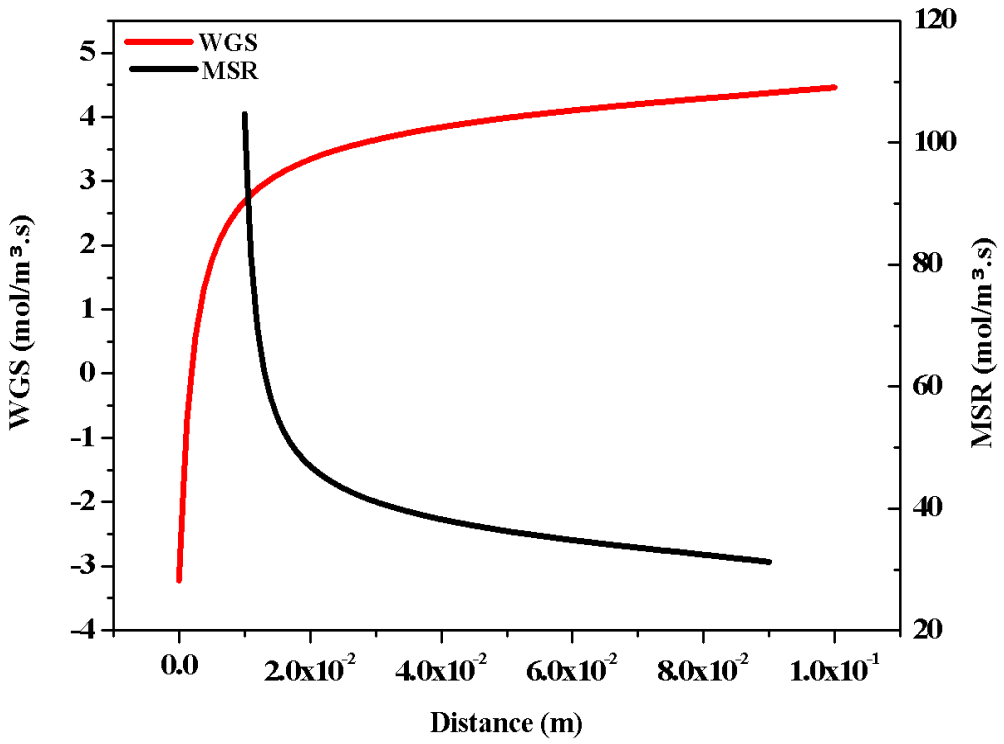

Figure 6.11 MSR and WGS reaction rates distribution at section D.

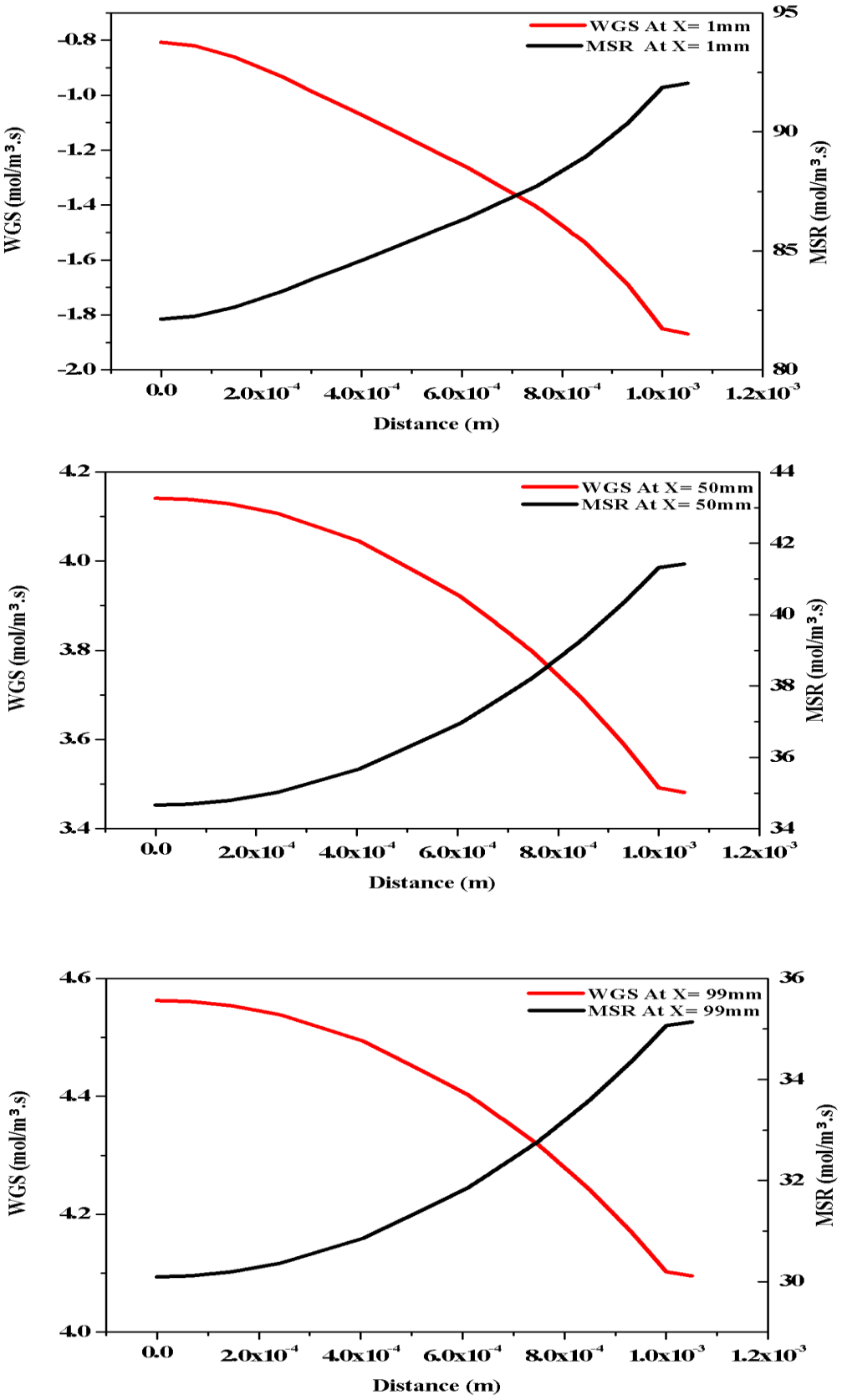

Figure 6.12 MSR and WGS reaction rates distributions at sections Es and F.

6.4.5 Heat source/sink related with MSR and WGS

The heat is consumed because of endothermic MSR reaction and generated due to exothermic electrochemical and WGS reactions, which contribute to the overall cell energy balance. The heat consumption during MSR reaction is high as compared to WGS reaction, as can be seen from Figure 6.13. The maximum MSR heat sink and WGS heat source are -23.66 MW/m^3 and 0.16 MW/m^3 at cell inlet and outlet, respectively. The heat source/sink terms are predicted at different locations along the cell thickness and the results are displayed in Figure 6.14. The consumption of energy decreases slightly from channel to anode/electrolyte interface because of the electrochemical reaction at this location.

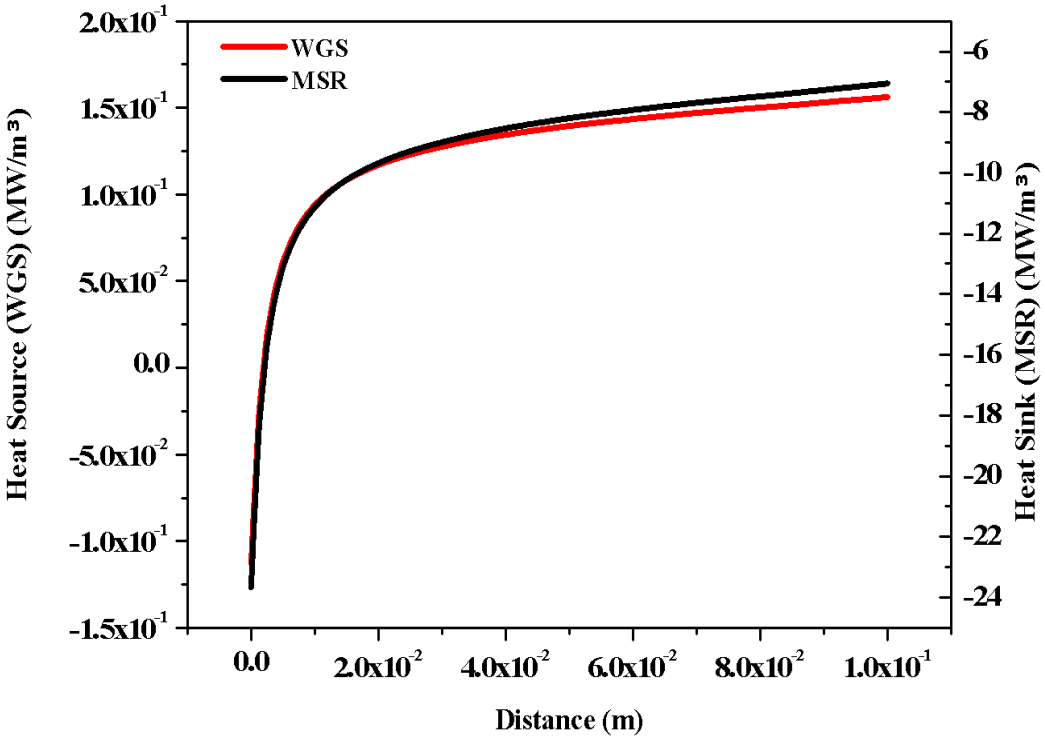

Figure 6.13 MSR and WGS heat sink/source distributions at section D.

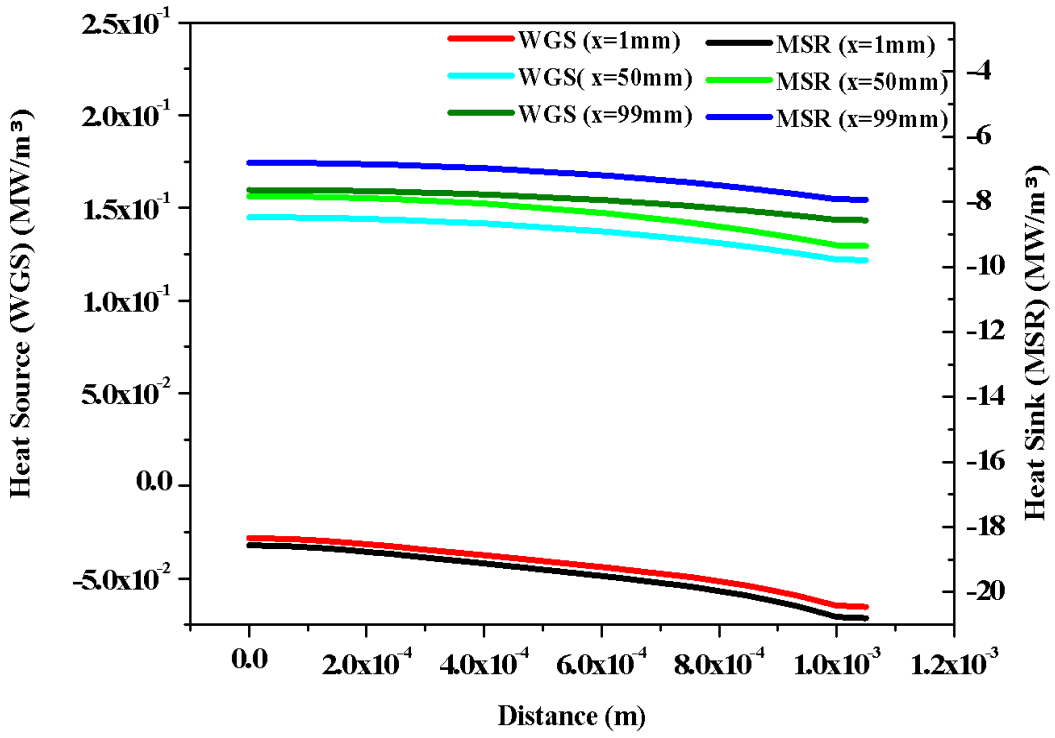

Figure 6.14 MSR and WGS heat sink/source distributions at sections Es and F.

6.4.6 Heat Source and reaction rate for electrochemical reaction

The heat is generated during electrochemical reaction and acts as a heat source. The distribution profile is same as that of temperature, as shown in Figure 6.15. The heat source is maximum 9.25E-4 MW/m^2 at inlet and drops to 7.13E-4 MW/m^2 at outlet. The heat generation is very low as compared to the heat absorbed during MSR reaction (refer to Figure 6.13). The consumption of H_2 depends on electrochemical reaction rate meanwhile the generation during MSR is higher than consumption. The electrochemical reaction rate is predicted at anode/electrolyte interface and the distribution along the cell length is shown in Figure 6.15. The rate is minimum -8.05E-3 mol/m^2s at cell inlet and increases to -0.0062E-3 mol/m^2s at cell outlet.

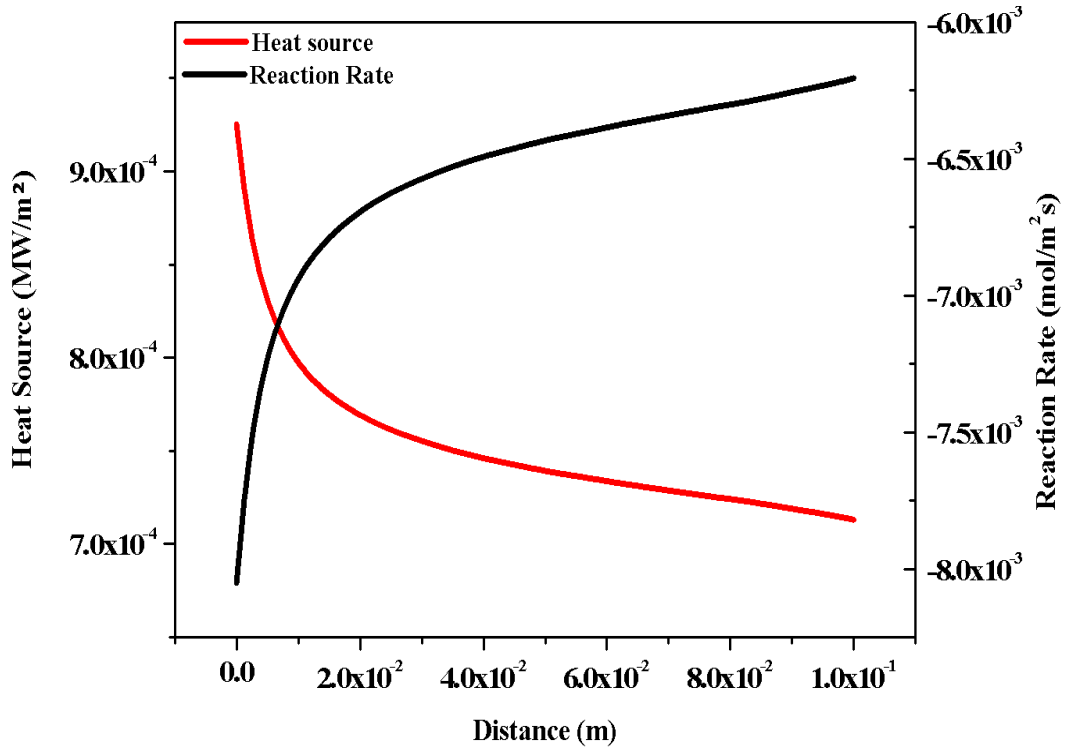

Figure 6.15 Electrochemical reaction rate and heat source distributions at sections F.

6.4.7 Thermal Strain and Stress Distribution

The thermal strain distribution is predicted by the same method as explained in section 5.4.6 and the results are displayed in Figure 6.16. The distribution profile is similar as that of temperature (refer to Figure 6.8). It is noticed from the results that thermal deformation for anode, electrolyte and cathode is higher at cell inlet because of greater cell local temperature at this location. The maximum thermal strain in anode, electrolyte and cathode is 0.0114, 0.0088 and 0.0097, respectively.

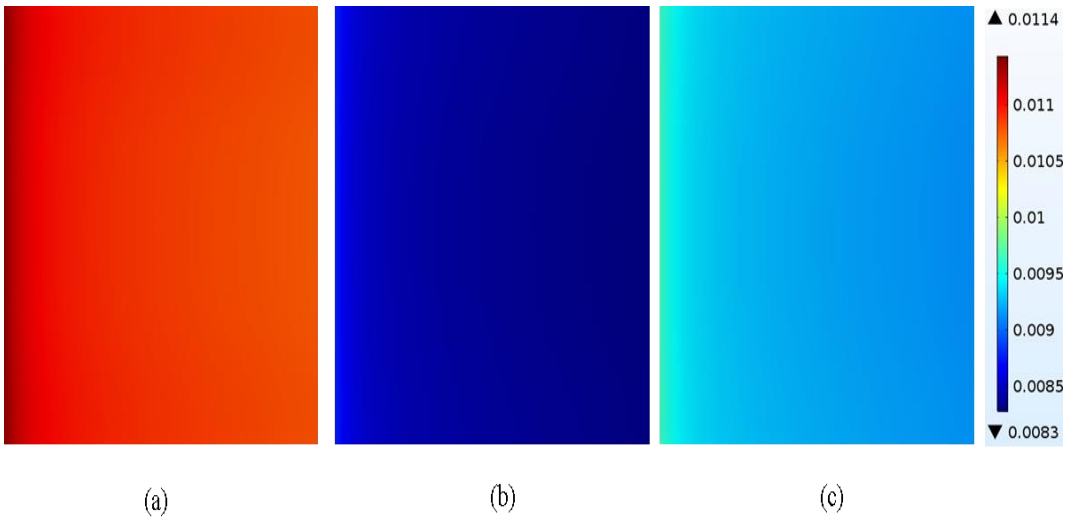

Figure 6.16 Thermal strain distribution at sections A (a), B (b) and C (c).

The thermal stresses show the same behavior as those of thermal strains. Taking the same spatial distribution the thermal stresses are predicted in the centre of anode, electrolyte and cathode and the results are shown in Figure 6.17. The maximum thermal stress generated in the centre of anode, electrolyte and cathode is 629.18 MPa, 1891.81 MPa and 338.79 MPa, respectively. The reason for high thermal stress generation in the electrolyte is same as that of explained in section 5.4.8.

The thermal stress along the cell height is larger at anode/electrolyte interface in comparison of cathode/electrolyte interface because of the heat generated at this position and also due to the larger thermal expansion coefficient, as shown in Figure 6.18 . The electrolyte thermal stress at anode/electrolyte interface is maximum 2441.86 MPa at cell inlet. The differences in maximum and minimum thermal stresses close to inlet, in the centre and close to the outlet are 374.792 MPa, 358.3 MPa and 355.29 MPa, respectively.

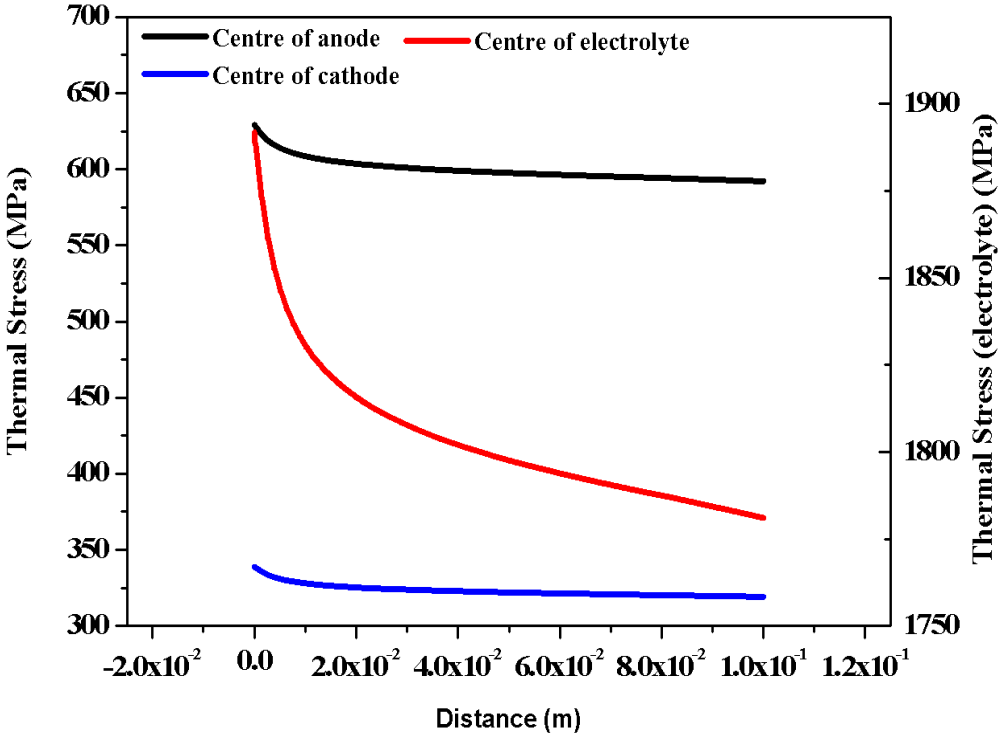

Figure 6.17 Thermal stress distribution from coupled models at sections A, B and C.

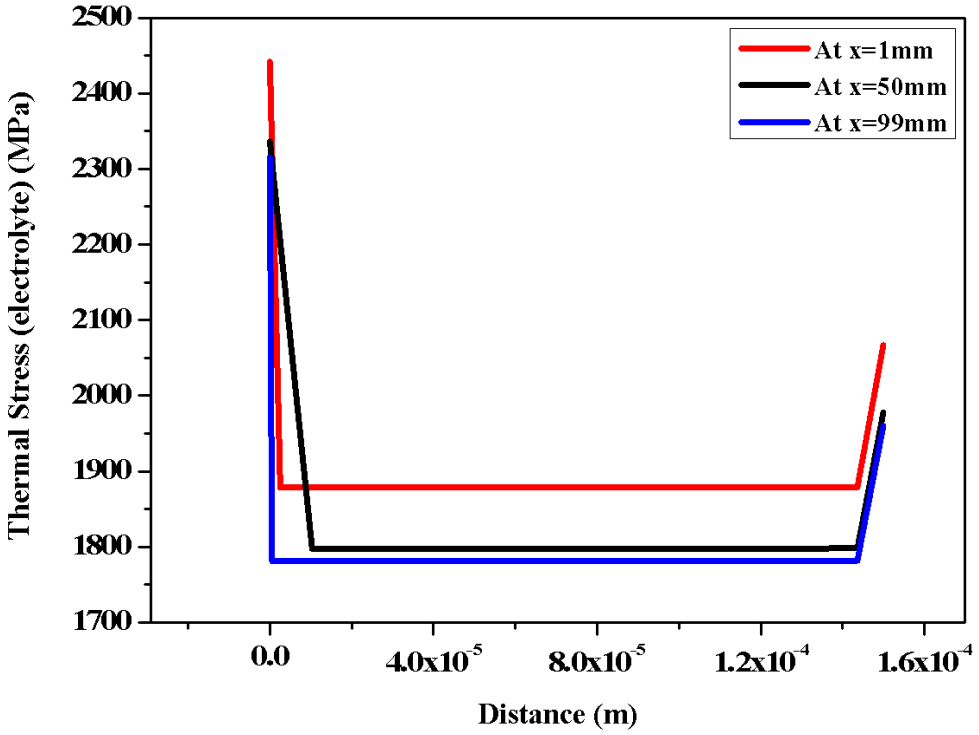

Figure 6.18 Electrolyte thermal stress distribution from coupled models at section Es.

6.5 Summary

A numerical model of a single planar SOFC running on methane has been developed. The MSR, WGS and electrochemical reactions have been modeled. The electrochemical performance of the developed model compared with IEA bench mark report and showed good agreement. The mechanisms of heat generating and absorption by electrochemical and chemical reactions have been investigated and their contributions to cell energy balance are presented. The temperature, species, electrochemical and chemical reactions and thermal strains and stresses distributions over the cell are discussed. The mole fraction of CH_4 decreases along the main flow direction because of its consumption during MSR. The H_2 and H_2O have opposite behavior. The electrochemical and chemical reactions are dependent on temperature. The maximum cell temperature is located at channel inlet and decreases along the main flow direction because of MSR reaction dominancy. A small temperature difference between fuel channel and anode/electrolyte interface is due to electrochemical reaction at this position. Even without CTE mismatch the temperature differences which are caused by the electrochemical and chemical reactions at different locations in the cell can induce significant thermal stresses. The maximum thermal strain is generated in anode, meanwhile the maximum thermal stress has been observed in the electrolyte because of its high mechanical properties.

Chapter 7- Parametric Study to Investigate the Effect of Operating Conditions on the Cell Performance and Thermal Impact

In this chapter, parametric study of methane SOFC model has been performed. The mass flow rates and air and fuel compositions are same as that of described in chapter 6 (refer to section 6.1 and 6.2). Effects of the cell operating temperature, material properties (porosity), flow configurations, air fuel ratio, cell geometrical parameters (thickness) and cell operating voltage are investigated. The operating conditions with significant effects on the cell performance and thermal impact are recognized.

7.1 Introduction

As explained in Chapter 3, the parameters such as cell operating temperature, material properties (porosity, conductivity), flow configurations, air fuel ratio, cell geometrical parameters (thickness) and cell operating voltage affect the cell performance [106, 127, 129, 134, 135, 143, 144, 146, 157, 169]. However, to the best of the author's knowledge, most of the researchers studied the effect on the performance of the anode - supported SOFC and also no one has investigated the effect on thermal impact [156, 159, 205, 211-216]. In this study the electrochemical performance and thermal impact of an electrolyte supported SOFC has been analyzed and by understanding the effects of different parameters on the electrochemical performance and thermal impact will help to choose the optimize design parameters for SOFC applications. The simulation results from parametric study performed on methane fueled SOFC are discussed as follows;

7.2 Results and Discussion

7.2.1 Effects of the Inlet Temperature on the Cell Performance and Thermal Impact

The model is tested for different inlet temperatures (referred as operating temperatures) range between 800 to 1000 °C. The electrochemical performance which is checked by V-I curves at different operating temperatures are shown in Figure 7.1. The average current densities at 0.7 V for 800 °C and 1000 °C operational temperatures are 2142.74 A/m^2 and 3953.29 A/m^2 respectively. The reason for high current generation at higher temperature is due to reduction in electron flows (high ionic conductivity) which results in lower ohmic losses. The 25% increases in operating temperature results in 84.5 % increase in current density while the cell operating at 0.7 V.

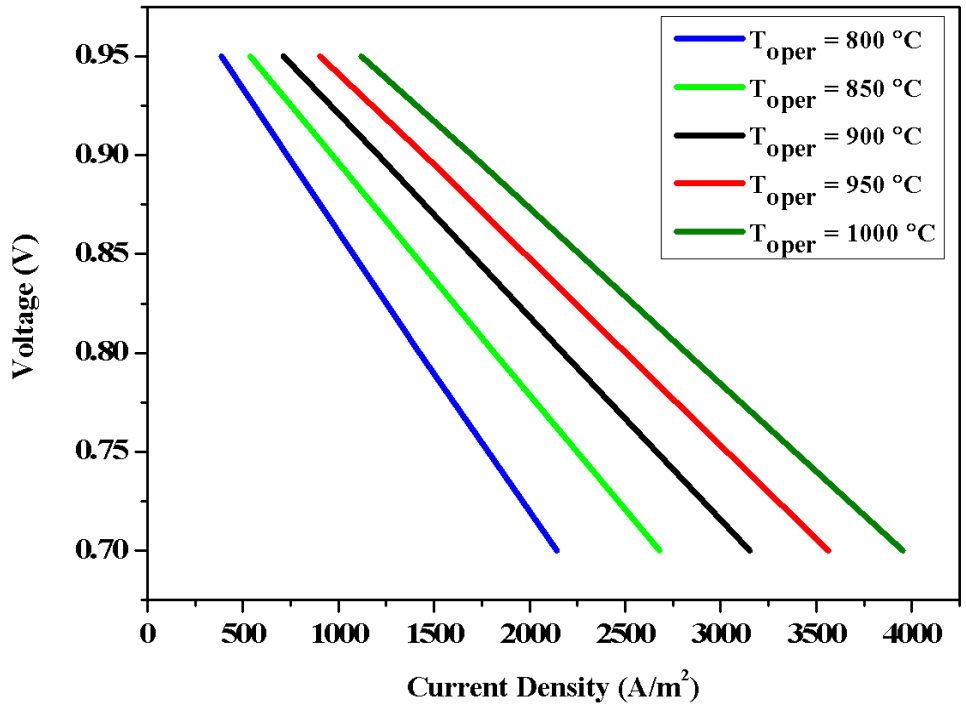

Figure 7.1 V-I characteristics at different operating temperatures.

The temperature distribution is predicted in the centre of the electrolyte for each operational temperature and the results are displayed in Figure 7.2. The difference in maximum and minimum cell local temperature at 800 °C and 1000 °C operational temperature cases is 2 °C and 122 °C respectively. The difference at higher temperature is larger which supports the fact that increase in temperature results in higher reaction rates and more heat is generated during electrochemical and chemical reactions.

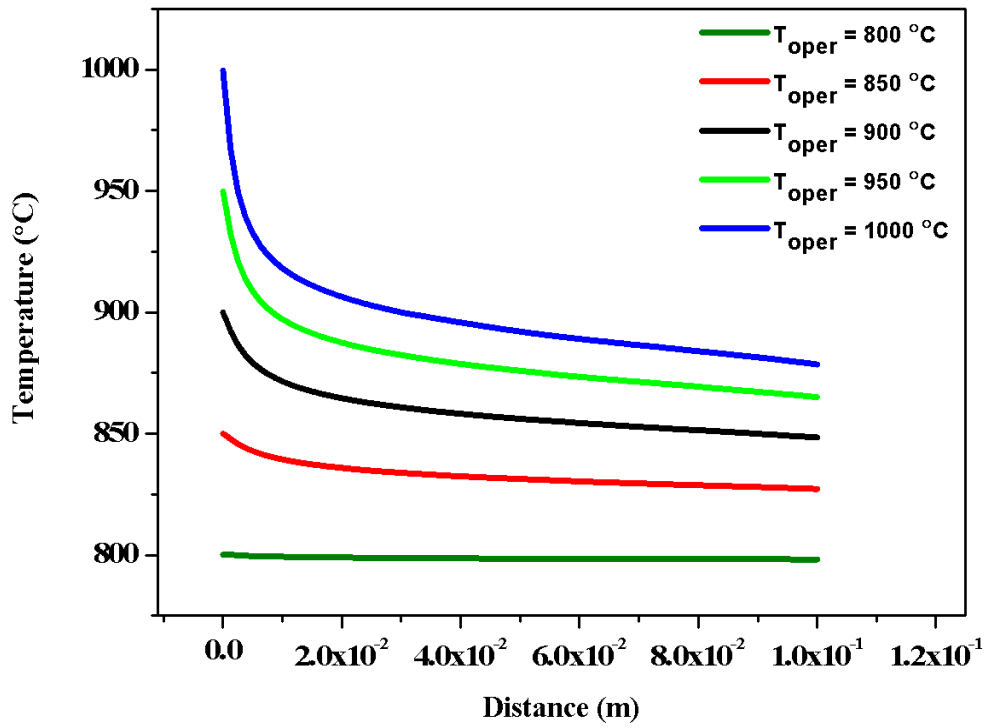

Figure 7.2 Temperature distribution from different operating temperatures at section B.

The thermal strain distribution in the centre of anode, electrolyte and cathode at different operating temperatures is shown in Figure 7.3. The increase in operating temperature results in larger temperature difference which referred to greater thermal strain generation. The distribution profile is same as that of temperature. The maximum thermal strain generated in anode close to inlet at 850 °C, 900 °C and 1000 °C is 0.0108, 0.0114 and 0.01274, respectively. The electrolyte has maximum thermal strain generation 0.0083, 0.0088 and 0.0098 at 850 °C, 900 °C and 1000 °C, respectively. The maximum thermal strain generated in cathode is 0.0091, 0.0097 and 0.0108 at 850 °C, 900 °C and 1000 °C, respectively.

The effect of the operating temperature on the thermal strain generation in the cell is predicted by the relative change which is calculated as;

$$\text{Relative Change } (\delta) = \frac{(\delta_{ref} - \delta_{operational})}{\delta_{ref}} \times 100 \tag{7.1}$$

Where δ_{ref} indicates the thermal strain generation at reference temperature (900 °C) and $\delta_{operational}$ the thermal strain generation at various operating temperature.

The results for relative change in thermal strain generation at different operating temperatures at the same spatial positions are shown in Figure 7.4. The relative change at a specific operating temperature is identical for all three components. The maximum relative change in thermal strain is 11.36 %, which is located near the cell inlet and decreases along the cell length.

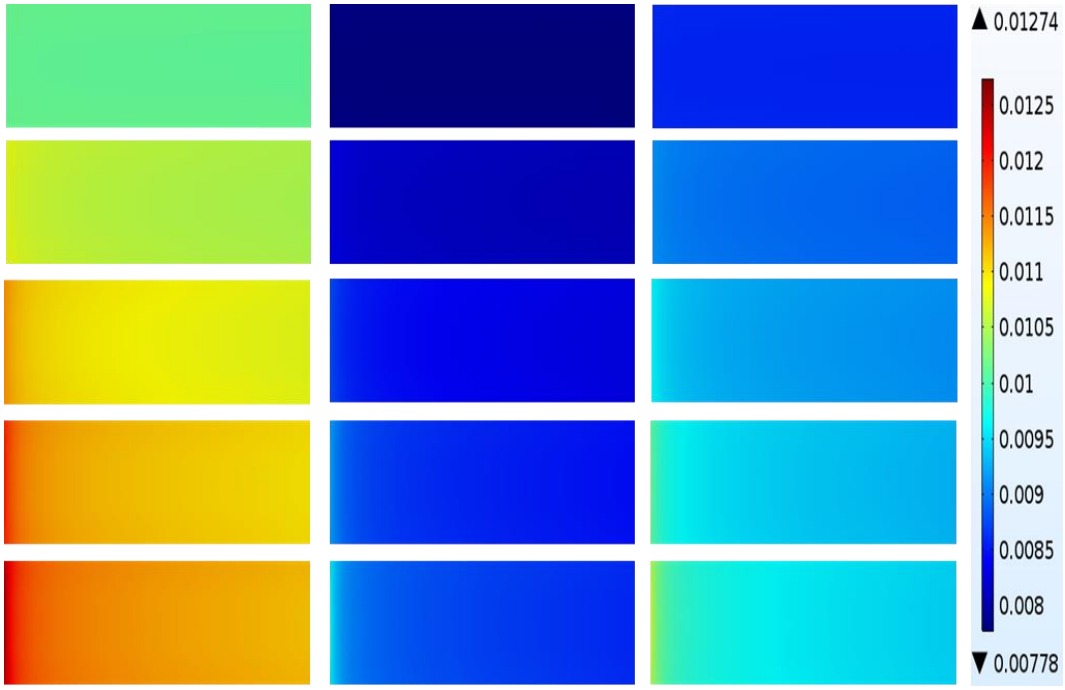

Figure 7.3 Thermal strain distribution at sections A (a), B (b) and C (c). Rows from top 1st, 2nd, 3rd, 4th and 5th at 800 °C, 850 °C, 900 °C, 950 °C and 1000 °C, respectively.

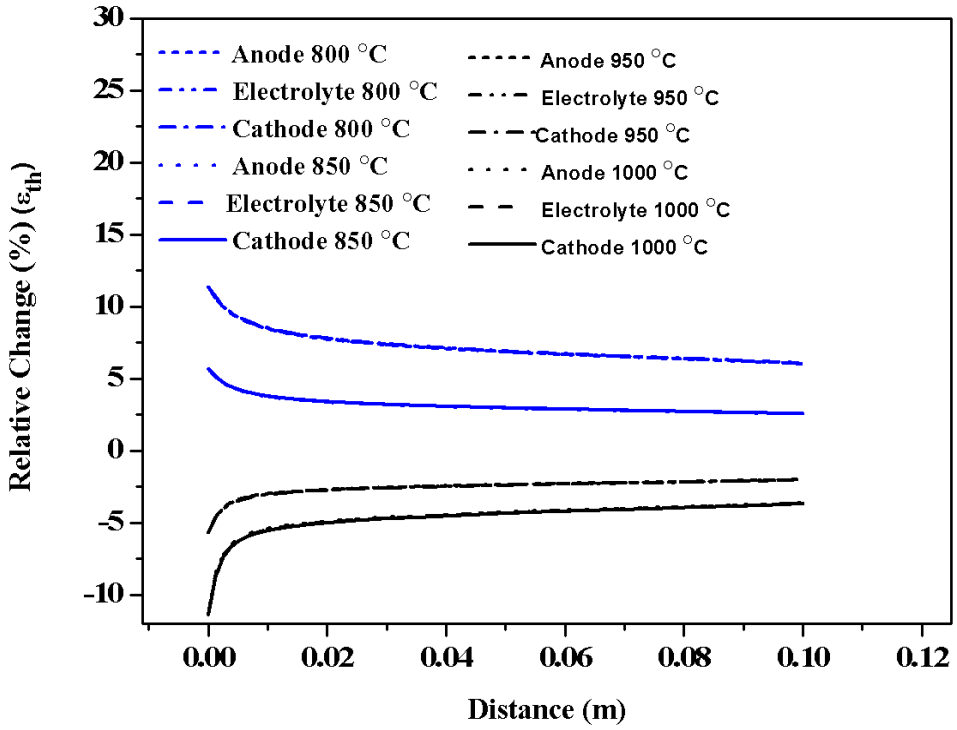

Figure 7.4 Relative change in thermal strain generations between different operating temperatures at sections A, B and C.

The maximum thermal stress is generated in the electrolyte and the distribution profile is same as that of thermal strain. The maximum thermal stress generated in the cell operated at 800 °C is 1677 MPa and at 1000 °C is 2106 MPa, as shown in Figure 7.5. The difference in maximum thermal stress is 429 MPa which refers that a 25% increase in operating temperature results an increase of same percentage in thermal stress generation. The minimum thermal stress 1845.67 MPa which is generate at 1000 °C is still higher than the maximum thermal stress at 800 °C.

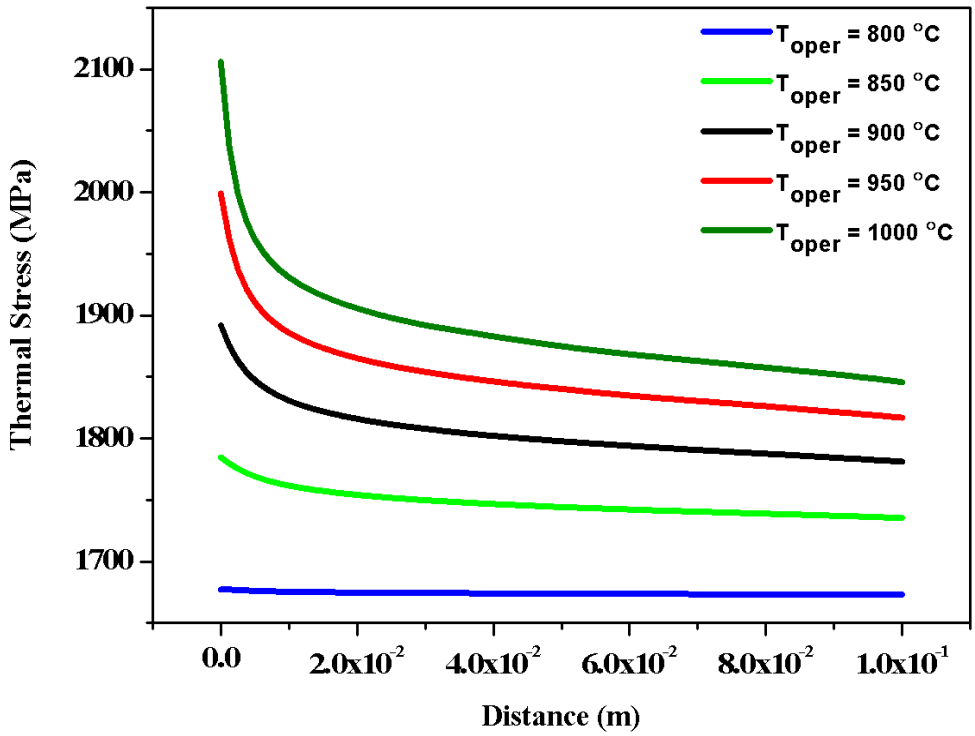

Figure 7.5 Thermal stress distribution from different operating temperatures at section B.

7.2.2 Effect of the Porosity on the Cell Performance and Thermal Impact

The model is simulated for different porosities range from 30 to 60%. The equations explained in section 4.9 are used to calculate the active surface area. The space between the particles is less at low porosity, meanwhile the active surface area for electrochemical reactions is large, as shown in Figure 7.6. The active surface area is maximum 451059.2 m^{-1} at 30% porosity and decreases to minimum 256590.55 2 m^{-1} at 60%. It is evidenced from Figure 7.7 that higher active surface area results in larger current density generation. The average current density at 0.7 V from 30% porosity case is 3357.86 A/m^2 and decreases to 2514.77 A/m^2 at 60%. The 50% increase in porosity results in 25% decrease of current density.

The relative change in current density generation is formulated by implementing equation 7.1, where δ_{ref} replaces with the current density generation at 40% porosity and $\delta_{operational}$ the current density generation at other porosity cases.

The decrease in average current density at 0.7 V by varying the porosity from 30 to 40% is only -6.5% as can be seen from Figure 7.8. The relative change is maximum 20.22 % at 0.7 V between 40 and 60 % porosity cases which refers to decrease in current density generation.

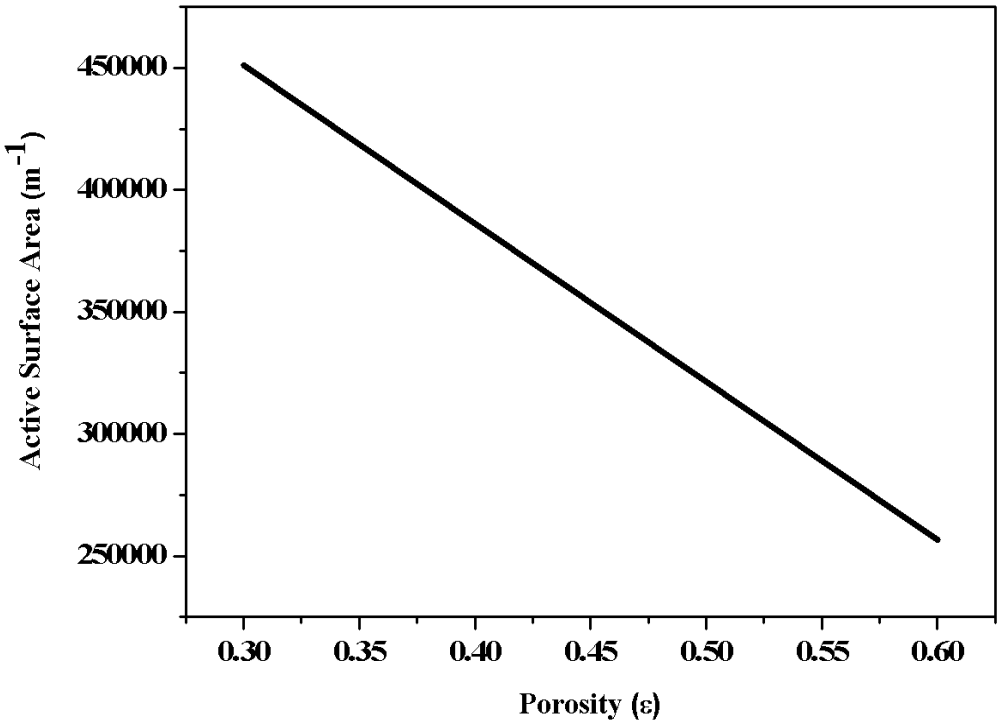

Figure 7.6 Active surface area versus porosity.

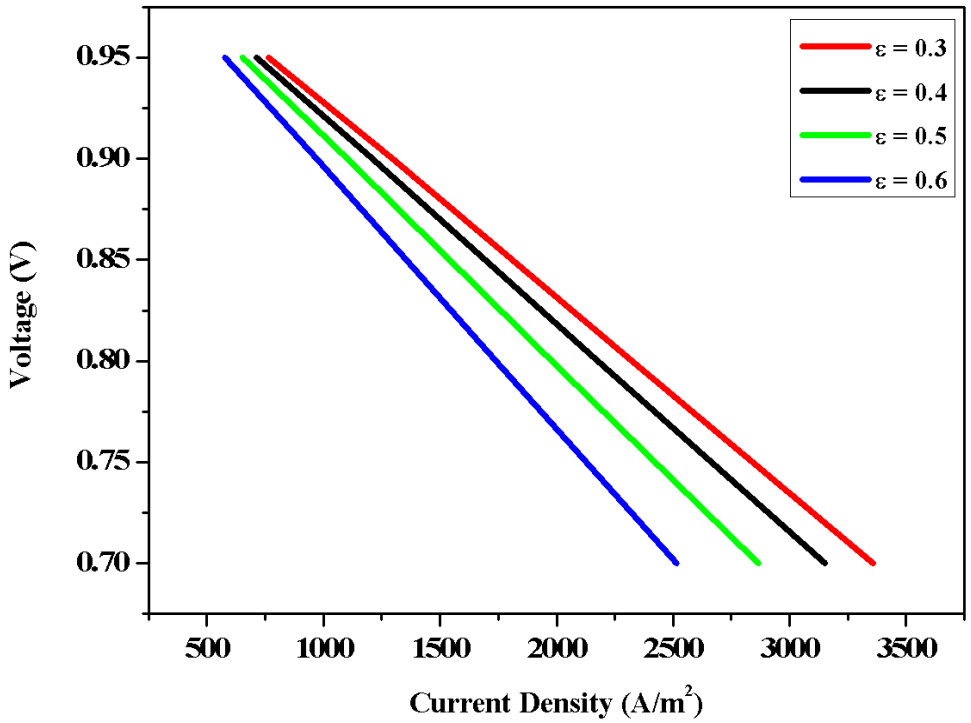

Figure 7.7 V-I Characteristics at different porosities.

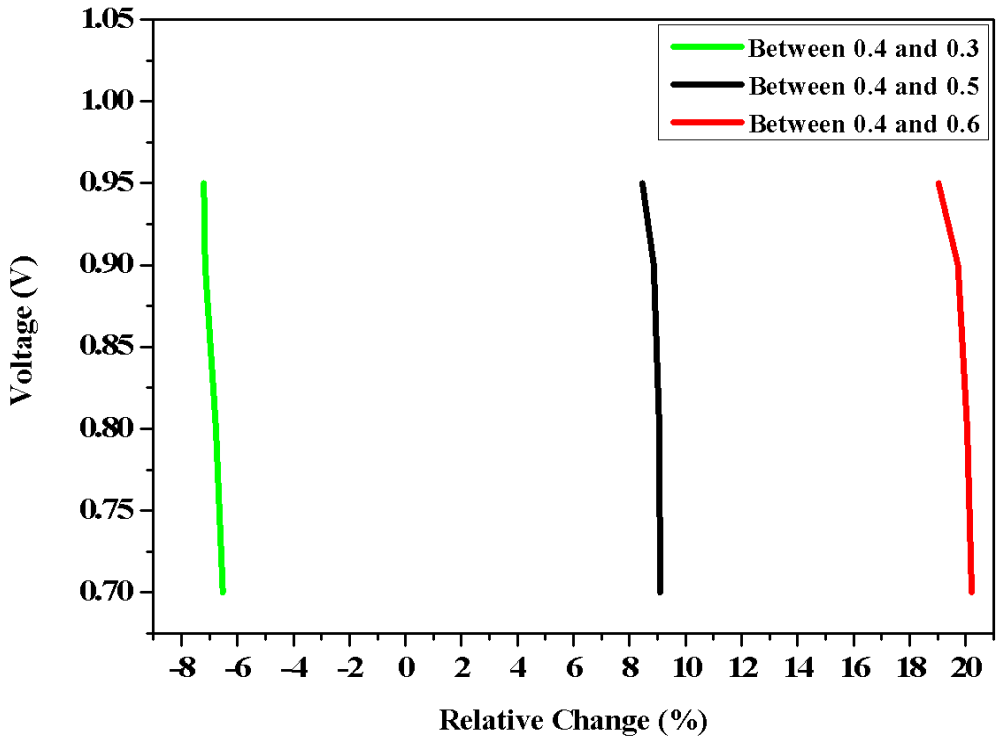

Figure 7.8 Relative change in average current density generations at different cell voltage between different porosity cases.

The increase in the porosity results in higher permeability which ultimately enhance the fluid flow. The decrease in porosities hinders the multicomponent flow and the difference between the mole fraction at reaction sites and flow channels is high. The distribution of the Hydrogen mole fractions in the centre of the fuel channel and anode along the cell thickness for different porosities is shown in Figure 7.9. The difference in the mole fractions between the channel and the anode/electrolyte interface for 60 % porosity is 0.05% and for 30% porosity is 0.1%.

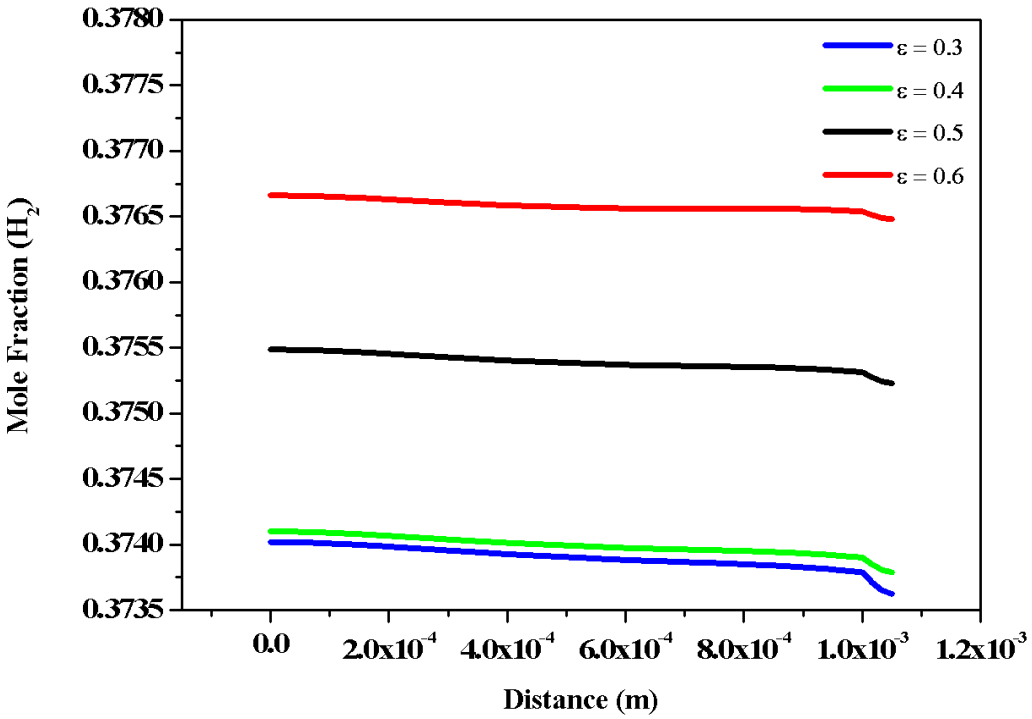

Figure 7.9 H_2 mole fraction distribution from different porosity cases at sections D and F.

Under the effect of different porosities the differences between temperature distributions are less significant, as can be seen from Figure 7.10. The minimum temperature at cell outlet from 30 and 60% porosity cases is 849 °C and 845.7 °C, respectively. The relative change in temperature between different porosity cases is estimated by using equation 7.1 and the results are illustrated in Figure 7.11. The maximum relative change in temperature distribution between 40 and 60 % porosity cases is 0.34 %.

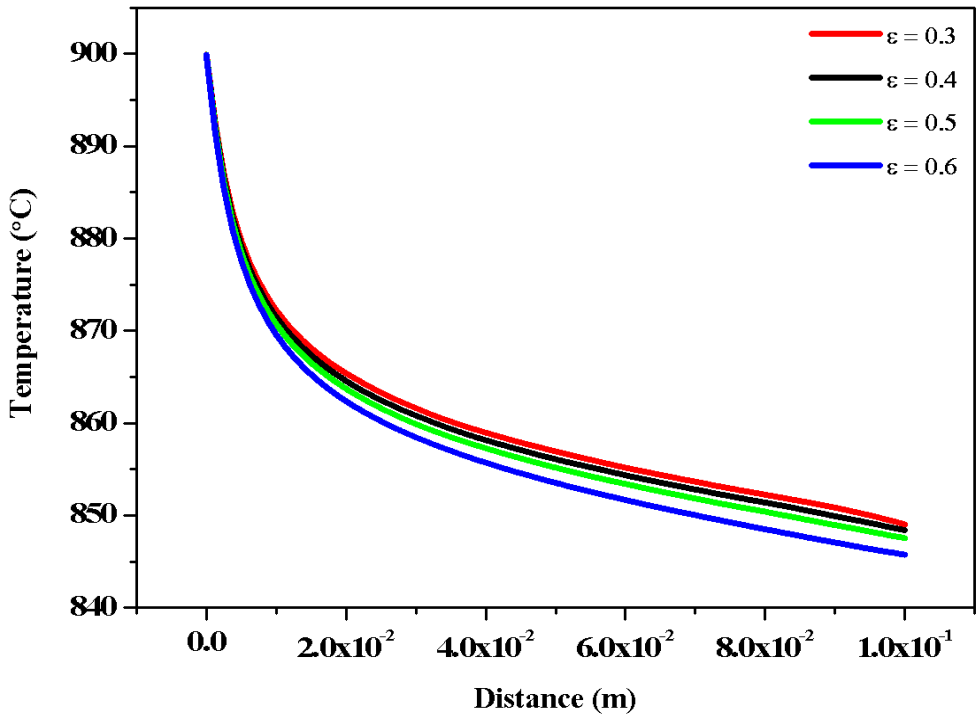

Figure 7.10 Temperature distribution from different porosity cases at section B.

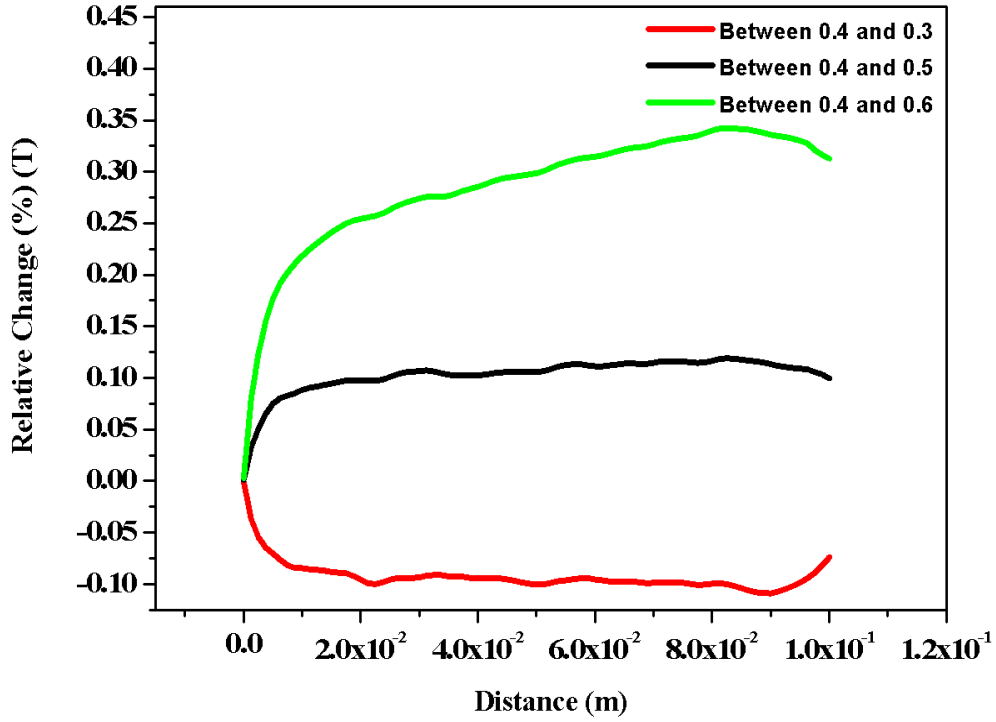

Figure 7.11 Relative change in temperature distribution between different porosity cases at section B.

The thermal strain distribution follows the same pattern as that of temperature which supports to the fact that the thermal strain generation is same at all porosity cases. The reason for same amount of thermal strain generation is the order of thermal expansion coefficient 10^{-6}. The thermal stress distribution profile in the centre of electrolyte along the cell length is shown in Figure 7.12. The difference in thermal stress generation between 30 and 60 % porosity cases is 0.4 %.

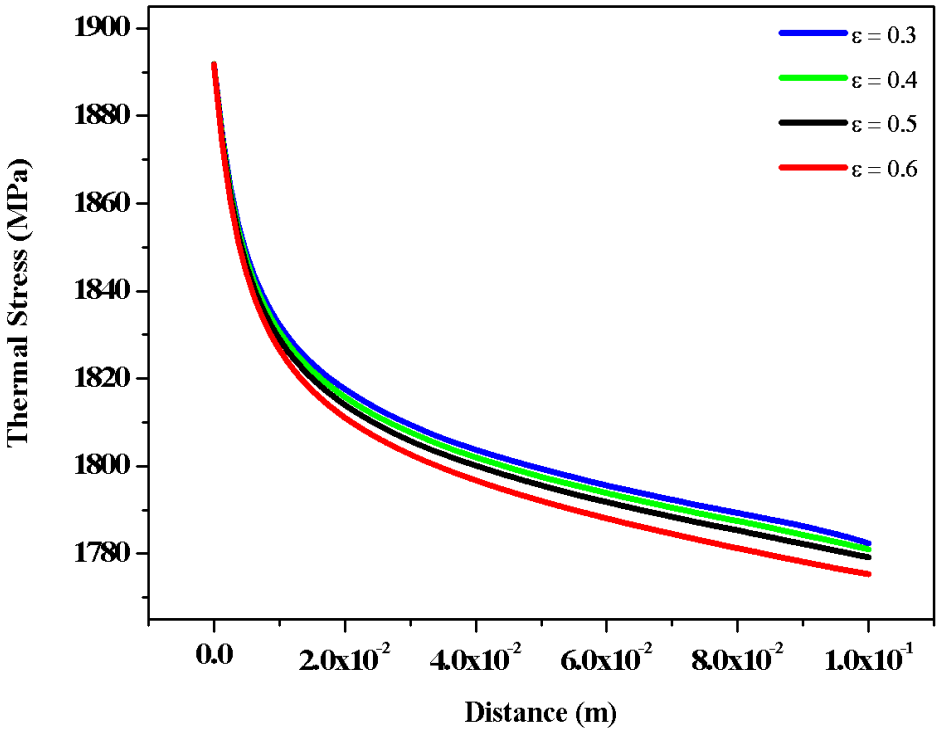

Figure 7.12 Thermal stress distribution from different porosity cases at section B.

7.2.3 Effect of the Flow Configurations on the Cell Performance and Thermal Impact

The difference in current density between co-flow and counter flow configurations is not significant, as can be seen from Figure 7.13. The average current density at 0.7 V for co-flow case is 40 A/m^2 higher than counter flow case. The current density distribution at anode/electrolyte interface along the cell length is plotted and the results are displayed in Figure 7.14. The current density distribution for co-flow case is more uniform than counter flow case. The current density for co-flow configuration decreases

along the flow direction because of the oxygen and hydrogen consumption. In counter flow the air and fuel enter in the opposite direction. The difference in current density distribution is because of different H_2 partial pressures.

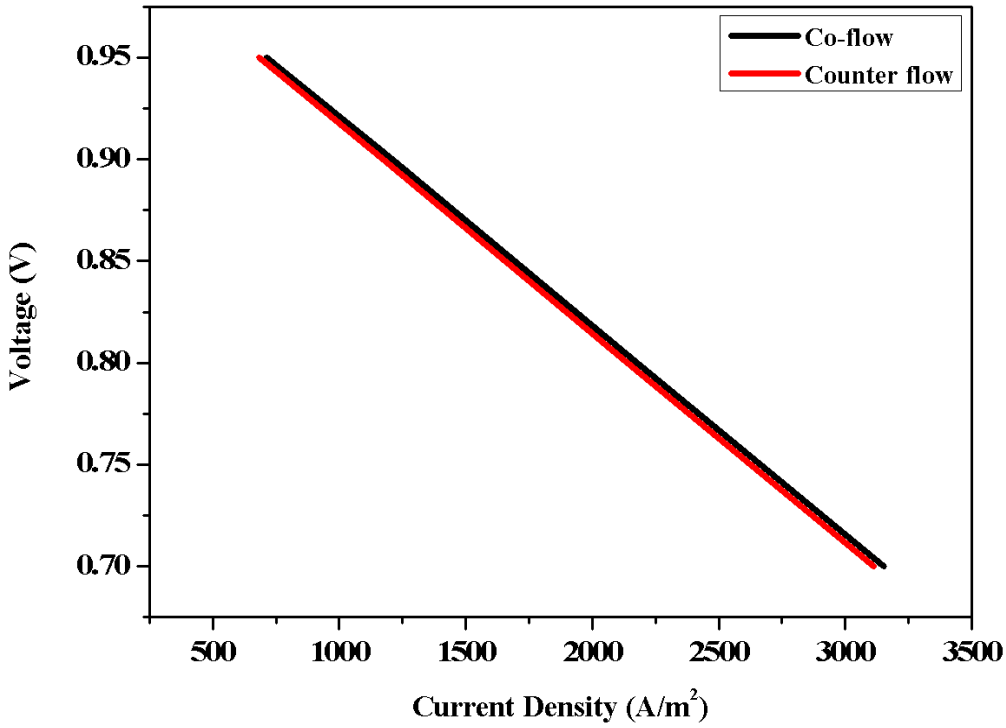

Figure 7.13 V-I Characteristics for co and counter flow configurations.

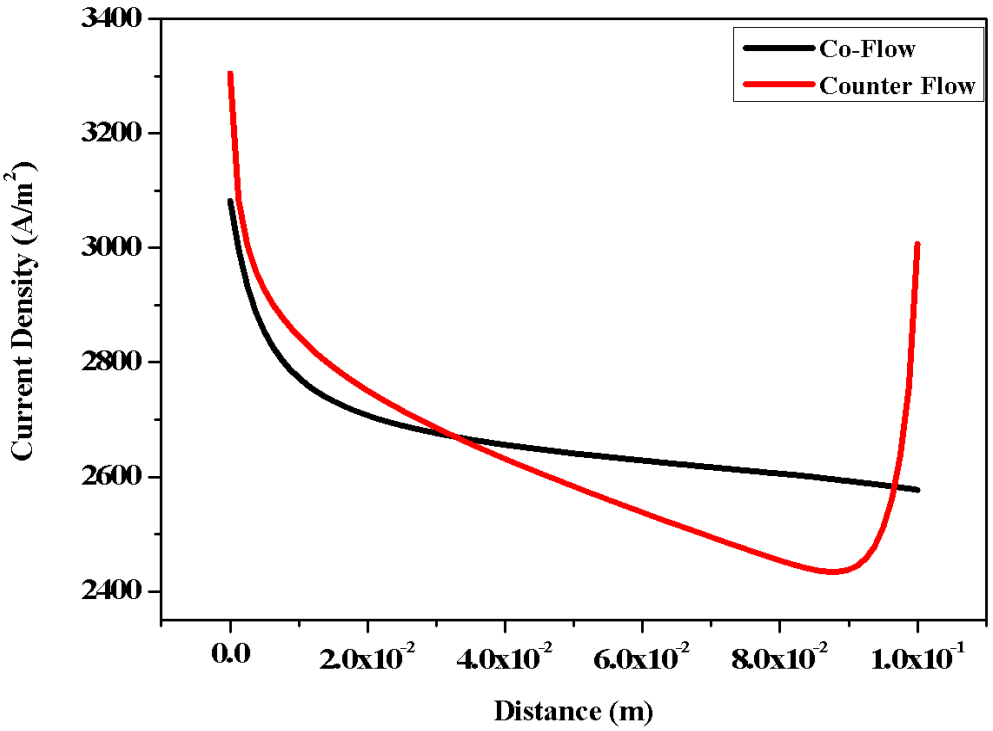

Figure 7.14 Current density distribution for co and counter flow configurations at section F.

The temperature near inlet is same but near the outlet the temperature for counter flow case is higher, as can be seen in Figure 7.15. The low temperature in co-flow case indicates that the heat absorbed by MSR reaction is high. The low temperature leads to decreases in thermal strain and stress generation. The thermal strain distribution for both flow configurations along the cell length is shown in Figure 7.16. The maximum thermal strain generation in all components located near the cell inlet and outlet because of the higher temperature at these positions. The thermal stress distribution profile is same as that of temperature and is displayed in Figure 7.17. In case of co-flow the thermal stress is highest at the inlet and decreases towards the outlet. The thermal stress in counter flow case is higher at inlet and outlet. The temperature, thermal strain and stress distributions in co-flow is more uniform as compared to counter flow and offers better thermo-mechanical stability of the cell.

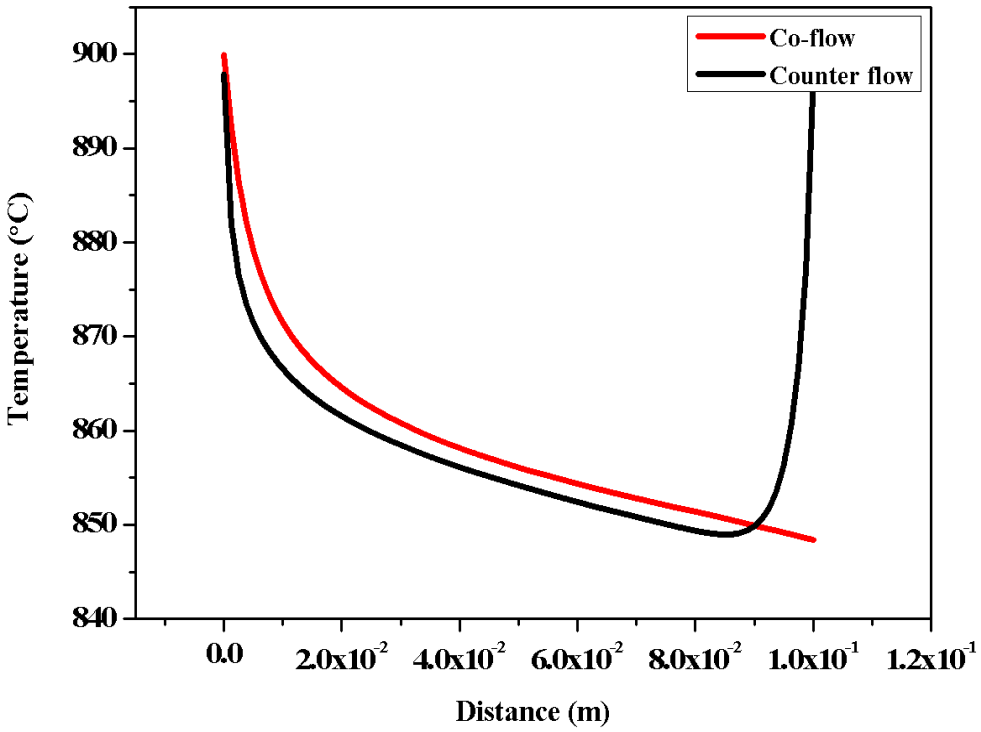

Figure 7.15 Temperature distribution for co and counter flow configurations at section B.

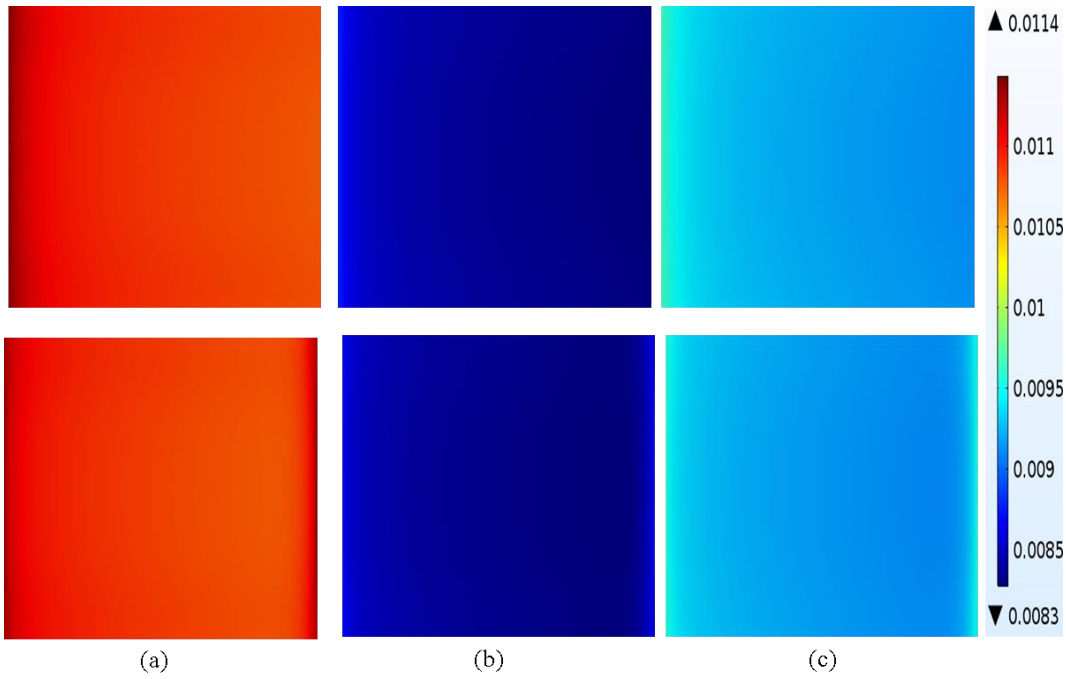

Figure 7.16 Thermal strain distribution from co-flow (top) and counter flow (bottom) configurations at sections A (a), B (b) and C (c).

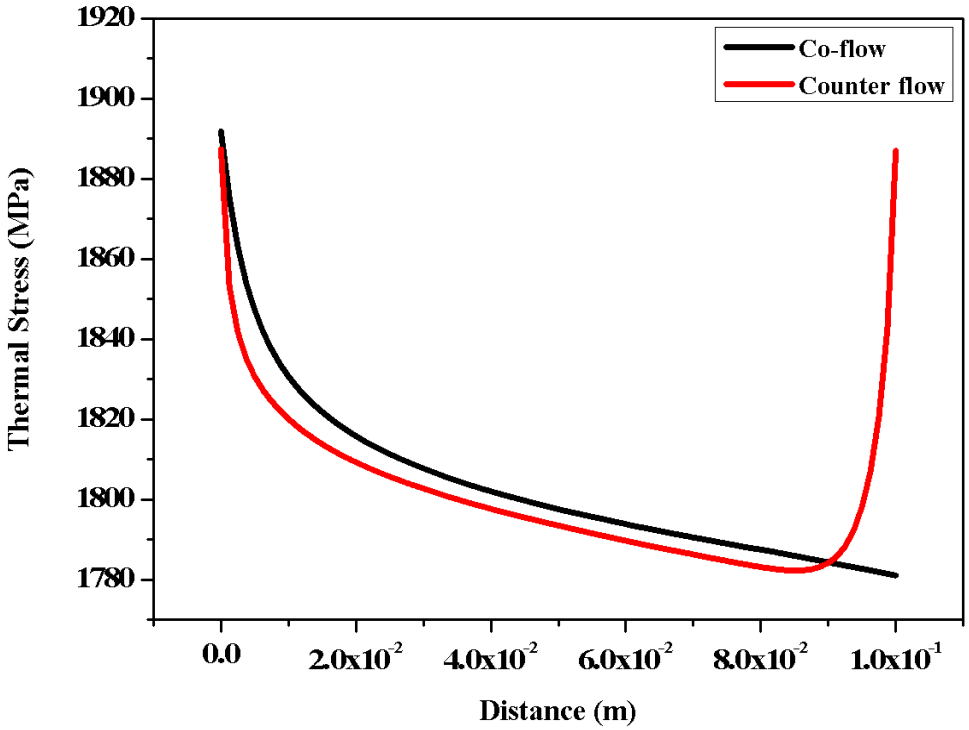

Figure 7.17 Thermal stress distribution from co and counter flow configurations at section B.

7.2.4 Effects of the Air Fuel Ratio on the Cell Performance and Thermal Impact

The model is tested for different air fuel ratios (AFR) and effect on the electrochemical performance of the cell is shown in Figure 7.18. The mass of the fuel remains unchanged and air mass flow rate is varied to alter the air fuel ratio. The increase in AFR results in higher current density because of the increase in oxygen ion flows and vice versa. The average current densities at 0.7 V for AFR 15.769, 31.537 (base case) and 63.074 are 3031.36 A/m^2, 3152.18 A/m^2 and 3268 A/m^2, respectively. The relative change is estimated by implementing equation 7.1, where δ_{ref} replaces with current density generation at AFR 31.537 and $\delta_{operational}$ with current density generation at various AFRs. The results are illustrated in Figure 7.20. The maximum relative change between AFR 31.537 and 63.074 in current density is -7.8 % at 0.95V and decreases to -3.7 % at 0.7 V. Meanwhile the relative change between AFR 31.537 and 15.769 is same in magnitude with opposite sign.

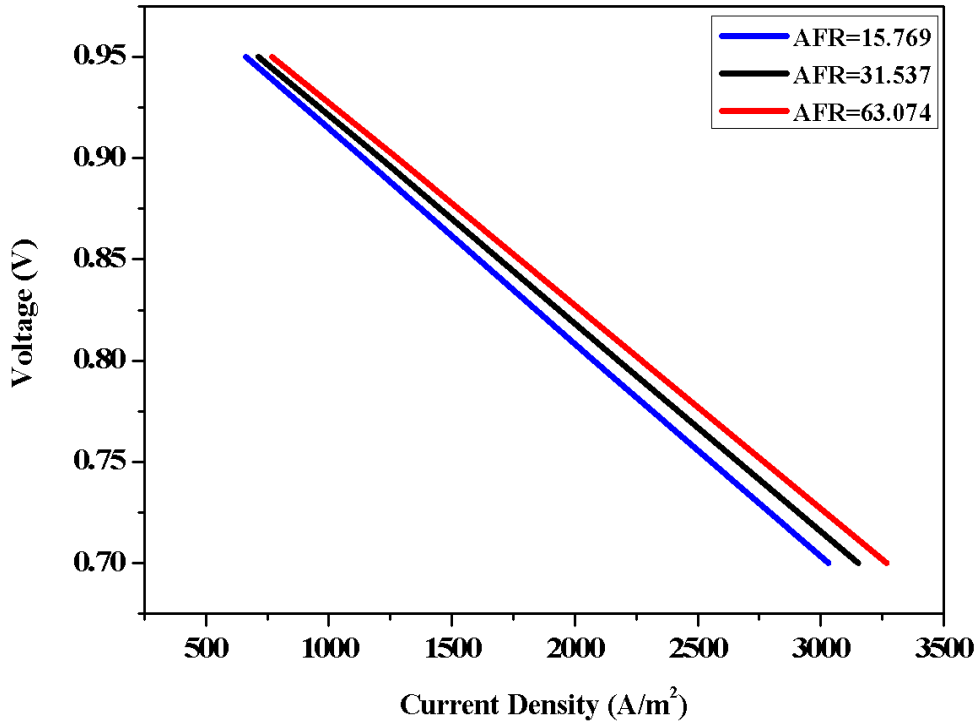

Figure 7.18 V-I Characteristics at different A/F ratios.

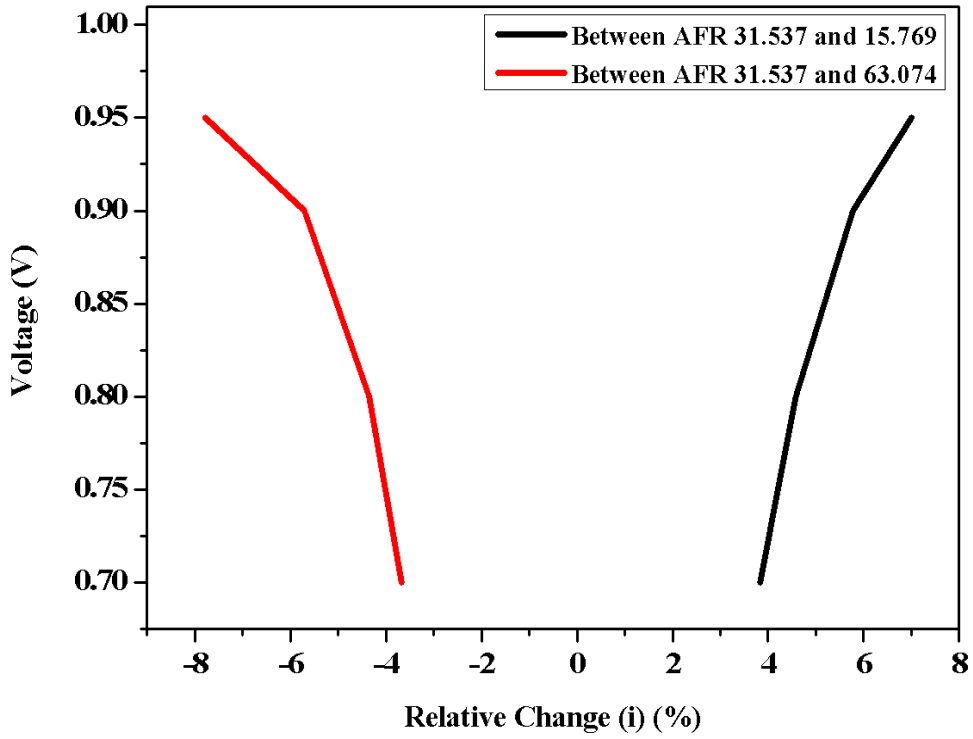

Figure 7.19 Relative change in average current density generations at different voltages between various air/fuel ratio cases.

The heat generated during the electrochemical reaction is taken away by the incoming air and the increase in the mass flow rate results in the decrease of cell local temperature as shown in Figure 7.20. The difference between maximum and minimum cell temperature for AFR 15.769, 31.537, 63.074 is 61 °C, 51.5 °C and 45 °C, respectively. The increase in AFR from 15.769 to 63.074 results in 26.3 % decrease in the cell temperature difference between the inlet and outlet which leads to more uniform temperature distribution. The effect of the AFR on temperature distribution is estimated by calculating the relative change with reference to base case. The results are presented in Figure 7.21. The maximum relative change 1.15 % in temperature distribution is near the cell outlet when the AFR decreases from the reference case and -0.8 % when AFR increases.

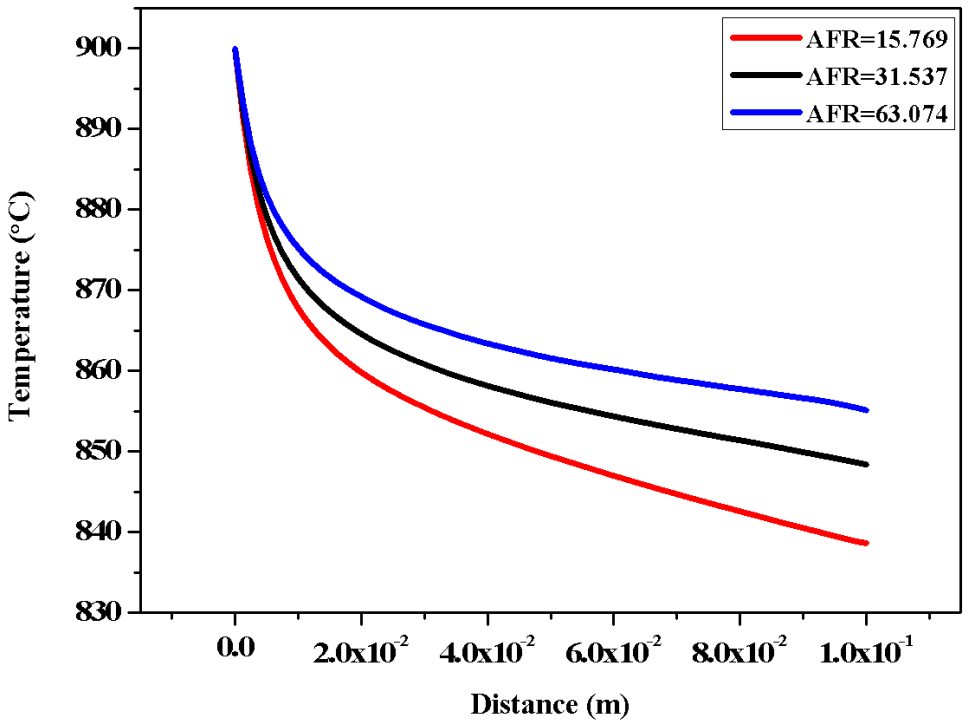

Figure 7.20 Temperature distribution for different A/F ratios at section B.

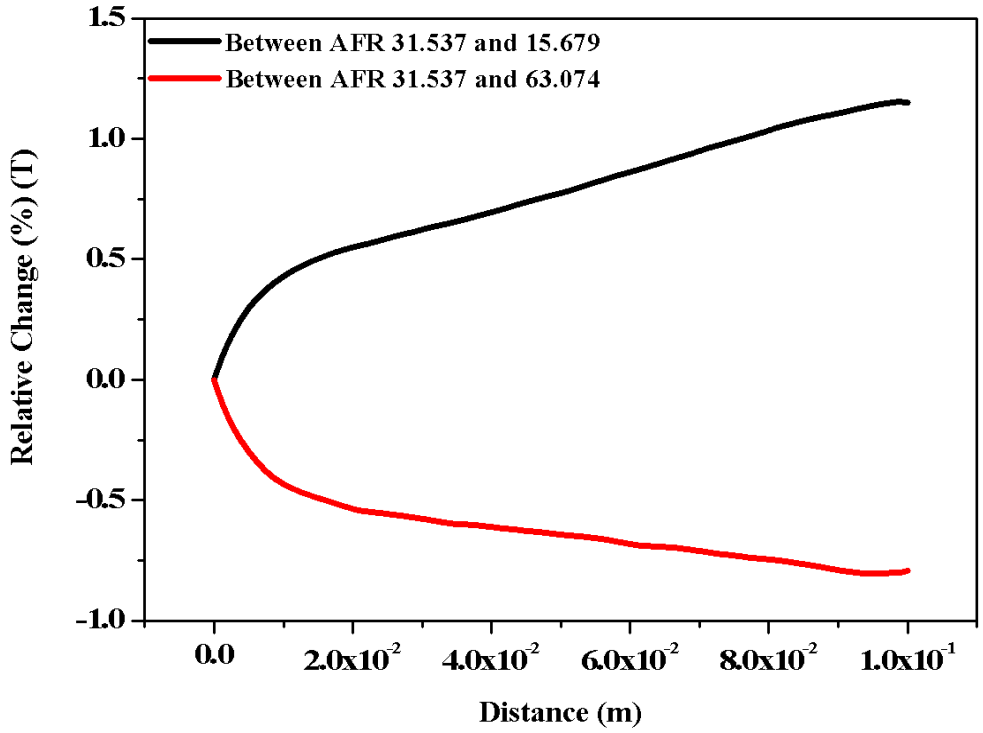

Figure 7.21 Relative change in temperature distribution between different air/fuel ratio cases at section B.

The thermal strain distribution for different AFRs in anode, electrolyte and cathode is shown in Figure 7.22. The thermal strain generation depends on the temperature difference between the cell temperature and strain free temperature which is taken as 20 °C. The maximum thermal strain generation for anode, electrolyte and cathode is identical for all AFRs as the temperature at the inlet is same for all three cases. The thermal strain generation of each component is different because of different thermal expansion coefficient. The thermal strain generation at AFR 15.769, 31.537 and 63.074 in anode close to the cell inlet is 0.0106, 0.0108 and 0.0109, respectively. The thermal strain for electrolyte is 0.0082, 0.0083 and 0.0084 and for cathode is 0.0090, 0.0091 and 0.0092.

The thermal stress distribution profile is opposite to temperature profile because of the high temperature at the cell outlet for AFR 63.074 with reference to 15.769 and 31.537 as shown in Figure 7.23 . The thermal stresses generated at the cell outlet for AFR

15.764, 31.537 and 63.074 are 1760.07 MPa, 1781.03 MPa and 1795.49 MPa, respectively.

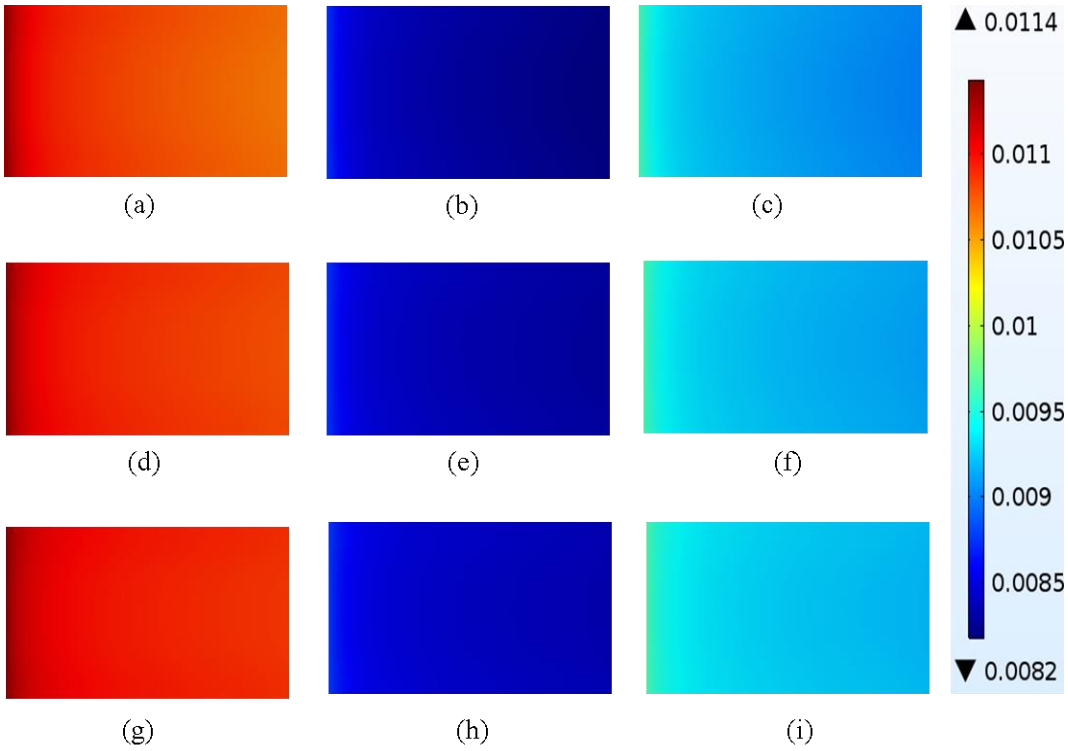

Figure 7.22 Thermal strain distribution at different AFRs at sections A (a) 15.769 (d) 31.537 (g) 63.074, B (b) 15.769 (e) 31.537 (h) 63.074 and C (c) 15.769 (f) 31.537 (i) 63.074.

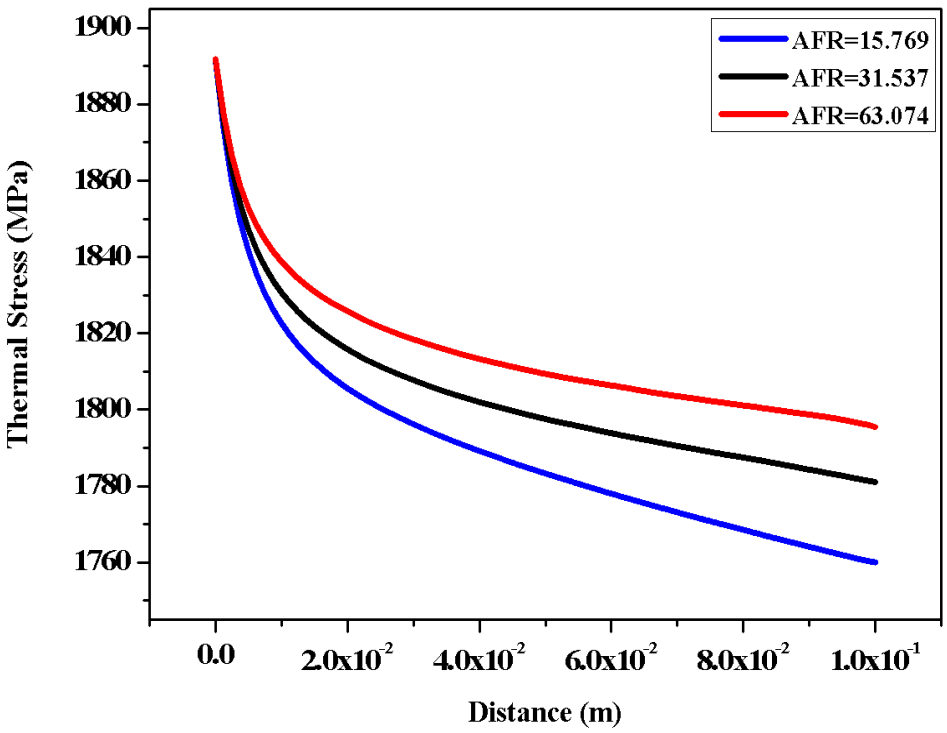

Figure 7.23 Thermal stress distribution from different A/F ratio cases at section B.

The AFR can also be changed by varying the fuel mass flow rate. The increase in the mass flow rate decreases the air fuel ratio and also tends to decrease the fuel utilization. The decrease in the mass flow rate results in higher AFR and also increases the fuel utilization. The increase in fuel utilization may cause the fuel starvation and cold spots that exacerbate the temperature non-uniformities.

7.2.5 Effect of the Cell Thickness on the Cell Performance and Thermal Impact

The ionic conductivity of SOFC strongly depends on temperature and at lower operating temperatures the ionic conductivity decreases and cathode or anode-supported configuration is preferable. In other words the lower ionic conductivity results in higher resistance to the flow of electrons and to recover this thin electrolyte is employed for the cell operation between 500 to 800 °C. The electrolyte is thin with thickness around 10 – 20 µm and the thickness of the electrodes varies between 350 to 1500 µm. The decrease in cell operating temperature also increases the opportunities to employ number of alternative materials for the cell components [49, 217-224].

The base case model is simulated with anode and cathode thickness as 50 µm and electrolyte thickness of 150 µm. The impact of the cell thickness on electrolyte supported SOFC performance is investigated. The analysis is carried out by keeping the anode and cathode thickness unchanged and the electrolyte thickness varies. The V-I curves are shown in Figure 7.24. It has been found that current density increases by varying the electrolyte thickness from 150 to 100 µm and decreases with increase in thickness from 150 to 200 µm.

The relative change is estimated by replacing δ_{ref} with current density generation for base case and $\delta_{operational}$ with change in electrolyte thickness cases. The results are presented in Figure 7.20. The current density for the base case is 3152.18 A/m^2 at 0.7 V which decreases 13.1% by the decrease in thickness, meanwhile the decrease in thickness results 17.5% high current density generation. It is consistent with the fact that less dense electrolyte offers low resistance and allows the more number of electrons to flow. However, the decrease in the thickness of the electrolyte reduces the strength of the cell which increases the possibilities of low life cycle.

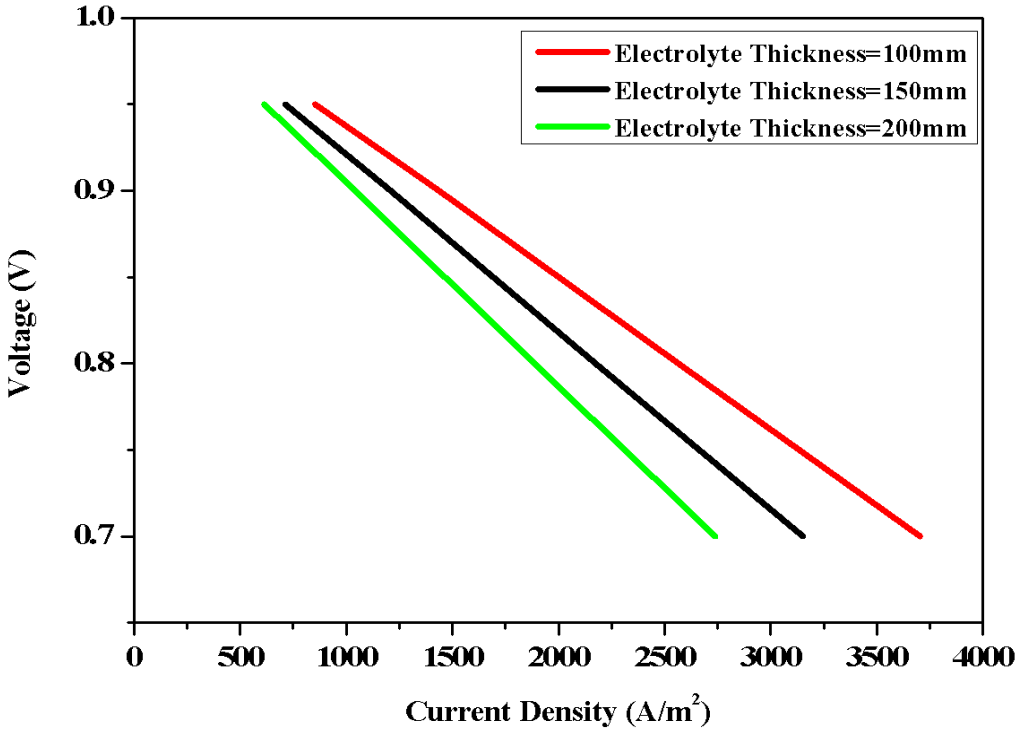

Figure 7.24 V-I Characteristics for different electrolyte thickness cases.

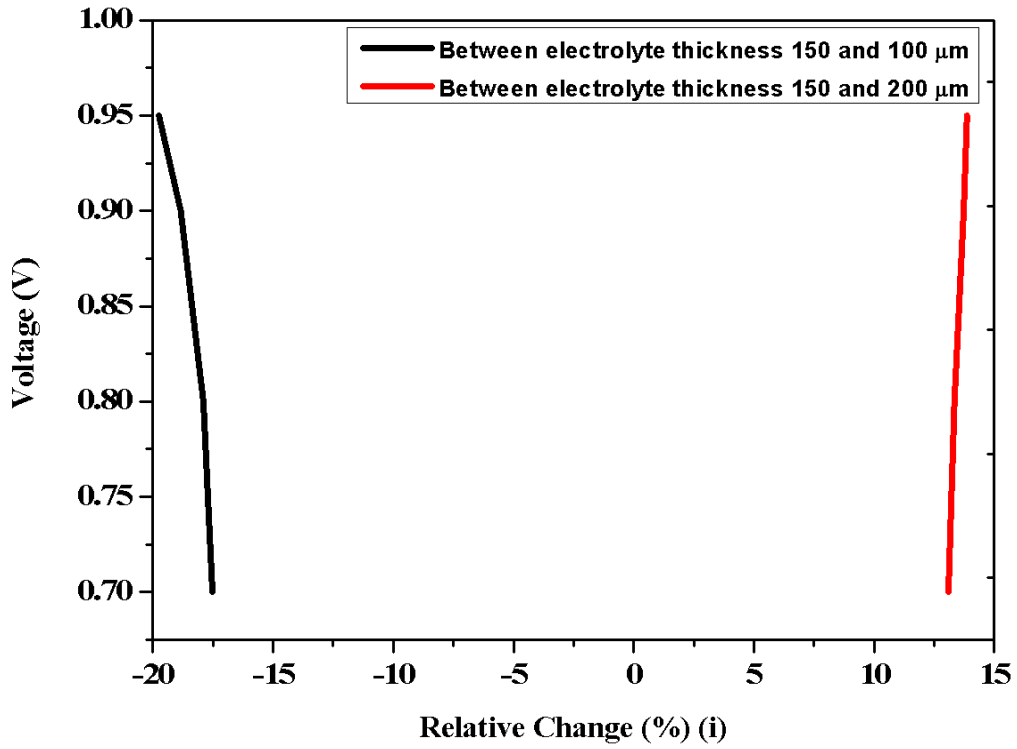

Figure 7.25 Relative change in current density generations at different voltages between different cell thickness cases.

The simulation results from the influence of electrolyte thickness on the temperature distribution, in the centre of the electrolyte, are presented in Figure 7.26. The temperature difference between maximum and minimum temperature of the cell increases while electrolyte thickness varies from 100 to 200 μm. The effect of the electrolyte thickness on the temperature distribution is not significant. The minimum temperatures for 100, 150 and 200 μm cases are 850.56 °C, 848.5 °C and 846.74 °C, respectively. The reason is that the thickness of the electrolyte does not have significant effect on the heat consumption and generation during chemical and electrochemical reactions. The results of the relative change in temperature distribution, which is calculated by using equation 7.1, are illustrated in Figure 7.27. The maximum relative change near cell outlet due to increase in thickness is 0.196 % and because of decrease in thickness is -0.26 %.

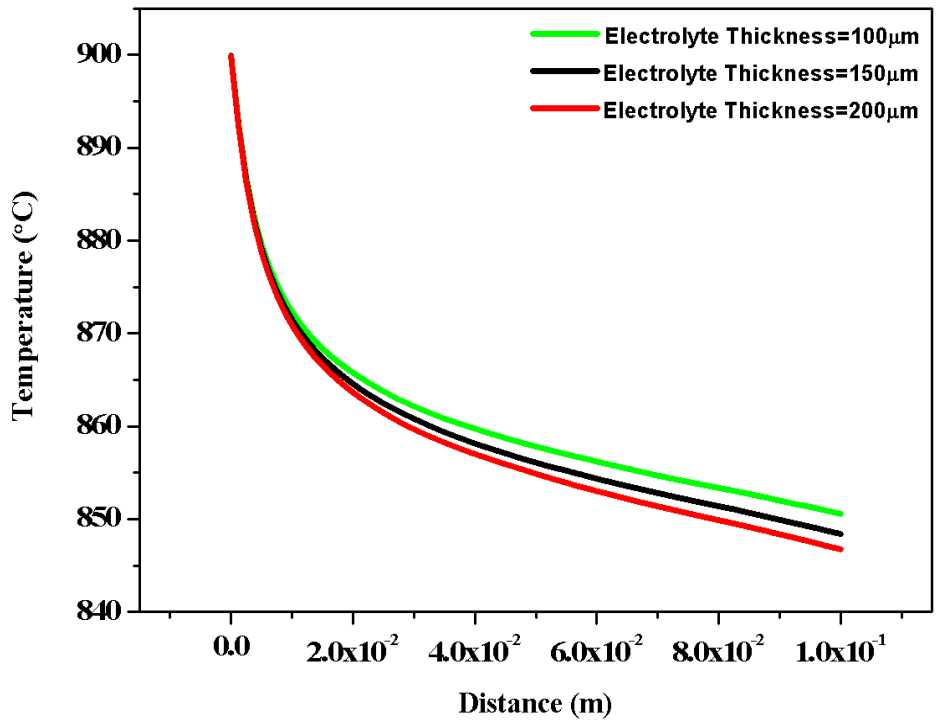

Figure 7.26 Temperature distribution from different electrolyte thickness cases at section B.

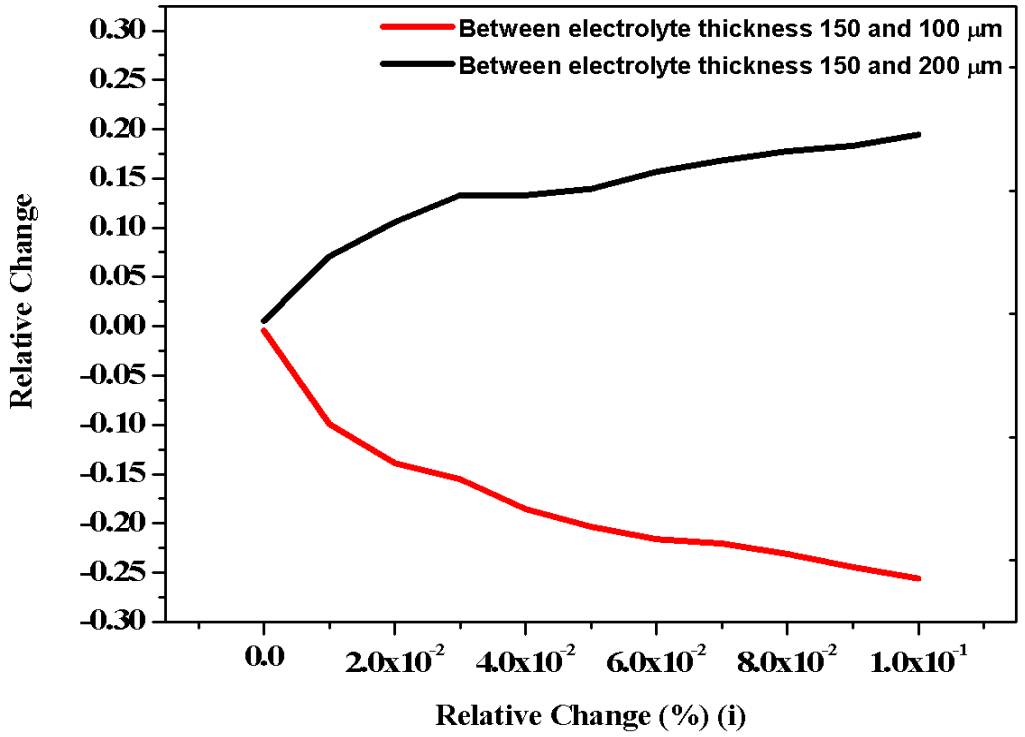

Figure 7.27 Relative change in temperature distribution between different cell thickness cases at section B**.**

The thermal strain distribution is same for all components and has same values for different electrolyte thicknesses, as can be seen from Figure 7.28. The thermal stress generation depends on thermal strain distribution and Mechanical properties of the different cell components. The thermal stress of the electrolyte is higher and distribution along the cell length is shown in Figure 7.29. The thermal stress at 100 μm electrolyte thickness is slightly higher than 200 μm electrolyte thickness. The minimum temperature at 100 μm electrolyte thickness is higher than 150 and 200 μm which results in greater thermal stress generation. The thermal stresses close to the cell outlet are 1785.70 MPa, 1781.03 MPa and 1777.49 MPa for 100, 150 and 200 μm cases, respectively.

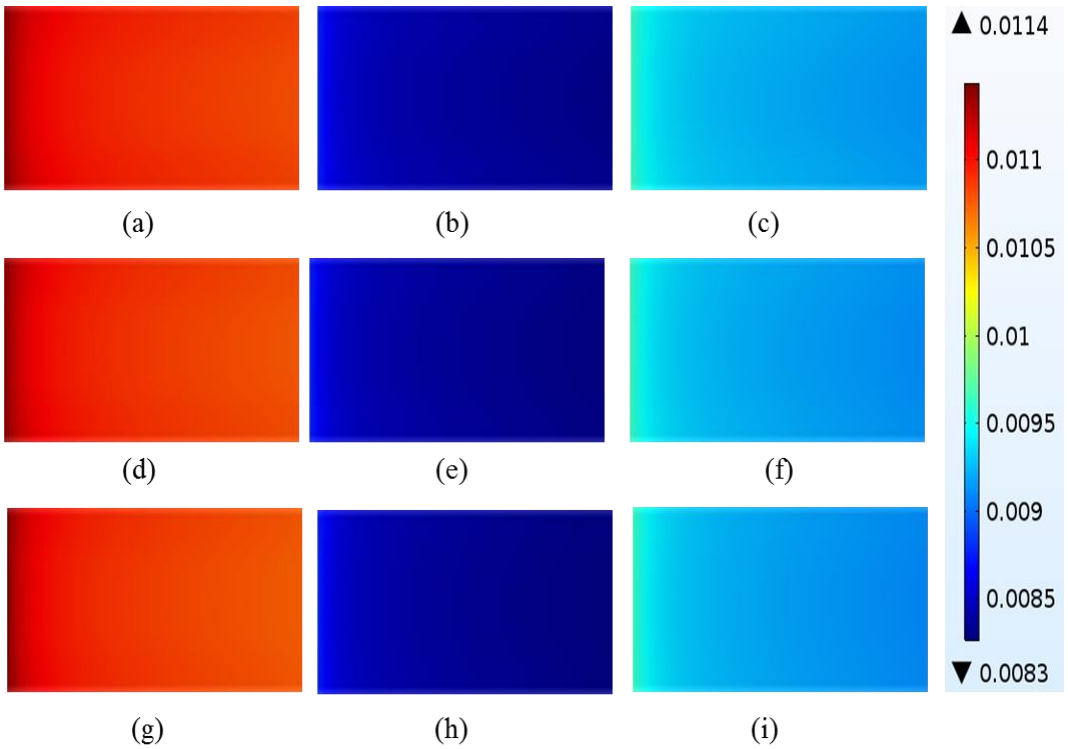

Figure 7.28 Thermal strain distribution at different electrolyte thickness cases (from top first, second and third row at 100E-6m, 150E-6 m and 200E-6 m, respectively) at sections A (a), B (b) and C (c).

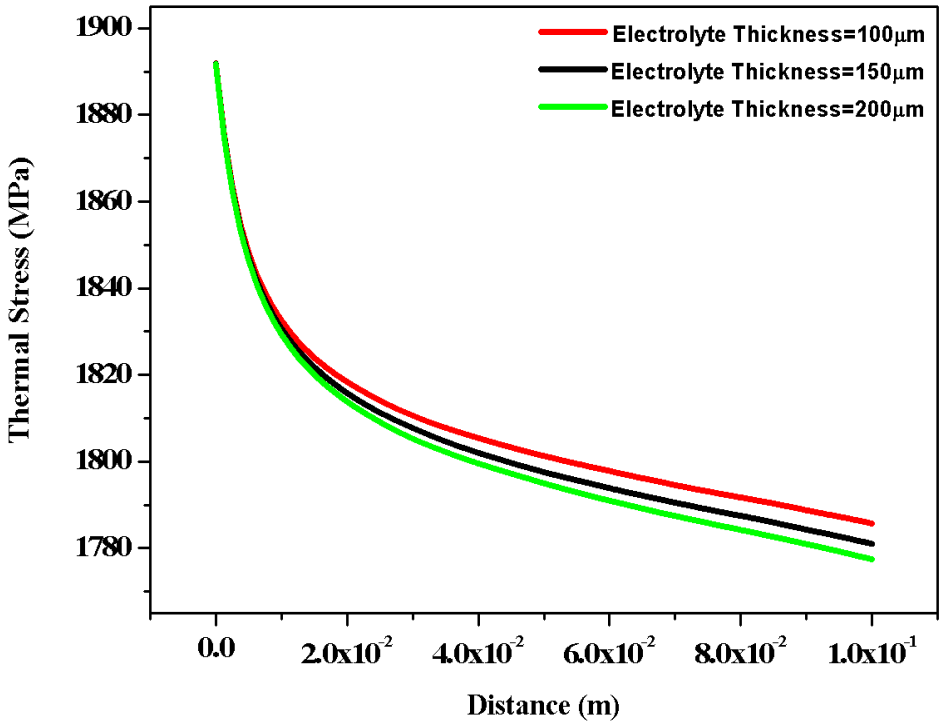

Figure 7.29 Thermal stress distribution from different electrolyte thickness cases at section B.

7.2.6 Effects of the Operating Voltage on the Cell Performance

One of the advantages of the developed model is load flexibility. The cell can operate at different voltage depending on the power needed. The current density generation at different cell voltage is shown in Figure 7.30. The current density and voltage are inversely proportional. The current density at 0.7 V is 3152.18 A/m^2 and reaches to 6422 A/m^2 at 0.4 V. The increase in current density is 103.73%. The fuel utilization depends on the cell operating voltage and further decrease in the voltage leads towards the fuel starvation, as shown in Figure 7.31. The methane mole fractions at cell outlet for 0.7 and 0.4 V are 0.04276 and 5.81E-5, respectively. The 75% of methane is utilized at 0.7 V and 99.97% at 0.4 V.

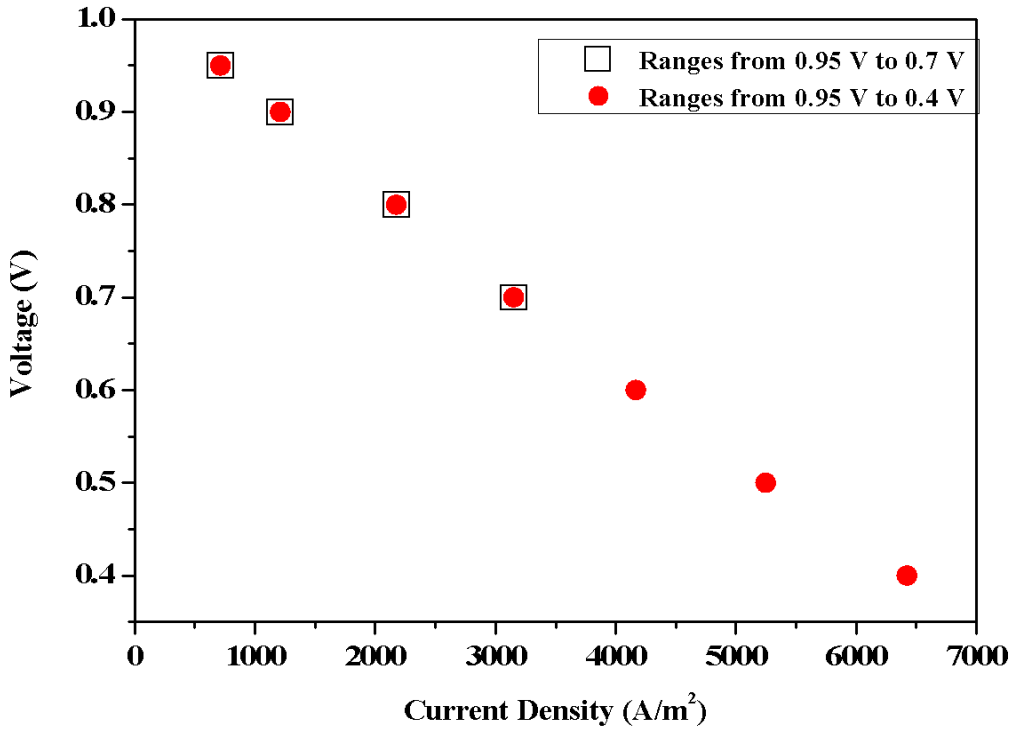

Figure 7.30 V-I Characteristics at different operating voltages.

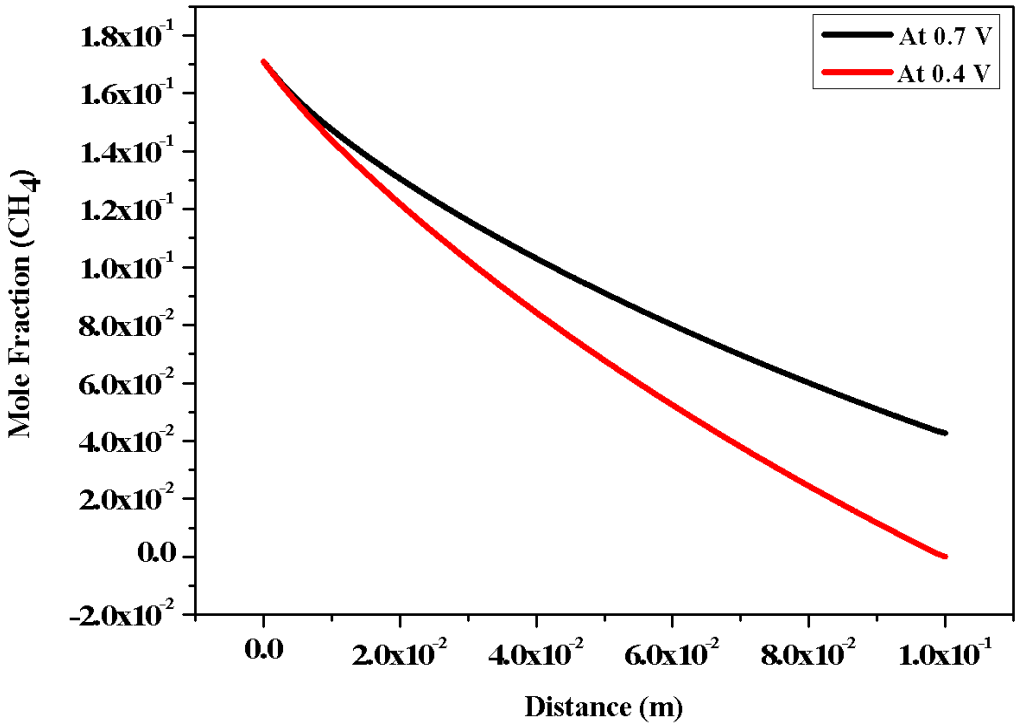

Figure 7.31 Methane mole fraction distribution from different operating voltages at section D.

The temperature at different cell operating voltage is predicted and the distribution in the centre of the electrolyte is shown in Figure 7.32 . The minimum cell temperature at 0.7 V is 848.4 °C and 871.5°C is observed at 0.4 V. The temperature difference between maximum and minimum cell temperature at 0.7 and 0.4 V is 51.6 and 28.5 °C, respectively. The decrease in temperature difference supports the fact that at lower voltage the current density is higher which results in more heat generation during the electrochemical reaction.

The thermal strain distribution in the centre of anode, electrolyte and cathode along the cell length and width is presented in Figure 7.33. The thermal strain generation at 0.4 V is slightly higher, near the cell inlet for all three components, in comparison of 0.7 V case. The maximum thermal strain 0.0115 is observed in anode follow by 0.00971 in cathode and 0.0082 in electrolyte. The effect of the cell operational voltage on thermal strain distribution is estimated by calculating the relative change. The equation 7.1 is used where δ_{ref} changes with the thermal strain generation for voltages range from 0.95 to 0.7 V and $\delta_{operational}$ with the thermal strain generation from 0.95 to 0.4 V. The

relative change is same for all the components, as can be seen in Figure 7.33. The relative change is maximum -2.79 % near the cell outlet.

The electrolyte thermal stresses from both voltage cases are predicted at the same spatial location and the distributions are shown in Figure 7.35. The thermal stresses at 0.7 and 0.4 V are 1781.04 MPa and 1830.67, respectively. The 2.8% increase in thermal stress generation is observed by varying the cell voltage. The reason for increase in thermal stress is high temperature at 0.4 V.

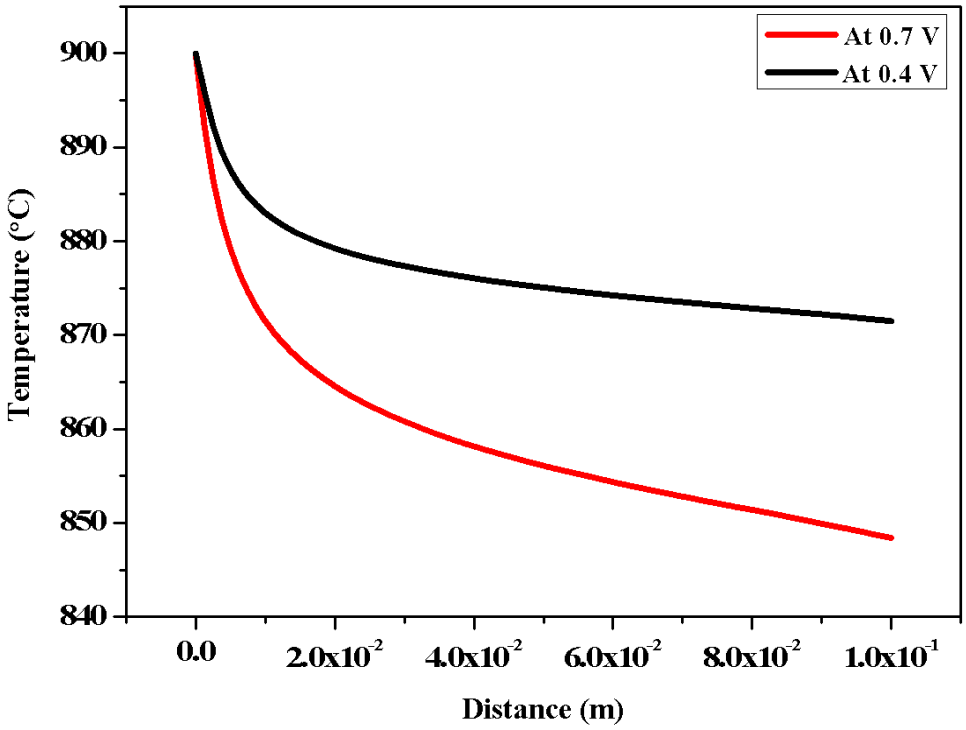

Figure 7.32 Temperature distribution from different operating voltages at section B.

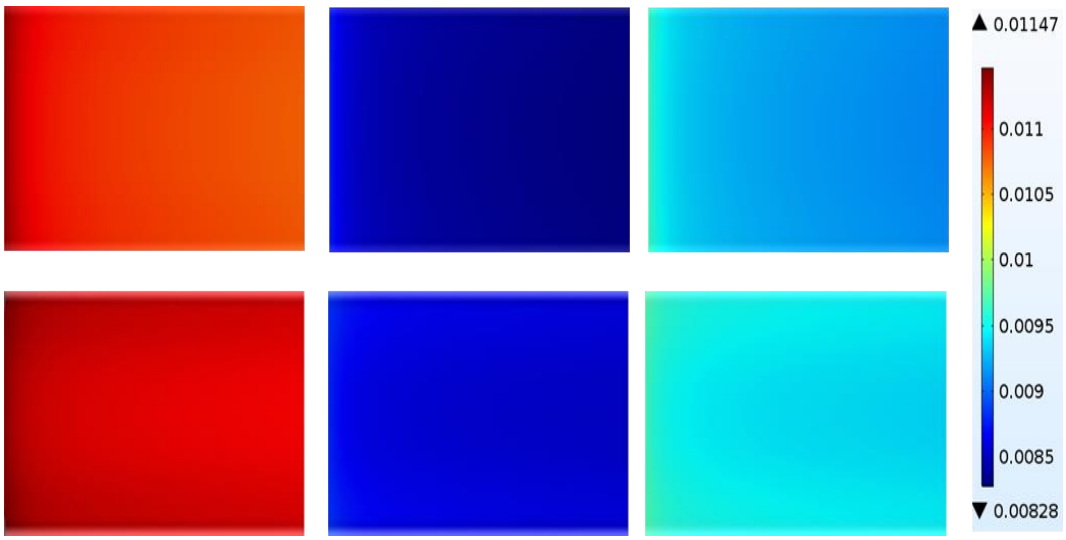

(a) (b) (c)

Figure 7.33 Thermal strain distribution for 0.7 V (top) and at 0.4 V (bottom) at sections A (a), B (b) and C (c).

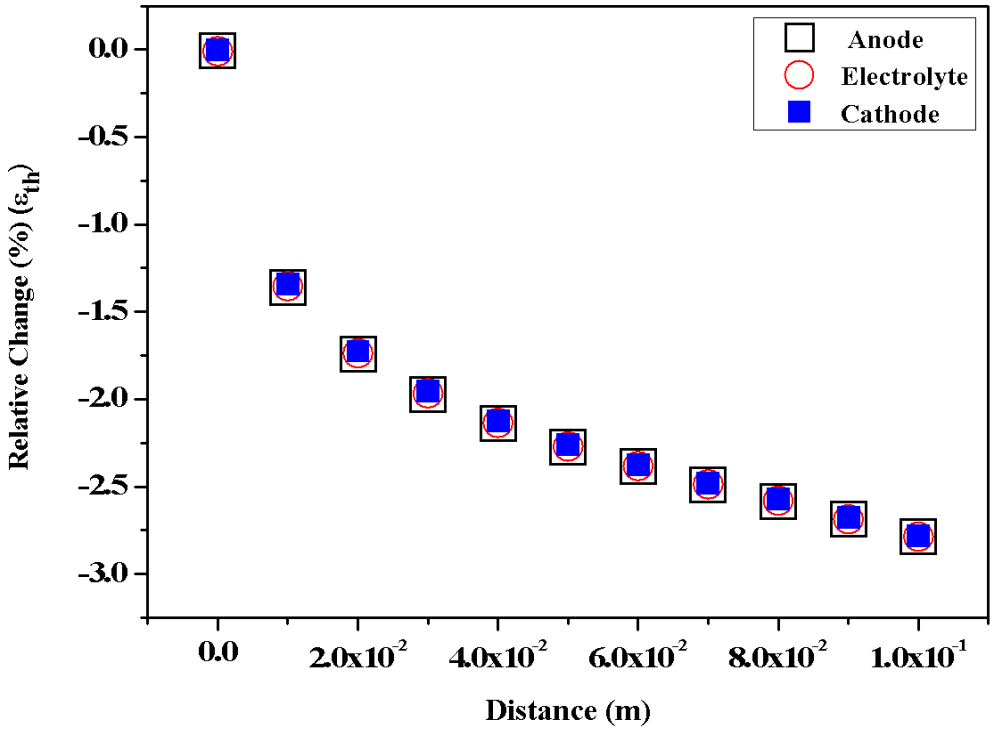

Figure 7.34 Relative change in thermal strain generations between 0.7 V and 0.4 V cases at sections A, B and C.

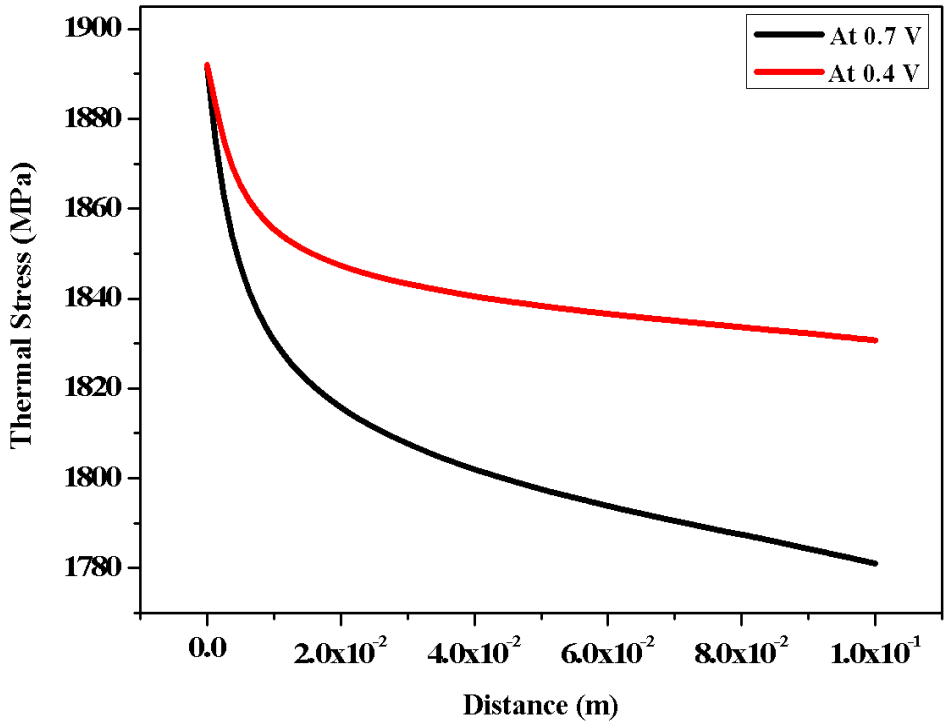

Figure 7.35 Thermal stress distribution from different operating voltages at section B.

7.3 Summary

The impact of the parameters such as cell operating temperature, material properties (porosity), flow configurations, AFR, cell geometrical parameters (electrolyte thickness) and operating voltage on the SOFC performance and thermal impact have been investigated. It has been identified that the cell electrochemical performance is most affected by the operating voltage follow by the temperature, material properties (porosity), cell thickness, and AFR. Regarding thermal impact the temperature has more effect on thermal strain and stress generations follow by the operating voltage, AFR, cell thickness and porosity. The flow configurations does not have much effect on the performance and thermal impact, however co-flow configuration offers more uniform current density, temperature and thermal stress distributions. The higher AFR generates more current, the difference between maximum and minimum cell temperature is low, whereas generates larger thermal stresses. It has been recognized that thin electrolyte results in higher current density and the effect on the temperature and thermal strain and stress distribution is not significant. The current density is directly linked with the cell operating voltage and lower voltage generates more current, greater fuel utilization, less

temperature difference between cell inlet and outlet and higher thermal strain and stress generation.

Chapter 8 – SOFC Stack Modeling

In practical applications a single cell is rarely used, instead, a fuel cell stack is constructed by connecting the cells either in electrical series or parallel or both. This chapter gives description about the SOFC stack model and provides the simulation results for the electrochemical performance, the species, reaction rates, temperature and thermal strain and stress distributions of the various cells.

8.1 Introduction

As explained in Chapter 3, the thermal strains and stresses are generated in SOFC due to high temperature operation. The thermal strains and stresses generated in methane fuel SOFC are less than hydrogen because of the heat consumption during MSR reaction. A single planar SOFC model running on methane fuel is upgraded to stack level. In order to draw useful amount of current the cells are connected in series [59, 112, 217, 225-227]. The connection of the cells in series or parallel is known as fuel cell stack. The 8 cells are connected in parallel flow configuration in such a way that air flow channel of one cell is linked to the fuel flow channel of the next cell and so on, as shown in Figure 8.1.The two cells are connected with each other by interconnect. The interconnect separates the two cells and also acts as a physical barrier and avoid the harmful mixing of the gases (e.g. hydrogen and oxygen). It is also worth mentioning here that interconnect also has a structural role to keep the solid and transportable stack. The Lanthanum Chromite ($La_{1-x}SrCrO_3$) is used as a material for interconnect. The thickness of interconnect is selected as 300 E-6 m.

The mechanical and electrochemical properties of Lanthanum Chromite are taken from the literature [225, 228-230] and listed in Table 8.1

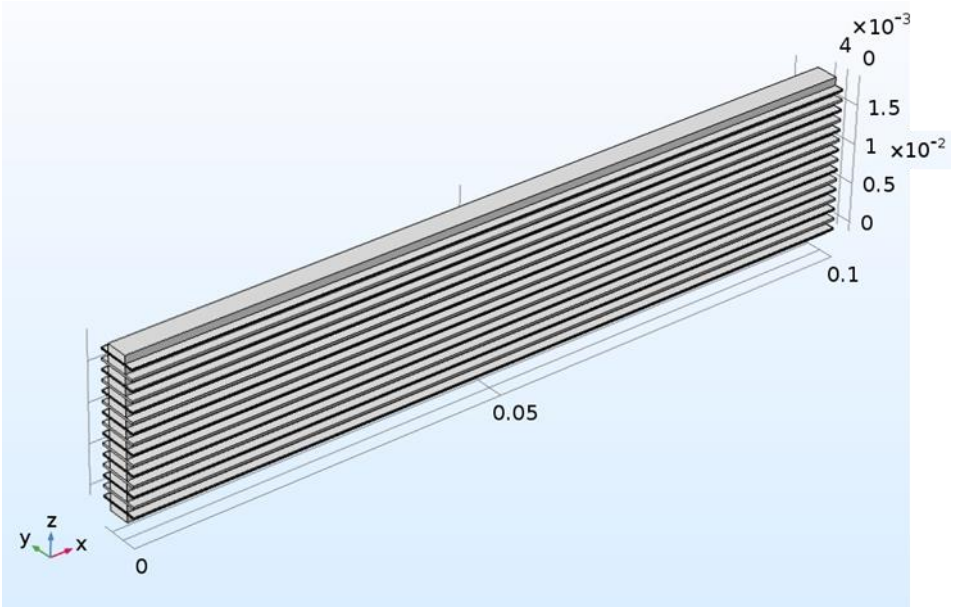

Figure 8.1 Stack of Planar SOFC consists of 8 cells. The cell length, width and height is in m.

Table 8.1 Properties of Lanthanum Chromite

Parameter	**Value**
Density ρ (kg/m3)	4640
Heat Capacity Cp (J kg-1K-1)	300
Thermal Conductivity k (W m-1 K-1)	2.2
Modulus of Elasticity E (GPa)	209
Poisson's ratio υ	0.30
Thermal expansion coefficient α (K-1)	9.4E-6
Conductivity (S/m)	100

8.2 Results and Discussion

8.2.1 Electrochemical Performance

The electrochemical performance of each cell in terms of V-I curves are shown in Figure 8.2. The current density generation at various voltages is identical for the middle

cells (from 2nd to 7th) such as 3290 A/m^2 at 0.7 V. The current densities for bottom (1st) and top (8th) cells are 3120.69 and 3326.86 A/m^2, respectively. The difference in the current density between different cells depends on the thickness and the materials use for interconnects.

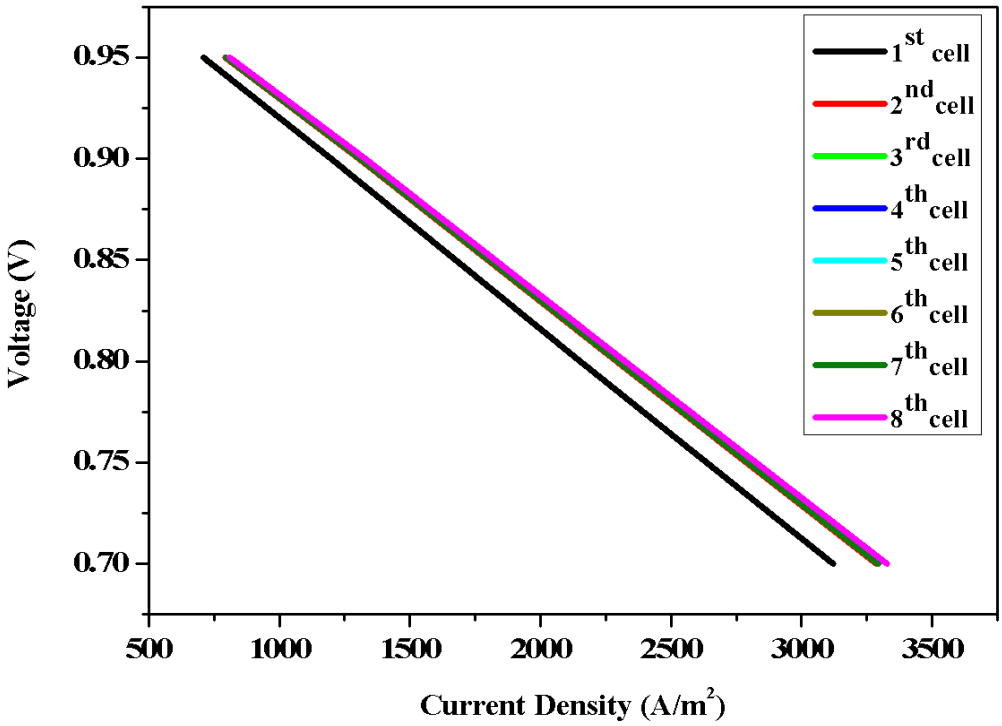

Figure 8.2 V-I Characteristics of different cells.

8.2.2 Species Distribution

The methane and hydrogen mole fractions distributions are estimated in the center of the fuel channels along the cell length and the profiles are shown in Figure 8.3. The methane mole fraction decreases along the flow direction because of the consumption during MSR reaction, meanwhile the hydrogen mole fractions increase due to formation during MSR and WGS reactions. The consumption of the methane varies from 72.5 % for bottom cell to 92.6 % for top cell. The higher consumption of methane results in higher production of the Hydrogen. The hydrogen production varies from 65.87 % to 88.5 % for bottom and top cells, respectively.

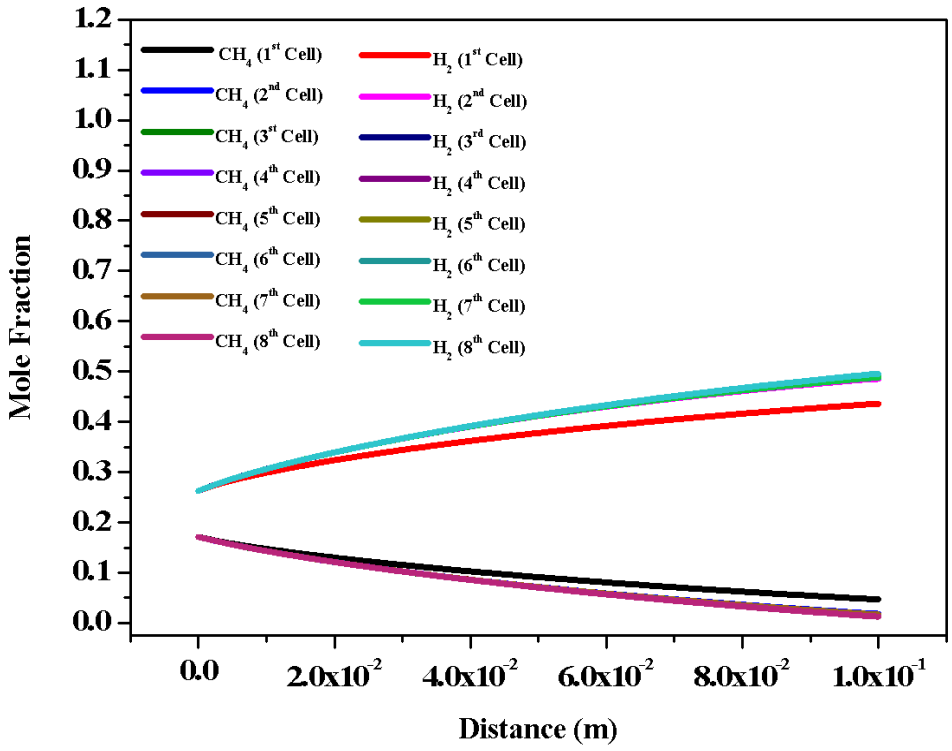

Figure 8.3 Methane and hydrogen mole fraction distributions for different cells at section D.

8.2.3 Reaction Rate

The consumption of Methane depends on MSR reaction rate. The reaction rates are strong function of the cell temperature. The distribution of the MSR reaction at the same spatial position as that for species is shown in Figure 8.4. Like current density the reaction rate for bottom and top cells is different from middle cells. The reaction rate is higher at the cell inlet because of the higher temperature at this location. The maximum MSR reaction rate for all the cells is identical because of the same temperature at the inlet. The minimum MSR reaction rates at outlet for bottom and top cells are 28.7mol/m^{3}s and 41.32mol/m^{3}s, respectively.

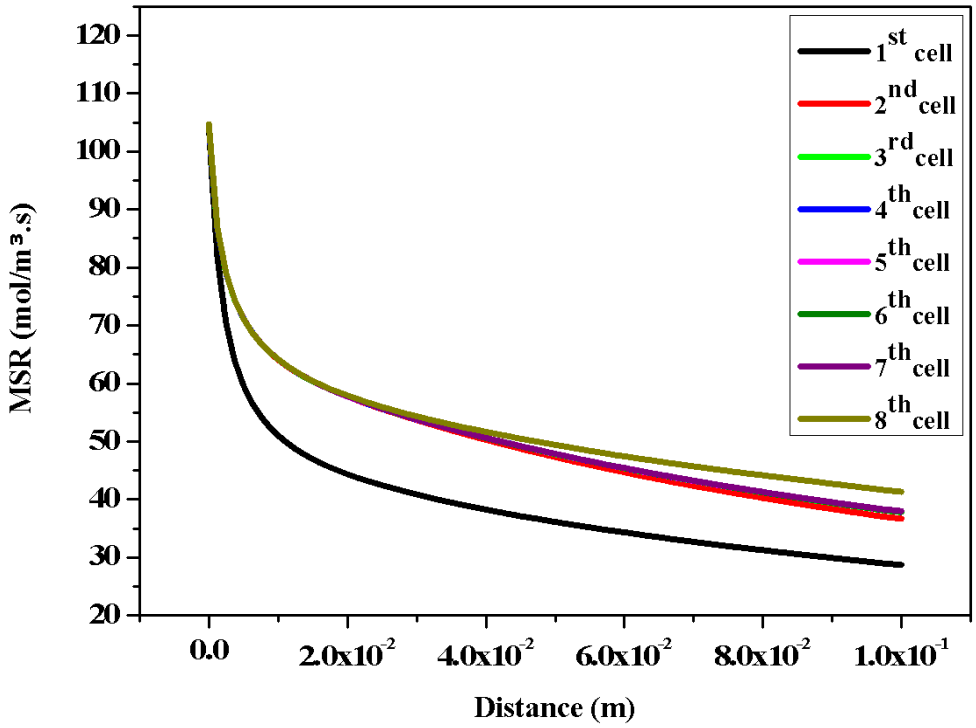

Figure 8.4 MSR reaction rate distribution for different cells at section D.

8.2.4 Temperature distribution

The temperature is predicted in the centre of the electrolyte along the cell length and distribution for various cells is shown in Figure 8.5. The temperature is highest at the inlet and decrease along the cell length due to the heat absorbed by MSR reaction. The temperature at the inlet is same for all the cells but the temperature at the outlet is different. The difference in the temperature at outlet between different cells depend on the conductivity of the material use for interconnect. The minimum temperature at outlet for bottom and top cells are 844.09 and 860.32 C, respectively. The temperature for rest of the cells is almost identical and in the range of 854 °C to 855 °C. The maximum temperature difference 55.91 °C between inlet and outlet temperature is for the bottom cell.

The temperature distribution is predicted in the centre of the cells along the stack height at three different locations. The distribution is not uniform along the cell height, as can be seen from Figure 8.6. The temperature is lower in the fuel channels of the cells, at all locations, because of the heat consumption during MSR reaction while the temperature in the air channels is higher. The minimum temperature 837.84 °C is located, close to

the cell outlet, in the fuel channel of the bottom cell. The difference between maximum and minimum stack temperature along the height, close to the cell inlet, in the centre and close to the outlet is 11.71 °C, 50.75 °C and 49.9 °C, respectively.

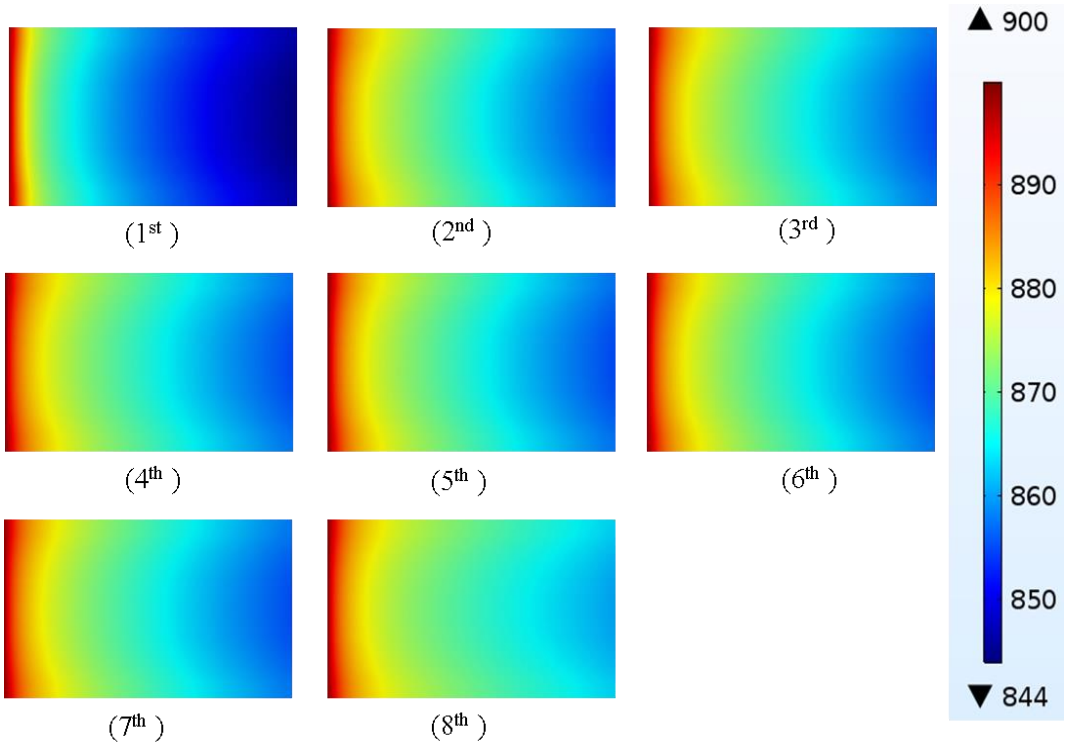

Figure 8.5 Temperature distribution for different cells at section B.

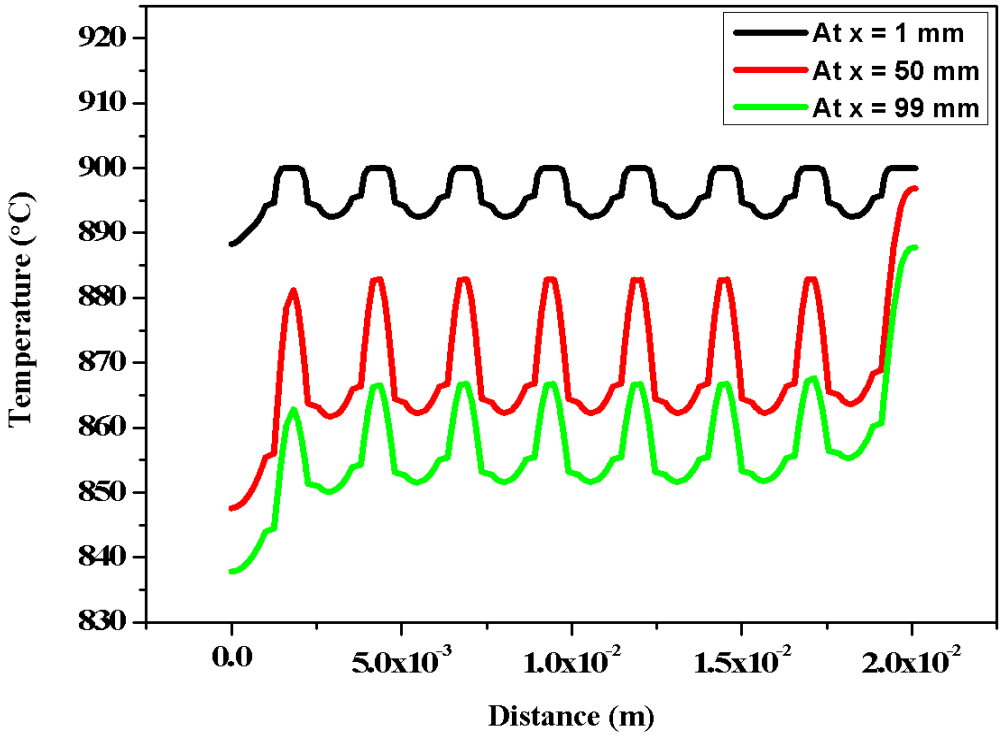

Figure 8.6 Temperature distribution in the centre of the 8 cells at section Es.

8.2.5 Thermal strain and stress distribution

The thermal strain generation depends on the cell temperature and thermal expansion coefficients. The largest thermal expansion coefficient results in high thermal strain such as in anode which increases the probability of the cell failure. The thermal strain distribution in the centre of the anode for all cells is displayed in Figure 8.7. The thermal strain distribution profile is same as that of temperature. The maximum thermal strain 0.0114 is same for all the cells because of same inlet temperature 900 °C. The minimum thermal strains for bottom and top cells are 0.0107 and 0.0109, respectively. The minimum thermal strain for the middle cells is 0.0108.

The thermal strain distribution along the stack thickness is predicted at section E. The profile is similar as that of temperature (refer to Figure 8.6). It is evident from the Figure 8.8 that the thermal strain generation in anode for all the cells at all positions is higher than those of electrolyte, cathode and interconnect. The maximum thermal strain for all the components located near the cell inlet due to larger temperature difference at this location. The difference in thermal strain generation between different cells is not

significant. The maximum thermal strains generated, for all cells, in anode, electrolyte, cathode and interconnect are 0.0114, 0.0088, 0.0096 and 0.0082, respectively.

The thermal stress generation in the electrolyte is higher because of the greater Modulus of Elasticity (215 GPa) as compared to anode and cathode. The electrolyte thermal stress distribution for all cells at same spatial position as that for temperature is shown in Figure 8.9. The minimum thermal stress is generated for the bottom cell because of the less temperature difference between the cell local temperature and strain free reference temperature at this position. The minimum thermal stresses those are generated at the cell outlet for the bottom and top cells are 1689.38 and 1722.67 MPa, respectively. The difference in thermal stresses between different cells is because of the different temperatures at the cell outlet. The modulus of elasticity for the $LaCrO_3$ interconnect is less than YSZ but higher than anode and cathode. Therefore thermal stresses generated in interconnect are higher than anode and cathode.

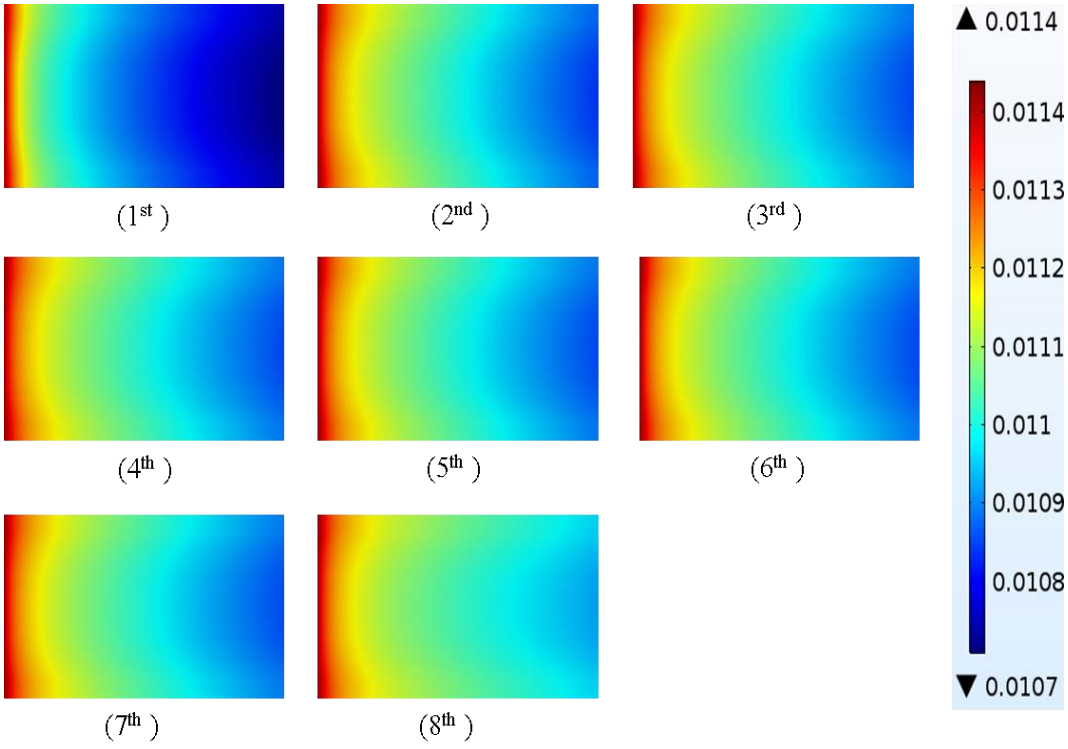

Figure 8.7 Thermal strain distribution at section A.

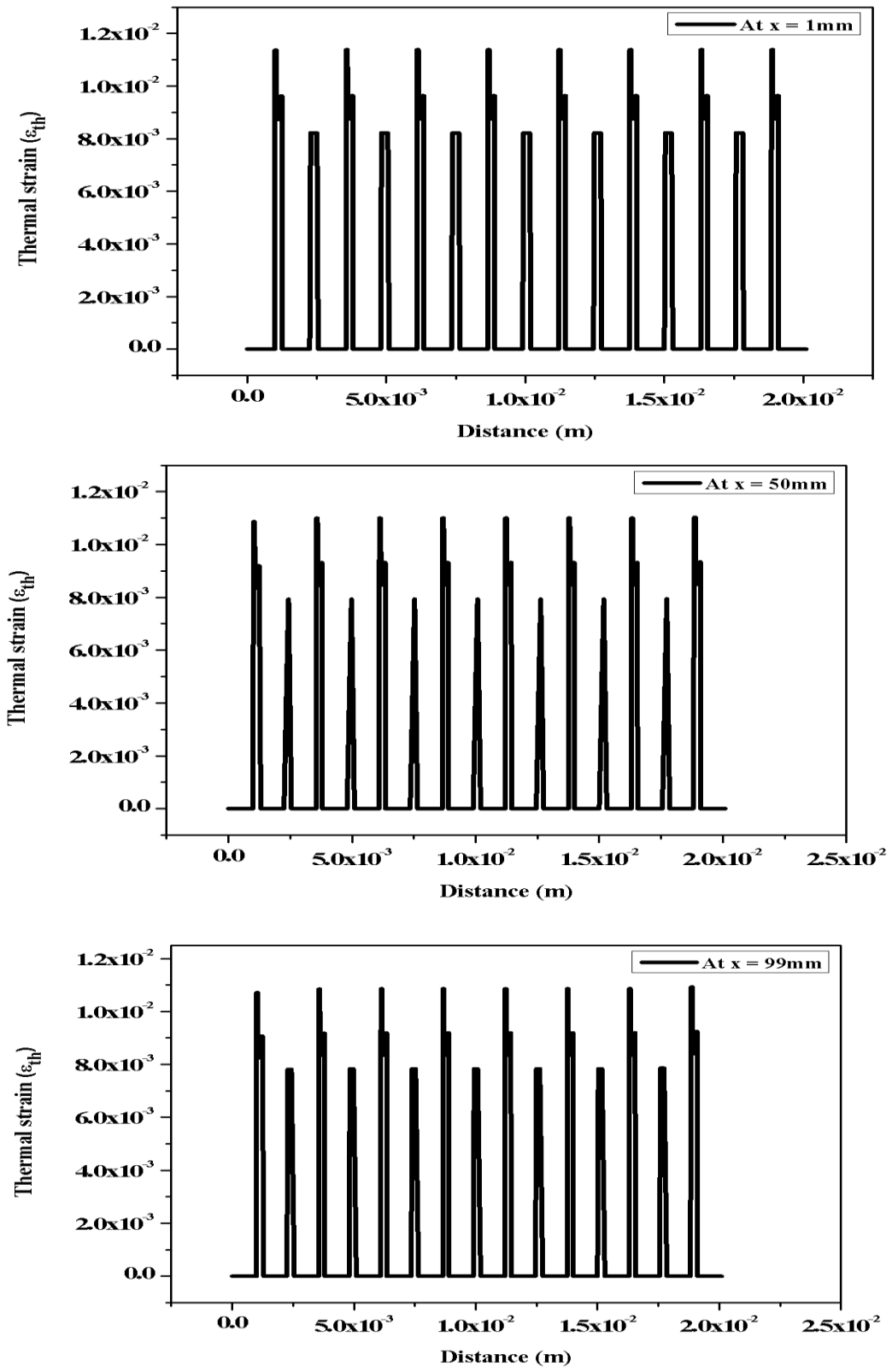

Figure 8.8 Thermal strain distribution at section Es.

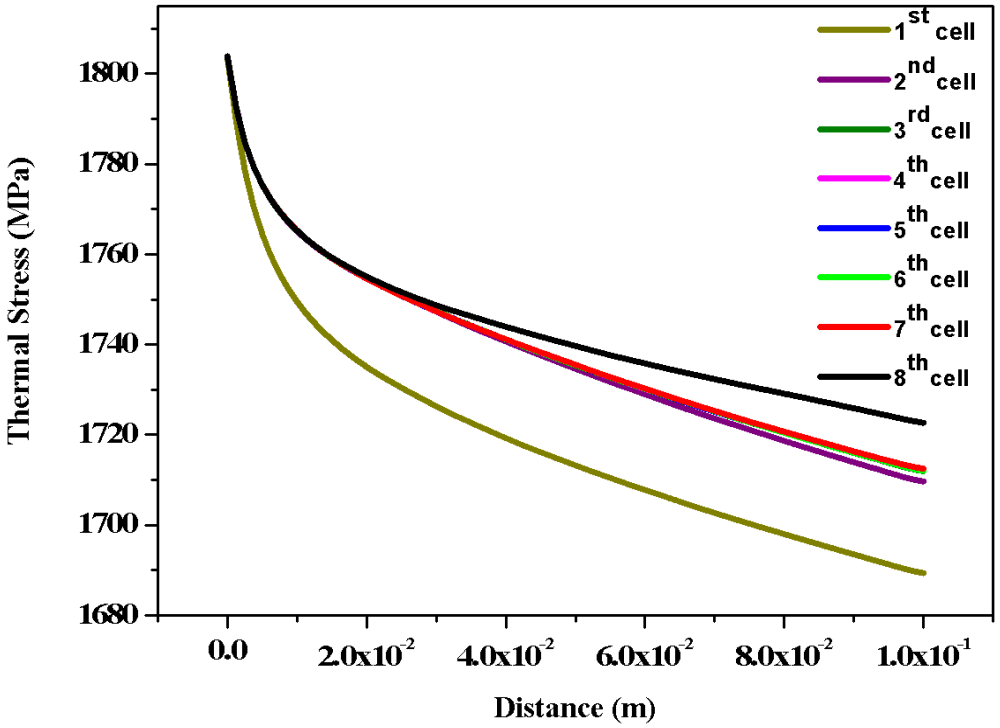

Figure 8.9 Thermal stress distribution for various cells at section B.

8.3 Summary

In this chapter the performance and thermal impact of methane fuel planar SOFC stack has been analyzed. The electrochemical performance, species, reaction rates, temperature, thermal strain and stress distributions for each cell are discussed. It has been identified that the performance of the top and bottom cells are different from the middle cells because of interconnect. The temperature and thermal strain distributions are non-uniform along the stack height. The difference in the temperature and thermal stress generation depends on the properties of the material use for interconnect. Therefore materials for interconnect plays an important role in the structural and thermal stability of the cell.

Chapter 9 – Conclusions and Future Work Suggestions

The overall aim of this thesis is to develop a numerical model by coupling dynamics of electrochemical reacting flows, heat transfer, and thermal impacts (thermal strains and stresses) of solid electrolyte and porous electrodes for analysing the SOFC performance. Due to high operating temperature, thermal strains and stresses are generated in SOFC which can cause cell failure. In this context, the areas with larger thermal strains and stresses are identified to improve the cell performance.
The main conclusions of this research are outlined below, followed by suggestions for future work.

9.1 Conclusions

A 3D numerical model of a single Planar SOFC running on Hydrogen has been developed to investigate the electrochemical performance and thermal impact. Heat generated during exothermic electrochemical reactions made the cell temperature higher than operating temperature. The material properties, thermal strain and stress generation depend on the temperature. In this regard, temperature distribution is essential for better understanding of cell performance and design optimization. This model is based on thermal properties of materials (fluids and PENs) and electrochemical and chemical reactions those were estimated by the cell local temperature. The results from the numerical modeling well matched with the standard data of IEA [50]. Effects of cell operating temperature and material properties on cell electrochemical performance and thermal impact have been investigated. The high thermal expansion coefficient of anode materials causes the largest thermal strain in the cell. The modulus of elasticity of the electrolyte is greater than anode and cathode and thermal stress for the electrolyte is the largest.

The thermal strains, thermal and mechanical stresses generated in the cell are calculated at different operating temperatures, boundary restrictions and various operating voltages. The higher operating temperature resulted in higher cell temperature that could lead to larger thermal strain and stress generation. It has been found that the mechanical stress generations depend on the way the cell is fixed.

The SOFCs are high temperature fuel cells which enable the internal steam reforming of the hydrocarbon fuels. The model developed is tested for different fuels such as methane. The MSR and WGS reactions have been modelled. The heat source / sink

terms related to electrochemical, MSR and WGS reactions are calculated and their contribution towards overall cell energy balance is analyzed. It has been observed that heat absorbed during MSR reaction is more than the heat generated during electrochemical and WGS reactions that ultimately lowers the cell temperature. This drop in the cell temperature reduces the thermal strain and stress generation. Therefore, the methane fueled SOFC has smaller thermal strains and stresses than Hydrogen fueled SOFC.

Furthermore, the performance and thermal impact of methane fueled SOFC is analyzed by considering the effects of cell operating temperature, material properties (porosity), flow configurations, AFR, cell thickness and cell operating voltage. It has been found that cell performance is very sensitive to the operating voltage follow by the temperature, material properties (porosity), cell thickness and AFR. Regarding thermal impact temperature has more effect on thermal strain and stress generations follow by the operating voltage, AFR, cell thickness and porosity. The smaller porosity is found to be favorable for higher current density as more area would be available for electrochemical reaction. The lower porosity also restricted the flow which results in larger mole fraction gradient between the channels and the reaction sites. A porosity of 0.4 is suitable for SOFC operation. The temperature differences are created by the heat produced and consumed during chemical and electrochemical reactions at different locations. The flow configurations affect the temperature gradients. To minimize the generated thermal stresses, and size of the temperature gradient/differences, the flow should be made smoother (uniform temperature distribution).

The co-flow configuration offers better thermo-mechanical stability because of uniform distribution of the temperature and thermal stresses. The higher AFR results in higher current density and lower temperature difference between the cell inlet and outlet temperature. The temperature at cell outlet for higher AFR is larger than smaller AFR and causes the greater thermal strain and stress generation. The AFR 31.537 is safe for methane fueled SOFCs. The thinner electrolyte offers less resistance to the ions flow and generates more current density but reduces the mechanical stability of the cell. The fuel utilization depends on the cell voltage as lower cell voltage results in higher fuel utilization which may cause the fuel starvation during the cell operation.

Finally, the model is upgraded to stack level and the performance of the individual cell is predicted. It has been found that the current density, species mole fractions,

temperature, rates of reactions, thermal strains and stresses distributions are different for the top and bottom cells, meanwhile identical for the middle cells. The temperature distribution along the stack height is non-uniform resulting in uneven thermal strain and stress distribution. It has been recognized that interconnect plays an important role in the cell thermal and structural stability.

9.2 Future Work Suggestions

The developed 3D numerical model of SOFC is fuel flexible and greatest advancement. The model helps in predicting the location where failure may occur during the cell operation. It also helps in selecting suitable materials for various cell components which are required for better cell performance and structural stability. The future work should be aimed at extending the investigations carried out during this research in the following directions;

- The model could be tested by employing different fuels such as methanol and ammonia. The hydrogen from renewable sources such as wind and solar can be used in SOFC. The use of hydrogen in SOFC produced from renewable resources ultimately reduces the environmental impact.

- The anode-supported SOFCs are suitable for intermediate temperature cell operation. The different materials for various cell components could be tested for improved performance. The Stainless Steel could be an alternative material for interconnect of intermediate temperature SOFCs.

- The experimental and mathematical relations could be developed to find the effective material properties at the interface of the different cell components.

- The CO produced from the gasification of the biofuels could be used in SOFCs. Normally hydrogen participates in the electrochemical reaction and CO reacts with steam which generates the hydrogen. The electrochemical parameters for CO reduction reaction should be found experimentally so that it can participate in the electrochemical reaction and generates more current.

- In Stack model the exhaust fuel of one cell could be recycled to the inlet of the neighbouring cell and so on. The exhaust from the stack could be used in gas turbine for cogeneration.

Appendix A – Fuller Diffusion Volume Coefficients [231]

Component	H_2	H_2O	O_2	N_2	CH_4	CO	CO_2
Volume Coefficients	7.07	12.7	16.6	17.9	25.14	18.9	26.9

Appendix B – Thermal and Mechanical Properties [165]

Description	Anode	Electrolyte	Cathode
Thermal expansion coefficient α (K^{-1})	13 E-6	10 E-6	11 E-6
Modulus of Elasticity E (GPa)	55	215	35
Poisson's ratio υ	0.17	0.32	0.25

Appendix C – Nomenclatures and Abbreviations

A	Ampere
a	Anode
act	Activation
AFC	Alkaline Fuel Cell
Al_2O_3	Aluminium Oxide
A_v	Active Surface Area
C	Coulomb
c	Cathode
c	Molar Concentration
CaO	Calcium Oxide
CC	Combined Cycle
CCS	Carbon Capture and Storage
CFCL	Ceramic Fuel Cell Limited
CFD	Computational Fluid Dynamics
CH_4	Methane
CHP	Combined Heat and Power
CH_3OH	Methanol
CO	Carbon Monoxide
CO_2	Carbon Dioxide
CO_3	Carbon Trioxide

ch	Channel	
cm	Centimetre	10^{-2} m
CTE	Coefficient of Thermal Expansion	
DMFC	Direct Methanol Fuel Cell	
D_{ij}	Multicomponent Maxwell Stefan Diffusion Coefficient	
D^{m}	Molecular Diffusion Coefficient	
D^{mk}	Mixture Averaged Diffusivity	
D^{k}	Knudsen Diffusion Coefficient	
d_p	Pore Diameter	
e	Electrolyte	
E	Modulus of Elasticity	
F	Body Force	
F	Faraday Constant	
FEA	Finite Element Analysis	
FEM	Finite Element Method	
g	Gram	10^{-3} kg
GPa	Giga Pascal	
GT	Gas Turbine	
H	Height	
H_2	Hydrogen	

H_2O	Water
H_3PO_4	Phosphoric Acid
H_2S	Hydrogen Sulphide
ΔH	Reaction Enthalpy
i	Current Density
i_o	Exchange Current Density
ICE	Internal Combustion Engine
IEA	International Energy Agency
IG	Integrated Gasification
IP	Integrated Planar
J	Joule
J_2	Second Deviatoric Stresses Invariant
K	Kelvin
k	Thermal Conductivity
k^{eff}	Effective Thermal Conductivity
K_{eqr}	Equilibrium Constant of Steam Reforming
K_{eqs}	Equilibrium Constant of Shift Reaction
k_f	Fluid Thermal Conductivity
kg	Kilogram
KOH	Potassium Hydroxide

k_{rf}	Forward Rate Constant of Steam Reforming	
k_s	Solid Thermal Conductivity	
k_{sf}	Forward Rate Constant of Shift Reaction	
kW	Kilo Watt	
L	Length	
$LiAlO_2$	Lithium Aluminate	
LSC	Lanthanum Strontium Cobaltite	
LSCF	Lanthanum Strontium Cobaltite Ferrite	
LSGM	Lanthanum Strontium Gallate Magnesite	
M	Molecular Weight	
m	Metre	
MCFC	Molten Carbonate Fuel Cell	
mm	Millimetre	10^{-3} m
MPa	Mega Pascal	
MSR	Methane Steam Reforming	
MT	Micro Tubular	
MW	Mega Watt	
N	Newton	
NASA	National Aeronautics and Space Administrator's	
NEC	Nippon Electric Company	

n_{el}	Number fractions of the electron conducting particles
Ni	Nickel
NiO	Nickel Oxide
n_{io}	Number fractions of the ion conducting particles
NOx	Nitrogen Oxides
n_t	Total Number of Particles per Unit Volume
O_2	Oxygen
OECD	Organisation for Economic Co-operation and Development
OpenFoam	Open Field and Manipulation
p	Partial Pressure
Pa	Pascal
PAFC	Phosphoric Acid Fuel Cell
PEMFC	Polymer Electrolyte Membrane Fuel Cell
PEN	Positive Electrode Electrolyte Negative Electrode Structure
Q	Heat Source
Q_l	Ionic Current Source Term
Q_s	Electric Current Source Term
R	Gas Constant
ref	Reference
r_{el}	Radius of Electron Conducting Particles

r_{io}	Radius of Ion Conducting Particles
R_i	Species Production/Consumption Rate
S	Sulphur
s	second
SO_x	Sulphur Oxides
SOFC	Solid Oxide Fuel Cell
SSZ	Scandia Stabilized Zirconia
T	Temperature
t	Thickness
TPB	Three Phase Boundary
ΔT	Temperature Difference
u	Velocity
V	Molecular Diffusion Volume
V-I	Voltage Current
V_{pol}	Polarization
W	Watt
W	Width
WGS	Water Gas Shift
Y_i	Species Mass Fraction
YSZ	Yttria Stabilized Zirconia

Y_2O_3	Yttrium Oxide	
Z	Total Average Number of Contacts of Each Particle	
Z_{el}	Coordination Number of the Electron Conducting Particles	
Z_{io}	Coordination Number of the Ion Conducting Particles	
ZrO_2	Zirconium Oxide	
α	Thermal Expansion Coefficient	
α_a	Anodic Transfer Coefficient	
α_c	Cathodic Transfer Coefficient	
°C	Degree Celsius	
0D	Zero Dimensional	
1D	One Dimensional	
2D	Two Dimensional	
3D	Three Dimensional	
ε	Porosity	
ε_{th}	Thermal strain	
η	Overpotential	
μ	Dynamic Viscosity	
μm	Micrometre	10^{-6} m
υ	Poisson's Ratio	
φ_{el}	Volume Fraction of Electron Conducting Particles	

$\Delta\varphi_{eq}$	Equilibrium Potential
φ_l	Ionic Potential
φ_s	Electronic Potential
ρ	Density
σ_l	Ionic Conductivity
σ_{mises}	Von Mises Stresses
σ_s	Electronic Conductivity
σ_{th}	Thermal Stress
σ_{ys}	Yield Stress
θ	Contact Angle between ion and electron conducting particles
τ	Tortuosity

References

[1] A. M. Omer, "Energy, environment and sustainable development," Renewable and sustainable energy reviews, vol. 12, pp. 2265-2300, 2008.

[2] "International energy outlook," US Energy Information Administration, Washington, DC, 2011.

[3] I. Council, Lightning the Way: Towards a Sustainable Energy Future: IAC Secretariat, 2007.

[4] J. Goldemberg, World energy assessment: Energy and the challenge of sustainability: United Nations Pubns, 2000.

[5] E. Sher, Handbook of air pollution from internal combustion engines: pollutant formation and control: Academic Press, 1998.

[6] R. Andres, D. Fielding, G. Marland, T. Boden, N. Kumar, and A. Kearney, "Carbon dioxide emissions from fossil-fuel use, 1751–1950," Tellus B, vol. 51, pp. 759-765, 1999.

[7] C. Zou, Q. Zhao, G. Zhang, and B. Xiong, "Energy revolution: From a fossil energy era to a new energy era," Natural Gas Industry B, vol. 3, pp. 1-11, 2016.

[8] G. Kosmadakis, S. Karellas, and E. Kakaras, "Renewable and conventional electricity generation systems: Technologies and diversity of energy systems," in Renewable Energy Governance, ed: Springer, 2013, pp. 9-30.

[9] A. Franco and A. Russo, "Combined cycle plant efficiency increase based on the optimization of the heat recovery steam generator operating parameters," International Journal of Thermal Sciences, vol. 41, pp. 843-859, 2002.

[10] C. Descamps, C. Bouallou, and M. Kanniche, "Efficiency of an integrated gasification combined cycle (IGCC) power plant including CO_2 removal," Energy, vol. 33, pp. 874-881, 2008.

[11] T. N. Veziroğlu and S. Şahi, "21st Century's energy: Hydrogen energy system," Energy conversion and management, vol. 49, pp. 1820-1831, 2008.

[12] U. EPA, "Technology characterization: reciprocating engines," 2008.

[13] S. Henningsen, "Air Pollution from Large Two-Stroke Diesel Engines and Technologies to Control It-Chapter 14."

[14] I. Dincer, "Renewable energy and sustainable development: a crucial review," Renewable and Sustainable Energy Reviews, vol. 4, pp. 157-175, 2000.

[15] B. R. Singh and O. Singh, "Global trends of fossil fuel reserves and climate change in the 21st century," in Fossil Fuel and the Environment, ed: InTech, 2012.

[16] B. F. Möller, J. Arriagada, M. Assadi, and I. Potts, "Optimisation of an SOFC/GT system with CO_2 capture," Journal of Power Sources, vol. 131, pp. 320-326, 2004.

[17] IEA, "World energy outlook 2011," 2011.

[18] M. L. Parry, O. Canziani, J. P. Palutikof, P. J. van der Linden, and C. E. Hanson, "Contribution of working group II to the fourth assessment report of the intergovernmental panel on climate change, 2007," 2007.

[19] C. O. Colpan, "Thermal modeling of solid oxide fuel cell based biomass gasification systems," Carleton University, 2009.

[20] J. P. Dorian, H. T. Franssen, and D. R. Simbeck, "Global challenges in energy," Energy policy, vol. 34, pp. 1984-1991, 2006.

[21] S. A. Hajimolana, M. A. Hussain, W. Daud, M. Soroush, and A. Shamiri, "Mathematical modeling of solid oxide fuel cells: A review," Renewable and Sustainable Energy Reviews, vol. 15, pp. 1893-1917, 2011.

[22] F. Zabihian and A. Fung, "A review on modeling of hybrid solid oxide fuel cell systems," International Journal of Engineering, vol. 3, pp. 85-119, 2009.

[23] A. S. Adavbiele, "Solar Power Solid Oxide Fuel Cell With Thermoelectric Generator," Candian Journal of Technology and Scientific Management, vol. 1, pp. 7 - 20, 2012.

[24] S. R. Bull, "Renewable Energy Today and Tomorrow," Proceeding of IEEE, vol. 89, pp. 1216 - 1226, Aug 2001.

[25] P. P. Edwards, V. L. Kuznetsov, W. I. David, and N. P. Brandon, "Hydrogen and fuel cells: towards a sustainable energy future," Energy policy, vol. 36, pp. 4356-4362, 2008.

[26] X. Zhang, S. Chan, G. Li, H. Ho, J. Li, and Z. Feng, "A review of integration strategies for solid oxide fuel cells," Journal of Power Sources, vol. 195, pp. 685-702, 2010.

[27] H.-J. Neef, "International overview of hydrogen and fuel cell research," Energy, vol. 34, pp. 327-333, 2009.

[28] S. Ahmed and M. Krumpelt, "Hydrogen from hydrocarbon fuels for fuel cells," International journal of hydrogen energy, vol. 26, pp. 291-301, 2001.

[29] S. K. Park, T. S. Kim, J. L. Sohn, and Y. D. Lee, "An integrated power generation system combining solid oxide fuel cell and oxy-fuel combustion for high performance and CO_2 capture," Applied Energy, vol. 88, pp. 1187-1196, 2011.

[30] O. Maurstad, R. Bredesen, O. Bolland, H. M. Kvamsdal, and M. Schell, "SOFC and gas turbine Power Systems–evaluation of Configurations for CO2 Capture," in peer-reviewed conference proceedings of GHGT-7, Vancouver, Canada, September, 2004, pp. 5-9.

[31] H. M. Kvamsdal, K. Jordal, and O. Bolland, "A quantitative comparison of gas turbine cycles with CO2 capture," Energy, vol. 32, pp. 10-24, 2007.

[32] M. Haines, W. Heidug, K. Li, and J. Moore, "Progress with the development of a CO 2 capturing solid oxide fuel cell," Journal of power sources, vol. 106, pp. 377-380, 2002.

[33] O. Yamamoto, "Solid oxide fuel cells: fundamental aspects and prospects," Electrochimica Acta, vol. 45, pp. 2423-2435, 2000.

[34] S. C. Singhal, "Solid oxide fuel cells for stationary, mobile, and military applications," Solid State Ionics, vol. 152, pp. 405-410, 2002.

[35] M. Andersson, J. Yuan, and B. Sundén, "Review on modeling development for multiscale chemical reactions coupled transport phenomena in solid oxide fuel cells," Applied Energy, vol. 87, pp. 1461-1476, 2010.

[36] L. Blum, R. Deja, R. Peters, and D. Stolten, "Comparison of efficiencies of low, mean and high temperature fuel cell systems," International Journal of Hydrogen Energy, vol. 36, pp. 11056-11067, 2011.

[37] L. L. Stephen J. McPhail, Carlos Boigues-Muñoz, "International Status of SOFC deployment 2012-2013," Rome2013.

[38] N. Laosiripojana, W. Wiyaratn, W. Kiatkittipong, A. Arpornwichanop, A. Soottitantawat, and S. Assabumrungrat, "Reviews on solid oxide fuel cell technology," Engineering Journal, vol. 13, pp. 65-84, 2009.

[39] S. Campanari and E. Macchi, "Thermodynamic analysis of advanced power cycles based upon solid oxide fuel cells, gas turbines and rankine bottoming cycles," ASME paper, p. 585, 1998.

[40] S. J. McPhail, L. Leto, and C. Boigues-Munoz, "The yellow pages of SOFC technology," International Status of SOFC Deployment. IEA-Implementing Agreement Advanced Fuel Cells, ENEA National Agency for New Technologies, Energy and Sustainable Economic Development, Rome, Italy, 2013.

[41] N. Q. Minh, "Solid oxide fuel cell technology—features and applications," Solid State Ionics, vol. 174, pp. 271-277, 2004.

[42] G. J. Acres, "Recent advances in fuel cell technology and its applications," Journal of Power Sources, vol. 100, pp. 60-66, 2001.

[43] V. M. Janardhanan and O. Deutschmann, "Modeling of solid-oxide fuel cells," Zeitschrift für Physikalische Chemie, vol. 221, pp. 443-478, 2007.

[44] A. Choudhury, H. Chandra, and A. Arora, "Application of solid oxide fuel cell technology for power generation—a review," Renewable and Sustainable Energy Reviews, vol. 20, pp. 430-442, 2013.

[45] H. Schlegl and R. Dawson, "FEA analysis and modelling of thermal stress in SOFCs," 2016.

[46] E. Ivers-Tiffée, A. Weber, and D. Herbstritt, "Materials and technologies for SOFC-components," Journal of the European Ceramic Society, vol. 21, pp. 1805-1811, 2001.

[47] M. Santarelli, M. Cabrera, and M. Calì, "Solid oxide fuel based auxiliary power unit for regional jets: Design and mission simulation with different cell geometries," Journal of Fuel Cell Science and Technology, vol. 7, p. 021006, 2010.

[48] J. Shi and X. Xue, "CFD analysis of a novel symmetrical planar SOFC design with micro-flow channels," Chemical Engineering Journal, vol. 163, pp. 119-125, 2010.

[49] A. Weber and E. Ivers-Tiffée, "Materials and concepts for solid oxide fuel cells (SOFCs) in stationary and mobile applications," Journal of power sources, vol. 127, pp. 273-283, 2004.

[50] E. Achenbach, "Annex II: Modelling and Evaluation of Advanced Solid Oxide Fuel Cells: SOFC Stack Modelling (Final Report of Activity A2)," International Energy Agency, Germany, 1996.

[51] S. Mekhilef, R. Saidur, and A. Safari, "Comparative study of different fuel cell technologies," Renewable and Sustainable Energy Reviews, vol. 16, pp. 981-989, 2012.

[52] R. P. O'Hayre, S.-W. Cha, W. Colella, and F. B. Prinz, Fuel cell fundamentals, Second ed. Hoboken, New Jersey: John Wiley & Sons, Inc, 2009.

[53] J. Hirschenhofer, D. Stauffer, R. Engleman, and M. Klett, Fuel cell handbook, 1998.

[54] M. H. Nehrir and C. Wang, Modeling and control of fuel cells: distributed generation applications vol. 41: John Wiley & Sons, 2009.

[55] S. Thomas and M. Zalbowitz. (1999, Fuel cells-green power.

[56] S. Giddey, S. Badwal, A. Kulkarni, and C. Munnings, "A comprehensive review of direct carbon fuel cell technology," Progress in Energy and Combustion Science, vol. 38, pp. 360-399, 2012.

[57] J. Milewski, K. Świrski, M. Santarelli, and P. Leone, Advanced methods of solid oxide fuel cell modeling: Springer Science & Business Media, 2011.

[58] C. Rayment and S. Sherwin, "Introduction to fuel cell technology," University of Notre Dame, vol. 2, 2003.

[59] J. Larminie, A. Dicks, and M. S. McDonald, Fuel cell systems explained vol. 2: Wiley New York, 2003.

[60] B. Cook, "Introduction to fuel cells and hydrogen technology," Engineering Science & Education Journal, vol. 11, pp. 205-216, 2002.

[61] Fuel cell facts, Histroy of Fuel Cell. 2014. Available: www.cfcl.com.au/Assets/Files/(EN).5.History.of.Fuel.Cells.Dec-11.pdf

[62] V. S. Bagotsky, Fuel cells: problems and solutions vol. 56: John Wiley & Sons, 2012.

[63] J. M. Andújar and F. Segura, "Fuel cells: History and updating. A walk along two centuries," Renewable and sustainable energy reviews, vol. 13, pp. 2309-2322, 2009.

[64] L. Carrette, K. Friedrich, and U. Stimming, "Fuel cells–fundamentals and applications," Fuel cells, vol. 1, pp. 5-39, 2001.

[65] M. Winter and R. J. Brodd, "What are batteries, fuel cells, and supercapacitors?," ed: ACS Publications, 2004.

[66] J.-H. Wee, "Applications of proton exchange membrane fuel cell systems," Renewable and sustainable energy reviews, vol. 11, pp. 1720-1738, 2007.

[67] C. K. Dyer, "Fuel cells for portable applications," Fuel Cells Bulletin, vol. 2002, pp. 8-9, 2002.

[68] B. E. Logan and J. M. Regan, "Microbial fuel cells—challenges and applications," ed: ACS Publications, 2006.

[69] L. Carrette, K. A. Friedrich, and U. Stimming, "Fuel cells: principles, types, fuels, and applications," ChemPhysChem, vol. 1, pp. 162-193, 2000.

[70] A. Kirubakaran, S. Jain, and R. Nema, "A review on fuel cell technologies and power electronic interface," Renewable and Sustainable Energy Reviews, vol. 13, pp. 2430-2440, 2009.

[71] R. Shah, "Introduction to fuel cells," in Recent Trends in Fuel Cell Science and Technology, ed: Springer, 2007, pp. 1-9.

[72] H. Haydock. (1998, Introduction to Fuel Cells. 1-4. Available: http://www.ieafuelcell.com/documents/intro_fuel_cells.pdf

[73] Introduction to Hydrogen and Fuel cells. Available: http://www.fuelcelleducation.org/wpcontent/themes/sandbox/pdf/Introduction%20to%20hydrogen%20and%20fuel%20cells%20%20miniHYDROGEN.com.pdf

[74] S. Kakac, A. Pramuanjaroenkij, and X. Y. Zhou, "A review of numerical modeling of solid oxide fuel cells," International journal of hydrogen energy, vol. 32, pp. 761-786, 2007.

[75] F. C. H. F. Edition, "EG&G Services, Parsons, Inc. and Science Applications International Corporation for the US Department of Energy," ed, 2001.

[76] K. Sopian and W. R. Wan Daud, "Challenges and future developments in proton exchange membrane fuel cells," Renewable Energy, vol. 31, pp. 719-727, 2006.

[77] S. Basu, Fuel Cell Science and Technology: Springer, 2007.

[78] Fuel Cell Comparison Chart. Available: http://upload.wikimedia.org/wikipedia/commons/3/36/EERE_Fuel_Cell_Comparison_Chart.pdf

[79] T. Kariya, K. Uchiyama, H. Tanaka, T. Hirono, T. Kuse, K. Yanagimoto, et al., "Intermediate-temperature operation of solid oxide fuel cells (IT-SOFCs) with thin film proton conductive electrolyte," in Journal of Physics: Conference Series, 2015, p. 012057.

[80] A. B. Stambouli and E. Traversa, "Solid oxide fuel cells (SOFCs): a review of an environmentally clean and efficient source of energy," Renewable and Sustainable Energy Reviews, vol. 6, pp. 433-455, 2002.

[81] E. Ivers-Tiffée, A. Virkar, S. Singhal, and K. Kendall, "High-Temperature Solid Oxide Fuel Cells: Fundamentals, Design and Application," ed., SC Singhal and K. Kendall, Elsevier, UK, pp. 1 - 430, 2003.

[82] S. C. Singhal, "Solid oxide fuel cells: past, present and future," in Solid Oxide Fuels Cells: Facts and Figures, ed: Springer, 2013, pp. 1-23.

[83] B. Huang, Y. Qi, and M. Murshed, "Solid oxide fuel cell: Perspective of dynamic modeling and control," Journal of Process Control, vol. 21, pp. 1426-1437, 2011.

[84] I. EG&G Technical Services, Fuel Cell Hanbook, Seventh ed. West Virginia: U.S. Department of Energy, 2004.

[85] B. C. Steele and A. Heinzel, "Materials for fuel-cell technologies," Nature, vol. 414, pp. 345-352, 2001.

[86] S. C. Singhal, "Solid oxide fuel cells," The Electrochemical Society Interface, vol. 16, p. 41, 2007.

[87] I. Kosacki, "Nanoscaled oxide thin films for energy conversion," in Fuel Cell Technologies: State and Perspectives, ed: Springer, 2005, pp. 395-416.

[88] A. Smirnna, D. Kang, and N. Sammes, "Fuel Cell Technologies: State and Perspectives," 2005.

[89] T. Politova and J. T. Irvine, "Investigation of scandia–yttria–zirconia system as an electrolyte material for intermediate temperature fuel cells—influence of yttria content in system $(Y_2O_3)_x(Sc_2O_3)_{(11-x)}(ZrO_2)_{89}$," Solid State Ionics, vol. 168, pp. 153-165, 2004.

[90] R. N. Basu, "Materials for solid oxide fuel cells," in Recent trends in fuel cell science and technology, ed: Springer, 2007, pp. 286-331.

[91] A. J. Jacobson, "Materials for solid oxide fuel cells†," Chemistry of Materials, vol. 22, pp. 660-674, 2009.

[92] J. Irvine, T. Politova, N. Zakowsky, A. Kruth, S. Tao, R. Travis, et al., "Scandia-zirconia electrolytes and electrodes for SOFCs," in Fuel Cell Technologies: State and Perspectives, ed: Springer, 2005, pp. 35-47.

[93] R. M. Ormerod, "Solid oxide fuel cells," Chemical Society Reviews, vol. 32, pp. 17-28, 2003.

[94] J. T. Irvine and P. Connor, "Alternative Materials for SOFCs, Opportunities and Limitations," in Solid Oxide Fuels Cells: Facts and Figures, ed: Springer, 2013, pp. 163-180.

[95] E. P. Murray, T. Tsai, and S. Barnett, "A direct-methane fuel cell with a ceria-based anode," Nature, vol. 400, pp. 649-651, 1999.

[96] Y. Choi, C. Compson, M.-C. Lin, and M. Liu, "Ab initio analysis of sulfur tolerance of Ni, Cu, and Ni–Cu alloys for solid oxide fuel cells," Journal of Alloys and Compounds, vol. 427, pp. 25-29, 2007.

[97] S. Hui and A. Petric, "Evaluation of yttrium-doped $SrTiO_3$ as an anode for solid oxide fuel cells," Journal of the European Ceramic Society, vol. 22, pp. 1673-1681, 2002.

[98] S. Hui and A. Petric, "Electrical properties of yttrium-doped strontium titanate under reducing conditions," Journal of The Electrochemical Society, vol. 149, pp. J1-J10, 2002.

[99] P. Blennow, K. K. Hansen, L. Wallenberg, and M. Mogensen, "Electrochemical characterization and redox behavior of Nb-doped $SrTiO_3$," Solid State Ionics, vol. 180, pp. 63-70, 2009.

[100] J. W. Fergus, "Materials challenges for solid-oxide fuel cells," Jom, vol. 59, pp. 56-62, 2007.

[101] S. Ping Jiang, J.-P. Zhang, and K. Föger, "Chemical interactions between 3 mol% yttria-zirconia and Sr-doped lanthanum manganite," Journal of the European Ceramic Society, vol. 23, pp. 1865-1873, 2003.

[102] D. J. Brett, A. Atkinson, N. P. Brandon, and S. J. Skinner, "Intermediate temperature solid oxide fuel cells," Chemical Society Reviews, vol. 37, pp. 1568-1578, 2008.

[103] I. EG&G Technical Services, Fuel Cell Hankbook, 7th Edition. Morgantown, West Virginia: DOE, Office of Fossil Energy, National Energy Technology Laboratory,, 2004.

[104] L. Blum, R. Steinberger-Wilckens, W. Meulenberg, and H. Nabielek, "SOFC Worldwide—Technology Development Status and Early Applications," in Fuel Cell Technologies: State and Perspectives, ed: Springer, 2005, pp. 107-122.

[105] F. J. Gardner, M. Day, N. Brandon, M. Pashley, and M. Cassidy, "SOFC technology development at Rolls-Royce," Journal of Power Sources, vol. 86, pp. 122-129, 2000.

[106] P. Costamagna, A. Selimovic, M. Del Borghi, and G. Agnew, "Electrochemical model of the integrated planar solid oxide fuel cell (IP-SOFC)," Chemical Engineering Journal, vol. 102, pp. 61-69, 2004.

[107] M. G. Camprubı, "Multiphysics models for the simulation of solid oxide fuel cells," Citeseer, 2011.

[108] S. C. Singhal and M. Dokiya, "Solid Oxide Fuel Cells (SOFC VI): Proceedings of the Sixth International Symposium," 1999.

[109] C. O. Colpan, I. Dincer, and F. Hamdullahpur, "Thermodynamic modeling of direct internal reforming solid oxide fuel cells operating with syngas," International Journal of Hydrogen Energy, vol. 32, pp. 787-795, 2007.

[110] M. Irshad, K. Siraj, R. Raza, A. Ali, P. Tiwari, B. Zhu, et al., "A Brief Description of High Temperature Solid Oxide Fuel Cell's Operation, Materials, Design, Fabrication Technologies and Performance," Applied Sciences, vol. 6, p. 75, 2016.

[111] N. L. Garland, D. C. Papageorgopoulos, and J. M. Stanford, "Hydrogen and fuel cell technology: progress, challenges, and future directions," Energy Procedia, vol. 28, pp. 2-11, 2012.

[112] K. Huang and S. C. Singhal, "Cathode-supported tubular solid oxide fuel cell technology: A critical review," Journal of Power Sources, vol. 237, pp. 84-97, 2013.

[113] J. B. Goodenough and Y.-H. Huang, "Alternative anode materials for solid oxide fuel cells," Journal of Power Sources, vol. 173, pp. 1-10, 2007.

[114] D. Sánchez, R. Chacartegui, A. Munoz, and T. Sánchez, "Thermal and electrochemical model of internal reforming solid oxide fuel cells with tubular geometry," Journal of Power Sources, vol. 160, pp. 1074-1087, 2006.

[115] M. Cimenti and J. M. Hill, "Direct utilization of liquid fuels in SOFC for portable applications: challenges for the selection of alternative anodes," Energies, vol. 2, pp. 377-410, 2009.

[116] S. Douvartzides, F. Coutelieris, A. Demin, and P. Tsiakaras, "Fuel options for solid oxide fuel cells: a thermodynamic analysis," AIChE journal, vol. 49, pp. 248-257, 2003.

[117] S. Assabumrungrat, V. Pavarajarn, S. Charojrochkul, and N. Laosiripojana, "Thermodynamic analysis for a solid oxide fuel cell with direct internal reforming fueled by ethanol," Chemical Engineering Science, vol. 59, pp. 6015-6020, 2004.

[118] Y. Yi, A. D. Rao, J. Brouwer, and G. S. Samuelsen, "Fuel flexibility study of an integrated 25kW SOFC reformer system," Journal of power sources, vol. 144, pp. 67-76, 2005.

[119] A. Wojcik, H. Middleton, and I. Damopoulos, "Ammonia as a fuel in solid oxide fuel cells," Journal of Power Sources, vol. 118, pp. 342-348, 2003.

[120] F. Maréchal, S. Leuenberger, and D. Favrat, "Energy balance model of a SOFC cogenerator operated with biogas," Journal of Power Sources, vol. 118, pp. 375-383, 2003.

[121] Y. Lu and L. Schaefer, "A solid oxide fuel cell system fed with hydrogen sulfide and natural gas," Journal of power sources, vol. 135, pp. 184-191, 2004.

[122] S. Assabumrungrat, N. Laosiripojana, V. Pavarajarn, W. Sangtongkitcharoen, A. Tangjitmatee, and P. Praserthdam, "Thermodynamic analysis of carbon formation in a solid oxide fuel cell with a direct internal reformer fuelled by methanol," Journal of power sources, vol. 139, pp. 55-60, 2005.

[123] V. M. Janardhanan and O. Deutschmann, "Numerical study of mass and heat transport in solid-oxide fuel cells running on humidified methane," Chemical Engineering Science, vol. 62, pp. 5473-5486, 2007.

[124] Z. Shao, J. Mederos, W. C. Chueh, and S. M. Haile, "High power-density single-chamber fuel cells operated on methane," Journal of power sources, vol. 162, pp. 589-596, 2006.

[125] A. Fuerte, R. Valenzuela, M. Escudero, and L. Daza, "Ammonia as efficient fuel for SOFC," Journal of Power Sources, vol. 192, pp. 170-174, 2009.

[126] M. Liu, P. He, J. Luo, A. Sanger, and K. Chuang, "Performance of a solid oxide fuel cell utilizing hydrogen sulfide as fuel," Journal of Power Sources, vol. 94, pp. 20-25, 2001.

[127] F. Zhao and A. V. Virkar, "Dependence of polarization in anode-supported solid oxide fuel cells on various cell parameters," Journal of power sources, vol. 141, pp. 79-95, 2005.

[128] J. Wang, D. Yan, J. Pu, B. Chi, and L. Jian, "Fabrication and performance evaluation of planar solid oxide fuel cell with large active reaction area," International Journal of Hydrogen Energy, vol. 36, pp. 7234-7239, 2011.

[129] Y. Komatsu, G. Brus, S. Kimijima, and J. Szmyd, "Experimental study on the 300W class planar type solid oxide fuel cell stack: Investigation for appropriate fuel provision control and the transient capability of the cell performance," in Journal of Physics: Conference Series, 2012, p. 012162.

[130] S. Seidler, M. Henke, J. Kallo, W. G. Bessler, U. Maier, and K. A. Friedrich, "Pressurized solid oxide fuel cells: experimental studies and modeling," Journal of Power Sources, vol. 196, pp. 7195-7202, 2011.

[131] H. Jung, S.-H. Choi, H. Kim, J.-W. Son, J. Kim, H.-W. Lee, et al., "Fabrication and performance evaluation of 3-cell SOFC stack based on planar 10cm× 10cm anode-supported cells," Journal of power sources, vol. 159, pp. 478-483, 2006.

[132] J. Luo, D. Yan, D. Fang, F. Liang, J. Pu, B. Chi, et al., "Electrochemical performance and thermal cyclicability of industrial-sized anode supported planar solid oxide fuel cells," Journal of Power Sources, vol. 224, pp. 37-41, 2013.

[133] L. Andreassi, G. Rubeo, S. Ubertini, P. Lunghi, and R. Bove, "Experimental and numerical analysis of a radial flow solid oxide fuel cell," International Journal of Hydrogen Energy, vol. 32, pp. 4559-4574, 2007.

[134] S. Bedogni, S. Campanari, P. Iora, L. Montelatici, and P. Silva, "Experimental analysis and modeling for a circular-planar type IT-SOFC," Journal of Power Sources, vol. 171, pp. 617-625, 2007.

[135] V. Lawlor, K. Klein, C. Hochenauer, S. Griesser, S. Kuehn, A.-G. Olabi, et al., "Experimental and Numerical Study of Various MT-SOFC Flow Manifold Techniques: Single MT-SOFC Analysis," Journal of Fuel Cell Science and Technology, vol. 10, p. 011003, 2013.

[136] H. Yakabe, Y. Baba, T. Sakurai, and Y. Yoshitaka, "Evaluation of the residual stress for anode-supported SOFCs," Journal of Power Sources, vol. 135, pp. 9-16, 2004.

[137] W. Fischer, J. Malzbender, G. Blass, and R. Steinbrech, "Residual stresses in planar solid oxide fuel cells," Journal of Power Sources, vol. 150, pp. 73-77, 2005.

[138] Y. Hao, Z. Shao, J. Mederos, W. Lai, D. G. Goodwin, and S. M. Haile, "Recent advances in single-chamber fuel-cells: Experiment and modeling," Solid State Ionics, vol. 177, pp. 2013-2021, 2006.

[139] O. Razbani, I. Wærnhus, and M. Assadi, "Experimental investigation of temperature distribution over a planar solid oxide fuel cell," Applied Energy, vol. 105, pp. 155-160, 2013.

[140] B. Morel, R. Roberge, S. Savoie, T. W. Napporn, and M. Meunier, "An experimental evaluation of the temperature gradient in solid oxide fuel cells," Electrochemical and solid-state letters, vol. 10, pp. B31-B33, 2007.

[141] N. Akhtar, S. Decent, and K. Kendall, "Cell temperature measurements in micro-tubular, single-chamber, solid oxide fuel cells (MT–SC–SOFCs)," Journal of Power Sources, vol. 195, pp. 7818-7824, 2010.

[142] F. Fleischhauer, A. Tiefenauer, T. Graule, R. Danzer, A. Mai, and J. Kuebler, "Failure analysis of electrolyte-supported solid oxide fuel cells," Journal of Power Sources, vol. 258, pp. 382-390, 2014.

[143] R. Bove and S. Ubertini, "Modeling solid oxide fuel cell operation: Approaches, techniques and results," Journal of Power Sources, vol. 159, pp. 543-559, 2006.

[144] J. Shi and X. Xue, "Microstructure optimization designs for anode-supported planar solid oxide fuel cells," Journal of Fuel Cell Science and Technology, vol. 8, p. 061006, 2011.

[145] S. Hosseini, K. Ahmed, and M. O. Tadé, "CFD model of a methane fuelled single cell SOFC stack for analysing the combined effects of macro/micro structural parameters," Journal of Power Sources, vol. 234, pp. 180-196, 2013.

[146] K. P. Recknagle, R. E. Williford, L. A. Chick, D. R. Rector, and M. A. Khaleel, "Three-dimensional thermo-fluid electrochemical modeling of planar SOFC stacks," Journal of Power Sources, vol. 113, pp. 109-114, 2003.

[147] Thinh X. Hoa, Pawel Kosinskia, Alex C. Hoffmanna, Arild Vikb, "Numerical analysis of a planar anode-supported SOFC with composite electrodes," International Jounral of Hydrogen Energy, vol. 34, pp. 1 - 12, 2009.

[148] J. V. h. D. Larrain, F. Maréchal, D. Favrat, "Generalized model of planar SOFC repeat element for design optimization," Journal of Power Sources, vol. 131, pp. 304 - 312, 2004.

[149] E. C. R. Suwanwarangkula , , , M.W. Fowlera, P.L. Douglasa, E. Entchevb, M.A. Douglasb, "Performance comparison of Fick's, dusty-gas and Stefan–Maxwell models to predict the concentration overpotential of a SOFC anode," Journal of Power Sources, vol. 122, pp. 9 -18, 2003.

[150] M. H. H. Yakabe , M. Uratani, Y. Matsuzaki, I. Yasuda, "Evaluation and modeling of performance of anode-supported solid oxide fuel cell," Journal of Power Sources, vol. 86, pp. 423 - 431, 2000.

[151] K. Tseronis, I. Kookos, and C. Theodoropoulos, "Modelling mass transport in solid oxide fuel cell anodes: a case for a multidimensional dusty gas-based model," Chemical Engineering Science, vol. 63, pp. 5626-5638, 2008.

[152] M. García-Camprubí and N. Fueyo, "Mass transfer in hydrogen-fed anode-supported SOFCs," international journal of hydrogen energy, vol. 35, pp. 11551-11560, 2010.

[153] M. García-Camprubí, A. Sánchez-Insa, and N. Fueyo, "Multimodal mass transfer in solid-oxide fuel-cells," Chemical Engineering Science, vol. 65, pp. 1668-1677, 2010.

[154] A. Smirnov, A. Burt, and I. Celik, "Multi-physics simulations of fuel cells using multi-component modeling," Journal of power sources, vol. 158, pp. 295-302, 2006.

[155] Y. Qi, B. Huang, and J. Luo, "Dynamic modeling of a finite volume of solid oxide fuel cell: The effect of transport dynamics," Chemical Engineering Science, vol. 61, pp. 6057-6076, 2006.

[156] M. Hussain, X. Li, and I. Dincer, "Mathematical modeling of planar solid oxide fuel cells," Journal of Power Sources, vol. 161, pp. 1012-1022, 2006.

[157] H. Severson and M. Assadi, "Modeling of overpotentials in an anode-supported planar SOFC using a detailed simulation model," Journal of Fuel Cell Science and Technology, vol. 8, p. 051021, 2011.

[158] M. Navasa, M. Andersson, J. Yuan, and B. Sundén, "Transport phenomena in solid oxide fuel cell electrodes focusing on heat transfer related to chemical reactions," in Journal of Physics: Conference Series, 2012, p. 012086.

[159] P. Chinda, W. Wechsatol, S. Chanchaona, and P. Brault, "Microscale Modeling of an Anode-Supported Planar Solid Oxide Fuel Cell," Fuel Cells, vol. 11, pp. 184-199, 2011.

[160] Y. Xie and X. Xue, "Multi-scale electrochemical reaction anode model for solid oxide fuel cells," Journal of Power Sources, vol. 209, pp. 81-89, 2012.

[161] V. M. J. a. O. Deutschmann, "Modeling of solid oxide fuel cells," Z. Phys. Chem, vol. 221, pp. 443 - 478, 2007.

[162] C. Yang, "Mass and Heat transfer processes in Solid oxide fuel cell," Lund University, Sweden2012.

[163] K. Fischer and J. R. Seume, "Location and magnitude of heat sources in solid oxide fuel cells," Journal of fuel cell science and technology, vol. 6, p. 011002, 2009.

[164] A. Atkinson and A. Selcuk, "Residual stress and fracture of laminated ceramic membranes," Acta materialia, vol. 47, pp. 867-874, 1999.

[165] A. Selimovic, M. Kemm, T. Torisson, and M. Assadi, "Steady state and transient thermal stress analysis in planar solid oxide fuel cells," Journal of Power Sources, vol. 145, pp. 463-469, 2005.

[166] A. Nakajo, C. Stiller, G. Härkegård, and O. Bolland, "Modeling of thermal stresses and probability of survival of tubular SOFC," Journal of Power Sources, vol. 158, pp. 287-294, 2006.

[167] A. Nakajo, F. Mueller, J. Brouwer, and D. Favrat, "Mechanical reliability and durability of SOFC stacks. Part II: Modelling of mechanical failures during ageing and cycling," International Journal of Hydrogen Energy, vol. 37, pp. 9269-9286, 2012.

[168] C.-K. Lin, L.-H. Huang, L.-K. Chiang, and Y.-P. Chyou, "Thermal stress analysis of planar solid oxide fuel cell stacks: effects of sealing design," Journal of Power Sources, vol. 192, pp. 515-524, 2009.

[169] T. Zhang, Q. Zhu, W. L. Huang, Z. Xie, and X. Xin, "Stress field and failure probability analysis for the single cell of planar solid oxide fuel cells," Journal of Power Sources, vol. 182, pp. 540-545, 2008.

[170] S. Vaidya and J.-H. Kim, "Finite element thermal stress analysis of solid oxide fuel cell cathode microstructures," Journal of Power Sources, vol. 225, pp. 269-276, 2013.

[171] R. Ihringer, N. M. Sammes, G. Tompsett, K. Kendall, K. Yamada, C.-j. Wen, et al., "Concept and technology of SOFC for electric vehicles," Solid State Ionics, vol. 132, pp. 333-342, 2000.

[172] P. Pianko-Oprych, T. Zinko, and Z. Jaworski, "Simulation of thermal stresses for new designs of microtubular Solid Oxide Fuel Cell stack," International Journal of hydrogen energy, vol. 40, pp. 14584-14595, 2015.

[173] M. Peksen, A. Al-Masri, L. Blum, and D. Stolten, "3D transient thermomechanical behaviour of a full scale SOFC short stack," International Journal of Hydrogen Energy, vol. 38, pp. 4099-4107, 2013.

[174] P. Pianko-Oprych, T. Zinko, and Z. Jaworski, "A Numerical Investigation of the Thermal Stresses of a Planar Solid Oxide Fuel Cell," Materials, vol. 9, p. 814, 2016.

[175] S. Chan, K. Khor, and Z. Xia, "A complete polarization model of a solid oxide fuel cell and its sensitivity to the change of cell component thickness," Journal of Power Sources, vol. 93, pp. 130-140, 2001.

[176] D. Larrain, F. Maréchal, and D. Favrat, "Generalized model of planar SOFC repeat element for design optimization," Journal of Power Sources, vol. 131, pp. 304-312, 2004.

[177] D. Cui and M. Cheng, "Numerical analysis of thermal and electrochemical phenomena for anode supported microtubular SOFC," AIChE Journal, vol. 55, pp. 771-782, 2009.

[178] A. Le, S. Beale, and J. Pharoah, "Validation of a solid oxide fuel cell model on the international energy agency benchmark case with hydrogen fuel," Fuel Cells, vol. 15, pp. 27-41, 2015.

[179] Y. M. Barzi, M. Ghassemi, M. Hamedi, and E. Afshari, "Numerical analysis of output characteristics of a tubular SOFC with different fuel compositions and mass flow rates," ECS Transactions, vol. 7, pp. 1919-1928, 2007.

[180] J. Yuan, Y. Huang, B. Sundén, and W. G. Wang, "Analysis of parameter effects on chemical reaction coupled transport phenomena in SOFC anodes," Heat and Mass Transfer, vol. 45, pp. 471-484, 2009.

[181] H. Zhu and R. J. Kee, "A general mathematical model for analyzing the performance of fuel-cell membrane-electrode assemblies," Journal of Power Sources, vol. 117, pp. 61-74, 2003.

[182] L. Fan, M. Pourquie, A. Thattai, A. Verkooijen, and P. Aravind, "Kinetics of Internal Methane Steam Reforming in Solid Oxide Fuel Cells and Its Influence on Cell Performance–Coupling Experiments and Modeling," ECS Transactions, vol. 57, pp. 2741-2751, 2013.

[183] M. Ni, "Modeling of SOFC running on partially pre-reformed gas mixture," International journal of hydrogen energy, vol. 37, pp. 1731-1745, 2012.

[184] R. J. Kee, H. Zhu, A. M. Sukeshini, and G. S. Jackson, "Solid oxide fuel cells: operating principles, current challenges, and the role of syngas," Combustion Science and Technology, vol. 180, pp. 1207-1244, 2008.

[185] A. Pramuanjaroenkij, S. Kakaç, and X. Yang Zhou, "Mathematical analysis of planar solid oxide fuel cells," International Journal of Hydrogen Energy, vol. 33, pp. 2547-2565, 2008.

[186] T. X. Ho, P. Kosinski, A. C. Hoffmann, and A. Vik, "Numerical analysis of a planar anode-supported SOFC with composite electrodes," International Journal of Hydrogen Energy, vol. 34, pp. 3488-3499, 2009.

[187] M. Andersson, J. Yuan, and B. Sundén, "SOFC modeling considering electrochemical reactions at the active three phase boundaries," International journal of heat and mass transfer, vol. 55, pp. 773-788, 2012.

[188] H. Mahcene, H. B. Moussa, H. Bouguettaia, D. Bechki, and M. Zeroual, "Computational modeling of the transport and electrochemical phenomena in solid oxide fuel cells," Energy Procedia, vol. 6, pp. 65-74, 2011.

[189] M. Xu, T. Li, M. Yang, and M. Andersson, "Solid oxide fuel cell interconnect design optimization considering the thermal stresses," Science bulletin, vol. 61, pp. 1333-1344, 2016.

[190] Z. Qu, P. Aravind, S. Boksteen, N. Dekker, A. Janssen, N. Woudstra, et al., "Three-dimensional computational fluid dynamics modeling of anode-supported planar SOFC," International Journal of Hydrogen Energy, vol. 36, pp. 10209-10220, 2011.

[191] D. Mu, Z.-S. Liu, C. Huang, and N. Djilali, "Prediction of the effective diffusion coefficient in random porous media using the finite element method," Journal of Porous Materials, vol. 14, pp. 49-54, 2007.

[192] B. Todd and J. Young, "Thermodynamic and transport properties of gases for use in solid oxide fuel cell modelling," Journal of power Sources, vol. 110, pp. 186-200, 2002.

[193] N. Akhtar, S. P. Decent, D. Loghin, and K. Kendall, "A three-dimensional numerical model of a single-chamber solid oxide fuel cell," International Journal of Hydrogen Energy, vol. 34, pp. 8645-8663, 2009.

[194] E. Achenbach and E. Riensche, "Methane/steam reforming kinetics for solid oxide fuel cells," Journal of Power Sources, vol. 52, pp. 283-288, 1994.

[195] K. Ahmed and K. Foger, "Kinetics of internal steam reforming of methane on Ni/YSZ-based anodes for solid oxide fuel cells," Catalysis Today, vol. 63, pp. 479-487, 2000.

[196] K. Hou and R. Hughes, "The kinetics of methane steam reforming over a Ni/α-Al 2 O catalyst," Chemical Engineering Journal, vol. 82, pp. 311-328, 2001.

[197] B. Haberman and J. Young, "Three-dimensional simulation of chemically reacting gas flows in the porous support structure of an integrated-planar solid oxide fuel cell," International Journal of Heat and Mass Transfer, vol. 47, pp. 3617-3629, 2004.

[198] W. Lehnert, J. Meusinger, and F. Thom, "Modelling of gas transport phenomena in SOFC anodes," Journal of Power Sources, vol. 87, pp. 57-63, 2000.

[199] P. Ivanov, "Thermodynamic modeling of the power plant based on the SOFC with internal steam reforming of methane," Electrochimica acta, vol. 52, pp. 3921-3928, 2007.

[200] P. Aguiar, C. Adjiman, and N. P. Brandon, "Anode-supported intermediate temperature direct internal reforming solid oxide fuel cell. I: model-based steady-state performance," Journal of power sources, vol. 138, pp. 120-136, 2004.

[201] P. Costamagna, P. Costa, and V. Antonucci, "Micro-modelling of solid oxide fuel cell electrodes," Electrochimica Acta, vol. 43, pp. 375-394, 1998.

[202] S. Sunde, "Simulations of composite electrodes in fuel cells," Journal of Electroceramics, vol. 5, pp. 153-182, 2000.

[203] P. Chinda, S. Chanchaona, P. Brault, and W. Wechsatol, "Mathematical modeling of a solid oxide fuel cell with nearly spherical-shaped electrode particles," Journal of Sustainable Energy & Environment, vol. 1, 2010.

[204] J. Ferguson, J. Fiard, and R. Herbin, "Three-dimensional numerical simulation for various geometries of solid oxide fuel cells," Journal of Power Sources, vol. 58, pp. 109-122, 1996.

[205] Y. Shi, N. Cai, and C. Li, "Numerical modeling of an anode-supported SOFC button cell considering anodic surface diffusion," Journal of Power Sources, vol. 164, pp. 639-648, 2007.

[206] K. Daneshvar, G. Dotelli, C. Cristiani, R. Pelosato, and M. Santarelli, "Modeling and Parametric Study of a Single Solid Oxide Fuel Cell by Finite Element Method," Fuel Cells, vol. 14, pp. 189-199, 2014.

[207] J. Gazzarri and O. Kesler, "Non-destructive delamination detection in solid oxide fuel cells," Journal of power sources, vol. 167, pp. 430-441, 2007.

[208] N. Autissier, D. Larrain, and D. Favrat, "CFD simulation tool for solid oxide fuel cells," Journal of Power Sources, vol. 131, pp. 313-319, 2004.

[209] B. Lin, Y. Shi, M. Ni, and N. Cai, "Numerical investigation on impacts on fuel velocity distribution nonuniformity among solid oxide fuel cell unit channels," International Journal of Hydrogen Energy, vol. 40, pp. 3035-3047, 2015.

[210] M. Ni, M. K. Leung, and D. Y. Leung, "Parametric study of solid oxide fuel cell performance," Energy Conversion and Management, vol. 48, pp. 1525-1535, 2007.

[211] T. Suzuki, T. Yamaguchi, Y. Fujishiro, and M. Awano, "Improvement of SOFC performance using a microtubular, anode-supported SOFC," Journal of the Electrochemical Society, vol. 153, pp. A925-A928, 2006.

[212] P. Chinda, S. Chanchaona, P. Brault, and W. Wechsatol, "Mathematical modeling of a solid oxide fuel cell with nearly spherical-shaped electrode particles," Journal of Sustainable Energy & Environment, vol. 1, pp. 185-196, 2010.

[213] D. Larrain, F. Maréchal, and D. Favrat, "Thermal modeling of a small anode supported solid oxide fuel cell," Journal of Power Sources, vol. 118, pp. 367-374, 2003.

[214] Y. Patcharavorachot, A. Arpornwichanop, and A. Chuachuensuk, "Electrochemical study of a planar solid oxide fuel cell: Role of support structures," Journal of Power Sources, vol. 177, pp. 254-261, 2008.

[215] J. Laurencin, F. Lefebvre-Joud, and G. Delette, "Impact of cell design and operating conditions on the performances of SOFC fuelled with methane," Journal of Power Sources, vol. 177, pp. 355-368, 2008.

[216] S. Campanari and P. Iora, "Definition and sensitivity analysis of a finite volume SOFC model for a tubular cell geometry," Journal of Power Sources, vol. 132, pp. 113-126, 2004.

[217] J. Yuan and B. Sundén, "Analysis of intermediate temperature solid oxide fuel cell transport processes and performance," Journal of heat transfer, vol. 127, pp. 1380-1390, 2005.

[218] T. L. Cable and S. W. Sofie, "A symmetrical, planar SOFC design for NASA's high specific power density requirements," Journal of Power Sources, vol. 174, pp. 221-227, 2007.

[219] X. Xu, C. Xia, G. Xiao, and D. Peng, "Fabrication and performance of functionally graded cathodes for IT-SOFCs based on doped ceria electrolytes," Solid State Ionics, vol. 176, pp. 1513-1520, 2005.

[220] A. V. Virkar, J. Chen, C. W. Tanner, and J.-W. Kim, "The role of electrode microstructure on activation and concentration polarizations in solid oxide fuel cells," Solid State Ionics, vol. 131, pp. 189-198, 2000.

[221] J. W. Kim, A. V. Virkar, K. Z. Fung, K. Mehta, and S. C. Singhal, "Polarization effects in intermediate temperature, anode-supported solid oxide fuel cells," Journal of the Electrochemical Society, vol. 146, pp. 69-78, 1999.

[222] B. Timurkutluk, C. Timurkutluk, M. D. Mat, and Y. Kaplan, "Development of high-performance anode supported solid oxide fuel cell," International Journal of Energy Research, vol. 36, pp. 1383-1387, 2012.

[223] J. Ding and J. Liu, "An anode-supported solid oxide fuel cell with spray-coated yttria-stabilized zirconia (YSZ) electrolyte film," Solid State Ionics, vol. 179, pp. 1246-1249, 2008.

[224] Q. Ma, F. Tietz, A. Leonide, and E. Ivers-Tiffée, "Anode-supported planar SOFC with high performance and redox stability," Electrochemistry Communications, vol. 12, pp. 1326-1328, 2010.

[225] W. Z. Zhu and S. Deevi, "Development of interconnect materials for solid oxide fuel cells," Materials Science and Engineering: A, vol. 348, pp. 227-243, 2003.

[226] V. V. Kharton, Solid state electrochemistry II: electrodes, interfaces and ceramic membranes: John Wiley & Sons, 2012.

[227] W. Z. Zhu and S. Deevi, "Opportunity of metallic interconnects for solid oxide fuel cells: a status on contact resistance," Materials Research Bulletin, vol. 38, pp. 957-972, 2003.

[228] S. Paulik, S. Baskaran, and T. Armstrong, "Mechanical properties of calcium-substituted yttrium chromite," Journal of materials science letters, vol. 18, pp. 819-822, 1999.

[229] H. Hayashi, M. Watanabe, and H. Inaba, "Measurement of thermal expansion coefficient of LaCrO 3," Thermochimica acta, vol. 359, pp. 77-85, 2000.

[230] N. Sakai, H. Yokokawa, T. Horita, and K. Yamaji, "Lanthanum Chromite-Based Interconnects as Key Materials for SOFC Stack Development," International Journal of Applied Ceramic Technology, vol. 1, pp. 23-30, 2004.

[231] E. N. Fuller, P. D. Schettler, and J. C. Giddings, "New method for prediction of binary gas-phase diffusion coefficients," Industrial & Engineering Chemistry, vol. 58, pp. 18-27, 1966.